UNIVERSITÀ
DEGLI STUDI
FIRENZE

PhD in
Earth Sciences

CYCLE XXXV

COORDINATOR Prof. Moretti Sandro

Study of the seismo-acoustic energy radiation by debris flows

Academic Discipline (SSD) GEO/10

Doctoral Candidate
Dr. Belli Giacomo

Supervisor
Prof. Marchetti Emanuele

_____ _____

Coordinator
Prof. Moretti Sandro

_____

Years 2019/2022

Contents

Abstract

This doctoral thesis is focused on the study of the seismo-acoustic energy radiation by debris flows. Occurring within steep mountain catchments as sudden floods carrying large amounts of boulders and solid debris, debris flows represent a major hazard in worldwide mountain environments.
The debris-flow monitoring is traditionally performed following a wide range of approaches, involving rainfall forecast and measurements and catchment observations. In the last 20 years, the use of seismo-acoustic signals for the study and monitoring of debris flows gained attention worldwide.
Indeed, a debris flow radiates elastic energy both in the atmosphere, in the form of infrasound, and in the ground in the form of seismic waves. Seismic waves are believed to be generated by solid particle collisions, turbulent structures and friction with riverbed and banks, while infrasound is believed to be generated by flow waves that develop at the free surface of the debris flow. However, the radiation processes of both wavefields are not yet fully understood and open questions remain in linking the generated geophysical signal to the debris-flow dynamics and parameters.

To investigate the seismo-acoustic radiation processes within debris flows, this thesis presents the analysis of the infrasonic and seismic signals generated by the debris-flow activity in the Illgraben catchment (Switzerland, Canton Valais) between 2017 and 2019, when 18 events were observed. Each event was characterized in terms of hydraulic and physical parameters (front velocity, flow depth, flow density).
The infrasonic and seismic signals were analysed both in the time domain, performing the root mean square amplitude (RMSA) analysis, and in the frequency domain, computing the signal spectra with the Fourier analysis. These analyses allowed to characterize the signals in terms of amplitude envelope, maximum infrasonic and seismic RMSA, frequency content and peak frequency.
Despite an excellent match resulted between the recorded infrasonic and seismic maximum amplitudes and despite the RMSA analysis showed that the Illgraben debris-flow events are characterized by a distinctive succession of the seismo-acoustic source processes, which tend to be repeated during each event, the infrasonic and seismic signals show clearly different frequency contents, indicating that the two wavefields are generated by different decoupled processes simultaneously acting at the flow surface and at the riverbed respectively.

The relation between seismo-acoustic signals was further investigated by applying the cross-correlation analysis. The strong cross-correlation resulted between infrasonic and seismic primary signal components indicates that the two wavefield are closely related and suggest that, despite being decoupled, they are equally modulated in amplitude. In addition, results showed that the seismo-acoustic cross-correlation can be used to roughly locate the debris-flow events along the Illgraben channel.

Furthermore, to deeply investigate the infrasound source mechanism within debris flows, the array processing was applied to the recorded infrasonic data. The analysis revealed that the infrasound by debris flows is dominated by coherent signal components generated in fixed position along the channel, in particular in correspondence of check dams and other significant topographic irregularities of the Illgraben channel. Furthermore, the infrasonic array processing permits to identify the position of the infrasonic source, thus allowing to track the motion of the debris flow along the entire Illgraben channel.

To investigate if and how the hydraulic parameters influence and control the seismo-acoustic energy radiation, the amplitude and frequency content of the infrasonic and seismic signals were then compared to the measured front velocity, depth and peak discharge. Results show a positive correlation with both infrasonic and seismic maximum RMSA, suggesting that seismo-acoustic amplitudes are controlled by these flow parameters. The comparison between seismo-acoustic peak frequencies and flow parameters instead revealed that, unlike seismic signals, characterized by a constant peak frequency regardless of the magnitude of the flow, infrasound peak frequency decreases with increasing flow velocity, depth and discharge.

Based on presented results and on previous models and experiments, a simplified conceptual source mechanism is proposed for the seismo-acoustic energy radiation by debris flows, according to which the infrasonic and seismic waves are generated by different source processes acting simultaneously at the ground and at the surface of the debris flow respectively, which, despite being intimately related to each other and equally modulated in amplitude, are clearly decoupled. In addition, results highlighted a strong influence of the flow parameters on the generated seismo-acoustic signals.

For seismic signals, presented results agree with previous models and observations of seismic energy radiation by rivers and debris flows, indicating that seismic waves are generated by solid particle collisions and friction with the riverbed and banks and by fluid dynamic structures.

For infrasound, non-stationary turbulence-induced waves and oscillations that develop at the free surface of the flow are thought to be the most likely source mechanism. The formation of such surface waves is enhanced wherever the flow encounters channel irregularities, such as significant

topographic steps, like check dams, and steep bends, which result as locations of preferential infrasound radiation, consistently with the results obtained from the infrasonic array processing. Moreover, large flow depth and/or velocity is expected to generate higher and larger waves at the free surface of the flow. The development and the motion of these flow surface waves pushes the atmosphere and thus radiates infrasound. This motion of the flow surface can be modelled as a series of vertical pistons generating infrasound at the frequency of the piston motion, which is controlled by flow parameters and channel geometry. This model is also in agreements with the empirical relationships resulted between the infrasonic features and flow parameters.

Finally, presented results highlight how the infrasonic and seismic recordings could be used for monitoring and warning purposes, not only for event detection, but also for the real time estimation of the event parameters.

Introduction

This doctoral thesis focuses on the analysis of the infrasonic and seismic energy radiation by debris flows. Debris flows are episodic, highly impacting mass movements, consisting of mixtures of water and solid debris in varying proportion [Coussot and Meunier, 1996], typically occurring within steep mountain catchments as a result of a sudden water supply [Badoux et al., 2009], mostly given by strong rainfalls or rapid snow melt [Dowling and Santi, 2014]. They tend to occur as several surges that flow long distances in steep torrential channels [Iverson, 1997], with a flow behaviour that has been described has intermediate between floods and landslides [Iverson and Vallance, 2001]. Given their high momentum and impact force, combined with the relatively high unpredictability, debris flows represent one of the major natural hazards in worldwide mountain environments [Dowling and Santi, 2014].

Despite the suddenness of the process trigger, the realization of accurate monitoring and early warning systems, aimed to reduce the debris-flow risk, is still possible. Indeed, given the moderate speed of the flows (generally < 10 m/s [Pierson, 1980]) and the relatively high length of the active stream channels (up to a few kilometres), the detection of a debris flow in its initial phases can allow the identification of an ongoing event some minutes before it reaches the most sensible sites, allowing them to be promptly secured.

Debris-monitoring is traditionally performed following a wide range of approaches [Arattano and Marchi, 2008; Badoux et al., 2009; Hurlimann et al., 2019], involving rainfall forecast and measurements as well as catchment observations, aimed at predicting the probability of triggering an event, and direct in-channel flow measurements, aimed at the real-time detection of an ongoing debris flow.

In the last 20 years, with the advancement of technology, new approaches have been adopted in the study and monitoring of debris flows. Among these, the use of the seismo-acoustic signals generated by the debris flows for research and monitoring purposes has gained attention worldwide [Arattano, 1999; Burtin et al., 2009; Burtin et al., 2014; Walter et al., 2017; Lai et al., 2018; Marchetti et al., 2019]. As a matter of fact, similarly to what has been observed for other mass movements, such as snow avalanches [Kogelnig et al, 2011; Marchetti et al., 2015] and pyroclastic density currents [Delle Donne et al., 2014], while flowing along the channel, a debris flow radiates elastic energy both in the ground, in the form of seismic waves, and in the atmosphere, in the form of infrasound (low frequency sound).

The use of these geophysical signals to study and monitor debris flows guarantees many advantages, as they allow a safe remote observation of the event and, being generally deployed in easy accessible sites out of the invasion area of the debris flows, involve lower maintenance and repair costs compared to in-channel sensors, which are instead frequently damaged or destroyed by the flows. In

addition, seismic and infrasonic measurements, when combined together or used in networks of sensors, have proven to be a very powerful tool for the study and monitoring of mass movements [Yamasato, 1997; Allstadt et al., 2018; Ulivieri et al., 2011; Vilajosana et al., 2008; Ripepe et al., 2009] and provide crucial information also on debris-flow events, since many characteristics of the geophysical signals reflect the hydraulic and physical features of the flows [Lai et al., 2018; Marchetti et al., 2019; Belli et al., 2022]. However, the radiation processes of both the infrasonic and seismic wavefields within debris flows remain not yet fully understood, especially in case of infrasound, and several open questions persist on linking flow behaviour and processes to resulting seismo-acoustic signal features.

This thesis presents the study of infrasonic and seismic signals generated by the debris-flow activity in the Illgraben catchment (Switzerland, Canton Valais) between 2017 and 2019, when 18 events were observed.

The main objective of this research is to investigate the mechanism of the seismo-acoustic energy radiation by debris flows and to understand how the generated signals are related to each other and how they relate to flow hydrodynamics. Particular attention is paid to the investigation of the source mechanism for the infrasonic waves, for which an accurate radiation model is still missing for debris flows. Eventually, this thesis aims to investigate how the recorded infrasonic and seismic signals could be used for the debris flow monitoring and early warning.

To achieve these goals, the infrasonic and seismic signals recorded for the 2017-2019 Illgraben debris flows are analysed, both in the time and in the frequency domain, respectively by applying the root mean square amplitude (RMSA) analysis and by computing spectra and spectrograms of the signals. These analyses allow to characterize the signals in terms of amplitude envelope, maximum infrasonic and seismic RMSA, frequency content and peak frequency. These parameters, obtained for both infrasonic and seismic signals, are then used to compare the two wavefields, highlighting the similarities and the differences between them. The relation between seismo-acoustic signals is further explored by applying the cross-correlation analysis, in which the waveform and spectral features of the signals are compared to investigate how closely the recorded signals are related to each other.

Furthermore, to investigate the infrasound source mechanism within debris flows, the array processing is applied to the recorded infrasonic data. The infrasonic array processing allows to discriminate coherent signals from noise and to characterize the signal in terms of wave parameters, which allow you to obtain crucial information on the source and its location.

The amplitude and frequency features determined for the seismo-acoustic signals are compared to the physical and hydraulic parameters (flow velocity, depth, density) measured for the analysed debris

flows. This comparison aims to investigate if and how the parameters of the debris flow influence and control its seismo-acoustic energy radiation.
All the collected evidence and results are then discussed and physically interpreted to characterize the seismo-acoustic radiation processes within debris flows and to develop a model for the infrasonic source mechanisms.
Eventually, based on the obtained results, the potential of using the seismo-acoustic recordings for the debris-flow early warning and monitoring is discussed.

The thesis is organized following the classical scheme for a scientific publication, based on the subdivision in the Introduction, Data, Methods, Results, Discussion and Conclusion sections.
The first chapter (Chapter 1) is an introductive framework on debris flows as a whole, focusing both on their physical description, composition, and triggering processes (Section 1.1), on their dynamics (Section 1.2), on their worldwide occurrence and impact (Section 1.3) and on their monitoring (Section 1.4).
Chapter 2 instead delineates the state of the art of the analysis and study of the debris flows based on seismic (Section 2.1) and infrasonic (Section 2.2) waves. This chapter also describes the source mechanism accepted nowadays for the two wavefields, also presenting the outcomes and results achieved by some of the most significant experimental, numerical and theoretical studies performed on these topics.
Chapter 3 ("Study site and dataset") is dedicated to the Illgraben study site, both describing the catchment and its debris-flow activity (Section 3.1) and presenting the existing debris-flow monitoring system (Section 3.2). Chapter 3 also describes the instrumental setup used (Section 3.3) and the database of the events analysed in this work (Section 3.4); in particular, for each event the measured flow parameters (flow volume, front velocity, maximum depth, density) and the recorded seismo-acoustic signals are presented.
The techniques of analysis applied in this thesis are presented in Chapter 4 (Methods). More specifically the chapter describes in detail the RMSA analysis (Section 4.1) and the spectral analysis (Section 4.2) of the seismo-acoustic data, the seismo-acoustic cross-correlation analysis (Section 4.3) and the infrasonic array processing (Section 4.4).
The presented techniques are then applied to the recorded debris-flow infrasonic and seismic signals and the obtained results are presented in Section 5.1 of the Chapter 5 ("Data analysis and results"). The Section 5.2 of this chapter presents instead the comparison between both the amplitude and frequency features of the seismo-acoustic signals and the measured flow parameters.

All the presented results are then discussed in Chapter 6 (Section 6.1 and Section 6.2), which also presents the physical interpretation (Section 6.3) of the experimental evidence, aimed at a characterisation of the seismo-acoustic source mechanism within debris flows. The implication for the debris-flow monitoring and early warning purposes are eventually discussed in Section 6.4.

Finally, after the “Conclusion” section, dedicated to the conclusive remarks, the “Appendix” section reports a table with all the variables used in the equations presented in the thesis together with additional figures of the results presented in this thesis.

Chapter 1

Debris flows

1.1 Physical description, composition and triggering processes

Debris flows are deeply impacting episodic gravitational currents that typical occur within steep (>20-30°) mountain stream catchments (Figure 1. 1, Figure 1. 2, Figure 1. 3). They consist of viscous highly concentrated mixtures of water, mud and solid debris particles in varying proportions [Coussot and Meunier, 1996; Pierson and Costa, 1987], of generally high density (~2000 kg/m^3 [Wang et al., 2018]). Their flow behaviour has been described by many authors as intermediate between floods and landslides [e.g., Iverson and Vallance, 2001].

Figure 1. 1 shows a debris-flow event occurred in the Gadria catchment (6.3 km^2, Vinschgau-Venosta Valley, BZ, Italy), one of the most active debris-flow catchments in Italy, producing an average of 1–2 events per year with volumes commonly exceeding 10,000 m^3 [Comiti et al., 2014].

Figure 1. 1: photo of a debris flow that occurred in the Gadria catchment (Italy) on 13 July 2018 (source: Civil Protection Agency of the Autonomous Province of Bozen-Bolzano). The channel is ~10 m wide.

Figure 1. 2 and Figure 1. 3 instead show two different debris-flow events in the Illgraben catchment (~10 km^2 [Schlunegger et al., 2009], Canton Valais, Switzerland). Triggering every year an average of 3-5 events with volumes of tens of thousands of cubic meters [Wenner et al., 2019] and being heavily instrumented by Swiss national authorities and institutes, the Illgraben basin is the best laboratory site for debris-flow study in Europe, and among the best in the world [Badoux et al., 2009].

Figure 1. 2: photogram (source: Pierre Zufferey, https://www.youtube.com/watch?v=0ENe7wDKP6I) of a debris flow observed in the Illgraben catchment (Switzerland) on 22 July 2016. The debris flow transported large boulders, mostly concentrated in the flow front, with diameters up to ~4 m. The channel is ~10 m wide.

Debris flows typically occur as several rapid gravity-driven surges flowing in steep mountain stream-channels, with volumes commonly exceeding thousands of m^3 [Coussot and Meunier, 1996; Iverson, 1997] and with flow heights commonly ranging between few tens of cm and 4 m, although volumes up to tens of millions of m^3 and heights up to 20-25 m have been observed in case of extreme events [Rickenmann, 1999].

Figure 1. 3: photo (source: WSL institute of Zurich [Meyrat et al., 2021]) of a debris flow that occurred in the Illgraben catchment (Switzerland) on 20 August 2020 and flowing over a check dam realized to dampen debris-flow impact.

Debris-flow velocities typically range between 0.5 and 10 m/s [Sharp and Nobles, 1953; Johnson, 1970; Pierson, 1980], although Rickenmann [1999] reports velocities up to 30 m/s. Flow velocity reflects flow rheology that, in turn, is determined by bed slope, flow depth, bed roughness and composition (water content, solid fraction, particles diameters) [Silbert et al., 2001; Johnson et al., 2012; Zhang et al., 2021b].

Depending on the morphology of the basin and the characteristics of the debris flow, the runout distance of the debris flow varies from a few hundred meters up to ~10 km [Rickenmann, 1999].

The observed variability in debris-flow features results thus from the variability in debris-flow composition and geomorphological settings where these phenomena occur.

Within debris flows, solid volume fraction typically ranges between 40 and 90 % [Coussot and Meunier, 1996; Iverson, 1997], with transported solid particles size varying from clay up to boulders of a few meters [Perez, 2001] (Figure 1. 1, Figure 1. 2, Figure 1. 3).

While larger boulders represent the most important feature for debris-flow impact on infrastructures [Ng et al., 2021], the debris-flow clay content plays a key role in the flow mobility, that depends on

the ability of the flow to support solid particles. A growth of the clay matrix content increases the density of the fluid phase of the debris flow; this leads to a larger buoyancy of the solid particles and therefore to an increased ability of the debris flow to support the solid load, thus resulting in a higher flow mobility.

Therefore, based on the fine fraction content, debris flows are classified between two end members: muddy and granular debris flows. On one side, the *muddy* or *cohesive debris flows*, within which the clay content is large enough (>10%) for the fine particles-water mixture to form an interstitial fluid which lubricates grain motions and imposes its behaviour type on the whole material [Coussot and Meunier, 1996]. On the other side the *granular debris flows* (or *not cohesive*), within which, due to the lower clay content, the direct grain contacts and collision play a major role on the whole mass behaviour. Obviously, various intermediate flow conditions exist in nature [Coussot and Meunier, 1996].

Debris-flow initiation requires a large amount of loose debris, steep slopes, and a source of abundant water [Badoux et al., 2009], generally given by intense rainfall events, natural or artificial dam collapses or rapid snowmelt. Most debris flows initiate when static water-laden sediment begins sliding frictionally, liquefies and propagates downstream in the form of a heterogeneous surge, characterized by a high-friction coarse-grained flow front and a more fluid body [Costa and Williams, 1984; Iverson, 1997].

Two main type of initiation processes are reported in literature for debris flows [Coussot and Meunier, 1996]. The first one [Sheko, 1988] consists in the progressive transition of a landslide into a debris flow due to an energy increase or due to a water supply. The second class of triggering processes, which is the most frequent in the Alps, essentially relies on a generalized erosion of the surface of a stream basin [Bossan, 1992]. Debris flows are likely due to the conjunction of small-scale bank slides or collapses, bed erosion and solid transport [Davies, 1986]. In some cases, all these phenomena can contribute to a chain reaction in the form of an irreversible increase in solid concentration, due to a progressive transition in transport and erosion capacity of the flowing fluid [Sheko, 1988]. However, exceptional rainfall events (i.e. monsoons, winter storms, tropical cyclone storms and summer thunderstorms or rainstorms) are the most common debris-flow triggering processes [Dowling and Santi, 2014]. Other exceptional initiation processes may also trigger a debris flow, like natural river dam failures or moraine lake edge ruptures [Takahashi, 1981; Liliboutry et al., 1977], rapid snowmelt [Dowling and Santi, 2014], ice avalanches [Plafker et al., 1971], volcanoes flank collapses [Dowling and Santi, 2014] or earthquakes [Solonenko, 1963]. Finally, lahars, a particular kind of volcanic mudflows or debris flows, are then intimately linked to volcanic activity or settings [Pierson, 1986].

1.2 Fluid dynamics

Debris-flow motion and behaviour is unsteady and nonuniform [Iverson et al., 1997] and, from a rheological point of view, debris-flow propagation must be modelled with non-Newtonian fluid mechanics [Coussot and Meunier, 1996]. As a first approximation, a debris flow can be represented as a mass of a single viscous material undergoing homogeneous deformations without significant changes to its mechanical properties.

Debris flows are non-Newtonian mixtures of water and solid particles that can be described as viscoplastic fluids [Whipple and Dunne, 1992], Bingham fluids [Bingham and Green, 1919; Johnson, 1970], or Bagnold fluids [Chen, 1988]. The Bingham model represents the simplest constitutive equation for non-Newtonian fluids [Bingham and Green, 1919; Wang, 2002]:

$$\tau = \eta\varepsilon + \tau_B \qquad \text{(Eq. 1. 1)},$$

where τ is the shear stress of the flow, ε is the shear rate, which in a laminar flow is equal to the velocity gradient, and η is the rigidity coefficient. τ_B is the yield shear stress, i.e. the minimum shear stress that needs to be overcome to allow the material to move and the flow to develop. A Bingham fluid can flow into an open channel only if the driving shear stress τ is larger than the yield shear stress of the fluid τ_B, or, equally, if the flow depth is larger than the critical depth (h_{cB}) [Wang, 2002], for which the resulting shear stress is larger than the fluid yield stress. Therefore, for material mobilization, it is required that the material thickness overcomes a threshold value. This critical threshold depth depends on the slope of the channel and on the fluid density (ρ_f) as:

$$h_{cB} = \frac{\tau_B}{E_S g \rho_f} \qquad \text{(Eq. 1. 2)},$$

where E_S is the energy slope, i.e. the amount of energy lost to friction along a given length of channel. Debris-flow yield stress likely results from the solid particle interaction network which develops within the material [M'Ewen and Pratt, 1957; Firth and Hunter, 1976; Coussot and Piau, 1994] and it needs to be broken to allow the flow to take place. The yield stress increases exponentially with increasing solid fraction [Coussot and Meunier, 1996]. Any rheological model that does not takes into account the yield stress, such as a Newtonian fluid model, is incapable of predicting flow mass stoppage, typically leading to massive poorly structured and granulometrically heterogeneous debris-flow deposits [Johnson, 1970; Friedman et al, 1992; Phillips and Davies, 1991].

1.2.1 Debris-flow dynamical composition

Debris flows consist of a mass of solid particles (boulders and stones) surrounded by a liquid phase, represented by a muddy fluid. Their motion is strongly dependent on the relative amount of solid and fluid masses [Meyrat et al., 2021].

Based on flow dynamics and composition, a debris flow generally can be longitudinally subdivided in three main flow parts (Figure 1. 4, Pierson, 1986): the boulder-rich front (or snout), the flow body and the flow tail [Coussot and Meunier, 1996].

The boulder-rich front transports rocks of all sizes and mud and tends to hydraulically act as a compressive granular flow, dominating flow resistance to motion [Iverson, 1997]. The steep boulder-rich snout can reach several meters in height [Arattano and Marchi, 2008] and is typically the most impactful portion of the flow (Figure 1. 5). After the boulder-choked head passes, the river channel remains filled with a debris-laden torrent of mud and boulders clanking and grinding together, i.e. the more fluid flow body [Johnson and Rodine, 1984; Iverson, 1997]. The flow tail is the final part of the flow that gradually leads to the restoration of the normal stream flow conditions in the channel and is characterized by lower and progressively decreasing solid fraction and flow height, compared to flow front and body.

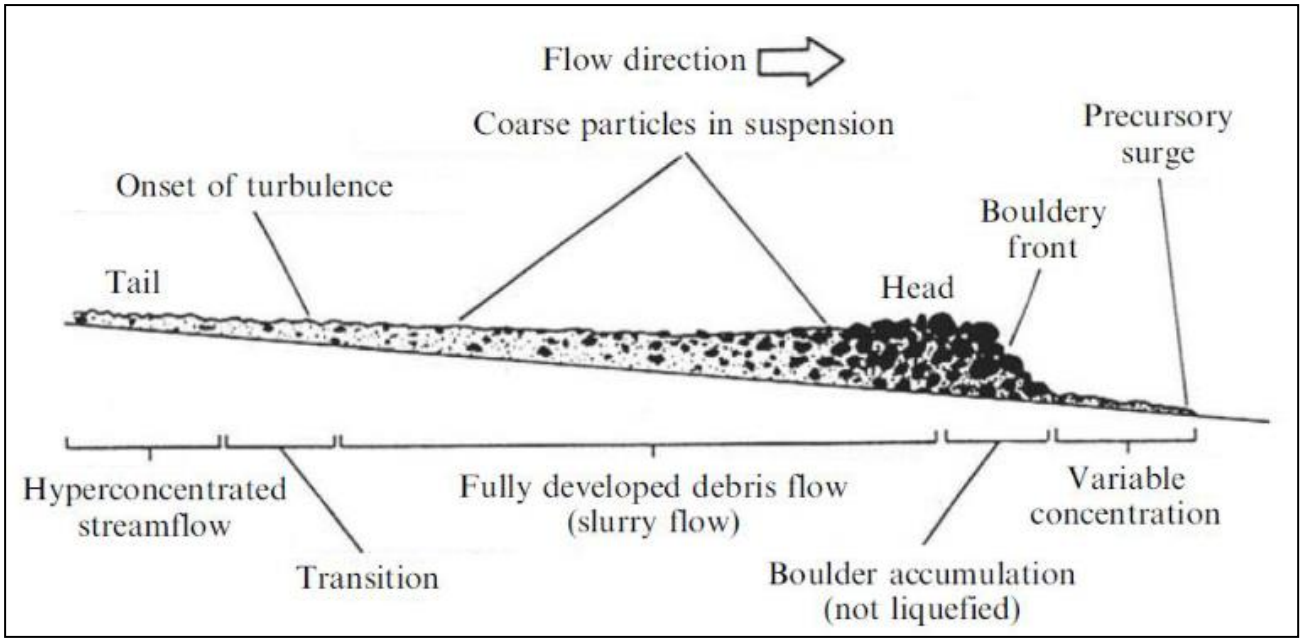

Figure 1. 4: sketch of the typical debris-flow structure [Pierson, 1986].

Figure 1. 5: photo of the boulder-rich front of the 2019/08/11 Illgraben debris flow passing over a check dam (source: WSL). At the dam brink, the flow is ~6-7 m wide.

Parallel to this longitudinal subdivision, Meyrat et al. [2021] propose a vertical subdivision of the flow based on the relation between the solid and the fluid phases. In particular they suggest a stratification in two superimposed layers (Figure 1. 6). The first basal layer consists of a mixture of solid particles and an *intergranular muddy fluid* that is dynamically bounded to the solid phase. The second layer instead consist of the *free fluid*, i.e. the part of the muddy fluid that is free to move independently from the solid phase and from the first layer. Being dynamically independent of the solid phase, the free fluid can escape the solid phase, leading to debris-flow de-watering and eventually to its stoppage and sedimentation, as the debris flow gradually slows down [Meyrat et al., 2021].

While the first layer is distributed along the entire flow, despite with decreasing both its solid content and its height from the debris-flow front to the tail, the second layer develops at the roof of the first layer only behind the end of the flow front (Figure 1. 6).

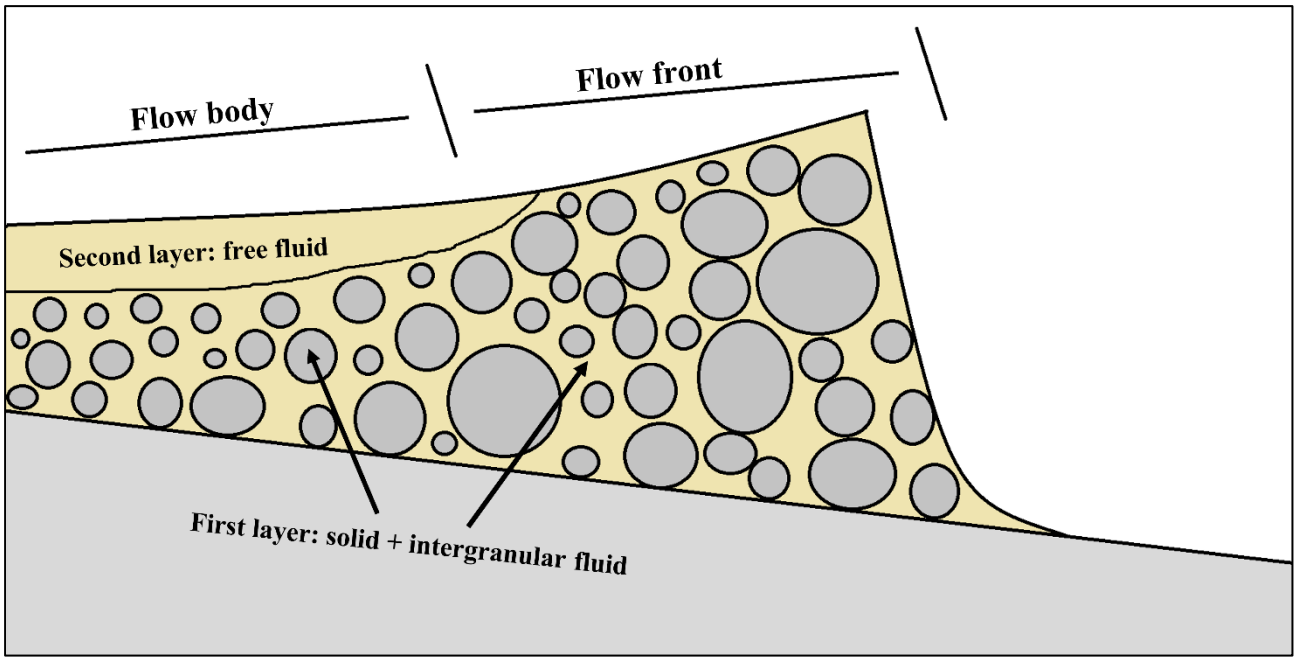

Figure 1. 6: vertical stratification of a debris flow in two layers (redrawn from Meyrat et al., 2021). The first layer consists of the solid mass and the intergranular fluid, which is bound to the solid phase. The second layer is composed of the free fluid, which is free to move independently from the solid phase.

From a fluid mechanics point of view, flow front and body (at the level of the first layer) can be considered as a one-phase flow of a viscous fluid, within which relative velocity of two close elements (water and solid) is low [Pierson, 1986; Costa and Williams, 1984], so that the whole mass apparently undergoes very large and approximately continuous deformations.

The flow tail instead typically consists in a two-phase hyperconcentrated flow, within which there is a significant relative velocity between coarser solid particles and water-solid suspension [Smart and Jaeggi, 1983; Coussot and Meunier, 1995]. The hyperconcentrated debris-flow tail generally has a high solid fraction (40-55%) [Pierson, 1985a] compared to typical hyperconcentrated flows (1-25%) [Coussot and Meunier, 1996], but significantly lower than the solid fraction observed for the flow front and body (50-90%).

The fluid mechanical differences between the flow tail and the previous two parts of the flow reflect the observed solid fraction jump. As a matter of fact, for given solid material and flow characteristics, there certainly exists a certain particles concentration threshold beyond which a continuous interacting network between solid particles develops. This gives rise to material strength or rigidity within the flow [Coussot and Piau, 1994], increasing the solid particles transport capability of the flow. In the first stages of the flow (flow front and body), the solid particles fraction and, therefore, the flow strength, are sufficiently high to allow the debris flow to transport even larger boulders and the flow behaves as a monophasic flow. Eventually, due to lateral deposition or a decrease in sediment

supply, the flow particles concentration falls below the critical threshold and coarser particles start to be deposited on the riverbed and the flow no longer behaves as monophasic flow but as a two-phase flow (flow tail). As it flows downward the catchment, a debris flow progressively deposits particles and its solid fraction decreases (<50%), leading to the transition to hyperconcentrated flow.

However, debris flows may also act as an erosive flow, characterized by a stream erosion action significantly different from that of other flows. Indeed, once formed, debris flows intensely scrape the streambed [Coussot and Meunier, 1996] and, if the torrent bed slope increases, a debris flow may also turn into an erosive flow, thus increasing its solid fraction while flowing. This phenomenon, known as *bulking*, perturbs the debris-flow dynamic transition to hyperconcentrated-flow [Cannon et al., 2003; Frank et al., 2015] and extends the life of the solid transport capability, thus increasing debris-flow runout distance.

Water content is an important control factor in determining dynamic mechanism of debris flows, as it lubricates some relative motion of the granular material or it behaves as the vehicle of colloidal interactions between clay particles in the flow [Coussot and Meunier, 1996]. Furthermore, high pore-fluid pressures, leading to sediment liquefaction, can significantly reduce the debris-flow resistance to motion [Iverson, 1997], thus increasing flow runout distance. As a matter of fact, many authors observed that, during slope failure, within the debris-flow body, pore-fluid pressure can apparently rise to levels sufficient to liquefy the sediment, thus promoting the flow motion [Iverson et al., 1997; Major et al., 1997; Reid et al., 1997]. In contrast, the flow front lacks high pore pressures and resists motion as the low-friction flow body pushes it from behind.

1.2.2 Flow behaviour: open channel flow

Debris flows fall into the open channel flow domain. Unlike flow within pipes, open channel flows are characterized by a free water-air interface at the flow surface [Henderson, 1996; Chaudhry, 2008]. This reduces the importance of the fluid pressure in the flow dynamics, that instead plays a key role in pipe flows, and leads to a hydrostatic pressure distribution within the flow, so that open channel flows are basically gravity driven [Henderson, 1996; Chaudhry, 2008].

In rivers and creeks, the channel is uneven, due to the presence of a rough floor and both natural and artificial irregularities, such as steps, bends and channel width changes among the former, and weirs, sills and check dams among the latter. Such disturbances operate on the flow, leading to development

of waves or oscillation at the surface of the flow as a result of unsteady flow conditions [Henderson, 1996].

These waves are gravity waves [Ferrick, 1985; Chaudhry, 2008], i.e. waves that are generated in a fluid or at the interface between two fluid when the force of gravity tries to re-establish an equilibrium previously perturbed. River waves are characterized by a wavelength that is much larger than the depth of the flow and therefore are classified as shallow-water waves [Ferrick, 1985; Chaudhry, 2008]. Shallow-water waves, resulting from any irregularity or obstacles, in open channel propagate at the surface of the flow with a velocity (v_w), defined as [Henderson, 1996; Chaudhry, 2008]:

$$v_w = \sqrt{gH} \qquad \text{(Eq. 1. 3)},$$

where H is the flow depth and g is the acceleration of gravity. Disturbances in open channel flow, such as the one generated at channel irregularities, propagate over the water surface at the velocity v_w, that is measured with respect to the water, not to the banks, and, according to Eq. 1. 3, depends only on the flow depth [Henderson, 1996; Chaudhry, 2008].

v_w is equal to critical velocity (v_c):

$$v_w = v_c = \sqrt{gH} \qquad \text{(Eq. 1. 4)},$$

which is measured relative to the banks and is the velocity of the flow at critical conditions, corresponding to the minimum value of specific energy of the flow (E) [Henderson, 1996], defined as:

$$E = H + \frac{v^2}{g} \qquad \text{(Eq. 1. 5)},$$

where v is the flow velocity measured with respect to the banks and the ratio $\frac{v^2}{g}$ defines the velocity head.

The relative values of the potential energy (depth) and the kinetic energy (velocity head), that sum up into the total specific energy (E), are important for the analysis of open channel flow, as they determine flow conditions.

An important parameter to describe flow conditions relative to criticality for open channel flows is the Froude number (Fr), that, in case of a rectangular channel section, is defined as [Henderson, 1996; Chaudhry, 2008]:

$$Fr = \frac{v}{\sqrt{gH}} \qquad \text{(Eq. 1. 6).}$$

For non-rectangular section H should be replaced with the ratio between cross-section area and flow free-surface width [Henderson, 1996]. As defined, the Froude number expresses the ratio between flow velocity and the velocity of any perturbation generated in the flow as the result of encountered channel irregularities and obstacles, like natural and anthropogenic topographic steps or variations in the channel geometry [Henderson, 1996].

Such perturbations propagate at the free surface of open channel flows at the same velocity (v_w) both upstream and downstream. However, the velocity of perturbations vectorially sums up with the flow velocity. Indeed, the waves induced by the channel irregularities migrate along the channel with a velocity (v_{wc}) which is equal to the vectorial sum of the wave velocity and the flow velocity as:

$$\overrightarrow{v_{wc}} = \vec{v} + \overrightarrow{v_w} \qquad \text{(Eq. 1. 7),}$$

where v_{wc} is measured with respect to the banks.

For all the velocity vectors, the norm is here considered positive if its direction is downstream, and negative vice versa. Therefore, the norm of the flow velocity is of course always positive. In contrast, since the surface waves propagate both upstream and downstream, the verse of $\overrightarrow{v_w}$ will be negative and positive respectively.

Therefore, the norm of $\overrightarrow{v_{wc}}$ is given by:

$$v_{wc} = v + |v_w| \qquad \text{(Eq. 1. 8),}$$

for the waves propagating in same direction of the flow, and:

$$v_{wc} = v - |v_w| \qquad \text{(Eq. 1. 9),}$$

When the perturbations travel against the flow.

For $Fr < 1$, the flow is subcritical (slow); the perturbations caused by channel irregularities propagate at a speed (v_w) that is higher than the velocity of flow (v), so that v_{wc} can be both negative and positive (Eq. 1. 8 and Eq. 1. 9) and the perturbations can thus travel both upstream and downstream in the channel. Therefore, in subcritical flows any channel feature acting as a control for the flow (i.e. setting a specific relationship between flow depth and discharge) determines the further upstream flow conditions [Henderson, 1996].

Critical flow, instead, is set when Froude number equals unity and represents the condition in which, for a given discharge per unit channel width, the flow has the minimum specific energy and its velocity equals the critical velocity (v_c; $v = v_c$) [Henderson, 1996; Chaudhry, 2008]. At critical flow conditions the velocity of perturbations equals flow speed ($v_w = v = v_c$), and, for the waves travelling against the flow, we obtain $v_{wc} = 0$ (Eq. 1. 9); the surface perturbations are thus not able to propagate upstream and standing waves develop at channel irregularities. For an observer standing on the banks, these waves appear to be stationary in the channel. For the waves travelling in the same direction as the flow, on the other hand, we obtain $v_{wc} = 2v$ (Eq. 1. 8): these waves therefore propagate downstream with a velocity that, with respect to the banks, is exactly double the velocity of the flow.

For $Fr > 1$ supercritical flow conditions develop. In these conditions the flow velocity is higher than the speed of perturbations inside it. Therefore, v_{wc} is always positive (Eq. 1. 8 and Eq. 1. 9) and the flow surface waves caused by channel irregularities are thus no longer able to travel upstream and can only propagate downstream. Therefore, any important channel feature controls and rules the downstream flow but it is not able to influence the upstream flow regime in the slightest [Henderson, 1996]. In supercritical conditions upstream flow is thus completely independent of downstream channel features.

Computations of Froude number revealed that, within debris flows, flow conditions range from subcritical to critical and supercritical [Pierson, 1995], reflecting the wide variability observed in flow velocity and, to a lesser extent, depth.

For example, in case of a debris flow with $H = 3$ m, a low flow velocity of 2 m/s will lead to a $Fr = 0.37$, representative of a subcritical flow. In contrast, for a debris flow with the same height, a higher flow velocity of 20 m/s will set $Fr = 3.7$, defining a debris flow well inside the supercritical domain. A debris flow with a velocity of 5 m/s will be instead incharacterized by a supercritical $Fr = 2.3$, in case of a flow depth of 0.5 m, and by a subcritical $Fr = 0.80$, if the flow depth is equal to 4 m.

The Froude number is therefore indicative of the flow regime conditions relative to surface perturbations. According to flume experiments modelling shallow water flows in mountain torrents with a gravel bed [Horoshenkov et al., 2013], water level undulations at the free surface of the flow are produced along the entire flow by the interaction of the flow with the bed roughness (Figure 1. 7), generating turbulence structures and inducing inherent instabilities and oscillations at the flow surface [Henderson, 1970]. The generated water profile tends to reproduce the shapes of the riverbed, drawing structures in phase with the irregularities of the riverbed [Chanson, 2000; Comiti and Lenzi, 2006].

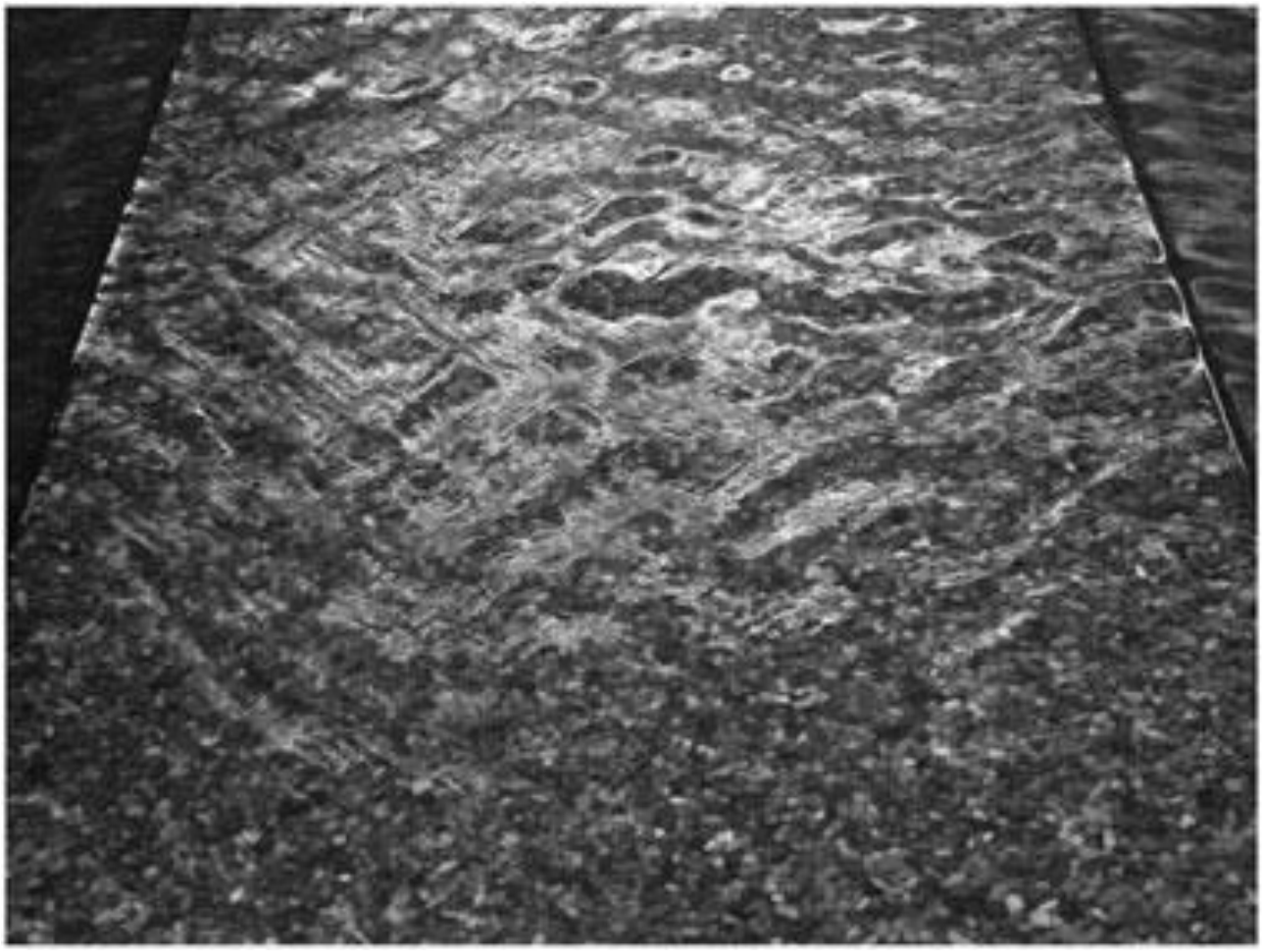

Figure 1. 7: photo of the flow surface pattern (oscillations) observed in the flume experiment performed by Horoshenkov et al. [2013]. The surface irregularities are generated due to flow interaction with the bed roughness.

However, the formation of these surface waves, water splashes and oscillations in natural streams is enhanced in fixed position along the flow, in correspondence with substantial channel irregularities, such as major topographic steps, like at check dams [Henderson, 1996; Tokyay and Yildiz, 2007; Feng et al., 2014; Coco et al., 2021]. According to fluid dynamic models and flume experiments on water flows, irregularities (waves and splashes) are induced at the flow surface by turbulence structures generated in the flow for water falling at free overfall [Coco et al., 2021; Feng et al., 2014; Tokyay and Yildiz, 2007]. Indeed, at the base of free overfall at dams, there is a strong energy dissipation (up to >50% of the initial energy), due to water falling and impacting the floor and setting up vigorous circulation and turbulence, that in turn induce waves and heavy water splashes at the flow surface [Tokyay and Yildiz, 2007].

The dimensioning of surface irregularities generated in open channel flows is important for river engineering, and therefore has been subject of several studies [e.g. Comiti and Lenzi, 2006; Tokyay and Yildiz, 2007].

Comiti and Lenzi [2006] analysed the dimension of standing waves generated at artificial drops in critical flows within steep gravel bed, performing both targeted flume experiments and field surveys. The authors indicate that the amplitude and the length of generated water waves depend on several parameters, related both to hydraulic features (flow depth, flow velocity, Froude number, drop height) and to sediment characteristic (sediment size, sediment density) and increase with increasing flow depth. They also found a linear positive relationship between the length of generated flow waves and the Froude number.

Tokyay and Yildiz [2007], performing flume experiments on supercritical water flows, observed that the height of the water splashes or waves (A_{sp}) generated at the base of a supercritical free overfall linearly scales with the Froude number (Fr) (which increases with flow velocity) and with the square root of the product between the flow depth over the brink of the fall (H_b) and the height of the fall (z) as:

$$A_{sp} = 0.4532\, Fr\sqrt{z\, H_b} \qquad \text{(Eq. 1. 10)},$$

where A_{sp} is measured from the channel bottom (Figure 1. 8). They also found that the length of generated waves (L_{sp}) increases with the flow depth.

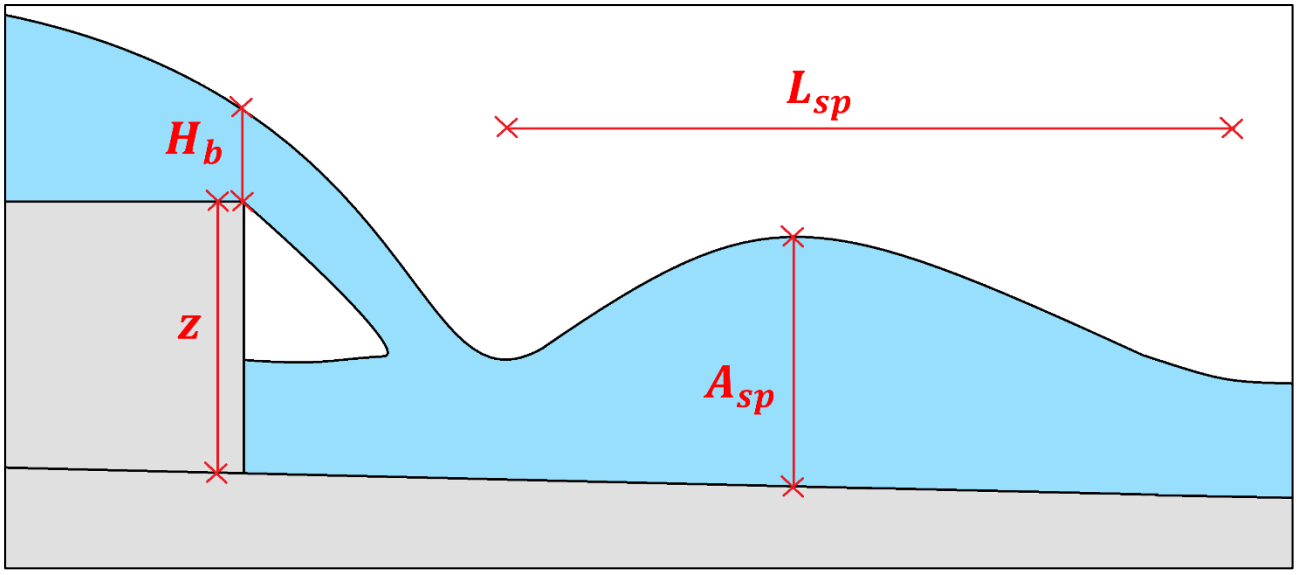

Figure 1. 8: dimensioning of a wave generated at the base of a supercritical free overfall (redrawn from Tokyay and Yildiz, 2007).

Concerning flow conditions, it is also important to distinguish between laminar and turbulent flow. In the laminar regime, the flow occurs along parallel streamlines that do not intersect each other. In the turbulent regime, the fluid flows in irregular paths, which are not fixed with respect to either time or space, and the streamlines intersect each other, giving rise to eddies and other flow structures and leading to energy dissipation [Henderson, 1996; Chaudhry, 2008].
In case of water flow (Newtonian fluids) the distinction between laminar and turbulent regimes is explicated by the Reynolds number (Re) defined as [Enos, 1977]:

$$Re = \frac{\rho v L_f}{\mu} \qquad \text{(Eq. 1. 11)},$$

where L_f is a characteristic dimension of flow that, in case of open channel flow, corresponds to the flow depth [Enos, 1977; Chaudhry, 2008], and μ is the dynamic viscosity of the fluid.
The Reynolds number physically represents the ratio between inertial forces and viscous force acting on a moving particle of fluid. Indeed, it is the relative magnitude of viscous and inertial forces that determines whether the flow is laminar or turbulent: when viscous forces dominate, the flow is laminar (low Re); if instead the inertial forces prevail, the flow is turbulent (high Re) [Chaudhry, 2008].
For a given fluid, therefore, the flow regime is controlled by flow velocity: increasing the flow velocity the transition from laminar to turbulent flow is observed. However, in real-life applications, laminar free-surface water flows are extremely rare [Chaudhry, 2008].
Indeed, in case of water flows in open channels (flow with a free air-water interface), the laminar regime is stable for $Re < 500$, while the turbulent regime fully develops for $Re > 2000$. A transition regime is established for intermediate Reynolds numbers [Enos, 1977]. If we consider a flow depth of 1 m, from Eq. 1. 11, turbulent flow is stable for flow velocity above a few mm/s.

In case of Bingham fluids, like debris flows, where flow mobility is ruled by the yield shear stress [Bingham and Green, 1919], the flow regime is not determined only by the Reynolds number, but is controlled also by another dimensionless parameter, the Bingham number, defined as [Enos, 1977]:

$$B = \frac{\tau_b L_f}{\mu_b v} \qquad \text{(Eq. 1. 12)}.$$

Investigating the transition between laminar and turbulent regimes of Bingham materials in pipe flows, Hedstrom [1952] found that the critical Reynolds number depends only on the Bingham number.

However, extrapolating this finding to open channel Bingham flows is challenging, so that the regime transition in these conditions is not defined by a unique threshold value [Enos, 1977].

Estimations of the Reynolds numbers suggested that generally debris flows are laminar [Coussot and Meunier, 1996]. Indeed, Bagnold [1954] found that an increase of the solid particle content in a flow leads to a decrease in turbulence, so that debris flows are likely more prone to the laminar regime compared to open channel water flows, for which this regime is quite unlikely [Choudhry, 2008]. However, the complexity increases due to various and complex solid particle interactions within the flow [Coussot and Meunier, 1996; Addison et al., 1987] and to the generally strong irregularity of the stream channel [Belli et al., 2021(a)], so that, depending on flow velocity and composition, turbulent debris flows are widely observed [Addison et al., 1987; Enos, 1977; Cui et al., 2015; Hürlimann et al., 2019]. In particular, the turbulent regime is generally observed in the boulder-rich snout, while the flow body and tail tend to fall into the laminar flow regime [Cui et al., 2015].

1.3 Debris-flow worldwide occurrence and impact

Debris-flow destructive potential, resulting from their high impact forces and their long runout distances, combined with the elevated unpredictability, due to the rapidity of the process trigger and the sudden initiation, makes debris flows among the most the dangerous processes in worldwide mountain environments [Dowling and Santi, 2014]. The occurrence of debris flows requires a sudden influx of water and steep mountain slopes, conditions easily met in many mountain catchments around the world and under different climatic conditions [Arattano and Marchi, 2008], so that this phenomenon threatens populated areas of more than 35 countries in South America, Europe, Asia and North America [Dowling and Santi, 2014], with the Andean, the Alpine and the Himalayan areas resulting the most debris-flow affected geographical settings [Sepulveda et al., 2006; Dowling and Santi, 2014; Singh et al., 2018]. Their huge boulder-rich debris load, characterized by high densities (~2000 kg/m^3) and volumes up to millions of cubic meters [Arattano and Marchi, 2008], combined

with the high velocities of the flow (commonly ~5 m/s, but up to >20 m/s) causes an enormous impact force [Hübl et al., 2009], making debris flows highly dangerous phenomena for surrounding urban areas and infrastructures.

Dowling and Santi [2014] estimated that, between 1950 and 2011, 213 fatal documented debris-flow events caused more than 77,000 deaths worldwide (Figure 1. 13), with the two most massive events killing 23,000 (Nevado del Ruiz, Colombia, 1985) and 19,000 (Vargas, Venezuela, 1999) people respectively.

In particular, the Nevado del Ruiz volcano 1985 eruption generated several lahar surges that, on 13 November, buried the town of Armero (Figure 1. 9), killing more than 20,000 of its 29,000 inhabitants and making the Nevado del Ruiz 1985 lahar event the worst volcanic mudflow disaster ever recorded in historic time [Voight, 1990]. Its death toll (23,000) ranks fourth in the history of volcanic disasters, behind only Tambora in 1815 (92,000) and Krakatoa in 1883 (36,000), both in Indonesia, and Mount Pelèe (Martinique), in 1902 (28,000) [Voight, 1990].

Figure 1. 9: photo of the town of Armero (Colombia), buried by the 1985 Nevado del Ruiz lahar event, when ~ 23,000 people were killed [Voight, 1990] (source: Steve Raymer, National Geographic).

In contrast, the 1999 Venezuelan debris-flow event, known as Vargas tragedy, was caused by the extreme rainfall that occurred in the north-central Venezuelan coast in December 1999. On 16 December several simultaneous debris flows, occurring in adjacent basins, invaded the city of

Caraballeda, (Figure 1. 10), killing thousands of people and destroying tens of thousands of buildings [Garcia-Martinez and Lopez, 2005], for a total economic damage estimated at more than 2 billion of US dollars [Lopez et al., 2003]. The event is the worst disaster caused by a natural phenomenon ever recorded in Venezuela and amongst the largest in Latin America [Wieczorek et al., 2001; Garcia-Martinez and Lopez, 2005].

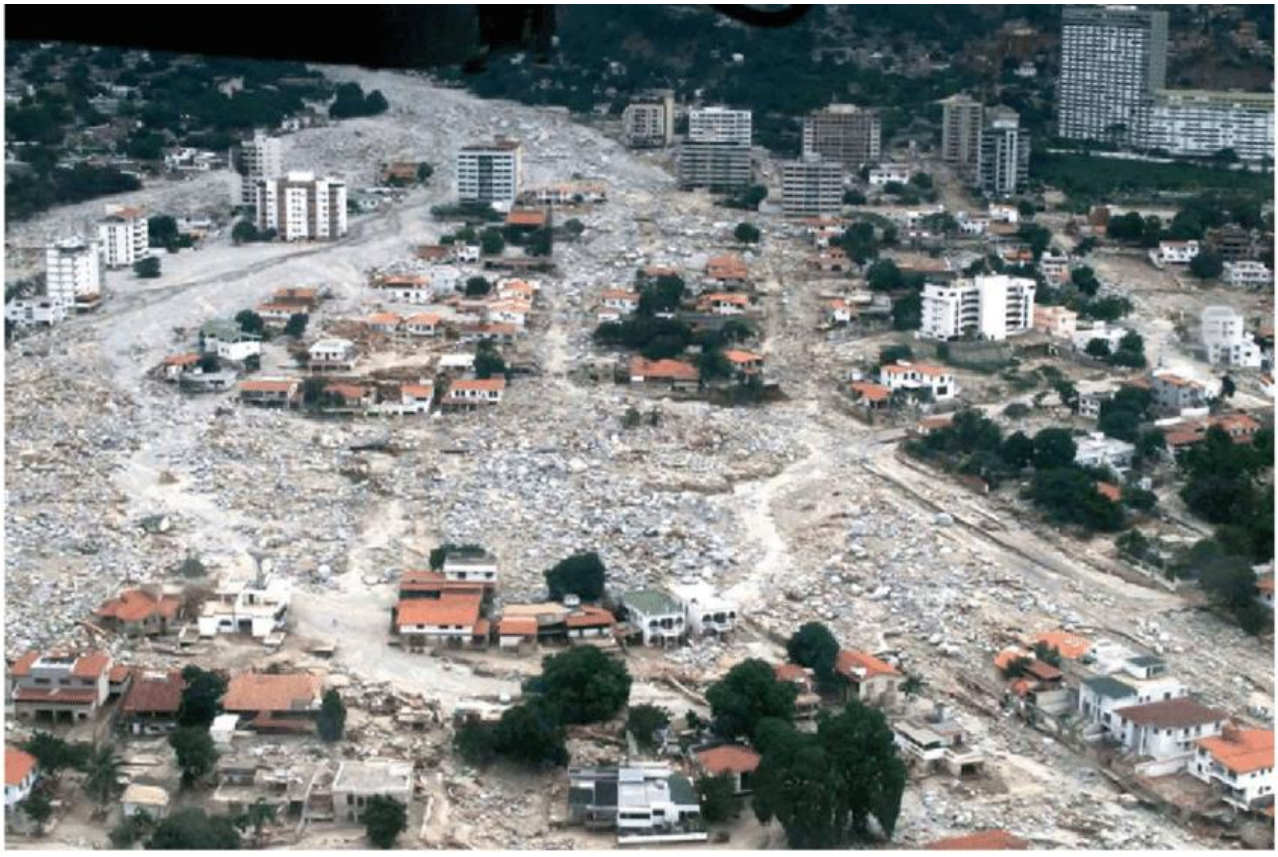

Figure 1. 10: photo of the city of Caraballeda (Vargas, Venezuela) invaded by the debris-flow events on 14-16 December 1999. In the event ~19.000 people died and thousands of houses and infrastructure were destroyed (source: Image: Smith, Lawson, US ACE; Paper: Wieczorek, G.F., Larsen, M.C., Eaton, L.S., Morgan, B.A. and Blair, J. L., Public domain, via Wikimedia Commons).

The highest debris-flow associated mortality is observed in South America and Asia, with the most affected countries being Colombia, Venezuela, Peru and Nepal [Dowling and Santi, 2014]. The reason for this negative primacy is probably to be attributed to their natural predisposition to debris-flow occurrence and to the high-density population that usually characterizes their mountain areas [Dowling and Santi, 2014]. However, even where debris flows do not directly threaten human lives they often cause severe damage to urban areas or infrastructures, such as roads or bridges, due to their high impact force [Arattano and Marchi, 2008].

Debris flows represent a serious hazardous phenomenon and a risk factor also in the Alps (Figure 1. 11), where Italy, Switzerland and Austria are among the countries with the highest number of reported debris flows in the world.

The Eastern Alps, where hundreds of debris-flow sites spread across Austria [Aulitzky, 1989; Schimmel and Hübl, 2015], Eastern Italy [D'Agostino and Marchi, 2000] and Slovenia [Mikoš and Majes, 2010], are more affected by debris-flow activity compared to the Western and Central sectors of the chain. Among the sites in Eastern Alps, the Lattenbach catchment (5.3 km^2), in Western Austria (Figure 1. 11), over the last decades generated several large (>10,000 m^3) debris flows, making this basin one of the most active debris-flow sites in the Alps [Hürlimann et al., 2019].

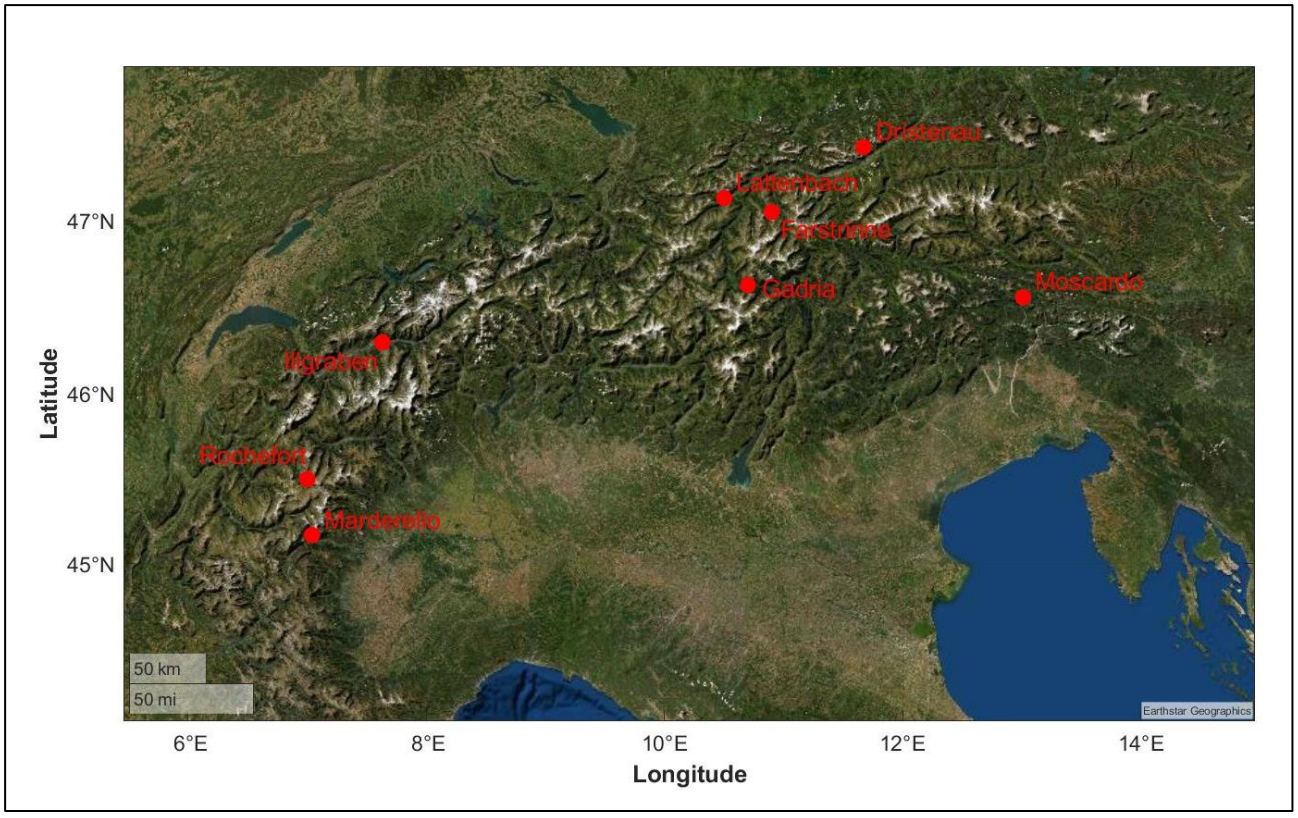

Figure 1. 11: location of some of the most active debris-flow sites in Europe.

In Switzerland, debris flows constitute a major threat for population and infrastructures [Zimmermann, 2004]. Schmid et al. [2004] reported an average of 17 documented damage-causing debris flows per year measured on a 30-year window, between 1972 and 2002, in the Swiss Alps. In particular, the Illgraben catchment, in the Swiss canton of Valais (Figure 1. 11), is the most active and the best instrumented debris-flow site in Europe [Badoux et al., 2009], frequently (3-5 times per year) generating flows exceeding tens of thousands of cubic meters [Belli et al., 2022].

In Italy there are several catchments prone to debris-flow activity (Figure 1. 11), mostly concentrated in the Dolomites and in the Carnic Alps. Among them the Gadria basin (Vinschgau-Venosta Valley; Autonomous Province of Bozen-Bolzano) in the Retic Alps, is probably the most important debris-flow site in Italy, producing an average of 1-2 event per year with volumes up to ~40,000 m^3 [Comiti et al., 2014]. Other very active sites in Italy are the Moscardo basin (Friuli Venezia Giulia, Udine), in the Carnic Alps [Marchi et al., 2002] and the Marderello basin (Cenischia valley, Piemonte, Torino), in the Graian Alps.

On 5 August 2022, a debris flow of several tens thousands of m^3 developed in the Rochefort stream, on the Italian side of the M. Blanc massive (Courmayeur, Aosta, Italy) (Figure 1. 11), primed by a rainstorm combined with a phase of heavy ice melting that hit the Western Alps throughout summer 2022. The flow invaded the main road in Val Ferret, causing serious damage to a bridge and temporarily interrupting the supply of drinking water to the municipality of Courmayeur (Figure 1. 12).

Figure 1. 12: the 5 August 2022 debris flow in the Rochefort stream (Aosta, Italy). Left: photo of the road invaded by the flow (source: Ansa.it, previously published by rainews.it). Right: photo of the road bridge destroyed by the event (source: Giacomo Belli).

The worldwide impact of debris flows on human lives and activities has increased in the last decades, both because, with the growth of the world population, the inhabited centres have largely expanded to piedmont regions [Dowling and Santi, 2014], and because of climatic changes, which involve more frequent extreme meteorological events, causing more catastrophic debris-flow, flood and landslide events [Stoffel et al., 2014].

In addition, in the Alps and in other mountain areas, where global warming impacts more heavily compared to other geographic settings [Inouye et al., 2020], the rising of temperature is leading to a gradual and progressive degradation of the high-altitude permafrost [Haeberli et al., 1993]. This causes an increase of slope instability [Ravanel et al., 2017], increasing the occurrence rate of mass movements, such as debris flows, in areas already affected by these phenomena, and also priming the debris-flow activity in previously unaffected areas [Sattler et al., 2011; Damm and Felderer, 2013].

Despite the high destructive potential of debris-flow activity, the moderate flow velocities (typically <10 m/s) make early warning in principle possible if an appropriate monitoring system, able to detect debris-flow events upon formation, is available.

Accurate studies and research on debris flows are thus necessary to achieve a deeper understanding of the flow dynamics and triggering processes, useful for developing early warning systems as accurate as possible and thus reducing the associated risk. Indeed, debris-flow impact and associated mortality are significantly higher in less developed countries (Figure 1. 13; Figure 1. 14) [Dowling and Santi, 2014], clearly indicating that scientific research and the monitoring of debris flows, combined with an appropriate infrastructural intervention for the risk reduction, can considerably reduce the destructive potential of debris flows and lahars. It is noteworthy, in fact, that although the largest number of debris-flow events are reported in countries such as the United States, Italy and Japan, these countries are not among the countries with the highest mortality or damage induced by debris flows [Dowling and Santi, 2014] (Figure 1. 13; Figure 1. 14 a). This is probably due to their greater effort, compared to least developed countries, in debris-flow research and associated risk reduction, performed with the realization of hydraulic works for the safety of the debris-flow channel and/or of efficient monitoring systems.

As an example, at the Illgraben catchment (Switzerland), to reduce the impact of the several debris flows affecting the basin every year, a series of 30 check dams (Figure 1. 15), including a ~50 m high retention dam, has been realized along the entire stream [Glassey, 2013], between 1967 and 1970, to stabilize the channel, damp erosion, and to dissipate the energy of the flow [Henderson, 1996].

Since then, despite the proximity of the Illgraben channel to rather populous inhabited centres, no significant damage has been caused by the hundreds of events that have occurred in the following decades.

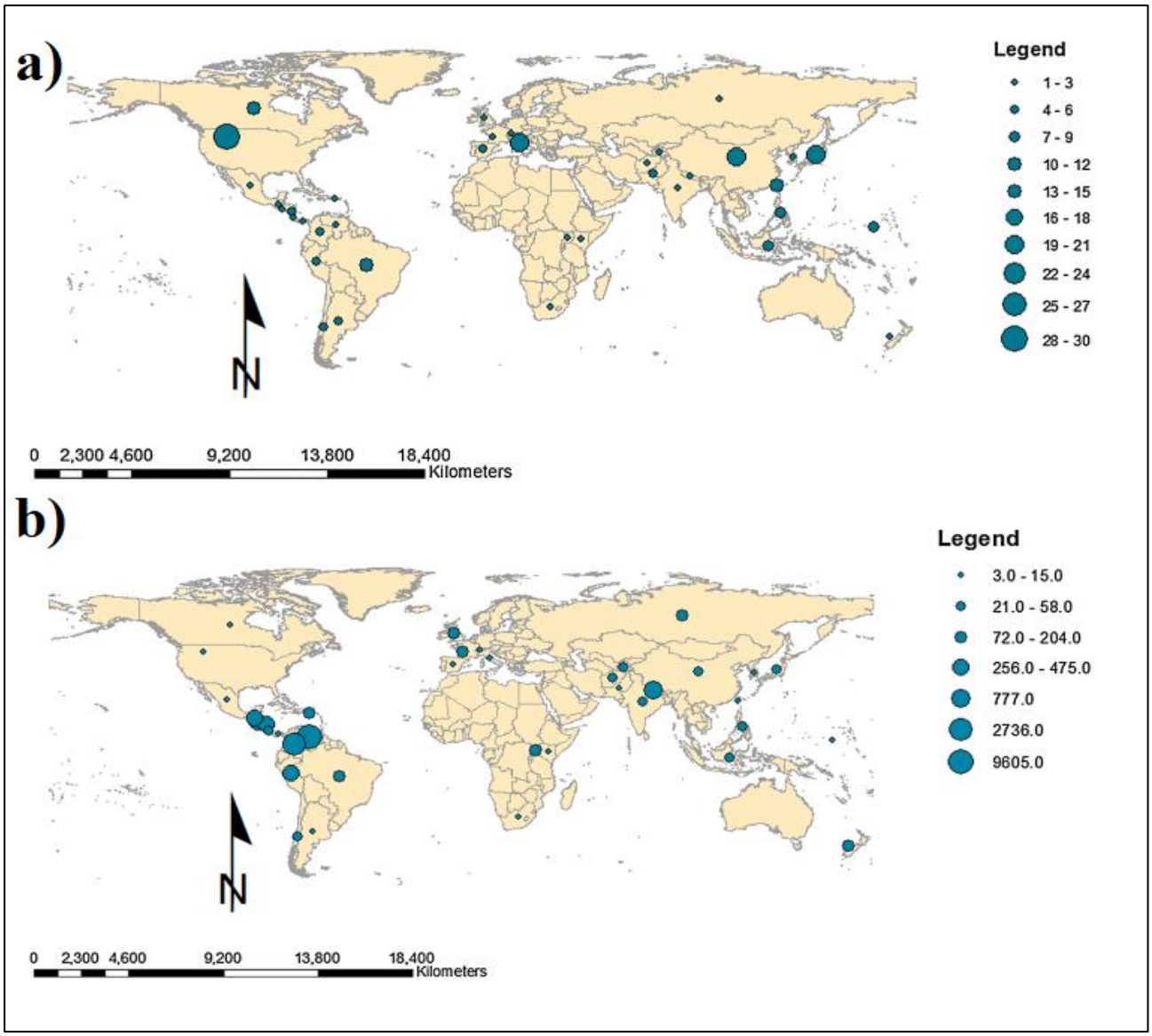

Figure 1. 13: global analysis of debris-flow fatalities from 1950 to 2011 [Dowling and Santi, 2014]. Number of recorded fatal debris flows in the different analysed countries (a): the size of the circles represents the number of recorded fatal debris flows in each country. Distribution of median debris-flow fatalities within analysed countries (b): the size of the circles represents the median number of fatalities for each country.

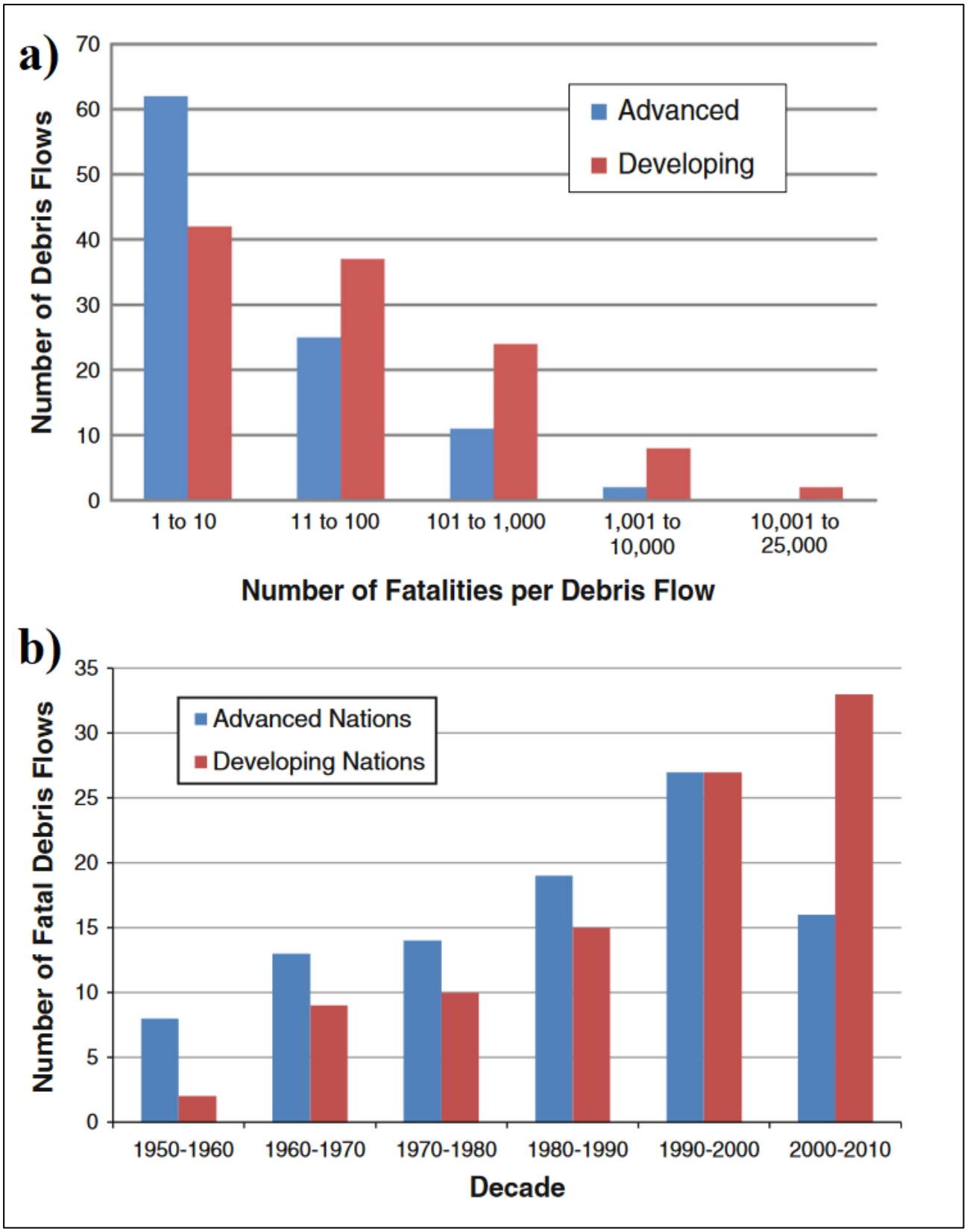

Figure 1. 14: fatal debris-flow impact through decades in advanced and developing nations [Dowling and Santi, 2014]. Number of debris flows with a certain number of fatalities per debris flow in advanced and developing countries (a). Number of recorded fatal debris flows through decades in advanced and developing countries (b).

Figure 1. 15: photo of the Check Dam 20, one of the 30 check dams built in the Illgraben channel at the end of the '60s. The dam is ~8 m high (source: Giacomo Belli).

Perhaps an even more massive intervention aimed at reducing the risk of debris flows was carried out at the Gadria basin (Bolzano, Italy). There, in the late 19th century the stream path was diverted to avoid the piedmont village of Laas (Bolzano, Italy), which had been flooded by debris flows several times through history [Comiti et al., 2014]. Then, starting in the early 20th century several consolidation check dams were built along the channel (Figure 1. 16), so that to date the Gadria main channel and its tributaries feature more than 100 check dams [Comiti et al., 2014].

Figure 1. 16: photo of two of the several check dams realized in the 19th century along the Gadria channel (source: Giacomo Belli).

Finally, in the '70s, the debris-flow risk for the Gadria piedmont area and inhabitants had been substantially zeroed with the realization of a filter check dam (Figure 1. 17), built at the apex of the piedmont colluvial debris fan and delimiting a more upstream storage basin of ~50,000 m^3 [Comiti et al., 2014]. Although since its realization no more flows have invaded the downstream inhabited areas, the filter check dam requires several and frequent interventions of sediment removal and disposal,

entailing very high maintenance costs (about 200,000 €/year) for local authorities [Comiti et al., 2014].

Figure 1. 17: upstream (left) and downstream (right) sides of the ~10 m high filter check dam built in the Gadria basin in the '70s (source: Giacomo Belli).

Thanks to the efforts made and to the attention paid to debris flow risk management, the number of deadly debris flows recorded in advanced countries has decreased in recent decades (Figure 1. 14b), further highlighting the importance of close monitoring and of risk reduction interventions. In contrast, the number of fatal debris flows is still increasing through the decades in the developing nations (Figure 1. 14 b), where a massive demographic growth and a strong invasion of piedmonts areas is not yet accompanied by an adequate debris-flow monitoring and/or by the realization of risk reduction infrastructure [Dowling and Santi, 2014].

1.4 Debris-flow monitoring: state of the art

Due to the complexity of the phenomenon and to the wide variability of flow types, catchment geomorphologic features and socio-economic settings of the involved areas, debris-flow monitoring is traditionally carried out following a wide range of approaches [Arattano and Marchi, 2008], involving rainfall forecast, catchment observations and in-channel flow direct measurements [Badoux et al., 2009].

In Europe, the first catchment instrumented for debris-flow monitoring was probably the Moscardo Torrent in the Eastern Italian Alps [Marchi et al., 2002]. Then, since the late 1990s, other sites have been instrumented in Italy [Tecca et al., 2003] and Switzerland [Hürlimann et al., 2003], including the Illgraben and the Gadria catchments that today represent real laboratory sites for debris-flow study [Badoux et al., 2009; Comiti et al., 2014].

In the last two decades the number of monitored debris-flow sites has increased outstandingly worldwide [Hürlimann et al., 2019], with monitoring systems implemented in Europe (many sites in Italy, Switzerland, Austria, France and Spain, in both Alps and Pyrenees) [Badoux et al., 2009; Comiti et al., 2014], Asia (Taiwan, China, Japan) [Shieh et al., 2009] and USA [Kean et al., 2013]. To these are added all the monitoring systems devoted to the surveillance of lahars in many volcanoes in South America [Johnson and Palma, 2015], USA [Allstadt et al., 2019], Mexico [Vazquez et al., 2016], Indonesia [Lavigne et al., 2000], Japan [Kataoka et al., 2018], Philippines [Marcial et al., 1996], New Zealand [Walsh et al., 2016].

Existing debris-flow warning systems can be classified into two main categories: *probabilistic warning systems*, based on the monitoring of the debris-flow triggering processes, and *event warning systems*, aimed at detecting debris flows in progress [Arattano and Marchi, 2008].

1.4.1 Probabilistic warning systems

Probabilistic warning systems are based on the monitoring of debris-flow hydrometeorological triggering and therefore use techniques typical of meteorology and hydrology [Arattano and Marchi, 2008]. As a matter of fact, these systems are based on empirical correlations between rainfall and debris-flow occurrence and therefore mostly rely on the monitoring and measuring of rainfall,

performed with rain gauges and weather radar, but also with the monitoring of water discharge in streams [Arattano and Marchi, 2008] and with soil water content measurement, provided by soil moisture and pore-water pressure sensors [Hürlimann et al., 2019].

The most commonly used device for rainfall measuring is the tipping bucket rain gauge [Hürlimann et al., 2019]. In monitoring debris-flow triggering rainfall the position of the rain gauge is critical, since debris flows are usually triggered by locally intense convective rainfall, characterized by a small storm cell [Hürlimann et al., 2019], with a diameter of few kilometres or less [Underwood et al., 2016]; therefore, in order to avoid false representations of the triggering rainfall conditions, it is crucial to locate the rain gauge as close as possible to the debris-flow initiation area [Hürlimann et al., 2019].

Pore pressure water and soil water content measurements provided by pore-water pressure sensors are important in case of the so-called landslide triggering of debris flows [Hürlimann et al., 2019], in which the development of positive pore pressure at the interface between layers of contrasting permeability induces the failure of a colluvial soil layer overlaying the bedrock on steep slopes, which eventually turns into a debris flow [Iverson et al., 1997].

Probabilistic warning systems are generally designed to issue an alert whenever measured rainfall exceeds pre-determined empirical thresholds on rainfall intensity or duration. Also cumulated event rainfall and antecedent rainfall are generally considered, because they control soil saturation and are therefore pivotal for landslide/debris-flow triggering [Arattano and Marchi, 2008]. Critical rainfall thresholds are established on the basis of past rainfall records as the mildest (lower intensity/duration) precipitation conditions that triggered a debris flow [Arattano and Marchi, 2008].

Probabilistic warning system are however easily victims of frequent false alarms spreading [Arattano and Marchi, 2008; Ponziani et al., 2020]. Indeed, the occurrence of a precipitation event characterized by parameters that exceed the thresholds foreseen for the debris-flow triggering often does not lead to actual start of a debris flow [Giannecchini et al., 2016]: that is because debris-flow triggering mechanisms are complex and are not bound only to the occurrence of a rainfall event with the right characteristics, but depends also on the availability of debris and on the small-scale status of the catchment [Arattano and Marchi, 2008]. Furthermore, there may be great uncertainty about the definition of the empirical rainfall thresholds, since a wide variability has been observed in the intensity and in the duration of rain events that trigger debris flows [Giannecchini et al., 2016; Hirschber et al., 2021] and also because rain gauges only provide single point measurements that need to be interpolated to the entire basin [Nikolopoulos et al., 2015].

In addition, warning systems based on weather forecast cannot predict debris flows primed by other triggering processes such as rapid snowmelt, earthquakes or natural dam collapses. Probabilistic

alarm systems are thus suitable for issuing warnings to the staff in charge of emergency management, whereas they are not generally satisfactory for population alerting [Arattano and Marchi, 2008].

1.4.2 Event warning systems

As an alternative solution, *event warning systems*, which can detect a debris flow when it is in progress, are necessary to ensure more reliable alerting and to effectively reduce debris-flow risk.
This type of systems, despite having a much smaller lead time, is definitely less prone to false alert [Arattano and Marchi, 2008] and therefore more reliable compared to *probabilistic warning systems*.
The operation of *event warning systems* is based on a wide range of techniques and relies on various types of sensors detecting the flow passage or measuring different flow parameters including flow depth, flow velocity, flow density, impact force etc. [Arattano and Marchi, 2008; Hürlimann et al., 2019].

1.4.2.1 Event detection

For monitoring and risk reduction purposes, it is essential to be able to detect an ongoing debris flow as quickly as possible, so that countermeasures can be taken before the flow reaches vulnerable locations and infrastructure.
The passage of a debris flow at a specific location in the channel can be detected using many types of sensors, including ultrasonic sensors, photocells and infrared photobeam, geophones, pore-fluid pressure sensors, cross-section wires and others [Arattano and Marchi, 2008; Hürlimann et al., 2019].
These sensors work by taking advantage of the fact that debris flows have a very steep front [Iverson, 1997; Coussot and Meunier, 1996]]; the passage of the debris-flow front generates a sudden signal, such as a large increase in ground motion recorded by a geophone or a large increase in the measured flow depth, which represents a clear break with the pre-flow conditions.
Among the simplest devices used to detect a debris flow are wire sensors (Figure 1. 18). These, stretched across the channel, are broken by the passage of a debris flow, allowing its detection [Arattano and Marchi, 2008].

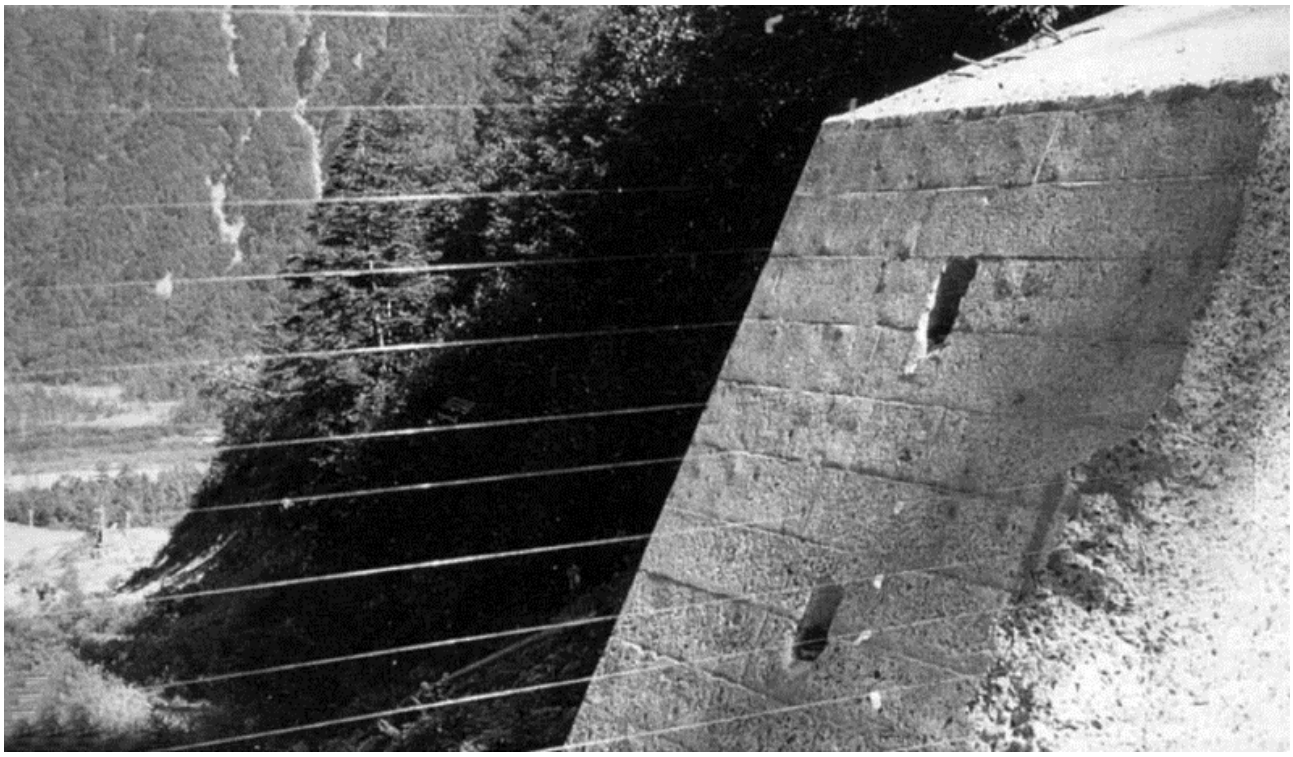

Figure 1. 18: wires stretched across the channel for flow depth estimate (source: Arattano and Marchi [2008]).

Similarly, a debris flow can be detected also using photocells and infrared photobeam sensors, as the passage of the flowing mass interrupts the beams emitted by the sensors [Arattano and Marchi, 2008]. Debris-flow passage can be detected also using a pendulum hung on the channel: the tilting of the pendulum, caused by the flow impact on it, triggers a signal that make it possible to recognise an ongoing debris flow [Arattano and Marchi, 2008].

In many catchments, including the Illgraben and Gadria basins, event detection is performed mainly by means of geophones, that record ground vibration induced by the debris-flow passage. Geophones are usually installed behind steel plates within the channel, or sometimes they are buried on the stream banks [Arattano and Marchi, 2008], usually in correspondence of check dams (Figure 1. 19).

The passage of the boulders of the flow snout over the steel plate produces vertical vibration that activates the geophones inducting voltage impulses [Badoux et al., 2009]; debris-flow front arrival is defined when the generated signal exceeds a previously chosen threshold voltage. The ability to detect the passage of an occurring debris flow at different measuring points along the channel has obviously a strong meaning for monitoring purposes and a simple debris-flow warning system can be designed to issue an alert when the flow passage in a given position is detected [Arattano and Marchi, 2008].

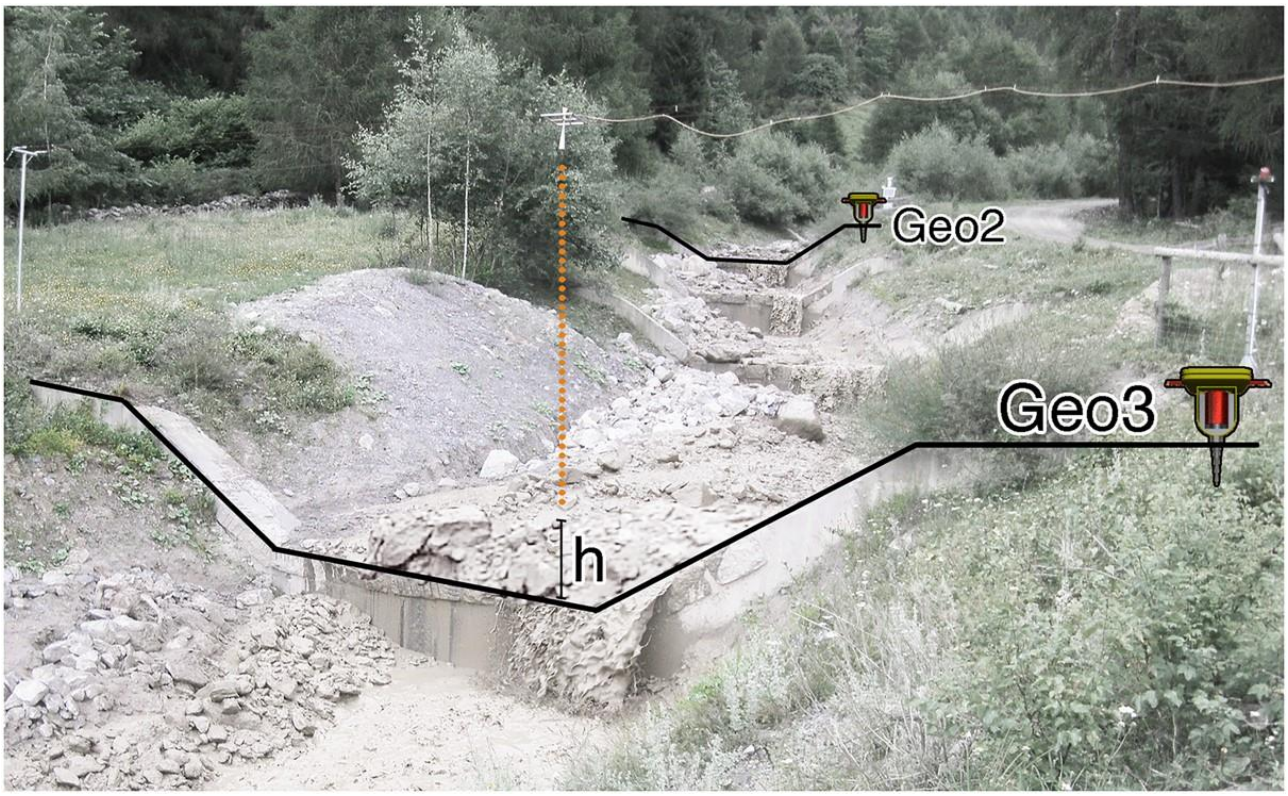

Figure 1. 19: image showing the location of two geophones for debris-flow detection and of an altimeter for flow stage measurements in the Gadria stream (Bolzano, Italy) (source: Coviello et al. [2019]).

1.4.2.2 Flow depth measurements

Debris-flow depth (or stage) and its evolution through time (hydrograph), providing an accurate picture of the magnitude and of the evolution of the flow, are critical for monitoring and research purposes and are usually measured by laser, ultrasonic or radar altimeters [Arattano and Marchi, 2008; Badoux et al., 2009]. These sensors, suspended over the channel (Figure 1. 19; Figure 1. 20), measure at any time the distance between the underlying flow surface and the sensor itself and are therefore able to supply hydrographs [Arattano and Marchi, 2008]; because of the rapid variability of debris-flow height, consecutive depth measurements are separated by very short time intervals (typically 1 second) [Arattano and Marchi, 2008].

To avoid misestimates, flow stage should be measured at cross-section controlled by check dams and bedrock [Hürlimann et al., 2019], where bed erosion by debris flows is prevented and where, in the case of check dams, the cross-section geometry is known, allowing for more accurate discharge estimations (Figure 1. 19; Figure 1. 20).

Figure 1. 20: ultrasonic sensor for flow depth measurement suspended over the channel at a check dam (source: Arattano and Marchi [2008]).

Ultrasonic, radar and laser altimeters can be used also for debris-flow detection, as a sudden increase of the flow depth can be the evidence of an ongoing flow (Figure 1. 21).

Alternative flow depth estimates can be achieved through the analysis of videos of the debris flows provided by cameras.

Peak flow depth can also be obtained by means of wires stretched at different heights across the channel: the peak depth value is detected as the level of the highest wire that has been broken by the flow [Arattano and Marchi, 2008] (Figure 1. 18). These wires, although easy to install and operate, are however not able to provide any information on the flow stage evolution and, in addition, they need to be restored after each debris-flow event [Arattano and Marchi, 2008] and, therefore, are not as effective as laser/ultrasonic/radar altimeters.

Other devices for flow stage measurements include photocell and infrared photobeam sensors; similar to the wires deployed across the channel, if several sensors are installed at different heights at the

same cross-section, it is possible to estimate the peak flow stage as the height of the highest beam obscured by the flow [Arattano and Marchi, 2008].

1.4.2.3 Flow velocity and volume estimates

Direct flow velocity measurement is instead trickier. Indirect measurements can be however easily obtained by detecting the passage of the debris flow at different points along the channel located at a known distance between them (Figure 1. 21).

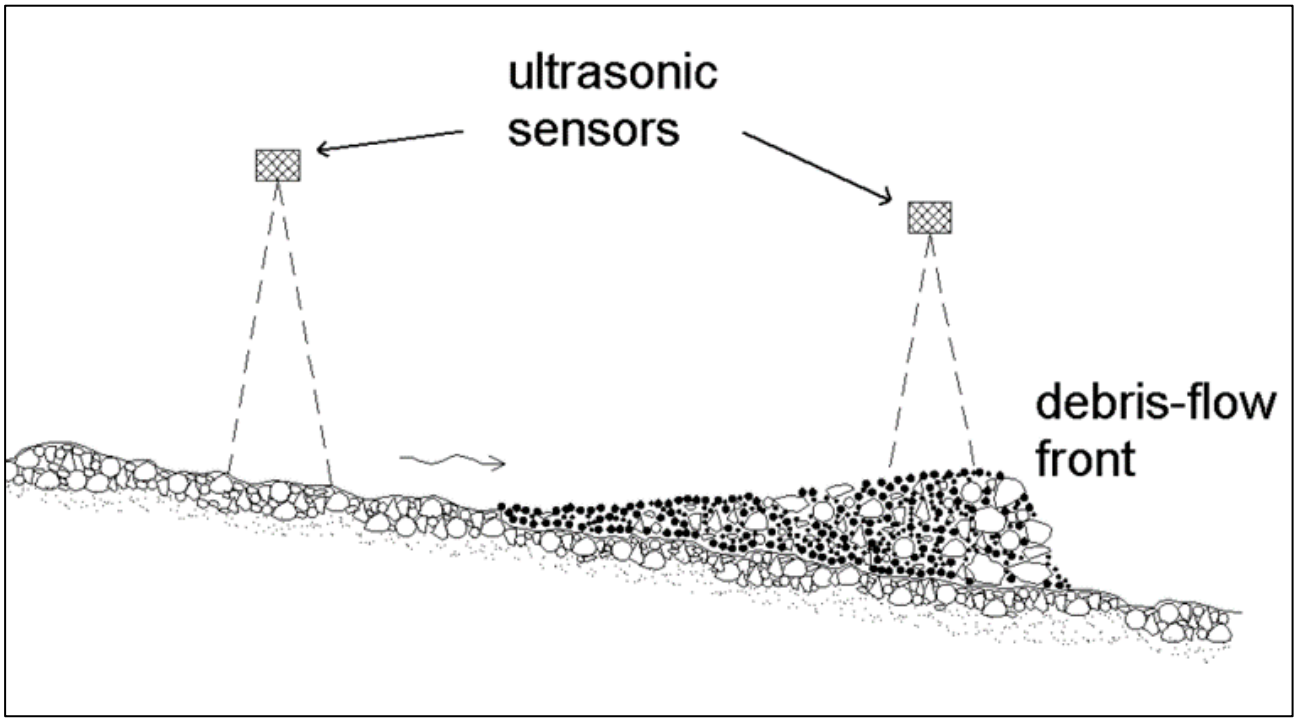

Figure 1. 21: scheme showing two ultrasonic altimeters that, being able to detect the arrival of the debris-flow front, can be used to estimate the flow velocity as the ratio between their distance and the difference between the two recorded arrival times (source: Arattano and Marchi [2008]).

As discussed above, because of its steep front, a debris-flow arrival at specific positions along the channel can be easily traced using ultrasonic sensors, photocells and infrared photobeam, geophones, pore-fluid pressure sensors or any other device able to detect the passage of the flow wave [Arattano and Marchi, 2008; Hürlimann et al., 2019] (Figure 1. 21). Once the debris-flow front arrival time is defined at two specific positions along the channel, flow velocity can be computed as the ratio between the distance the flow covered, to go from the more upstream position to the further

downstream one, and the time difference between the detection of the flow front at the two gauging sites [Arattano and Marchi, 2008].

In order to assess flow velocity after the flow front has passed, similar computation can be performed considering secondary distinguishable flow waves or peaks. Problems could arise in estimating flow velocity in case of debris-flow events that lack a univocal front or other clear secondary features: in these cases, clear flow peaks lack and it might be very difficult to detect the flow arrival at the gauging positions, thus preventing an accurate velocity estimation [Arattano and Marchi, 2008]. In these cases, flow surface velocity can be measured thanks to Doppler speedometers, or several other methods based on video or image processing techniques [Arattano and Marchi, 2008; Hürlimann et al., 2019].

In addition to being a valuable tool for measuring flow velocity, cameras are widely used in debris-flow monitoring as video recordings provide an unrivaled database for the recognition and interpretation of flow dynamical processes, effectively supporting quantitative monitoring performed by other sensors [Arattano and Marchi, 2008].

Measurements of flow depth and velocity and their evolution during a debris-flow event allow estimations of the volumetric discharge and the total volume of the flow. The latter can be computed by integrating debris-flow discharge on the hydrograph [Arattano and Marchi, 2008]. Such estimates, providing a valuable image of the area potentially overrun by the flow and a realistic picture of the expected magnitude of the events, are extremely valuable for monitoring debris flows and for the design of hydraulic works aimed at controlling and reducing debris-flow risk.

1.4.2.4 Flow impact and basal force measurements and density estimates

For risk reduction purposes, it is critical to perform debris-flow impact estimations: debris flows indeed exert huge impact forces on all obstacles encountered along their path, such as bridge piers, defensive walls and other buildings.

The exerted impact force consists of two main components [He et al., 2016]: the dynamic pressure of fluid and the collisional force of single boulders. The latter often causes damage to engineering structures [Arattano and Marchi, 2008]. Each flow phase (i.e. flow front, body and tail) is marked by a characteristic impact force signature, that reflects its flow rheology [Cui et al., 2015]. The turbulent flow front is the most impacting phase and exerts a sudden strong impact dominated by the random collision force of boulders. Flow front impact is generally more than 1.5 times the continuous hydrodynamic pressure that marks the flow body [Cui et al., 2015]. The flow tail instead exerts a slight static pressure that does not represent a serious threat factor [Cui et al., 2015].

The impact force of debris flows is usually measured using different kind of devices [Arattano and Marchi, 2008], including pressure mark gauges [Okuda et al., 1980] and strain sensors [Hu et al., 2011], generally mounted on vertical pillars installed in the middle of the channel (Figure 1. 22).

Figure 1. 22: photo showing different sensors and devices installed in the Gadria channel (Bolzano, Italy) for debris-flow study, monitoring and risk reduction, including the filter check dam in the background, the sensor pillar for flow impact measurements in the middle of the channel, an altimeter suspended over the channel and a camera on the left bank (source: Giacomo Belli).

Flow basal forces can be measured with a force plate deployed at the bottom of the debris-flow channel (Figure 1. 23). The force plate is equipped with vertical and horizontal load cells, measuring normal and shear stresses exerted at the base of the flow [McArdell et al., 2007; Arattano and Marchi, 2008]. In addition to load cells, the force plate can host pore-fluid pressure sensors, providing measurements of excess pore pressures accompanying and highlighting the passage of a debris flow [Hürlimann et al., 2019].

At few better instrumented debris-flow sites, e.g. in the Illgraben (Switzerland) and Gadria (Italy) catchments, a “sensor wall” or “sensor pillar” (Figure 1. 22) recording flow velocity, shear force and impact forces at different depths within the flow, is installed in the channel to monitor flow properties as a function of the flow depth [Hürlimann et al., 2019].

Figure 1. 23: photo of the force plate (highlighted in red) installed at Check Dam 29 at the Illgraben (Switzerland) (source: Giacomo Belli).

Another flow parameter that is very important for debris-flow research and monitoring purposes is flow bulk density. Direct density measurements of an occurring debris flow are very challenging because samplers are easily crushed and washed away. Furthermore, the deposit of a debris flow is hardly representative of the actual density of the flow, as, when the sample is collected, the fluid part has flowed out or dried [Arattano and Marchi, 2008]. In addition, the density of a debris flow varies during the event, depending on flow structure, section and composition [Iverson, 1997].

However, an accurate estimation of the average flow density can be obtained by installing a force plate equipped with load cells at the bottom of the channel (Figure 1. 23), allowing for normal stress measurements. Combining measured normal stress values with flow stage measurements provided by an altimeter suspended on the load cell, it is possible to compute the mean bulk density of the

moving debris flow and its variation over time, as the ratio of normal stress to flow depth [McArdell et al., 2007; Arattano and Marchi, 2008].

Sensors measuring direct flow parameters or detecting the flow passage described in the Sections above provide a robust base for debris-flow research and monitoring. However, to operate efficiently, all these devices must be suspended over the flow (altimeters, wires) or installed near the channel (cameras, geophones) or even within it (force plate, geophones). Therefore, the installation and maintenance of such an instrumental set up can be difficult and expensive, especially because debris flows occur in step mountain catchments that are usually difficult and hazardous to access and hard to reach with instrumentation.

In addition, due to the destructiveness of the debris-flow phenomenology itself, sensors deployed near/within the channel or suspended over it are prone to be easily and frequently destroyed, or at least buried (Figure 1. 24), by a debris-flow event [Arattano and Marchi, 2008]; this can involve replacing or repairing instruments after an event, thus increasing risk and cost associated with the monitoring system maintenance.

Figure 1. 24: workers removing the deposit of a debris flow from the force plate deployed at Illgraben (source: Giacomo Belli).

Sensors used for detecting debris flows are only one component of *event warning systems*, that further include a data acquisition and processing unit and devices to spread the alarm [Arattano and Marchi, 2008] (Figure 1. 25).

Debris flows typically occur as rapid surges flowing in short steep mountain catchments, so that event warning times seldom exceed 5 minutes [Arattano and Marchi, 2008]. Therefore, population alerting is generally carried out by means of sirens and traffic lights meant to warn people who at the time of the event are in proximity to the channel and to close to traffic infrastructure that can be invaded or destroyed by the flow.

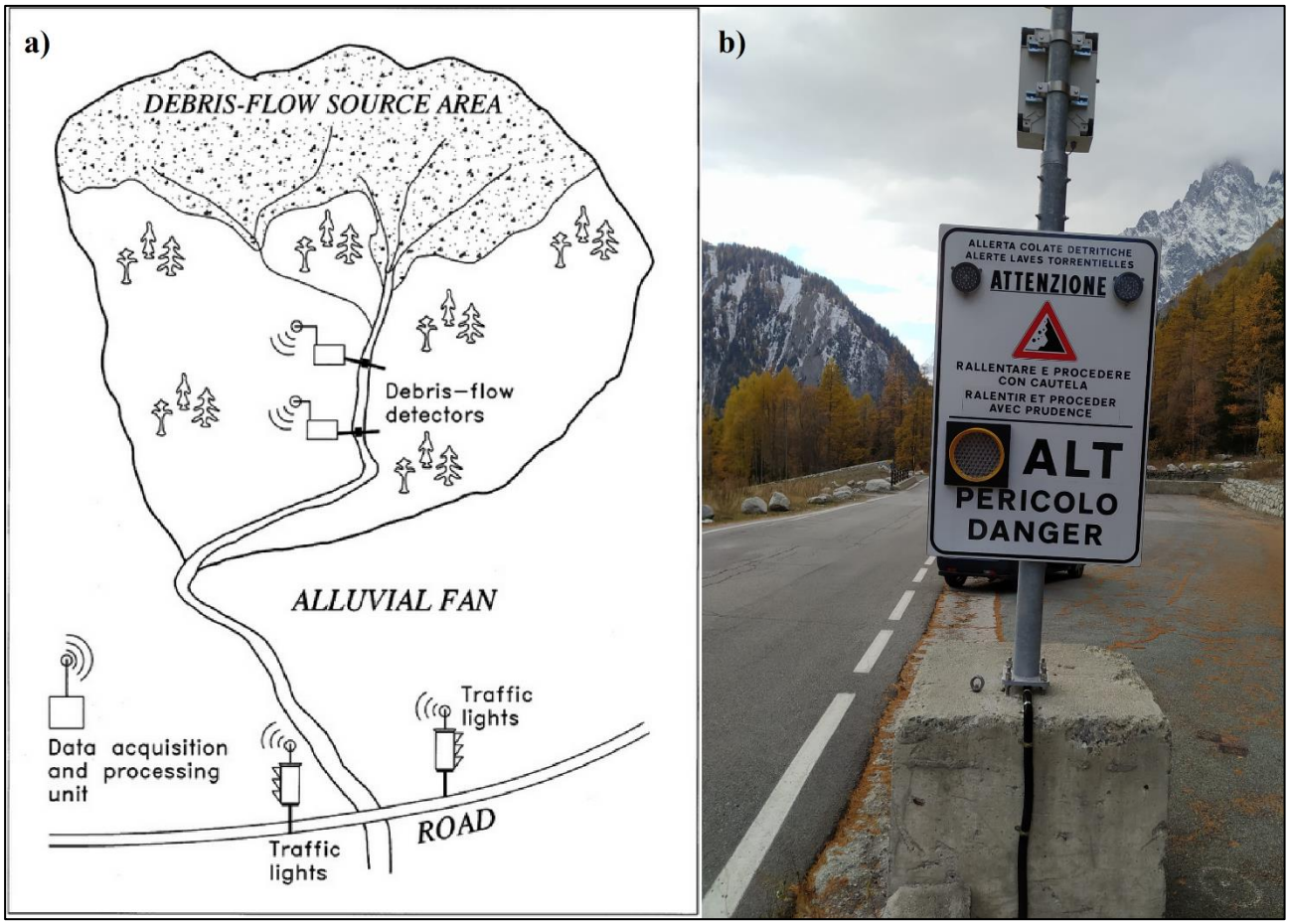

Figure 1. 25: schematic sketch of debris-flow event warning system [Arattano and Marchi, 2008] (a). Traffic light for debris-flow occurrence notification deployed on the Rochefort stream, in Valle d'Aosta (Italy) (b) (source: Giacomo Belli).

Chapter 2

Seismo-acoustic analysis of debris flows: state of the art

Traditionally, monitoring of mass movements has been based on in situ measurements, e.g. through strain gauges and tilt meters for landslides and flow phase measurements for debris flows and floods [Angeli et al., 2000; Arattano and Marchi, 2008]. In the last 20 years, with the advancement of technology, new approaches have been adopted in the study and monitoring of mass movements, such as snow avalanches, pyroclastic density currents, landslides and debris flows, able to remotely detect the movement directly, e.g. with a radar [Luzi et al., 2004; Eckerstorfer et al., 2016], or indirectly, from the elastic energy radiated by the process [Marchetti et al, 2015; Allstadt et al., 2018; Marchetti et al., 2019].

In this context, the use of geophysical signals for studying and monitoring debris flows has gained attention worldwide [Arattano, 1999; Burtin et al., 2009; Burtin et al., 2014; Walter et al., 2017; Lai et al., 2018; Marchetti et al., 2019]. These techniques are based on the analysis of both seismic and infrasonic signals generated by a debris flow. As a matter of fact, similarly to what is observed for other mass movements, such as snow avalanches [Kogelnig et al, 2011; Marchetti et al., 2015] and pyroclastic density currents [Delle Donne et al., 2014], while flowing along the stream catchment, a debris flow radiates elastic energy both in the ground, in the form of seismic waves, and in the atmosphere, in the form of infrasound. Seismic and infrasonic debris-flow signals typically have emergent, cigar-shaped envelopes [Lai et al., 2018; Marchetti et al., 2019] and present a wide variability in duration and amplitude, reflecting the large variance in duration and size observed for the debris-flow events.

The use of seismic and infrasound sensors for the study and monitoring of debris flows guarantees many advantages. First, the geophysical network in principle allows a completely safe remote study and observation of the debris-flow event. Furthermore, seismo-acoustic sensors are usually located in easily accessible sites and, being generally deployed far from the creek channel, they do not risk to be damaged by debris flows and thus require little and infrequent maintenance. In addition to the low management and repair costs, a seismo-acoustic network has proven to be a very powerful tool for the study of mass movements [Yamasato, 1997; Allstadt et al., 2018; Ulivieri et al., 2011; Vilajosana et al., 2008; Ripepe et al., 2009] and indeed it is able to provide crucial information also on debris-flow events, since many characteristics of the geophysical signals reflect the hydraulic and physical features of the flows [Lai et al., 2018; Marchetti et al., 2019; Belli et al., 2022].

Nevertheless, the radiation processes of both these wavefield are not yet fully understood and, because of the complexity and the variability of the natural phenomenon and because geophysical signals generated by debris flows lack impulsive, easily detectable distinct phases [Wenner et al., 2019; Coviello et al., 2019; Marchetti et al., 2019], several open questions persist on linking flow behaviour and processes to resulting seismo-acoustic signals features.

2.1 Seismic analysis of debris flows

Several studies have been performed on debris-flow seismicity. To date, most of these studies have been focused on debris-flow monitoring and event detection [Arattano, 1999; Bessason et al., 2007; Kogelnig et al., 2011; Coviello et al., 2019; Walter et al., 2017; Lai et al., 2018; Chmiel et al., 2021], but several efforts have been made also in the investigation of the seismic source mechanism [Burtin et al., 2009; Kean et al., 2015; Lai et al., 2018; Zhang et al., 2021(a)].

Both theoretical and experimental studies suggest that seismic energy radiation by debris flows is similar to what is observed for rivers [Burtin et al., 2008; Tsai et al., 2012; Gimbert et al., 2014]. Analysing a year of data on seismic noise recorded by several station located along the Trisuli River, a major trans-Himalayan river, Burtin et al., [2008] observed that high-frequency (>1 Hz) seismic noise by rivers appears to be well correlated with flow depth (Figure 2. 1), with the amplitude of the generated seismic noise increasing with increasing the flow depth.

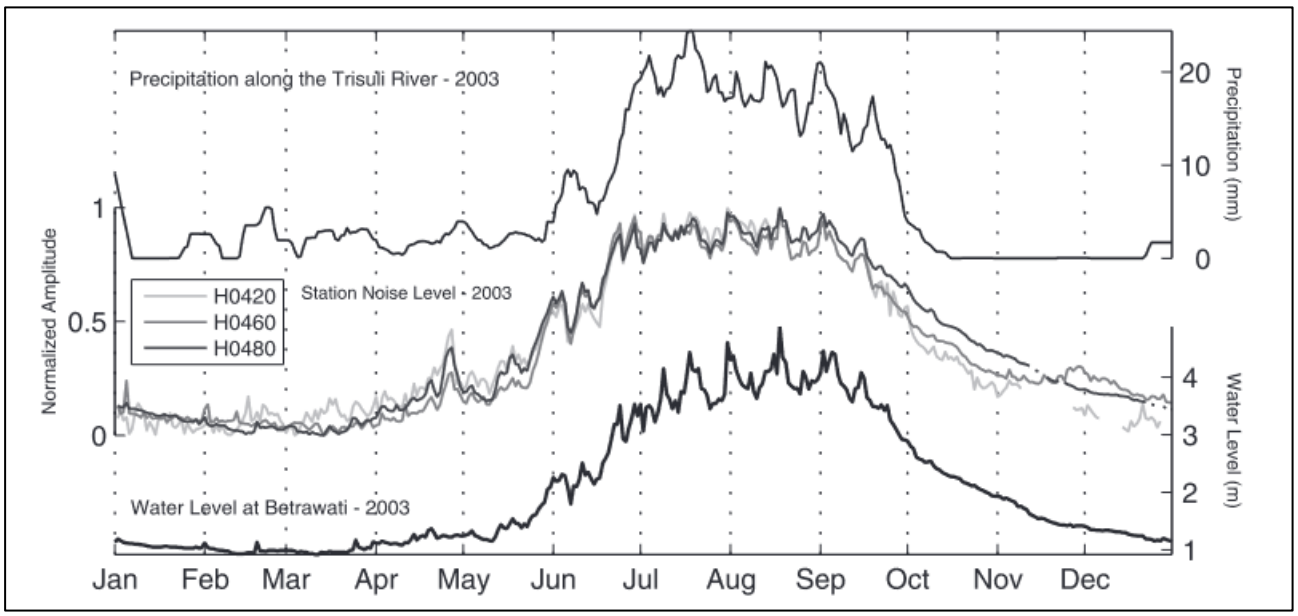

Figure 2. 1: comparison between daily precipitation rate (top), seismic noise (middle) and river water level (bottom) recorded along the Trisuli River during 2003 (source: Burtin et al. [2008]). The precipitation curve is the 10 days centred moving average of the daily precipitation rate in mm at 8 meteorological stations from the Department of Hydrology and Meteorology of Nepal (DHM) located along the valley of the Trisuli River. The high-frequency seismic noise level (averaged over the three components and the frequency band 3–15 Hz) was recorded at three seismic stations (H0420, H0460, and H0480). The Trisuli water level was measured at the town of Betrawati. The seismic noise level generated by Trisuli River correlates well with its flow depth.

Authors interpreted such evidence suggesting that fluid dynamic turbulence structures induced by an increased water level likely control the radiation of seismic energy in rivers [Burtin et al., 2008; Gimbert et al., 2014]. However, Burtin et al. [2008] stress that fluid dynamics is not the unique seismic source in rivers; an increased flow depth implies an increased basal shear stress at the riverbed. This leads to the initiation of bed load transport, which involves pebbles saltation and bed load creep of progressively larger particles as the flow depth increases. Each sediment impact on the riverbed induces a force impulse that excited seismic waves in the ground [Tsai et al., 2012], that contributes to the increased seismic energy radiation observed during phases of increased water level in the river. Bed load transport acts thus as a primary seismic source in rivers [Burtin et al., 2008; Tsai et al., 2012; Hsu et al., 2011]. Such an inference is further underlined by the observation of a clockwise hysteresis pattern in plot of seismic noise power as function of water level or discharge during a rainfall season or major storms (Figure 2. 2) [Burtin et al., 2008; Hsu et al., 2011; Tsai et al., 2011].

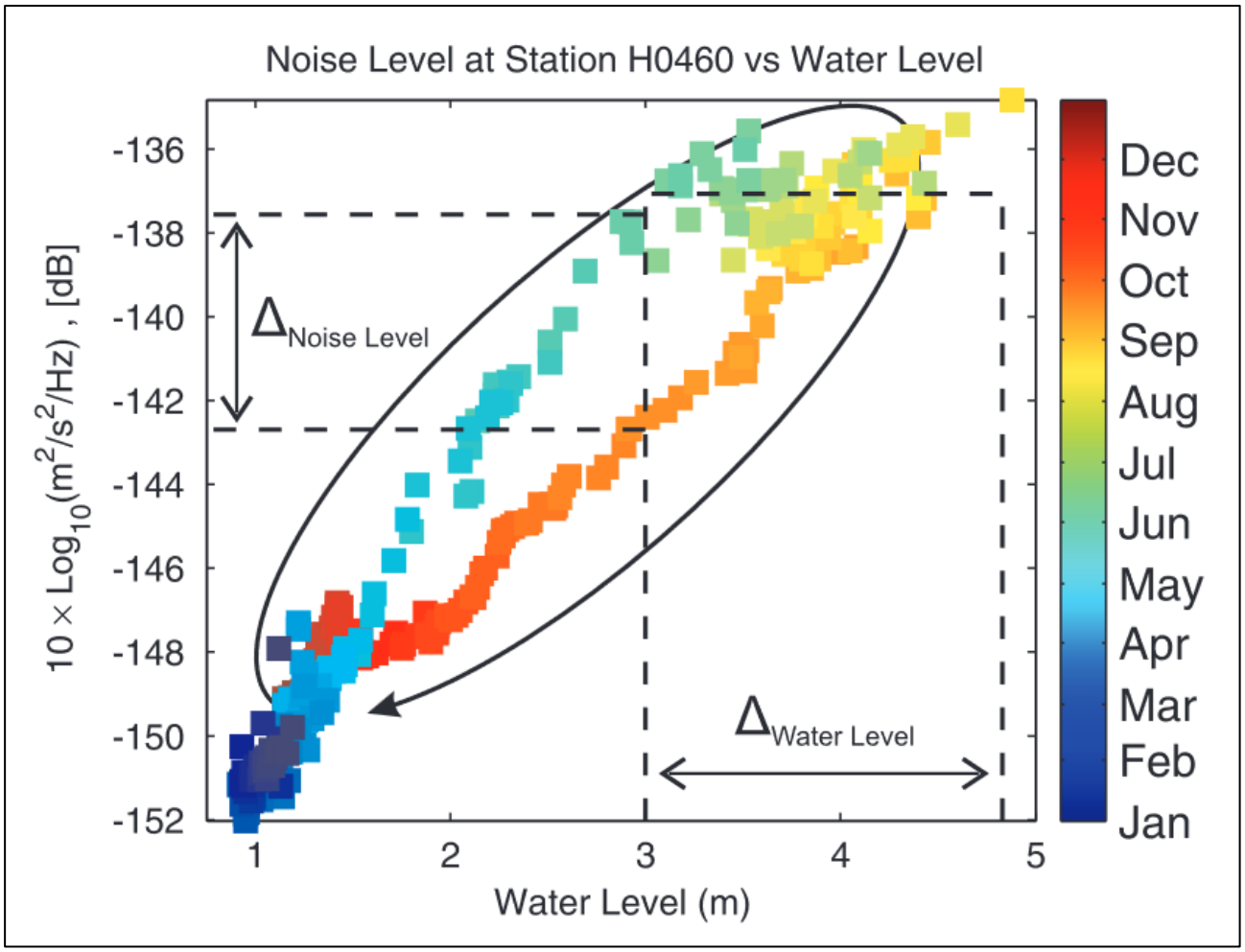

Figure 2. 2: clockwise hysteresis pattern observed during 2003 between water level in Trisuli River and seismic noise generated by the river (source: Burtin et al. [2008]). At the beginning of the monsoon season (Spring),

when there is a larger availability of solid debris in the river catchment, for the same water level, the river radiates higher energy seismic noise compared to the end of monsoon season (Autumn), when most of the sediment has already been removed by river action.

In several experimental studies on seismic noise by rivers it has been observed that for equivalent water level the seismic noise recorded at the beginning of the rainfall season or storm is larger than the one recorded at the end of the season/storm [Burtin et al., 2008; Hsu et al., 2011]. The clockwise hysteresis pattern confirms that fluid dynamics is not the unique source of seismic energy in rivers: if fluid dynamic turbulence structures were the only seismic source in rivers, one would expect a linear trend between seismic amplitude and water level [Burtin et al., 2008]. The explanation of this hysteresis trend is to be attributed to bed load transport. The extent of solid transportation in rivers does not depend only on water level but also on the availability of solid particles in the river catchment or channel [Tsai et al., 2012]. Part of the sediment that was available at the beginning of the rainfall season/storm is removed during the first phases of increased water discharge [Burtin et al., 2008]. This leads to the decrease of seismic noise observed, for similar water levels, at the end of the rainfall season/storm, since only the largest boulders remain available in the channel to be transported by the flow and to produce noise [Burtin et al., 2008]. The clockwise hysteresis pattern observed comparing seismic energy and water level in rivers highlights thus the importance of bed load transport in the radiation processes of seismic energy by rivers, in addition to turbulence [Burtin et al., 2008; Tsai et al., 2012; Gimbert et al., 2014]. Experimental observation revealed that turbulence induces lower frequency noise compared to bedload transport [Schmandt et al., 2013; Gimbert et al., 2014], so that, depending on the geometry of the recording seismic network, the two processes could also be analysed independently [Gimbert et al., 2014].

Schmandt et al. [2013], analysing both seismic and infrasonic radiation by a controlled flood in the Grand Canyon, found that the seismic response was concentrated in three different spectral windows (Figure 2. 3). The higher frequency band (15-45 Hz), showing clockwise hysteresis when compared with flow discharge, has been interpreted by the authors as generated by bedload transport. The other two components instead lack a clockwise hysteresis and are therefore attributed to water transport [Schmandt et al., 2013]. As the lower frequency band (0.5-2 Hz) is absent in the infrasound spectrum, authors suggest that it is produced by fluid traction exerted on the rough riverbed. The middle range frequency band (2-15 Hz) instead corresponds to the peak observed in the generated infrasonic amplitude and is likely associated to waves at the fluid-air interface [Schmandt et al., 2013].

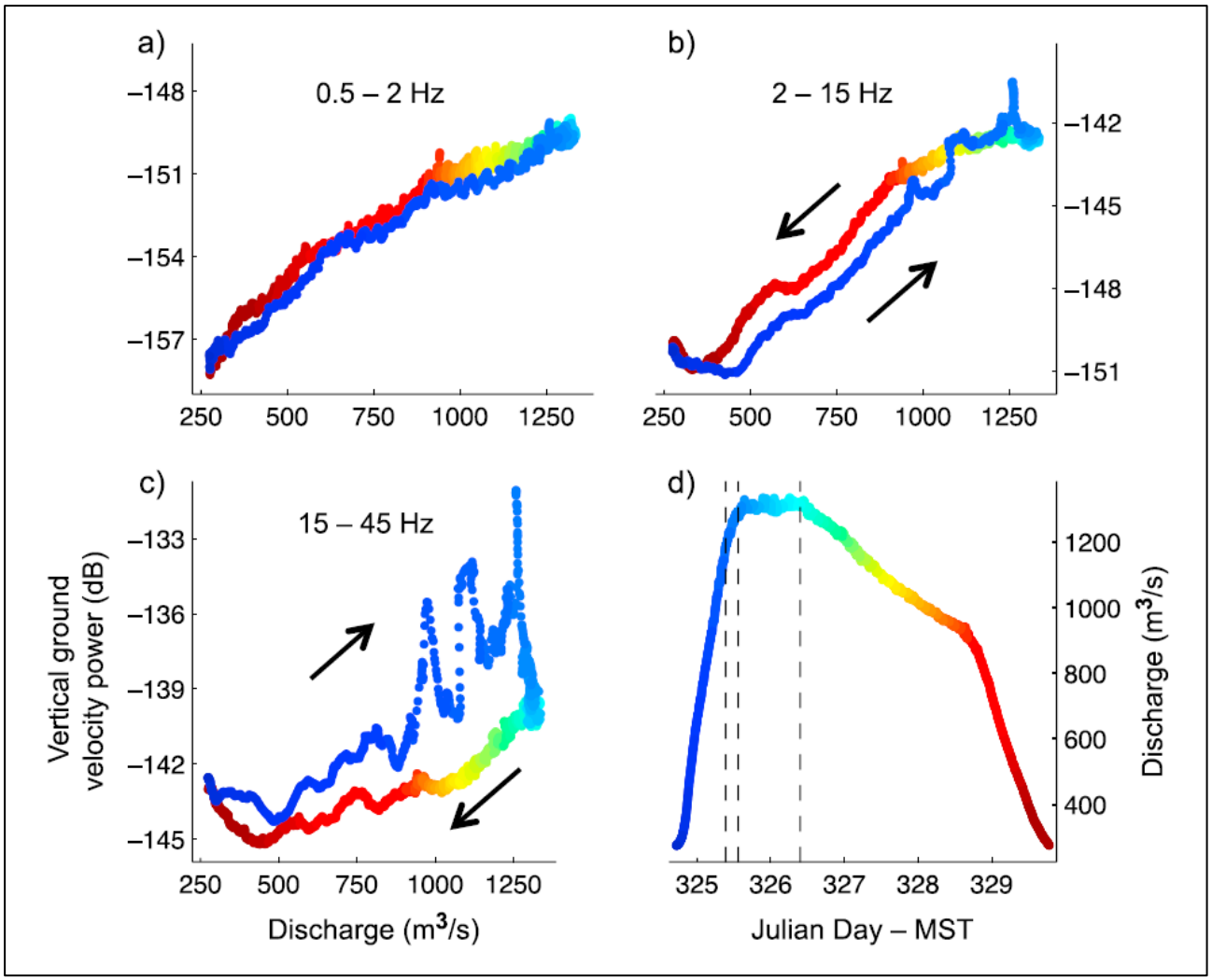

Figure 2. 3: vertical ground velocity power, in three different frequency bands, versus flow discharge (a, b, c) during a controlled flood in the Grand Canyon; flow discharge during the year (d) (source: Schmandt et al. [2013]).

Tsai et al. [2012] developed a theoretical model for seismic noise generated by bedload transport, modelling the seismic source as the result of single saltating particles impacting the riverbed and generating seismic waves. For simplicity, authors assume that surface waves dominate the produced seismic wavefield. Assuming that each particle impact on the riverbed induces a force impulse in the ground, we can expect that the particle impacts produce fluctuations of the basal force exerted by the flow on the bed, generating both vertical and horizontal stress and thus radiating high frequency seismic energy in form of both Rayleigh and Love surface waves [Gimbert et al., 2014].

Seismic waves radiated by a single particle impact depends on the particle size and on the particle impact velocity. The particle impact velocity is assumed to be normal to the riverbed, so that Rayleigh waves are expected to be the dominant seismic wave type. In the simplest case of perfectly elastic

Hertzian impacts, the maximum impact force of a particle and its contact time with the bed are easily computable [Johnson, 1987]. Obviously, within the flow there are several particles that are simultaneously impacting the bed, so that the generated seismicity depends on the particle impact rate, that in turn depends on the particle size and on other fluvial parameters, such as channel bed width, sediment flux, flow velocity and height of the bed load level [Tsai et al., 2012].

For a given grain size (D) and a given seismic frequency (f) and assuming an infinitely long and straight river, whose closest point from the seismic station is r_0, the power spectral density (PSD) of the ground velocity recorded at the station (P_v) can be modelled as [Tsai et al., 2012]:

$$P_v(f, D) \approx \frac{n_p}{t_i} \frac{\pi^2 f^3 m_p^2 w_i^2}{\rho_s^2 c_c^3 c_u^2} \chi(\beta) \qquad \text{(Eq. 2. 1)},$$

where n_p is the number of particles with diameter equal to D, m_p is the mass of the particle and ρ_s is the solid phase density. w_i is the particle impact velocity with the riverbed and t_i is the time interval between two impacts of each particle. c_c is the phase velocity of the Rayleigh-wave of frequency equal to f, while c_u is the group velocity. χ and β are dimensionless parameters accounting for the characteristics of the ground and for r_0. Modelled seismic PSD linearly scales with the number of particles of a given size and with the square of the linear momentum of the particles impacting the riverbed. When considering all grain size distribution of the bed load transport, the total power spectral density (P_v^T) can be derived integrating P_v over the entire grain size distribution, as:

$$P_v^T(f) = \int_D P_v(f, D) dD \qquad \text{(Eq. 2. 2)}.$$

Eq. 2. 1 and Eq. 2. 2 indicate that the amplitude of seismic noise PSD is strongly dependent on the sediment size (Figure 2. 4), with the seismic amplitude increasing as the dominant particle size increases [Tsai et al., 2012]. Furthermore, the seismic noise appears to be dominated by the component generated by the very coarse fraction of the load, that for a typical riverbed grain size distribution approximately corresponds to the 94th percentile of the distribution [Tsai et al., 2012; Lai et al., 2018].

In contrast, the modelled seismic peak frequency only depends on the minimum distance between the river and the seismometer [Tsai et al., 2012]: the peak of the PSD is indeed observed to migrate towards higher frequency when the minimum distance between the river and the seismometer decreases (Figure 2. 4). This is due to seismic wave propagation, which involves a stronger

attenuation at higher frequencies [Aki and Richards, 2002] and therefore leads to a decrease in the recorded seismic peak frequency as the source-to-receiver distance increases.

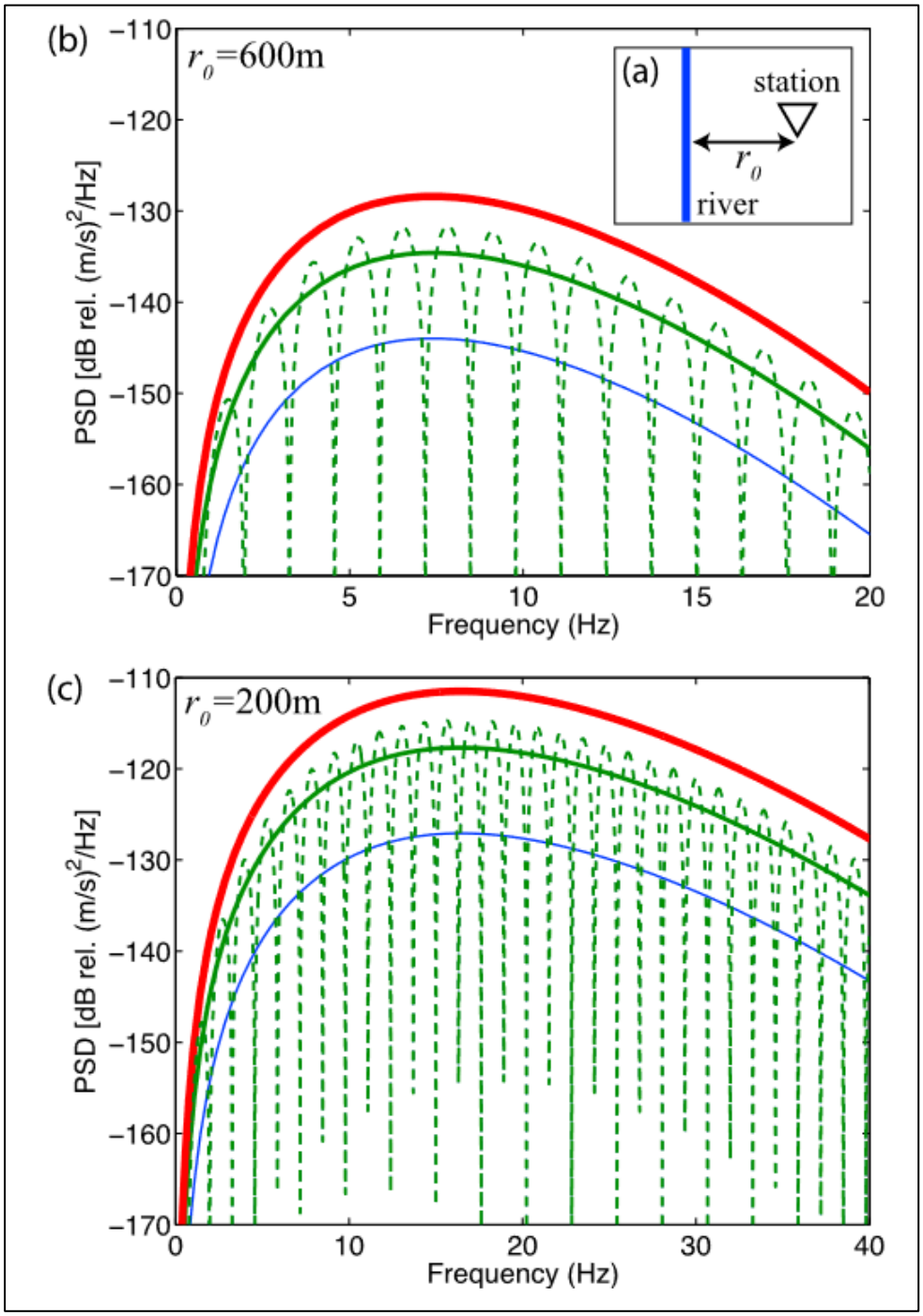

Figure 2. 4: seismic noise power spectral density (PSD) generated by particle impacts in rivers as modelled by Tsai et al. [2012] (source Tsai et al. [2012]). The PSD is shown for two different source-to-receiver distances (r); r=600 m (a) and r=200 m (b). In each panel, the PSD is computed for three different grain diameters (D): D=0.3 m (blue), D=0.5 m (green) and D=0.7 m (red). The green dashed line is instead obtained with D=0.5 m but considering that a single particle makes 2 hops (instead of one single hop) before the impact time becomes significantly different from an integer multiple of the timescale between impacts [Tsai et al.,

2012]. It is observed that particle size controls the amplitude of the generated seismic noise, with seismic amplitude increasing with increasing D. In addition, peak frequency of the PDS changes with the river-to-seismometer distance, migrating towards higher values when the distance decreases.

The model for seismic noise generation by rivers based on particle collisions and proposed by Tsai et al. [2012] has been extended and applied also to debris flows [Kean et al., 2015; Lai et al., 2018; Wenner et al., 2019; Farin et al., 2019; Zhang et al., 2021a]. Indeed, solid particle transport and collisions are believed to be a primary source of seismic energy in debris flows too [Lai et al., 2018; Zhang et al., 2021a], where the solid transport processes are extreme [Iverson et al., 1997]. Compared to rivers, debris flows are characterized by a significantly higher solid fraction [Coussot and Meunier, 1996; Iverson, 1997] and typically transport larger (up to few meters sized) boulders [Perez, 2001]; therefore more frequent and stronger particle impacts on the riverbed are to be expected, so that debris flows are realistically more powerful seismic sources compared to rivers.

As indicated by Tsai et al. [2012], impacts of the coarser particles dominate the seismic noise generation in rivers. In debris flows, the coarser particles are preferentially concentrated in the boulder rich snout, that therefore is expected to dominate the seismic radiation by debris flows, so that the modelled seismic spectral amplitudes are primarily influenced by the grain sizes of the boulder-rich debris-flow front [Lai et al., 2018; Farin et al., 2019]. For debris flows, where the boulders concentrated in the flow front are pushed from the flow behind and dragged along the riverbed [Iverson et al., 1997], it is reasonable to state that the particle impact velocity scales with the velocity of the flow [Lai et al., 2018]. Starting from the physical model by Tsai et al. [2012] and highlighting the role of the boulder rich debris-flow front in the seismic energy radiation, Lai et al. [2018] derived the following expression for the seismic power spectral density (P_v^T) generated by debris flows:

$$P_v^T(f) = 1.9\, L_s W_f D_{94}^3 v^3 \frac{f^{3+5\xi}}{c_c^5 r_0} e^{-\frac{8.8 f^{1+\xi} r_0}{c_c Q_f}} \qquad \text{(Eq. 2. 3)},$$

where L_s is the length of the boulder rich debris-flow snout, W_f the width of the flow, v is the flow velocity and D_{94} is the 94th percentile of the grain size distribution of the solid fraction of the debris flow. ξ is a site related parameter expressing how strongly seismic velocities increase with depth and Q_f is the quality factor of the site for Rayleigh waves.

From Eq. 2. 3 implicitly emerge some distinctive features of the seismic PSD signature of debris flows. The PSD peak frequency only depends on the minimum source-to-receiver distance (r_0) and

it is independent of debris-flow properties. In contrast, the PSD amplitude is strongly controlled by the boulder size, the flow velocity and the dimensions of the boulder-rich flow front. Surprisingly, the debris-flow thickness (flow depth) does not directly appear in Eq. 2. 3, even though in open channel flows, like debris flows, both the flow velocity and the maximum diameter of transported boulders are controlled by flow depth [Henderson, 1996; Chaudhry, 2008; Badoux et al., 2009].
Reworking Eq. 2. 3 and setting $dP_v^T/df = 0$ it is possible to make explicit the frequency dependence on the minimum source-to-receiver distance, as:

$$r_0 = \frac{(3+5\xi)v_c Q_f}{2\pi(1+\xi)^2 f_p^{1+\xi}} \qquad \text{(Eq. 2. 4)},$$

where f_p is the peak frequency derived from seismic PSD.

According to Eq. 2. 4, higher seismic peak frequencies correspond to shorter source-to-receiver distances and vice versa. Therefore, as the debris flow propagates along a catchment and approaches the recording seismic station, a shift toward higher frequencies is expected in the recorded seismic peak frequency, due to the progressive decrease of the source-to-receiver distance (Figure 2. 5).
On the other hand, Eq. 2. 4 can be used to estimate r_0 from recorded f_p: if the geometry of the channel is properly known, is then possible, at least theoretically, to invert the computed source-to-receiver distances for the actual location of the debris flow in different moments and therefore to trace the flow propagation along the channel [Lai et al., 2018]. In addition, once the position of the flow at different time steps is determined from measured seismic peak frequencies in time, one can estimate the velocity of the flow as the ratio between travelled space and time interval [Lai et al., 2018]. An analogous velocity estimate can be done also based on the recorded seismic amplitude, by measuring the arrival time of the flow front at different stations as the time when the seismic energy exceeds the background seismic level prior to the flow arrival [Burtin et al., 2016].

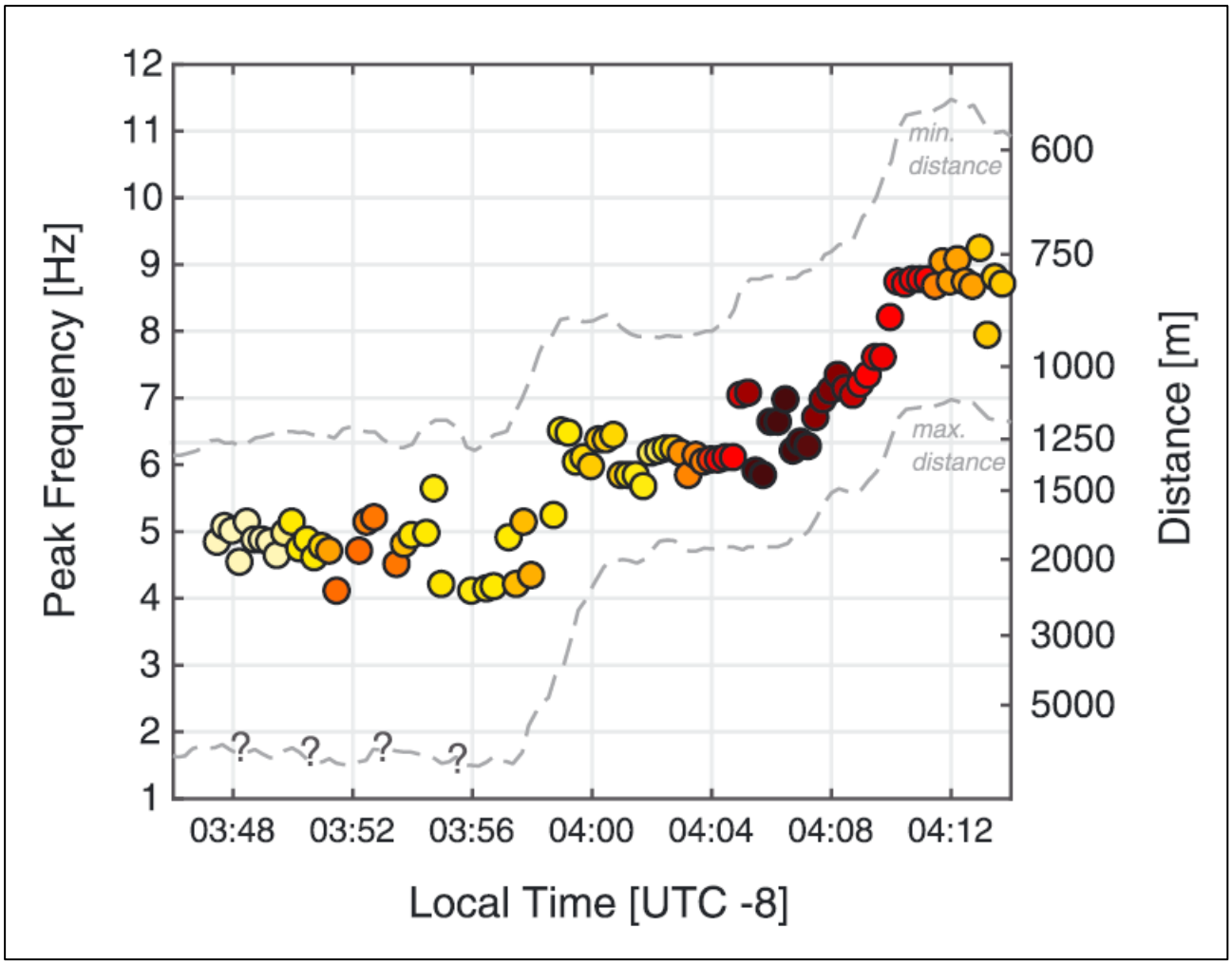

Figure 2. 5: seismic peak frequency obtained from PSDs computed at different times during a debris-flow event in California, USA (source: Lai et al. [2008]). The colour of the dots indicates the amplitude of the PSD, with darker colours corresponding to higher amplitudes. The peak frequency increases in time, as the debris flow approaches the recording seismometer. Source-to-receiver distances are computed using Eq. 2. 4: the dashed lines mark the estimation range linked to uncertainties in the seismic parameters of the ground.

Within a debris flow, solid particles are mainly responsible for the radiation of seismic waves, mostly produced by solid particle-ground collisions within the boulder-rich snout [Kean et al., 2015; Lai et al., 2018; Farin et al., 2019; Zhang et al., 2021(a)]. Indeed, though seismic energy is radiated along the entire debris flow, it appears that for large enough source-station distances the boulder-rich debris-flow front dominates seismic signal generation [Farin et al., 2019; Zhang et al., 2021]. This was also confirmed in the field by Coviello et al., [2019], who analysed the seismic energy produced by debris flows in the Gadria stream catchment (Eastern Italian Alps) showing that most energy transfer occurs during the passage of the surge fronts and is controlled by the mass and the velocity of each surge (Figure 2. 6).

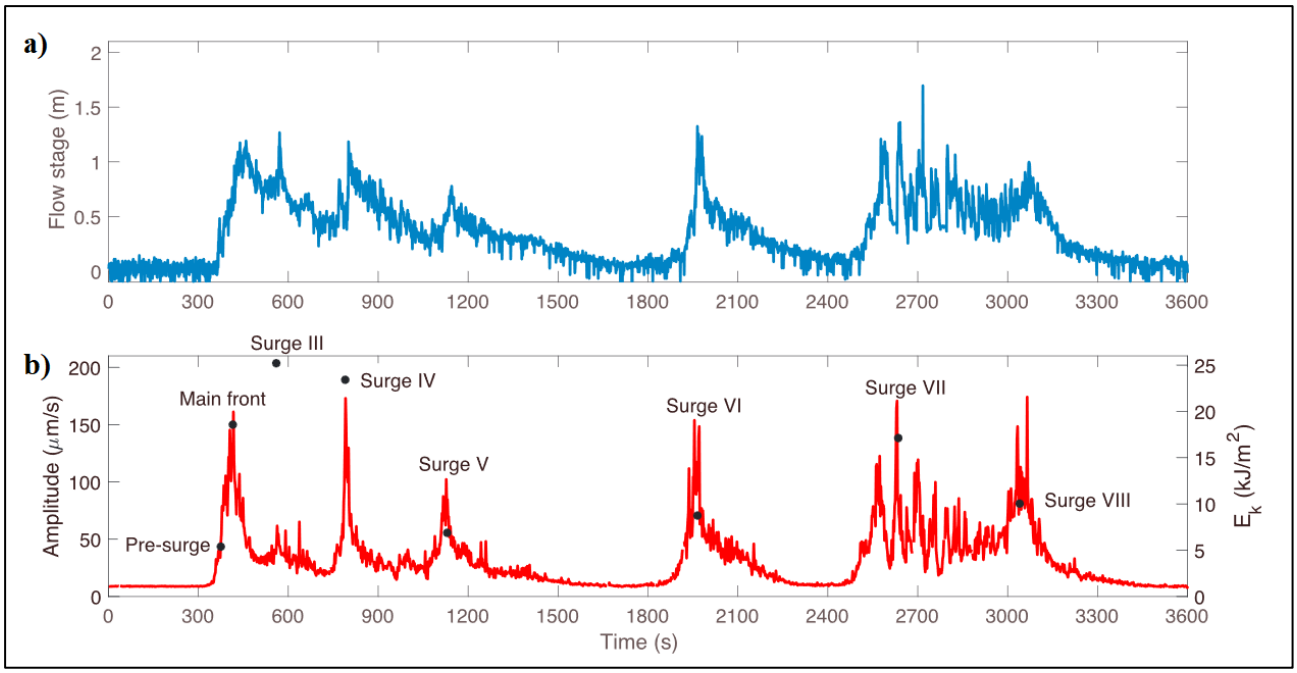

Figure 2. 6: flow stage (a) and envelope of the seismic signal (b) recorded for a debris-flow event of 9 June 2015 in the Gadria catchment (Italy) (source: Coviello et al., [2019]). The event was characterized by several subsequent surges. The seismic signal was recorded using a geophone located outside the channel at the same check dam where the flow depth is measured. For each surge, the seismic maximum amplitude is observed when the surge front passes over the instrumented check dam.

Within debris flows, particle collisions with the bed occur both in the form of single particle random impacts and in the form of force chains, networks of interacting particles that transmit the collision forces to the bed [Estep and Dufek, 2012; Zhang et al., 2021(b)] (Figure 2. 7). The force chain acts as an amplifier of the impact force, as the energy is transmitted and summed up from particle to particle along the particle chain [Zhang et al., 2021(b)]. The rate of particle impacts and force chain formation and the amount of friction within debris flows strongly depend on the solid particle content in the flow. The relative contribution of impacts by single particles or by force chains may vary significantly from event to event and also as a function of the position within the same event. Since the formation of a force chain is favoured for higher solid fraction and larger particle concentration, the contribution of force chains within a debris flow is expected to be stronger in the boulder-rich granular snout [Zhang et al., 2021].

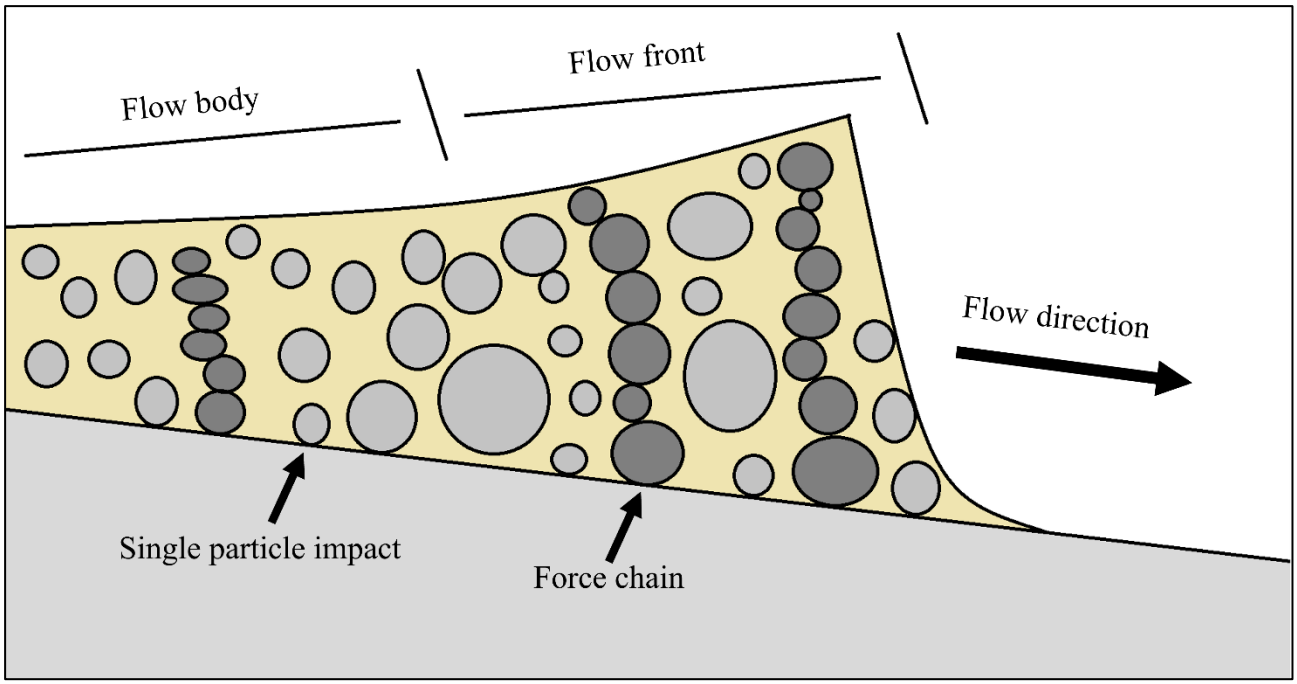

Figure 2. 7: conceptual sketch of a debris flow showing impacts from single saltating particles and force chains (redrawn from Zhang et al., 2021(b)).

The solid fraction of a debris flow strongly controls the radiation of seismic waves by the flow, with seismic wave radiation increasing with increasing solid particle content. However, Kean et al. [2015] showed that, during a debris flow, the radiation of seismic energy is controlled also by the status of the channel, with the amplitude of radiated seismic waves significantly decreasing with increasing the thickness of the sediment layer covering the bedrock channel, which acts as a damper. Particle impacts on loose sediment involves inelastic collisions, which imply significative energy dissipation into friction, and therefore are believed to radiate negligibly small surface waves compared to collision on bedrock [Kean et al., 2018]. This was confirmed also by Piantini et al. [2023], who performed flume experiments on granular flows with different solid content and observed a negative relation between the solid concentration and the measured force fluctuations and the base of the flows. They suggest that the observed inverse trend is due to the rheology of granular flows, where the solid concentration controls the particle agitation and therefore the capability of particles to collide with each other and impact the riverbed.

However, in our knowledge, field validations of proposed seismic models for debris flows are still missing and, as a result, it is not yet fully understood how flow parameters and processes affect the features of the generated seismic signals.

2.2 Infrasonic analysis of debris flows

Infrasound consists of low frequency (<20 Hz) acoustic waves, propagating in the atmosphere as longitudinal waves travelling at the speed of sound of the medium (~344 m/s in the air at a temperature of 20°C at a pressure of 1 atm) [Bedard and Georges, 2000]. The infrasound is generated as moving particles collide with atmosphere molecules and generate stress oscillations that transform into elastic air waves.

Infrasound can be radiated by any natural or anthropogenic process capable of generating a pressure perturbation in the atmosphere. Natural sources include explosive volcanic activity [Marchetti et al., 2009; Johnson and Ripepe, 2011], earthquakes [Mutschlecner and Whitaker, 2005; Marchetti et al., 2016], fireballs and meteoroids [Le Pichon et al., 2013; Belli et al., 2021(b)], mass movements, such as debris flows and snow avalanches [Marchetti et al., 2019; Kogelnig et al., 2011], thunderstorms [Liszka, 2004], sea waves [De Carlo et al., 2020] etc. Anthropogenic sources instead include air and ground traffic, explosions and other human activities [Liszka and Waldemark, 1995; Christie and Campus, 2010].

Infrasonic waves, due to their low attenuation in the air, can propagate long distances in the atmosphere, up to thousands of kilometres from the source [Drob et al., 2003; de Groot-Hedlin and Hedlin, 2014; Vergoz et al., 2022]. This makes infrasound a very powerful tool for studying and monitoring different processes.

The use of infrasonic signals for the study and monitoring of debris flows has a short history (~ 15 years, to the author's knowledge). To date, most of the efforts has been focused on the event detection, using infrasonic signals for early warning purposes [Schimmel and Hübl, 2015; Liu et al., 2015; Liu et al., 2018], sometimes combined with the seismic recordings of debris flows [Schimmel and Hübl, 2016], or on a simple description of the characteristics of the recorded infrasonic signals [Hübl et al., 2008; Kogelnig et al., 2011].

Instead, only a few attempts have been made aiming at understanding and investigating the source mechanism and the radiation processes of the infrasonic wavefield produced by debris flows [Marchetti et al., 2019; Coco et al., 2021; Belli et al., 2022]. Among them, Marchetti et al. [2019] analysed infrasonic and seismic signals generated by three debris-flow events at the Illgraben (Switzerland). They describe the recorded signals as emergent, long duration signals, whose amplitude scales with flow discharge. Based on the different spectral characteristics of the two wavefields (Figure 2. 8), the authors suggest that the infrasound and seismic waves of the debris flows are generated by two different source processes, acting at the flow surface and at the flow-ground

interface respectively. In particular, they propose that infrasound by debris flows is generated by flow waves and oscillations acting at the debris-flow free surface. These surface oscillations collide with the atmosphere and generate a pressure disturbance propagating as infrasonic waves [Marchetti et al., 2019; Ostrovsky and Bedard, 2002]. This interpretation is consistent with the one proposed for the infrasound radiation in rivers by Schmandt et al. [2013], who analysed the seismic and infrasonic radiation by a controlled flood in the Grand Canyon (USA) and suggested that the observed infrasonic energy, peaking at 6-7 Hz, is induced by the waves at the water-air interface.

Marchetti et al. [2019] also performed array analysis of infrasound signals (see Section 4.4 in this thesis for a description of this technique) and found that most of the signal does not show any correlation among the array elements (Figure 2. 8 b, c). Coherent infrasound is observed only in the form of few clusters of infrasonic detections (phase 2 and 3 in Figure 2. 8 b, c), characterized by constant back-azimuth and apparent velocity values, thus indicating stable sources of infrasound and likely pointing at some of the check dams located along the flow. Marchetti et al. [2019] interpret this overall lack of infrasound coherence as the evidence that the incoherent recorded signal results from the contribution of several sources with different amplitude and phase simultaneously active along the entire flow surface.

In order to validate this interpretation and to investigate the lack of coherence highlighted by the array processing, the authors performed numerical simulations to reproduce the main characteristic (signal envelope, spectral content and back-azimuth trend) of the recorded infrasonic signals (Figure 2. 9) [Marchetti et al., 2019]. In particular, the modelling was performed considering two different source mechanism endmembers. They first considered the infrasonic signal as produced only by a single moving source located in the flow front, like the boulder-rich debris-flow snout, that is the main source of seismic energy [Farin et al., 2019; Coviello et al., 2019], and coherent with the infrasonic radiation mechanism modelled for other density currents, like snow avalanches [Naugolnykh and Bedard, 2002; Marchetti et al., 2015; Marchetti et al., 2020] and pyroclastic density currents [Ripepe et al., 2009]. With this assumption, the simulation returns a highly coherent, cigar-shaped infrasonic signal (Figure 2. 9 c, e), and the infrasonic array processing is able to track the migration of the sound-radiating flow front along the channel, in terms of back-azimuth and apparent velocity (Figure 2. 9 e). However, this result is in disagreement with the results of the array processing applied to recorded infrasonic signals, showing no correlation over most of its duration (Figure 2. 8 b, c).

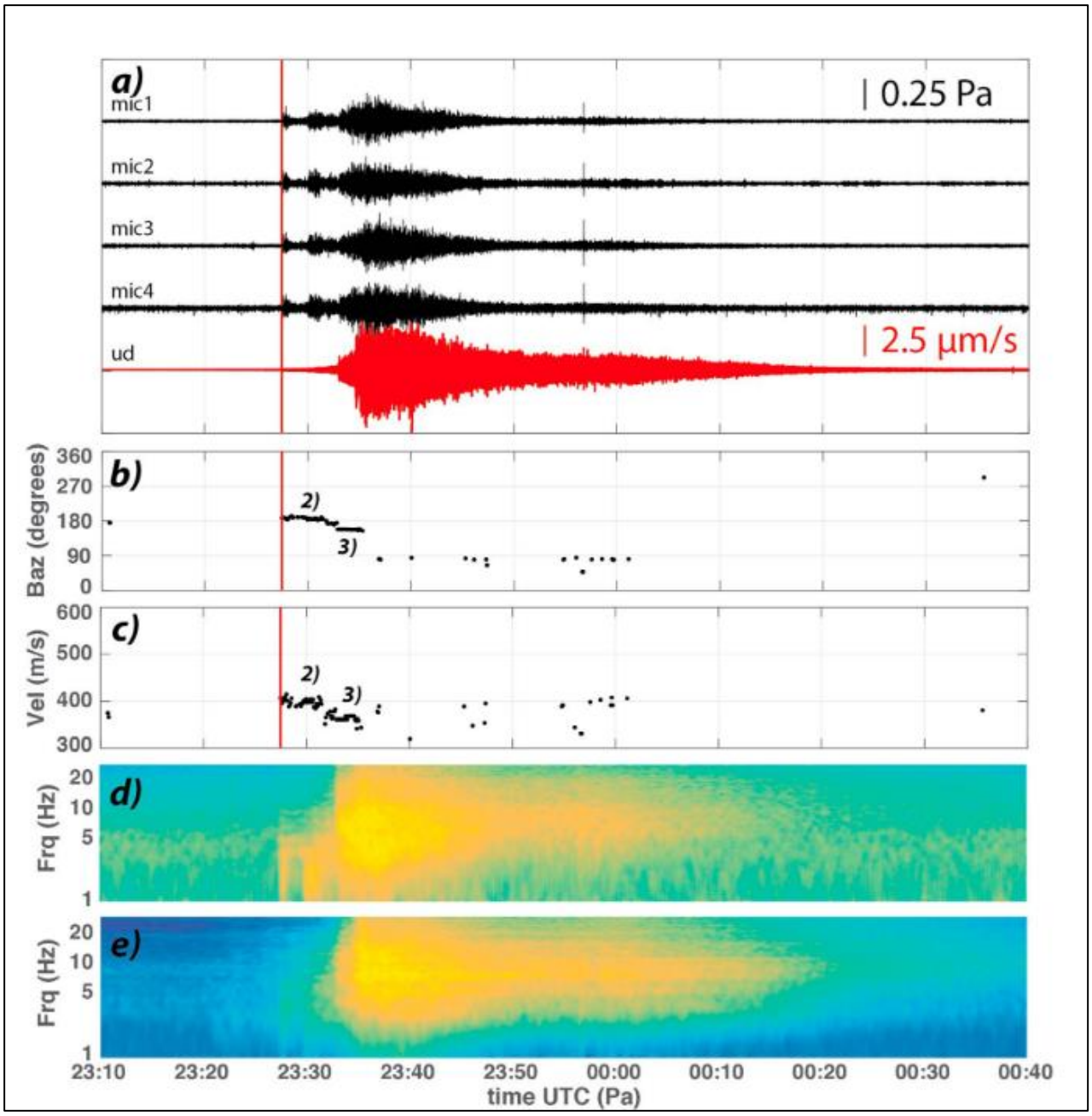

Figure 2. 8: seismo-acoustic analysis of the debris flow on 2017/06/03 at the Illgraben (source Marchetti et al. [2019]). Infrasound (black) and seismic (red) recordings (a). Back-azimuth (b) and apparent velocity (c) trends resulting from array processing of infrasonic tracks: within the array, no correlation is observed except for the two clusters of detections (phase 2 and 3) characterized by constant back-azimuth and apparent velocity values. Spectrograms computed on recorded infrasonic (d) and seismic (e) signals (with yellow marking the higher spectral amplitudes). The red line in plots a, b and c marks the flow arrival time at check dam 1.

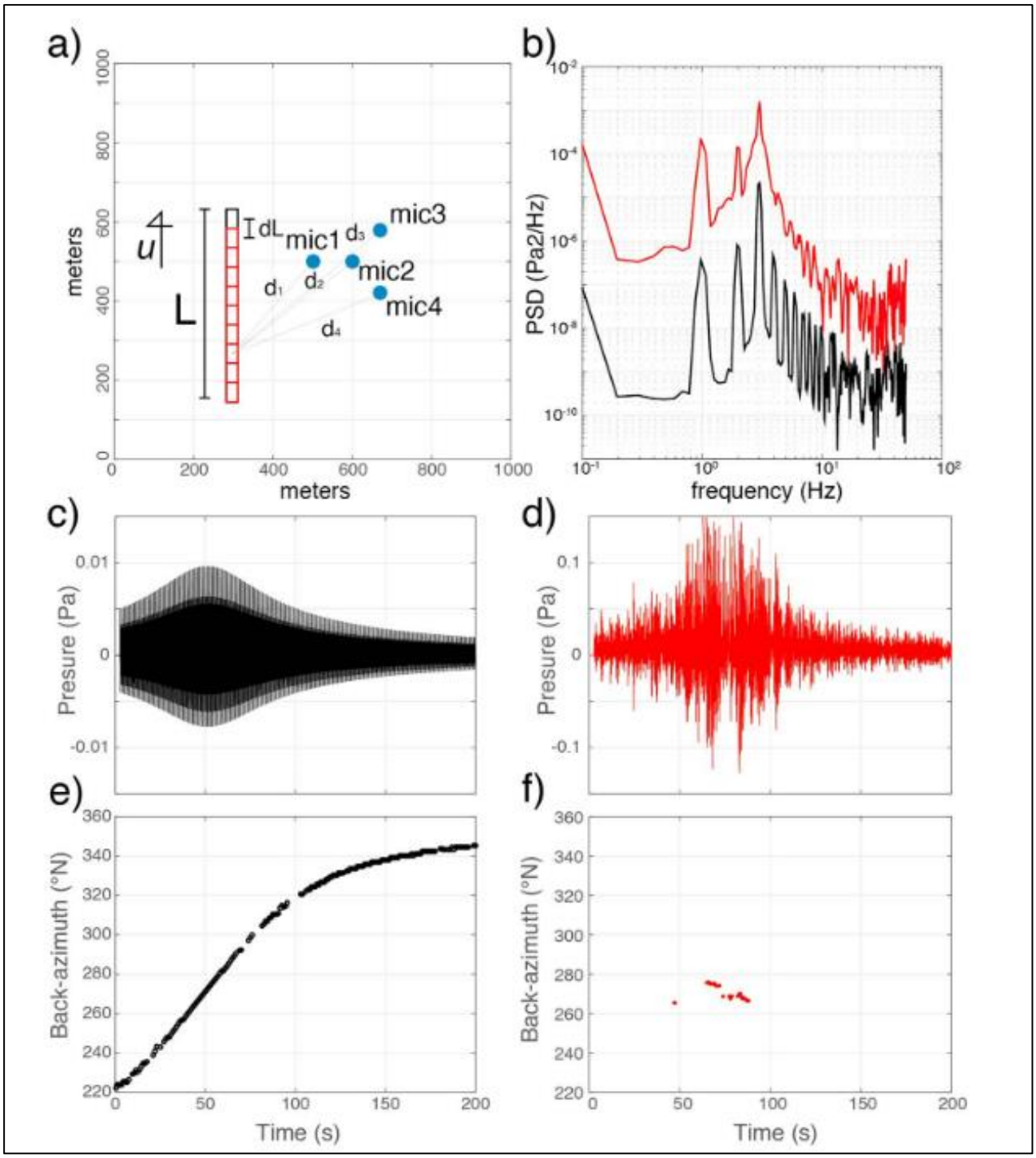

Figure 2. 9: numerical modelling of infrasound radiation by debris flows (source Marchetti et al. [2019]). Sketch of an extended moving source simulating a debris flow recorded by an infrasound array (a). Infrasonic elastic energy and corresponding power spectral density (b) are modelled as being radiated only at the head of the flow (black) or by the entire flow (red). Modelled infrasonic signals recorded at the array (c, d) and array processing results (e, f) in case of elastic energy being radiated by the point source (c, e) or by the extended source (d, f).

Marchetti et al. [2019] also modelled the flow as an extended moving linear source, resulting from the superposition of multiple, equally spaced, simultaneously active sources: each source is set to produce a pressure wave with the same amplitude and the same peak frequency, but with a different phase. The whole synthetic infrasound signal is obtained as the superposition of the contributions of each source, also accounting for the movement of the source and for the wave propagation from source to receiver. The resulting signal (Figure 2. 9 d, f) is incoherent and therefore array processing is not able to track the movement of the flow.

Based on signal features, array processing results and numerical modelling of the infrasonic source, Marchetti et al. [2019] suggest the infrasonic radiation mechanism of debris flows is different from other density currents, like snow avalanches and pyroclastic flows, within which a turbulent flow front develops, dominating the infrasound radiation and allowing to track the movement of the flow with array processing. Their numerical simulations were indeed able to synthetically reproduce the main characteristics of recorded infrasound as an incoherent signal resulting from the superposition of multiple acoustic sources acting simultaneously within the entire flow and located in different positions along the channel (Figure 2. 9 b, d, f), indicating that debris flows can be modelled as an extended source of infrasound, within which infrasonic waves are supposed to be generated by free waves at the flow surface acting along the entire flow length [Marchetti et al., 2019]. However, based on the observation of coherent infrasound indicating a stable infrasonic source at some check dams (Figure 2. 8 b, c), Marchetti et al. [2019] also suggest that the radiation of infrasound by Illgraben debris flows may be enhanced at check dams, that act as predominant sources of infrasonic energy.

This agrees with other experimental observation and numerical modelling on rivers and water flows, according to which infrasound radiation by water flows is strongly affected by the acoustic energy component generated in fixed positions, whenever waterfalls, dams or any topography changes are present [Kudo, 1993; Feng et al., 2014; Coco et al., 2021; Belli et a., 2021(a); Belli et al., 2022; Bedard, 2021]. Indeed, waterfalls constitute powerful sources of infrasound, with larger waterfalls capable of producing infrasonic pressure levels larger than 100 Pa in the nearfield (~500 m from the source) [Bedard, 2021]. Feng at al. [2014], according to previous models based on large objects impacting water [Ostrovsky and Bedard, 2002], modelled infrasound waves generated at dams as the result of surface waves induced by water entering an absorption pool (Figure 2. 10).

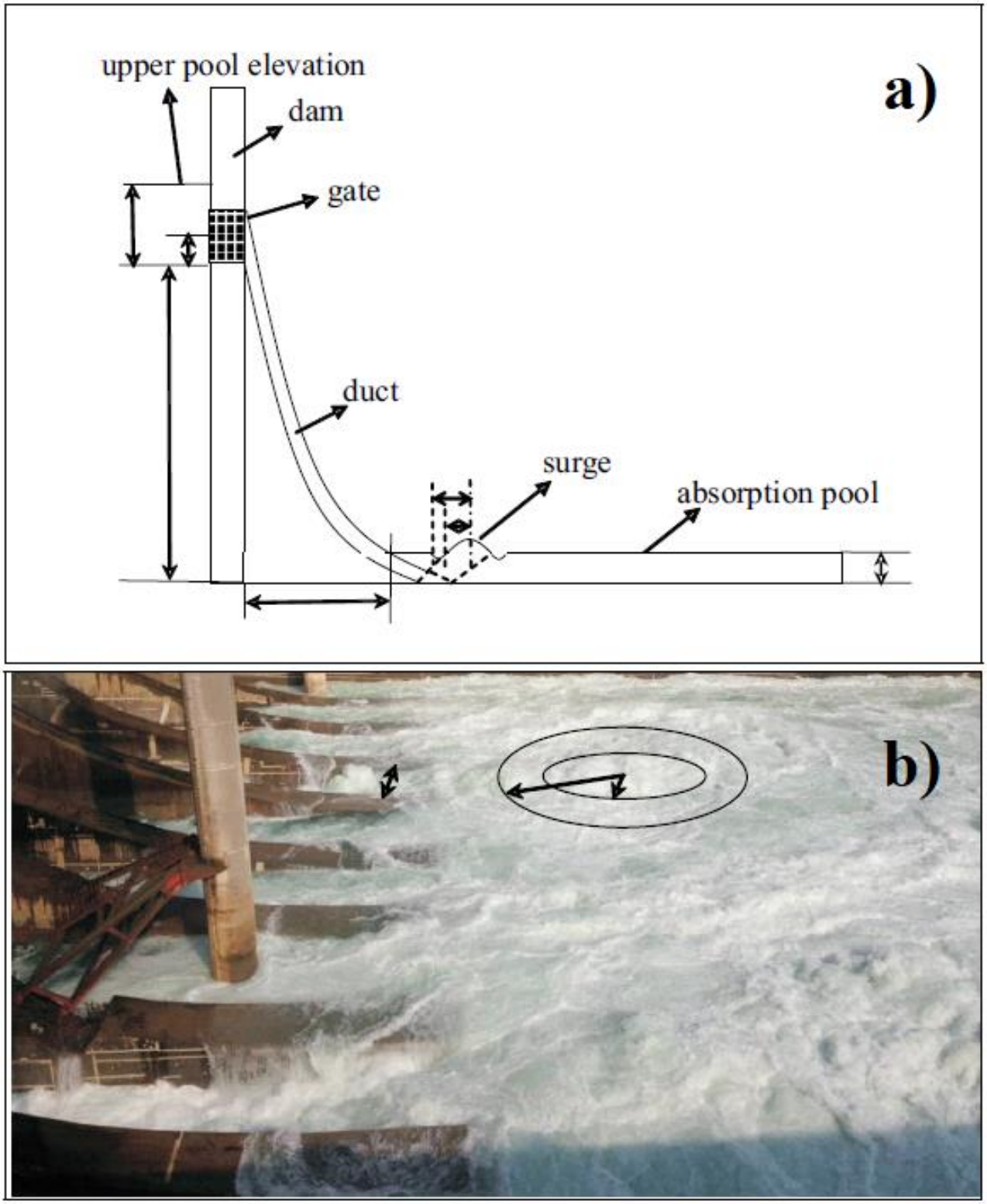

Figure 2. 10: infrasound radiation by a water dam (source: Feng et al. [2014]). Sketch of a water surge generated at the base of a waterfall for water falling into the absorption pool (a). Picture of the surface oscillations generated at the base of a waterfall (b).

They suggest a mechanism whereby water falling downstream of dams generates local water surface elevations surrounded by rings of descending water levels, which radiate infrasound as a dipole source [Feng et al., 2014].

The infrasonic source mechanism based on waves at the flow surface, whose formation is enhanced at the base of waterfall, is consistent with dynamic models and flume experiments on water flows, showing that irregularities (waves and splashes) are induced at the flow surface by turbulence structures generated in the flow for water falling at free overfalls [Coco et al., 2021; Feng et al., 2014; Tokyay and Yildiz, 2007]. Tokyay and Yildiz [2007], performing flume experiments on water flows, observed that at the base of a supercritical free overfall at drop structures along steep channels there is strong energy dissipation (up to >50% of the initial energy) and the development of heavy water splashes due to the jet hitting the floor and setting up vigorous circulation and turbulence. Such surface structures are added to the surface oscillations and waves induced by channel bed irregularities [Horoshenkov et al., 2013] and are likely responsible for most infrasound radiation by rivers [Schmandt et al., 2013] and debris flows [Marchetti et al., 2019].

The interpretation by Feng et al. [2014] agrees with Coco et al. [2021], who modelled the infrasonic wavefield generated by a water flow flowing over and falling at a topographic step (a dam). The numerical modelling, performed using the compressibleInterFoam solver available in the open-source simulation code OpenFOAM, allowed to model the flow evolution and the production of pressure perturbation in the in the surrounding atmosphere. The simulation was carried out for different step heights and different flow depths (Figure 2. 11; Figure 2. 12). They found that infrasonic waves are preferentially radiated by the flow at the base of the waterfall, where surface oscillations develop and push the atmosphere generating pressure disturbances. After the low frequency oscillations observed at the very beginning and produced by the input of material in the modelling grid, the modelled infrasonic signals show an initial high frequency transient (ii in Figure 2. 11 b and Figure 2. 12 b), which is interpreted to be associated to the water hitting the ground downstream the dam. Then, a lower frequency monochromatic pressure oscillation develops (iii in Figure 2. 11 b and Figure 2. 12 b), with emergent onset and cigar shape. Authors suggest that this lower frequency oscillation is likely related to the waves produced at the flow surface by the turbulence generated downstream the dam.

In contrast, Coco et al. [2021] predict the absence of significant infrasound radiation, regardless of the flow discharge, when the flow occurs within flat channels lacking any irregularities (bed roughness topographic steps, bends) (Figure 2. 11 a). Their results also show that the amplitude and the frequency of generated infrasound scale with flow depth and with the height of the step, with infrasonic peak frequency decreasing with increasing the flow depth and drop height, [Coco et al., 2021] (Figure 2. 11 c; Figure 2. 12 c).

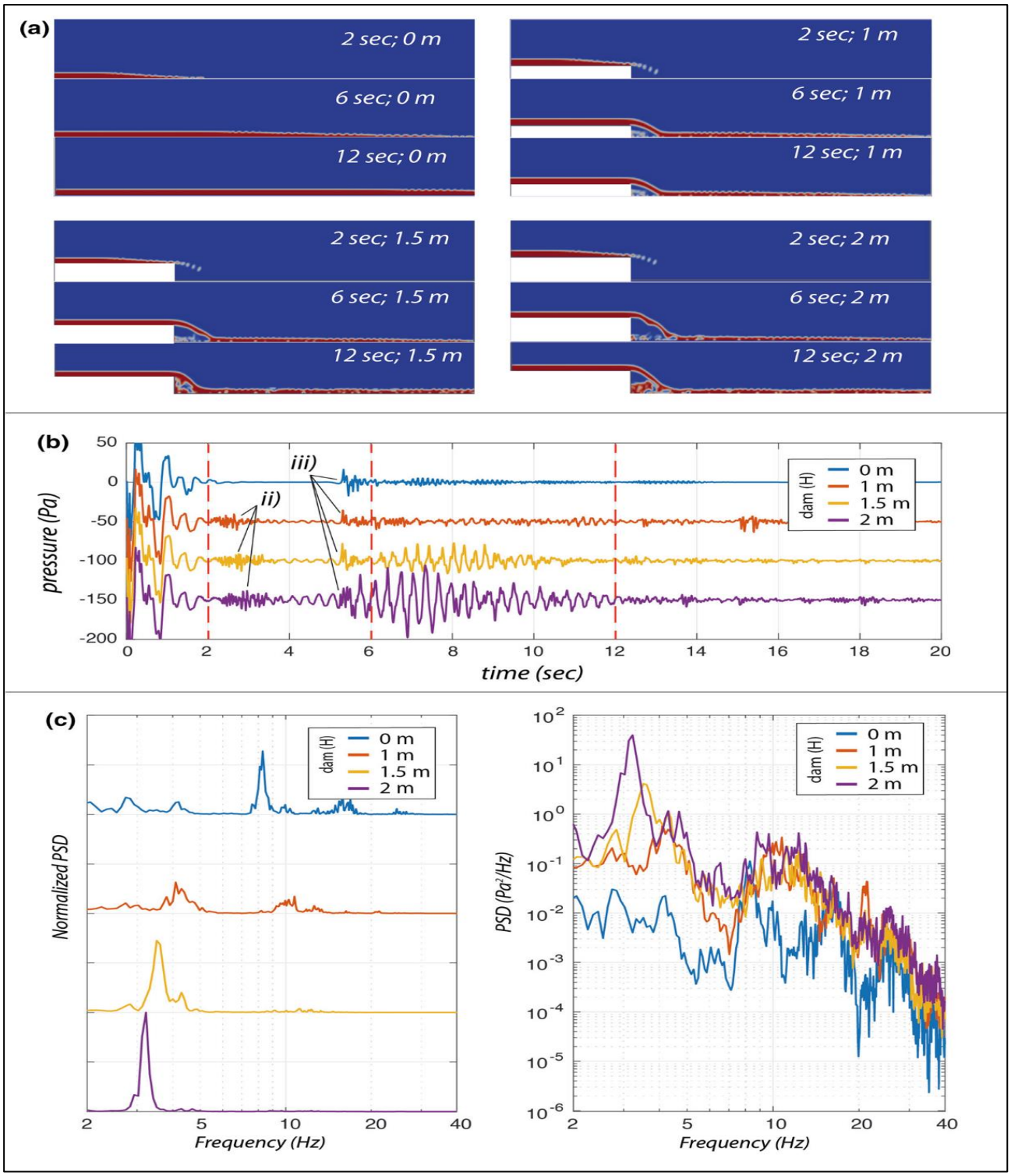

Figure 2. 11: numerical modelling of the infrasound generated by water flow over a dam (source: Coco et al. [2021]). Flow simulations with different dam heights (a). Resulting band-pass filtered (>2 Hz) synthetic infrasound (b): vertical dashed orange lines mark the timing of the snapshots in "a", while ii and iii respectively indicate the higher frequency and the lower frequency components of the modelled infrasonic signal described in the text. PSD of synthetic infrasonic signal (c).

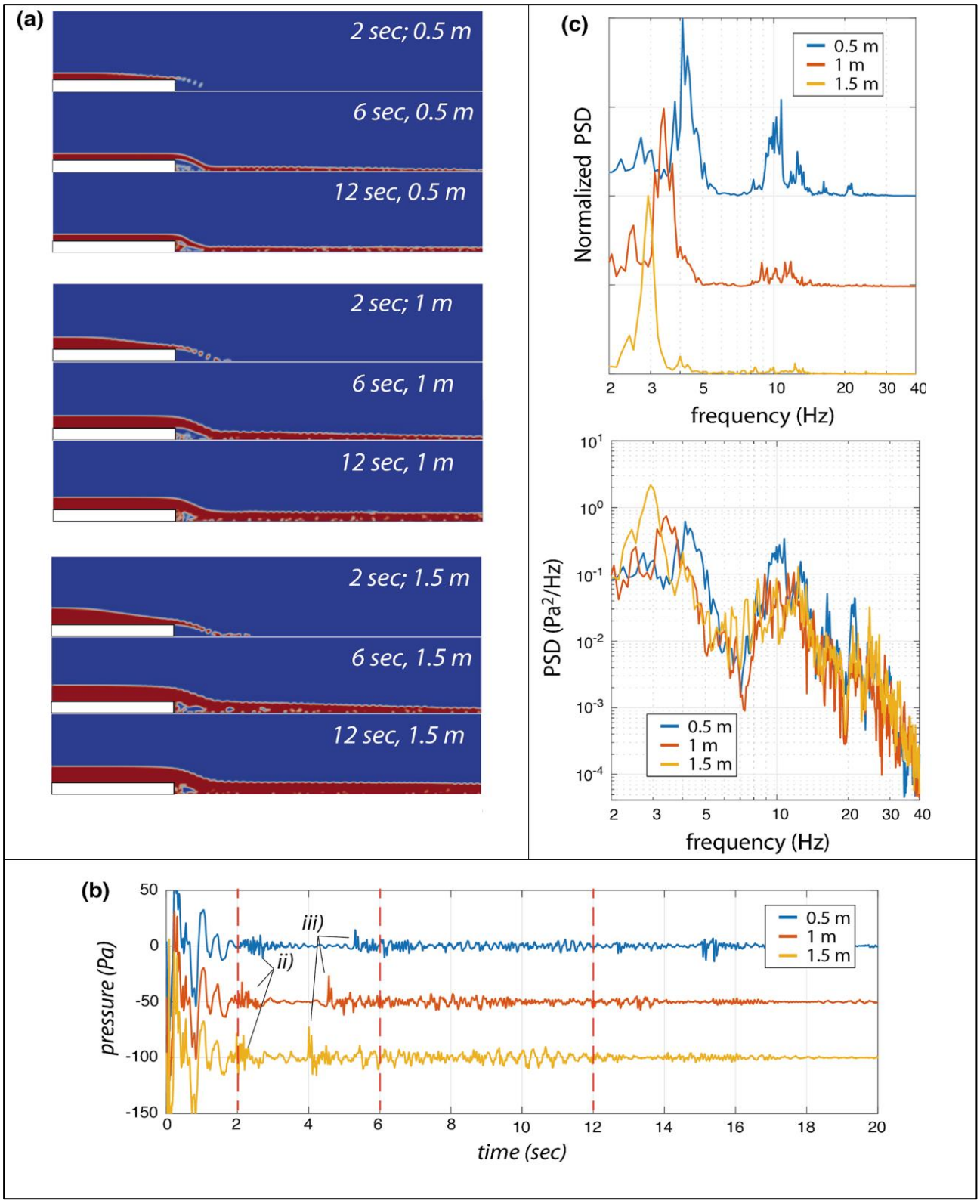

Figure 2. 12: numerical modelling of the infrasound generated by a water flow over a dam (source: Coco et al. [2021]). Flow simulations with different flow depths (a). Resulting band-pass filtered (>2 Hz) synthetic infrasound (b): vertical dashed orange lines mark the timing of the snapshots in "a", while ii and iii respectively indicate the higher frequency and the lower frequency components of the modelled infrasonic signal described in the text. PSD of synthetic infrasonic signal (c).

Debris flows, like rivers, are expected to have multiple sources of infrasound, according to flow dynamics and channel geometry [Marchetti et al., 2019; Coco et al., 2021; Belli et al., 2022]. However, an accurate physical model addressing the actual source mechanism and describing the link between flow parameters and the generated infrasound is still missing.

2.3 Seismo-acoustic analysis of debris flows

In the previous Section of this Chapter, we described how seismic and infrasonic signals have been used separately for studying debris flows.

However, an accurate seismo-acoustic analysis of these phenomena, combining the infrasonic and seismic records, is probably necessary and more complete. Indeed, since debris flows radiate elastic energy both in the ground, in the form of seismic waves, and in the air, as infrasound, only analysing both the wavefield it is possible to investigate the radiation process as a whole.

While the combined use of infrasonic and seismic sensors is not new for debris flows, to our knowledge, previous studies had been focused only on event detection for the purpose of designing reliable warning systems [Hübl et al., 2013; Schimmel and Hübl, 2016].

Among them, Schimmel and Hübl [2016] proposed a detection algorithm for detecting debris flows and debris floods based both on infrasonic and seismic signals recorded with an infrasonic sensor and a co-located seismometer deployed a few meters (< 20 m) from the channel. The detection algorithm is based on the analysis of the relative amplitude of the recorded seismo-acoustic signals and of the evolution over time of their frequency content and had been tested at different sites in Austria and Switzerland.

In contrast, to our knowledge, no studies have been published on the seismo-acoustic analysis of debris flows focused on the relation between the two wavefields and between their source mechanisms. Such an approach, also followed in this thesis, could allow to resolve several open questions on the seismo-acoustic energy radiation by debris flows and to investigate if and how the generated infrasonic and seismic signals and their source processes are related to each other.

Chapter 3

Study site and dataset

3.1 The Illgraben catchment and debris-flow activity

This thesis is focused on the analysis of the debris-flow activity in the Illgraben catchment, located in Switzerland's Canton Valais, near Leuk [Badoux et al., 2009] (Figure 3. 1). It is one of the most active and best instrumented debris-flow sites worldwide.

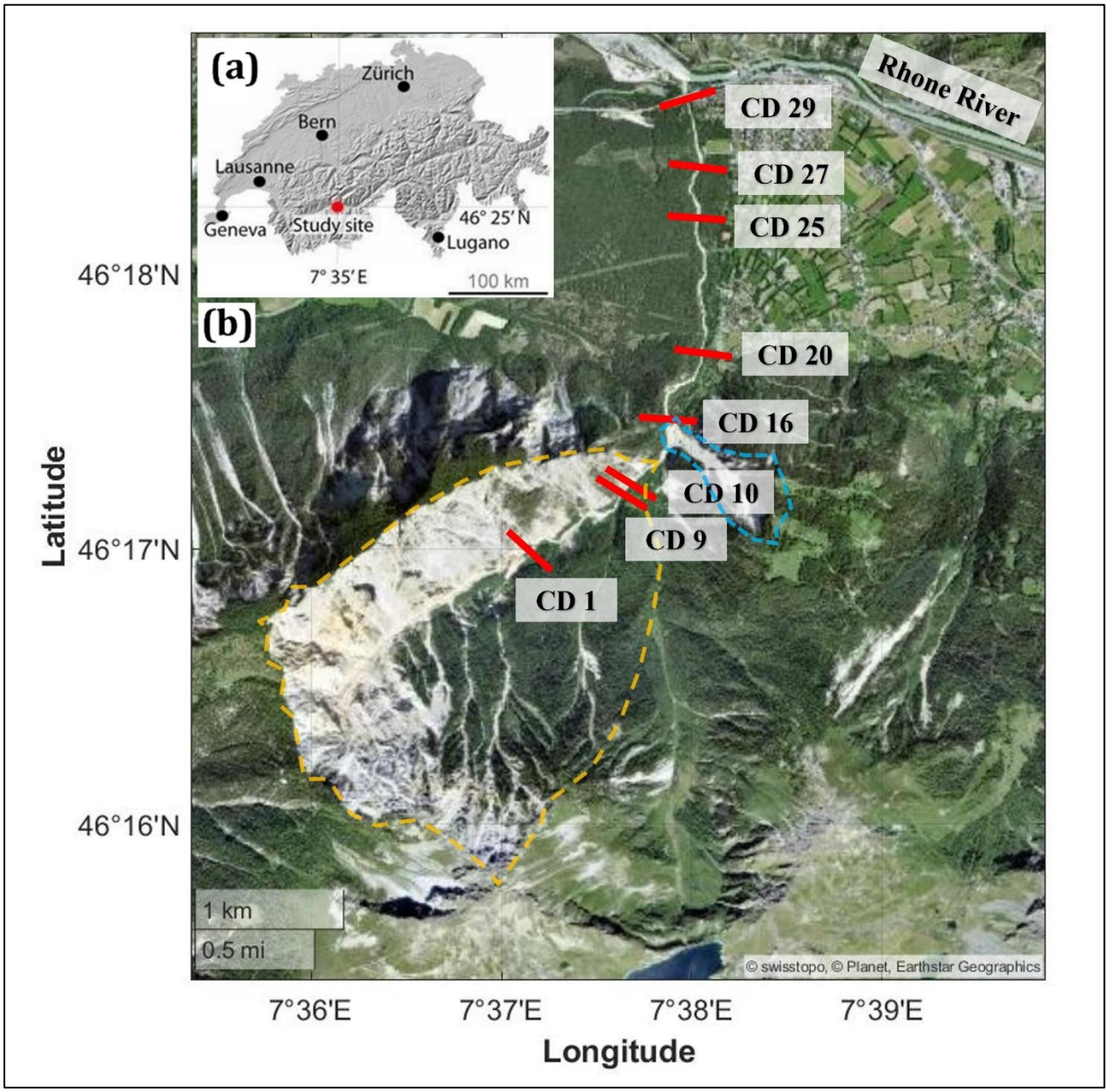

Figure 3. 1: Illgraben catchment geographic setting and instrumental setup. Switzerland and location of Illgraben (red dot) (a). Satellite image of the Illgraben catchment (b); the orange dashed line marks the boundary of the upper catchment, while the cyan dashed line highlights the Sagenschleif slope. Red bars with

alphanumerical labels indicate the position of 7 Illgraben check dams (CD 1, 9, 10, 16, 20, 25, 27, 29; CD=Check Dam).

Figure 3. 2: the upper Illgraben catchment as it appears from its southern rim (source: Giacomo Belli).

Such a massive debris-flow activity has built over time the large ~500 million of m^3 debris fan [Schlunegger et al., 2009; Badoux et al., 2009] in front of Illgraben canyon mouth, whose east side hosts the village of Susten and is densely inhabited (Figure 3. 3).

The sediment load available for debris flows occurring in the Illgraben channel is further increased by frequent landslide activity occurring on the east side of the catchment along the steep lateral slope called Sagenschleif. In recent years the Sagenschleif has produced numerous landslides and slope failures also leading to small debris-flow events [Zhang et al., 2021].

Figure 3. 3: the debris-fan in front of the Illgraben catchment and Susten village on its eastern side (source: Emanuele Marchetti).

Flow events occurring in the Illgraben catchment are characterized by an enormous variability in size, duration and in the hydraulic, physical and compositional features [Badoux et al., 2009]. As a matter of fact a wide range of flow types has been recorded, distinguished by solid particles concentration and size and resulting flow behaviour, spanning from debris flows, to muddy debris flows to hyperconcentrated flows [Badoux et al., 2009].

Typical debris-flow events at Illgraben are classified as granular debris flows, transport a huge load of solid particles with blocks up to several meters in diameter, mostly concentrated at the flow front. Muddy debris flows (or debris floods) are characterized by a lower sediment concentration and a higher water content and transport a significantly smaller amount of large meter-sized boulders. Other observed flow types range from hyperconcentrated flows to flood flows [Badoux et al., 2009].

Figure 3. 4: photo of the Sagenschleif lateral slope, where frequent landslide activity occurs. The slope, represents an important source of sediment for the Illgraben channel (source: Giacomo Belli).

In general, each flow type transports large boulders with a mean diameter as large as the flow depth [Badoux et al., 2009]. Therefore, due to their transport capability, both debris flows and hyperconcentrated flows may have a boulder rich front and a velocity up to several m/s and therefore

are equally dangerous. In addition, many of the flows occur as flash floods [Badoux et al, 2009]: in such kind of events the flow depth rises from zero to several meters in a short time span (few seconds or minutes), with strong implication for flow impact and associated hazard management.

In order to mitigate the impact and the risk associated to Illgraben debris-flow activity, a series of 30 check dams (CDs) has been realized and deployed along the lower 3.4 km of the Illgraben channel, from the upper catchment to the point where the Illgraben creek flows into the Rhone river [McArdell and Sartori, 2021] (Figure 3. 1, Figure 3. 5 and Figure 3. 6).

Figure 3. 5: photo of the check dam 20. With a height of ~8 m, it is the highest check dam outside the upper catchment (source: Giacomo Belli).

Figure 3. 6: photo of CD 8 and CD 9, located inside the upper catchment, whose south-west rim is visible in the background (source: Giacomo Belli).

Drop structures, such as free overfall and check dams, are usually built at intervals along steep rivers in order to reduce the bed slope and to dissipate flow energy without scouring the channel [Tokyay and Yildiz, 2007]. In addition, being realized with a known channel cross section, these structures are usually used as gauging point for flow discharge and other parameters [Tokyay and Yildiz, 2007]. The realization of these CDs in the Illgraben was meant to stabilize the channel, to reduce debris-flow discharge and to dampen erosive action of the flows on the creek channel. The check dams are characterized by very different heights (Figure 3. 5 and Figure 3. 6), ranging from < 2 meters up to the 44 m of the CD 1 (Figure 3. 7), located within the upper catchment at an altitude of 1090 m, that is the biggest Illgraben check dam [McArdell and Sartori, 2021].

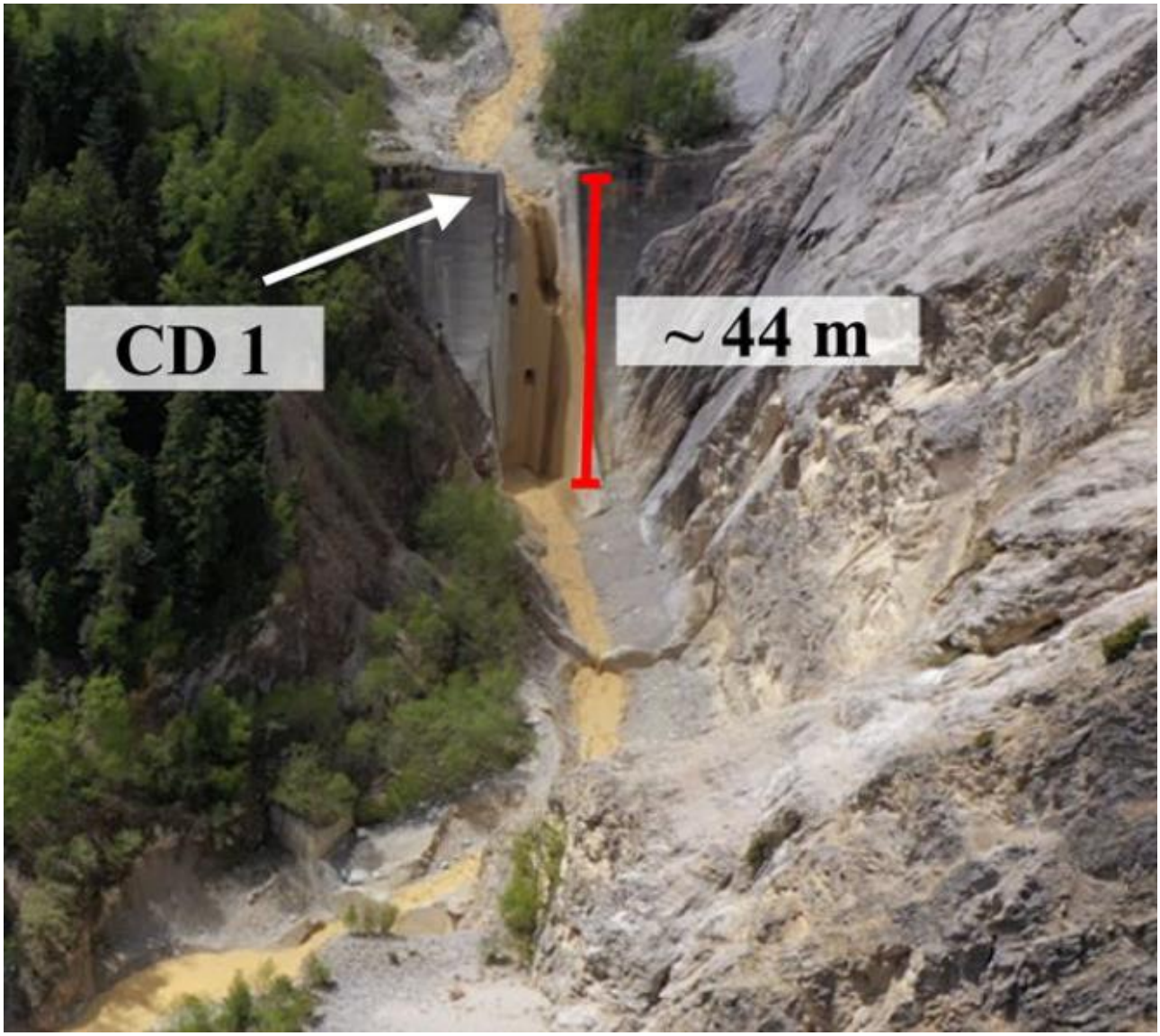

Figure 3. 7: photo of the 44 m high CD 1, located in the upper catchment (source: Zhang et al., [2021]).

The realization of those CDs led to a significative mitigation of the debris-flow damage potential; indeed, most debris flows no longer overtop the channel bank and significant damage last occurred in 1961, before the construction of the check dams, when a road bridge was destroyed by a large debris flow [Badoux et al., 2009]. This massive event was fed by the sediment deposited by a large rock avalanche of ~ of 3-5 10^6 m^3 occurred earlier in 1961 in the upper catchment [Badoux et al., 1961].

3.1.1 Debris-flow events at Illgraben

Typical Illgraben debris-flow events (Figure 3. 8) have volumes of ~20,000 m^3, but major events with volumes up to 70,000-100,000 m^3 are frequently observed [Badoux et al., 2009]. While smaller debris-flow events (<75,000 m^3) remain entirely within the stream channel, representing a risk only for people in or near the channel, larger debris flows may overflow the channel banks and reach inhabited areas, constituting a serious threat for local communities [Badoux et al., 2009]. A wide variability, reflecting the solid fraction variation, is observed also in flow velocity (v), typically ranging between 3 and 6 m/s [Wenner et al., 2019], even though both faster ($v > 6$ m/s) and slower ($v < 3$ m/s) debris flows are frequent. The transported sediment ranges from mud to meter-sized boulders, which are mostly concentrated in the debris-flow front (Figure 3. 8).

At Illgraben, each debris-flow event generally occurs every year between late spring and early autumn [Badoux et al., 2009] and in particular between the end of May and September [Berger et al., 2011]. Such a strict seasonal constraint results from debris-flow events being triggered by a sudden surface water influx, given by extreme rainfall events, such as the strong summer convective rainstorms affecting the site [Hürlimann et al., 2003; McArdell et al., 2007; Burtin et al., 2014], or snowmelt [Walter et al., 2017; Wenner et al., 2019]. Debris-flow triggering is also possible in the absence of precipitation or snowmelt, when natural lake dams formed by landslides or glacial ice suddenly break, giving rise to a critical runoff [Costa and Schuster, 1988; Evans and Clague, 1994]. Whatever the triggering process, the resulting significant runoff leads to a massive sediment mobilization along the steep (>40°) catchment slopes [McArdell et al., 2007], either on lateral slopes or within the torrent channel [Gregoretti and Dalla Fontana, 2008], possibly leading to the debris-flow event development. Initial sediment mobilization can also be triggered via increased ground porewater pressures leading to failure across a critical subsurface layer; this latter initiation mechanism is known in literature as

landslide triggering [Iverson et al., 1997]. Because of the inaccessibility of the upper catchment, Illgraben debris-flow triggering mechanisms are however not fully understood yet [Badoux et al., 2009].

Figure 3. 8: the 24/06/2021 Illgraben debris flow: two subsequent frames of the flow front at CD 29, where the force plate is located (source: WSL).

3.2 The Illgraben debris-flow monitoring system

Since summer storms are probably the most frequent of the several triggering processes, similar to other debris-flow and landslide settings [Keefer et al., 1987; Chan and Pun., 2004; Jakob et al., 2006], Illgraben debris-flow detection system is primarily based on the measurement and monitoring of the intensity and duration of rainfall events [Badoux et al., 2009], relying on empirical rainfall thresholds for debris-flow triggering determined in the region [McArdell and Badoux, 2007].

Rainfall measurements are provided by three rain gauges situated on the flanks of the Illhorn, within the catchment [Badoux et al., 2009]. However, such a surveillance approach is not reliable enough since, as previously highlighted, debris flows can occur even in the absence of significant rainfall and because large uncertainty exists on debris-flow triggering rainfall thresholds [Giannecchini et al., 2016].

In addition, based on historical events analysis, the largest Illgraben debris flows tend to occur in association with sudden catastrophic failure of natural dams delimiting temporary lakes formed by landslides in the upper catchment [Badoux et al., 2009], so that catchment status observations, relating to the general degree of sediment availability and the possible presence of torrent-blocking landslides, are another key-point of the existing Illgraben debris-flow alert system [Badoux et al., 2009]. These dam failures, able to be primed by both high-intensity short duration storm and long-duration low intensity rainfalls, are not directly correlated to a particular rainfall type or intensity [Badoux et al., 2009].

Furthermore, it has been observed that similar precipitation events may or may not trigger a debris flow [McArdell and Badoux, 2007] and, in the case that a debris flow develops, very similar rainfall events may induce different triggering processes, thus resulting into debris-flow events of even very different kind and magnitude [Badoux et al., 2009]. The non-univocal relation between rainfall types and debris-flow occurrence clearly indicates that other factors such as previous soil moisture, sediment availability, topography, catchment source subareas and debris-flow initiation processes, may be important for event triggering and evolution [Gregoretti and Dalla Fontana., 2008; Badoux et al., 2009].

In order to develop a debris-flow warning and monitoring system as accurately as possible, the Illgraben catchment has therefore been instrumented with the installation of various types of sensors and devices along the whole creek, close to or inside the channel, including cameras, laser/radar/ultrasonic altimeters for flow depth measurements, geophones and a debris-flow force plate etc [Hürlimann et al., 2003; McArdell et al., 2007; Badoux et al., 2009]. Furthermore, the Swiss

Federal Institute for Forest, Snow and Landscape Research WSL, installed a scientific observatory, devoted to debris-flow activity monitoring and operating since 2000 [Rickenmann et al., 2001; Hürlimann et al., 2003; McArdell et al., 2007].

Such an instrumental setup and such a monitoring system are able to provide a wide range of measurements concerning debris-flow hydraulic or physical features and guarantee the maintenance of an early warning system based on collected in-torrent debris-flow measurements and identification [Badoux et al., 2009].

The existing early warning system at Illgraben has been optimized to provide reliable early warning for the community [Badoux et al., 2009]. Warning is issued in form of acoustic alarms and flashing lights installed at channel crossings frequented by tourists and text messages delivered to the authorities. The detection of the ongoing debris-flows is first provided by geophones (Geospace Technologies, model GS-20DX) installed within the bed behind steel plates at CDs 1, 9, 10 [Badoux et al., 2009; Walter et al., 2017]. Other two geophones are deployed at CDs 27 and 29 (Figure 3. 1). The geophones detect the debris-flow front arrival at the check dams where they are deployed. The passage of the boulders of the flow front over the steel plate on the check dam brink produces vertical vibrations, which activate the geophones by inducting voltage impulses. The debris-flow front arrival is defined when the generated signal exceeds a previously determined empirical threshold voltage, allowing the debris-flow detection. In particular the early warning system is activated upon initial detection on the geophones at CD 1, 9 and 10. Ideally, the first detection is provided by the geophone installed on CD 1, which is the most upstream. Unfortunately, this system is prone to power outages due to limited sunlight and a weak GSM network signal. In contrast, detections at CD 9 and 10 are more reliable and are less susceptible to potential damage by rockfall. CD 10 also has a laser stage sensor and issues a warning when a predefined flow height is reached [Walter et al., 2017]. For this warning, the delay time, defined as the difference between the initial detection and its arrival at CD 27, is rather variable, ranging from 0 to 30 minutes [Badoux et al., 2009].

The warning system is implemented also with radar altimeters, able to detect the sudden increase of the flow stage associated with the passage of the debris flow. The choice of radar altimeters, rather than laser or ultrasonic ones, derives from the fact that, in conditions of rapid variation of the depth of the flow or splashes on the surface of the flow, the radar sensors are able to register a more stable depth signal, albeit more smoothed, compared to other types of sensors. For this reason, radar sensors are more reliable for early warning purposes, even if they are less useful for research [Badoux et al., 2009].

The altimeters are suspended over a check dam, just upstream its crest, where the channel bottom is expected to remain unchanged as sediment deposition is not expected, due to the acceleration of the

flow before the freefall. In particular, two radar sensors had been deployed at CD 10 (Figure 3. 9), to minimize the false alert associated with the geophones.

Figure 3. 9: two radar altimeters suspended over the channel at CD 10 for debris-flow detection (source: Badoux et al. [2009]).

In practice, a debris flow is detected, and the alert is issued, when both the signal recorded by the geophones and the flow depth measured by the two radar altimeters exceed the empirical thresholds. When a debris flow event is detected, the measuring system deployed along the further downstream channel section is activated.

Laser and ultrasonic altimeters suspended on the channel at different check dams provides in real time flow stage measurements [Arattano and Marchi, 2008]. The altimeter measures the distance from the surface of the flow, which, knowing the distance from the fixed riverbed, allows to determine the flow depth. When the flow depth is measured along the entire duration of the event, the debris flow hydrogram is obtained.

In addition, using differences of the flow front arrival time at different CDs, provided by the geophones, and knowing the distance travelled by the flow between the gauging points, it is possible to estimate the flow front velocity. In particular, the front velocity at Illgraben is computed from the differences between the flow front arrival times at CD 27 (or CD 28) and CD 29.

If the geometry of the channel section where the measurements are taken is known, the depth and the velocity of the flow can be combined to obtain the volumetric discharge rate. Flow volumes can also be estimated by integrating flow discharge over the entire debris-flow wave [Schlunegger et al., 2009].

The flow density instead can be estimated thanks to the force plate located on the edge of CD 29, which provides basal normal and shear stress measurements [McArdell et al., 2007] (Figure 3. 10). The force plate, previously destroyed by a debris flow in 2016, was reinstalled in 2019. It consists of a 4 m wide (perpendicular to flow direction) and 2 m long (in flow direction) concrete slab deployed within the channel bed ta the brink of CD 29.

Flow basal force is measured as the sum of the force data collected by four load cells placed underneath the corners of the force plate (Figure 3. 11), at either 2,400 or 9,600 Hz [Zhang et al., 2021]. The basal force data then resampled in 1-seconds long windows, in each of which the median value of the normal or horizontal forces are recorded [Zhang et al., 2021].

The computed normal force corresponds to the weight of the debris flow over the force plate, which is deployed under the altimeter installed at CD 29. Considering the channel geometry at CD 29 and the plate area, the flow bulk density is computed as the mass/volume ratio at the force plate, using the measured flow weight and the recorded flow depth over the force plate [McArdell et al., 2007; McArdell et al., 2016].

Figure 3. 10: photo of the 4×2 m force plate (highlighted by the red rectangle) deployed at the brink of CD 29 at Illgraben (source: Giacomo Belli).

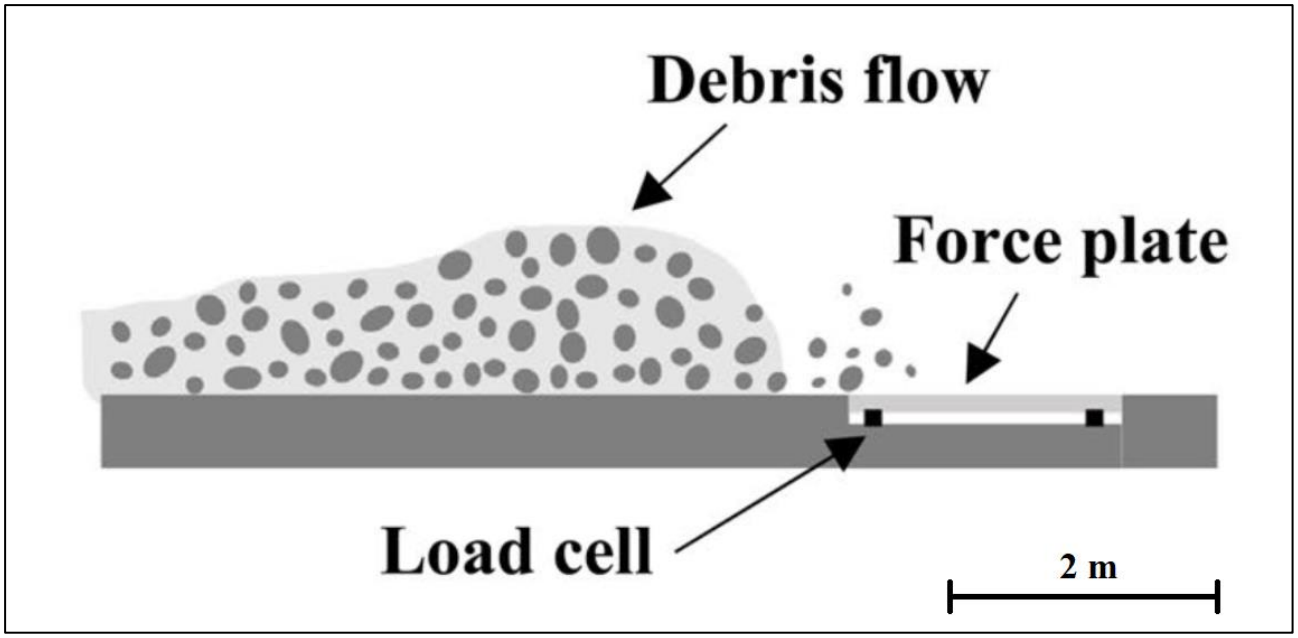

Figure 3. 11: schematic sketch of the force plate deployed on the brink of CD 29 at Illgraben. The force plate provides measurements of the forces exerted at the base of the debris flow, which can be used for the estimation of the debris-flow bulk density. The force plate consists of a 4x2 m concrete plate with four load cells located underneath the four corners of the plate (source Zhang et al. [2021]).

Illgraben debris-flow instrumentation requires great economic efforts to be operational and efficient; instruments, especially the ones located in the upper catchment, are generally not easily accessible. In addition, when located close to the channel or to landslide areas, the sensors are frequently damaged by debris flows or landslides (Figure 3. 12).

Figure 3. 12: a camera for debris-flow video recording before (left) and after (right) being hit by a debris-flow event in the 2021 debris-flow season at Illgraben (source: Giacomo Belli).

Recently the Illgraben instrumental set-up has been expanded with the installation of a series of seismic stations deployed all around and within the Illgraben catchment and on the debris fan in front (Figure 3. 13) [Walter et al., 2017; Walter et al., 2022]. The seismometers, Lennartz-1s sensors (flat

response between 1 and 100Hz) sampling at 100Hz, ensure a safe remote continuous recording of the seismic radiation of the debris flows occurring at Illgraben and only require modest management costs. An infrasonic array has also been installed north of Illgraben on the debris cone [Marchetti et al., 2019], providing excellent recordings of the acoustic waves generated by the debris flows.

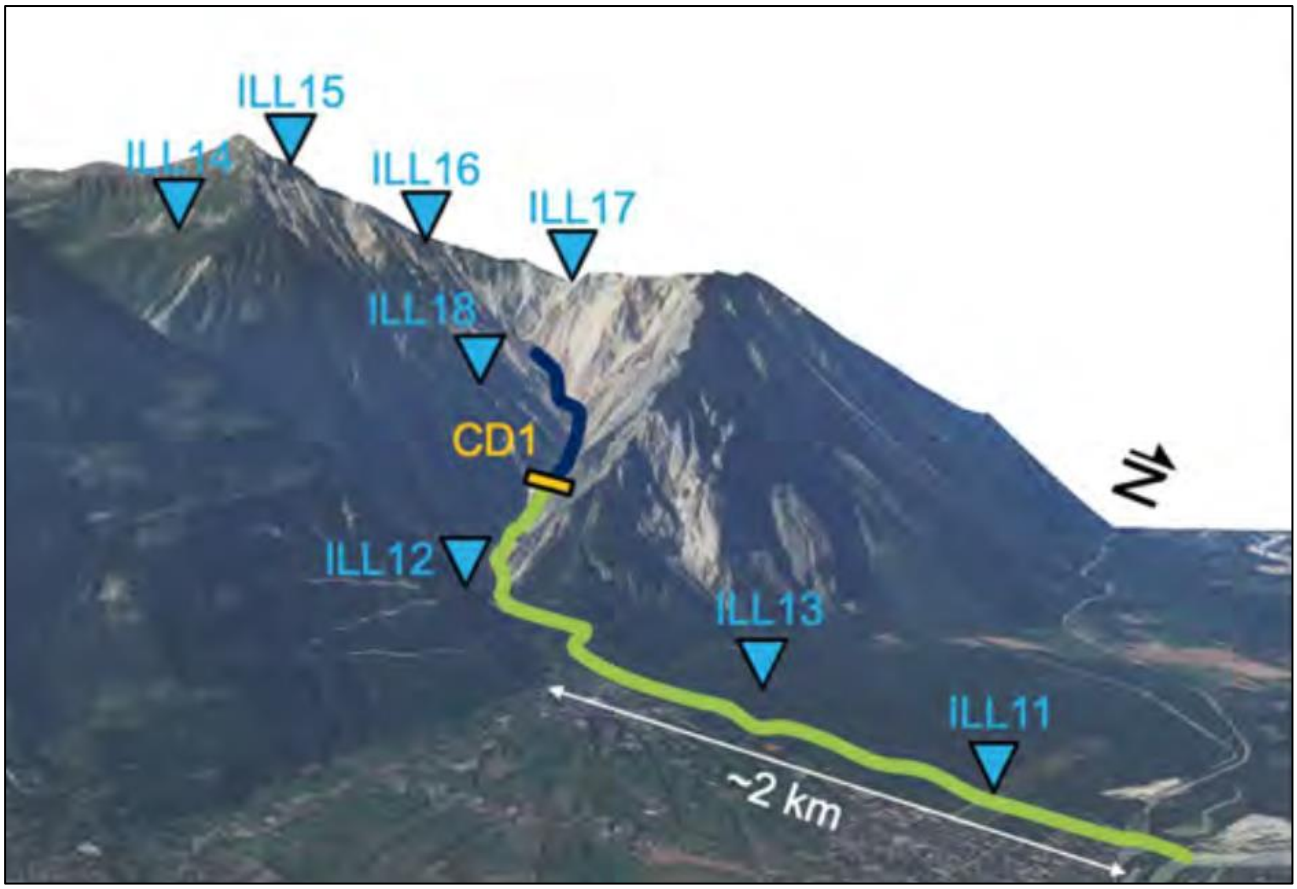

Figure 3. 13: the seismic network located within and around the Illgraben catchment. The seismic stations are indicated by the cyan triangles. The channel sector upstream CD 1 (orange bar) is highlighted in blue, while the remaining portion further downstream is highlighted in green (source: Walter et al. [2022]).

3.3 Instrumental set-up

For this study we used infrasound data recorded by the infrasonic array, named ILG, deployed north of Illgraben in a flat forested area at a minimum distance of ~550 m from the channel [Marchetti et al., 2019] (Figure 3. 14) The array is managed by the Dipartimento di Scienze della Terra of the University of Florence.

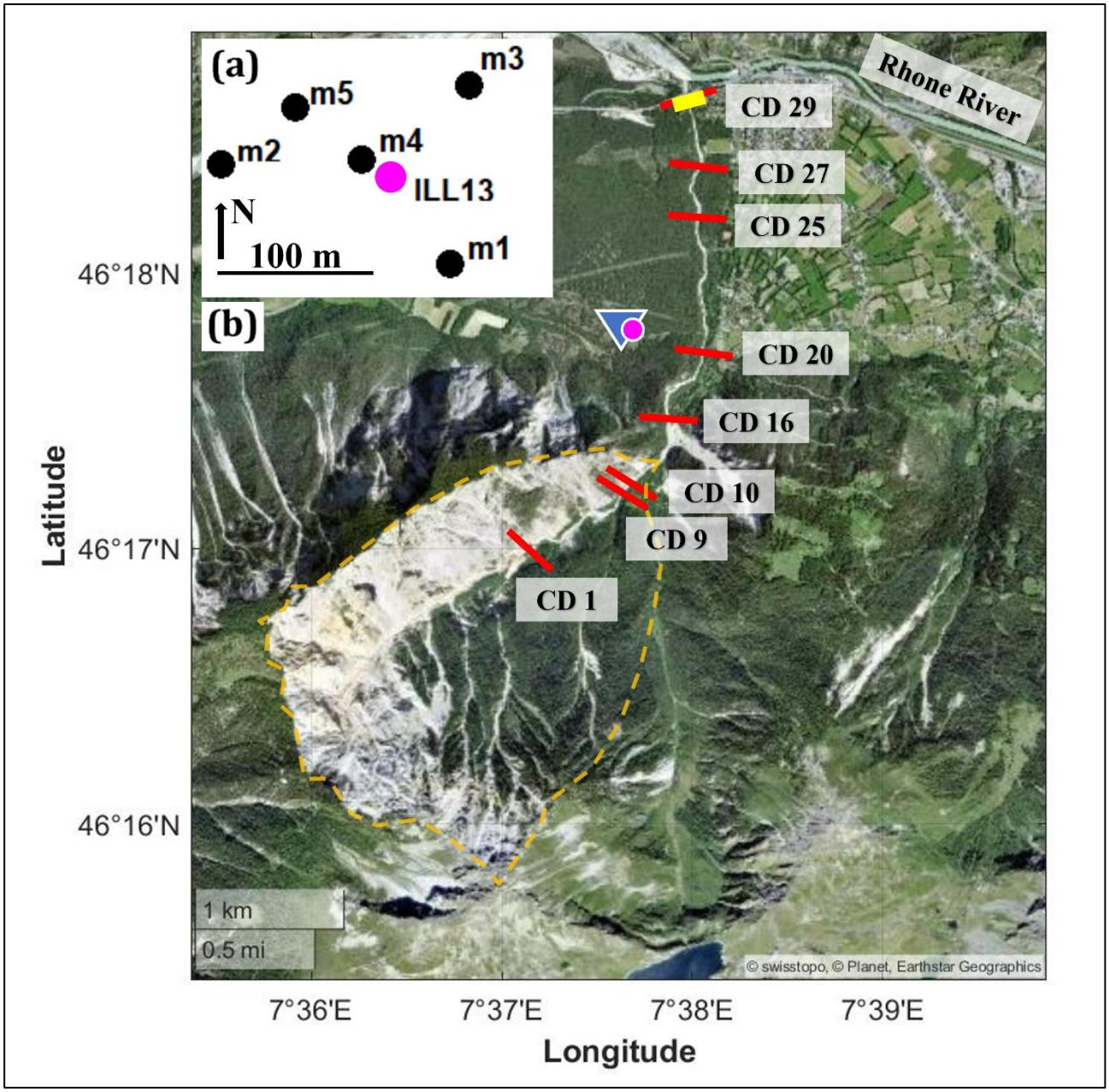

Figure 3. 14: map of the Illgraben channel showing the location of the sensors used in this work (b). The red bars mark the location of some of the check dams along the channel. The cyan triangle indicates the position of ILG infrasonic array, whose geometry is shown in the top left panel (a). The position of the ILL13

seismometer is indicated by the pink circle. The yellow bar indicates the position of the force plate, used for flow basal forces measurements, deployed on the brink of CD 29, where the flow altimeter used in this thesis is installed too. The orange dashed line delimits the Illgraben upper catchment.

The array was deployed on 15 May 2017 and operated until 2021 during the debris-flow season (late spring-early autumn). ILG is a FIBRA array, designed to operate with fibre optic connection up to 5 array elements. In the period 2017-2018, the array was equipped with four elements, while in 2019 and 2021 a 5th infrasonic sensor was added to the array. During the debris-flow season in 2020, due to technical problems, the array was not working. Within the array, sensors are deployed with a triangular geometry (Figure 3. 14 a), in order to have the best azimuthal resolution. Array aperture (maximum distance between two array elements) is 160 m and it is optimized to analyse infrasound signals in the frequency band between 1 and 10 Hz. The use of an array with fibre optic allows to significantly increase the signal-to-noise ratio and prevents the risk of damages related to lightning or electric discharges.

Each array element is equipped with a differential pressure transducer with a sensitivity of 400 mV/Pa in the pressure range of ± 12.5 Pa and frequency response ranges between 0.01 and 200 Hz. Analogue data provided by the pressure sensors are converted to digital at 16 bits and 50 Hz at each element of the array. Digital data are then transmitted through fibre optic to a central unit where data are synchronized, GPS time stamped, locally recorded and made available through the internet for data transmission. Power requirement is ~1W for the central unit and as low as ~0.1W for each peripherical array element and it is provided by solar panels.

Seismic data used in this study were collected by a Lennarzt LE3D 1s seismometer part of the dense seismic network deployed at Illgraben during the debris-flow season since 2017 [Wenner et al., 2020]. The seismic station, named ILL13, is deployed nearby the central element of the infrasonic array (Figure 3. 14, Figure 3. 1). The seismic station consists in a triaxial seismometer that has a flat response between the sensor's natural frequency of 1 Hz and 80 Hz. The sensor is placed into a 30 cm deep pit, subsequently filled up with sand. Ground motion is recorded with a Nanometrics Centaur digitizer. Data are collected at 100 Hz and continuously telemetered to the Swiss Seismological Service.

In our study, in addition to infrasound and seismic data, we also used debris-flow hydraulic and physical data collected thanks to in-torrent measurements, provided by sensors closely located along the stream path or directly within the creek channel, generally in correspondence of one of the check

dams. In particular we used flow-depth values measured at CD 29, flow velocities evaluated between CD 27 and 29, and flow density values estimated from the basal force measurements acquired by the force plate deployed at the brink of CD 29 (Figure 3. 14), as described in Section 3.2.

3.4 2017-2019 Illgraben debris-flow event data

This thesis is focused on the debris-flow activity that occurred in the Illgraben catchment in the three debris-flow seasons between 2017 and 2019. In particular, the analysis was performed on the infrasonic and seismic signals generated by the debris-flow events. In addition, the seismo-acoustic signals were compared to the flow parameters provided by in-channel measurements.

3.4.1 The hydraulic database

In the period of study, 18 debris flows or torrential events were observed at Illgraben (Table 3. 1), 3 in 2017, 4 in 2018 and 11 in 2019. Events are characterized by a high variability in size and in the hydraulic features (Table 3. 1, Figure 3. 15).

Among the observed events, the smaller ones may not fully qualify as debris flows and could be more properly defined as torrential events. For simplicity, from now on we will use the expression "debris flow" referring to both debris flows and minor torrential events.

For the events in 2017 and 2018, the force plate was not operational as a result to damage during a major flow event in 2016 and the flow depth measurements and related volume calculations are less accurate than after the re-installation of the force plate in 2019. Total volumes vary between few thousands of m^3 and 10^5 m^3 and reveal that the majority of Illgraben debris flows are small ($V < 20{,}000$ m^3), although several large flows ($V > 80{,}000$ m^3) are commonly observed (Figure 3. 15 a).

Table 3. 1: timing and hydraulic and physical features of the 2017-2019 Illgraben debris flows. The force plate was not present in 2017-2018, consequently some parameters are reported as n.m. (not measured) and some

derived quantities as n.c. (not computed). Froude number, peak flow discharge per unit channel width (unit peck flow discharge) and peak mass flux per unit channel width (unit peak mass flux) are computed using Eq. 1. 6, Eq. 3. 1 and Eq. 3. 2 respectively.

Date	CD 1 Arrival Time (UTC)	Volume (m^3)	Front Velocity (m/s) (CD 27-28-29)	Maximum Flow Depth (m) (CD 29)	Bulk Density (Kg/m^3)	Froude Number	Unit peak flow discharge (m^2/s)	Unit peak mass flux (t/m·s)
2017/05/29	16:58:31	100000	6.7	2.8	n.m.	1.3	18.76	n.c.
2017/06/03	23:27:38	9000	5.1	1.9	n.m.	1.2	9.69	n.c.
2017/06/14	19:30:48	35000	7.2	2.0	n.m.	1.6	14.40	n.c.
2018/06/11	10:46:39	n.m.	n.m.	n.m.	n.m.	n.c.	n.c.	n.c.
2018/06/12	18:29:16	n.m.	n. m.	n.m.	n.m.	n.c.	n.c.	n.c.
2018/07/25	16:56:40	n.m.	4.7	1.2	n.m.	1.4	5.64	n.c.
2018/08/08	17:49:25	n.m.	6.7	n.m.	n.m.	n.c.	n.c.	n.c.
2019/06/10	17:02:51	1800	0.9	0.77	1887	0.3	0.69	1.31
2019/06/10	22:01:17	5200	2.5	0.42	1631	1.2	1.05	1.71
2019/06/20	09:12:17	n.m.	n.m.	n.m.	n.m.	n.c.	n.c.	n.c.
2019/06/21	19:34:42	97000	6.6	2.59	1870	1.3	17.09	31.97
2019/07/01	23:00:29	73000	3.9	1.61	1971	1.0	6.28	12.38
2019/07/02	22:09:28	4100	0.8	0.77	2333	0.3	0.62	1.44
2019/07/03	16:43:15	n.m.	n.m.	n.m.	n.m.	n.c.	n.c.	n.c.
2019/07/15	03:40:21	9900	3.4	0.54	2191	1.5	1.84	4.02
2019/07/26	17:33:12	110000	8.7	1.05	2223	2.7	9.14	2.03
2019/08/11	17:02:34	88000	7.0	1.80	2323	1.7	12.60	2.93
2019/08/20	16:40:59	6100	0.9	0.44	2031	0.4	0.40	0.80

Estimated flow front velocity (v) ranges from <1 m/s to >8 m/s, suggesting a wide variability in flow dynamics, probably reflecting differences in composition and water content. Typical events have front velocities between 6.5 and 7.5 m/s (~36% of the events with measured velocity), but events with low velocity ($v < 2$ m/s) are observed too (Figure 3. 15 b). Flow velocity varies significantly along the channel, depending both on flow size and runout and on channel geometry (slope) [Schürch et al, 2011]. In addition, uncertainties on flow velocity measurement arise from detecting the flow front arrival times, which is often challenging, especially for smaller flows. Therefore, the velocity is

estimated over a 140 to 480 m long reach of the channel to obtain a more time-averaged estimate of front velocity.

Maximum flow depth (H_{max}), ranging from ~0.6 m to 2.8 m, is measured at CD 29. The maximum flow depth in debris flows is generally recorded when the flow front passes under the flow altimeters and therefore corresponds to the front height [Pierson, 2020], but the recorded value can be affected by the presence of flow waves [Hürlimann et al., 2019]. In our data, out of the 13 debris flows for which a flow depth measurement is available, a flow height ≥ 2 m was recorded only for 3 events (Figure 3. 15 c, Table 3. 1).

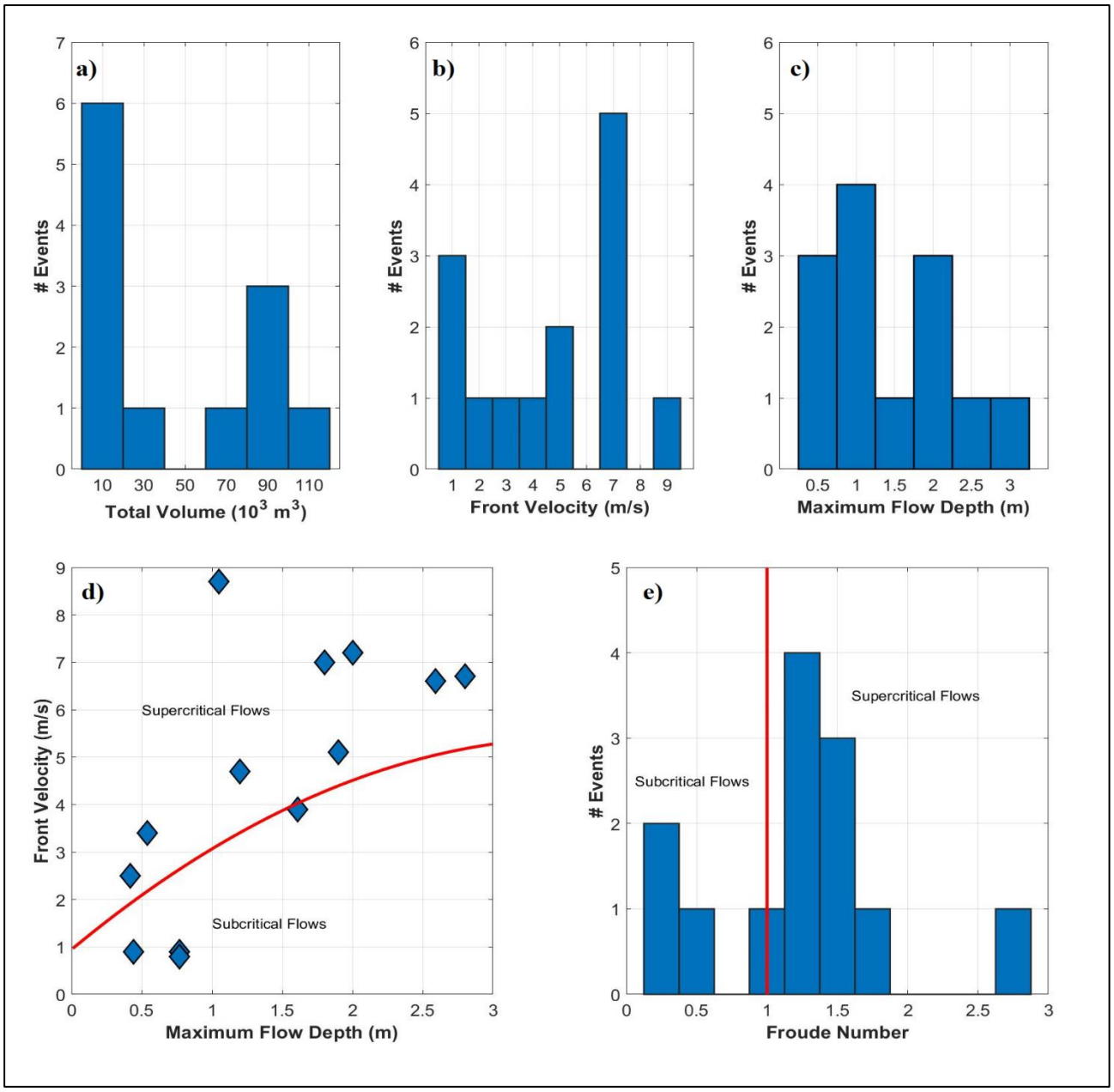

Figure 3. 15: histograms showing the distribution of total volume (a), front velocity (b), maximum flow depth (c) and Froude number (e) among the 2017-2019 Illgraben debris-flow events. Relation between measured

maximum flow depth and front velocity (d). In d) and e) the red line (drawn at Fr=1) marks the boundary between subcritical flows ($Fr < 1$) and supercritical flows ($Fr > 1$).

Comparison between front velocity and maximum flow depth revealed that the flow velocity appears to be at least partially controlled by the flow depth, with higher flow velocity generally corresponding to larger flow depth (Figure 3. 15 d), in agreement with theory of open channel flows [Henderson, 1996]. The red line in Figure 3. 15 d represents the critical velocity (v_c) and therefore marks the distinction between subcritical ($v < v_c$) and supercritical flows ($v > v_c$) [Henderson, 1996] (see Section 1.2, Chapter 1, in this thesis). Critical velocity is equal to the velocity (v_w) with which a wave or perturbation resulting from any disturbance or obstacles in open channel flow propagates over the water surface ($v_w = v_c$) [Henderson, 1996]. Criticality is the state at which the specific energy of the flow is minimum [Henderson, 1996] and the flow velocity (v) equals the critical velocity ($v = v_c = v_w$).

Flow conditions relative to criticality are described by the Froude number (Fr), given by the ratio between flow velocity (v) and the velocity (v_w) of surface perturbations [Henderson, 1996] (see Section 1.2, Chapter One, in this thesis).

Computed Froude numbers (Figure 3. 15 e, Table 3. 1), together with the comparison between debris-flow front velocity and critical velocity (Figure 3. 15 d), reveals that almost all Illgraben debris flows fall into the supercritical domain ($Fr > 1$), indicating that the flow is faster than surface perturbations, that therefore can propagate only downstream [Henderson, 1996]. In particular, we observe that among analysed events, all debris flows with $H_{max} > 1$ m are supercritical (Figure 3. 15 d), except for the 2019/07/01 event, which falls in the critical domain ($Fr = 1$). Uncertainties resulting from the measurements of flow depth and flow velocities combine in the computation of the Froude number. For larger flows with roll waves (steep fronted waves typically developing in shallow granular flows [Schonfeld, 1996]), where the surface flow waves are about 1/3 to 1/2 of the maximum measured depth, it is not clear which value of flow depth to use to calculate the Froude number. However, our values, computed using maximum flow depth values, are still representative of the flow conditions.

Flow bulk density (ρ), estimated as the mass/volume ratio at the force plate, is available for 9 events. Obtained values vary between 1600 and 2400 kg/m^3 (Table 3. 1), reflecting differences in solid fraction and water content.

Assuming a rectangular channel section, reasonable for the Illgraben, in order to further investigate the relationship between hydraulic parameters and seismo-acoustic signals, front velocity, maximum

flow depth and flow density values were combined to derive the peak flow discharge per unit channel width (Q_u) and the peak mass flux per unit channel width (MF_u) as:

$Q_u = \mathrm{H}_{\max} \cdot v$ (Eq. 3. 1),

$MF_u = Q_u \cdot \rho$ (Eq. 3. 2).

Obtained values are listed in Table 3. 1. If we assume that the width of the Illgraben channel between CD 28 and CD 29, where velocity and depth measurements are collected, remains constant over time, thereafter the computed peak discharge and peak mass flux per unit channel width are directly proportional to the peak volumetric discharge and mass flux, respectively. The stable width channel assumption is reasonable considering that the Illgraben channel is stabilized by the constructions of the check dams.

In addition, for two debris-flow events of the dataset, in particular the events of 2019/06/21 and of 2019/07/01, also the debris-flow hydrogram is available (source: Doc. B. McArdell, WSL institute of Zurich). The recorded hydrograms, presented in Figure 3. 16, show the variation over time of the flow depth and were acquired at 1 Hz using the altimeter at CD 29 along the entire duration of the debris-flow events.
The high amplitude spikes in the hydrograms are associated with water splash phenomena and do not reflect the actual debris-flow depth (Figure 3. 16).

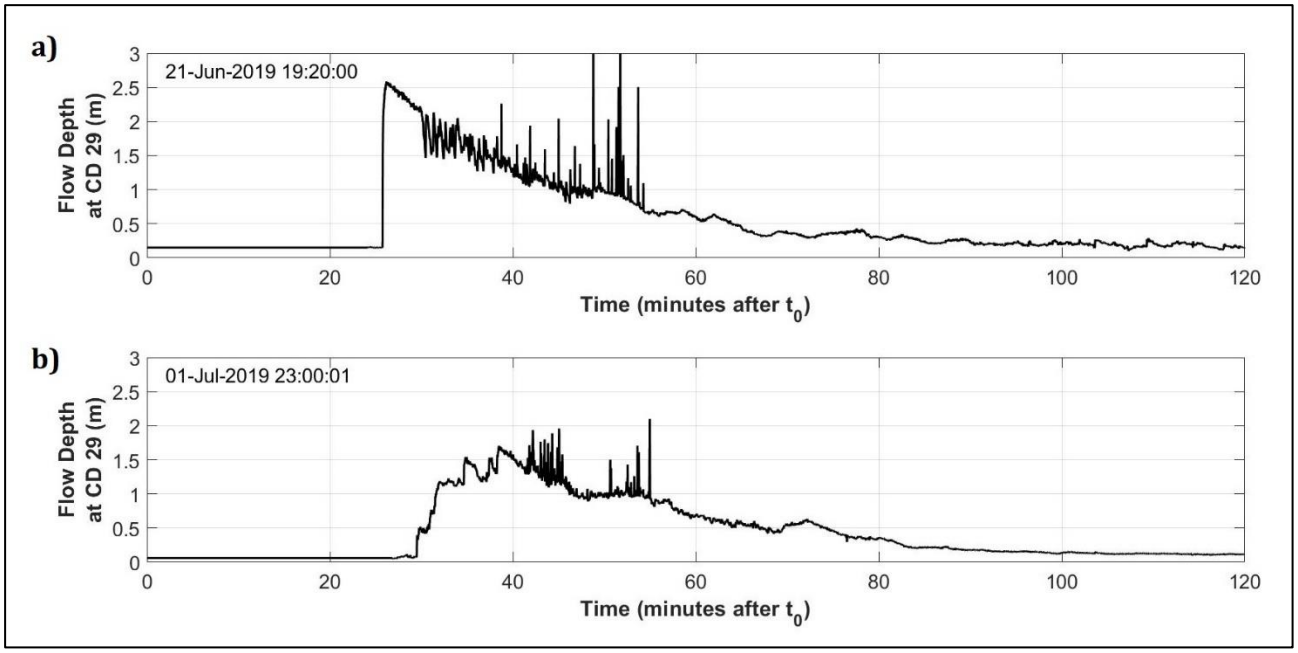

Figure 3. 16: hydrograms showing the evolution over time of the flow depth recorded at CD 29 during the 2019/06/21 (a) and the 2019/07/01 (b) debris-flow events.

It is observed that the flow depth of the 2019/06/21 event suddenly rises from 0 to the maximum recorded value (2.59 m) almost instantaneously, at the very beginning of the event (Figure 3. 16 a). After the peak, the flow depth gradually decreases, slowly returning to the pre-event levels.
For the 2019/07/01 event, instead, the flow depth increase is less sharp, gradually leading to a less evident depth peak around 1.6 m (Figure 3. 16 b). Also in this case, once the maximum value is reached, the flow depth smoothly decreases returning to the pre-event levels.

3.4.2 The seismo-acoustic dataset

The seismo-acoustic dataset consists of seismic and infrasonic signals generated by the 18 debris-flow events, recorded by the ILG infrasonic array and the ILL13 seismometer (Figure 3. 1). Infrasonic and seismic signals, band-pass filtered between 1 and 20 Hz are shown in Figure 3. 17. Here, the shown infrasonic tracks are recorded by the m1 sensor of the ILG array (Figure 3. 14), except for the 2018/07/25 event, for which the data recorded at m5 were used, because the m1 sensor was not working at the time of the event. Due to an outage of the operation of the infrasonic array, infrasound data for the 2018/08/08 event are missing. The seismic and infrasonic amplitudes of lower amplitude events are multiplied by an integer factor (2, 5 or 10, as indicated next to the infrasonic or seismic track in Figure 3. 17), to allow these signals to be visible at the same scale as the higher amplitude events.
Events are recorded as long lasting (30-100 min), emergent, cigar shaped infrasonic and seismic signals. Peak-to-peak seismic amplitudes span 2 orders of magnitude, ranging from ~3 μm/s, observed for the 2018/06/11 and 2018/06/12 events, up to ~200 μm/s, observed for the 2017/05/29 seismogram. In the infrasound record, peak-to-peak amplitudes vary from a maximum of ~1.5 Pa, observed for the 2017/05/29 debris flow (2 orders of magnitude above the background noise of around 0.05 Pa) down to 0.2 Pa observed for the 2019/07/15 event. The six smallest events, instead, did not produce discernible infrasonic signal above noise levels (Figure 3. 17).
The high-amplitude infrasound transients observed for several events, clearly visible in Figure 3. 17, are infrasonic signals generated by lightning activity and thus not related to debris flows [Marchetti

et al., 201]. The effect of the rainstorm on infrasound signal is particularly evident for the 2019/07/02 and 2019/07/26 debris flows, for which the infrasound signal produced by the lighting activity, having comparable amplitudes as the debris-flow infrasonic signal, strongly affects the entire waveform (Figure 3. 17).

On the basis of an accurate observation of the seismo-acoustic tracks, it is evident that, in general, seismic signals appear to be clearer, i.e. characterized by a higher signal-to-noise ratio, compared to infrasonic ones. Indeed, whereas every reported debris-flow event generated a detectable seismic signal, the six smallest debris flows did not generate a distinguishable infrasound signal above the background noise level (Figure 3. 17). Therefore, the analysis of Illgraben debris flows presented in this thesis has been limited to 11 out of 18 events in case of infrasound, while it has been carried out on all 18 events in case of seismic signals.

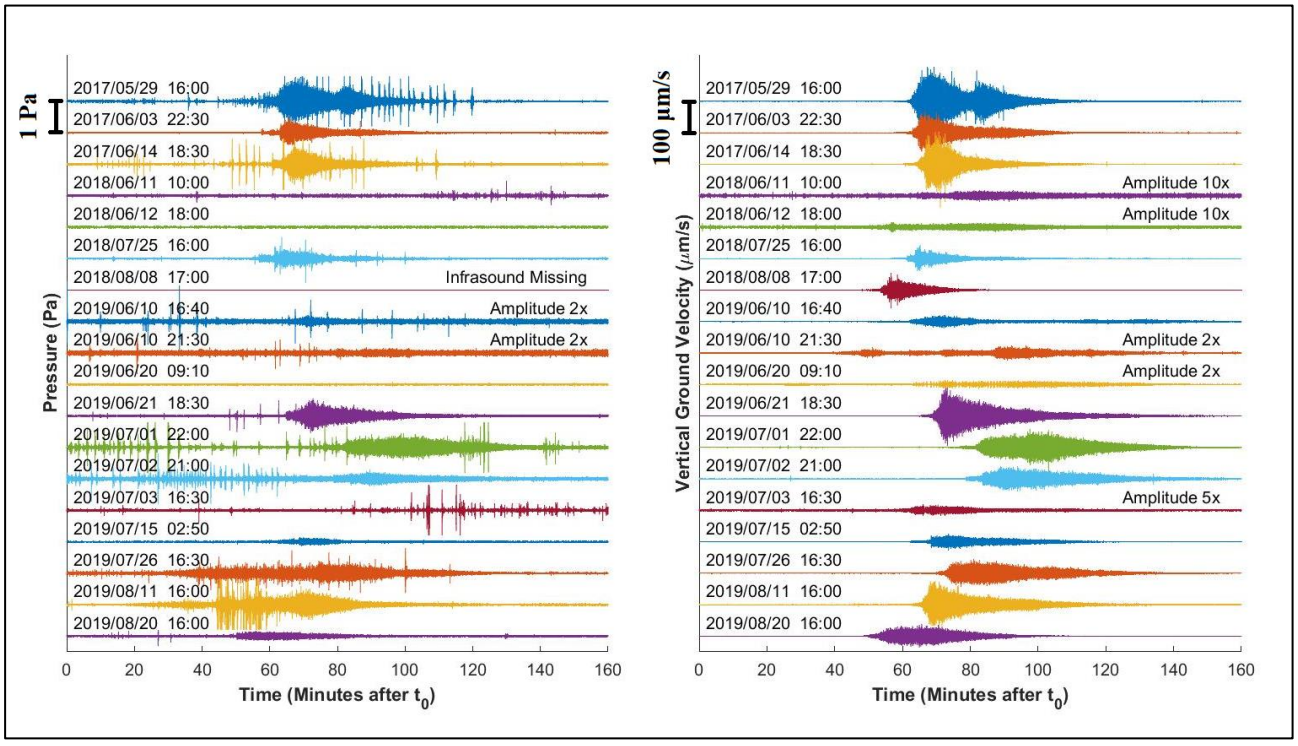

Figure 3. 17: 1-20 Hz band-pass filtered infrasonic (left) and seismic (right) recordings of the 2017-2019 Illgraben debris-flow events. For a better visualization, seismic and acoustic amplitudes of lower amplitude events are multiplied by an integer numerical factor (2, 5 or 10, as reported next to the tracks).

Chapter 4

Methods

4.1 Root mean square amplitude (RMSA) analysis

In order to investigate and compare the amplitude envelope of the infrasonic and seismic signals analysed in this study, the root mean square amplitude (RMSA) analysis was applied to seismo-acoustic data. In this procedure a signal is subdivided into subsequent time windows with fixed duration (d_w). The total number of windows (n_w), into which the signal is divided, is given by:

$$n_w = d_s / d_w \qquad \text{(Eq. 4. 1)},$$

where d_s is the signal duration.
If the recorded signal is a time series of data recorded with a specific sampling rate (smp), each time window will consist of a number of sample (ns_w) given by:

$$ns_w = smp \cdot d_w \qquad \text{(Eq. 4. 2)}.$$

Within each window, the RMSA is computed as the square root of the mean of the squared amplitude values of the ns_w data points recorded in that time window of analysis, as:

$$RMSA_i = \sqrt{\frac{\sum_{j=1}^{ns_w} A_j^2}{ns_w}} \qquad \text{(Eq. 4. 3)}, \qquad \forall\, i = 1, 2, \dots, n_w \;\cap\; \forall\, j = 1, 2, \dots, ns_w\,,$$

where A_j is the amplitude of a single data point.
The result of the RMSA is a time series of length n_w that represents the amplitude envelope of the signal.
Figure 4. 1 shows an example of the RMSA analysis, calculated according to Eq. 4. 3 considering 1-minute time windows of 1-20 Hz band-pass filtered infrasound and seismic data recorded for the Illgraben debris-flow event on 29/05/2017. This event was characterized by two main flow surges: this feature is easily observable in both in the seismo-acoustic tracks and in the resulting RMSA value, where two distinct main peaks are evident (Figure 4. 1 b, d). The high amplitude transients clearly visible in the infrasonic record (Figure 4. 1 a) are infrasonic signals generated by thunders: their presence perturbs the smooth envelope of the debris-flow infrasonic signal, resulting in secondary peaks in the infrasonic RMSA curve (Figure 4. 1 b). This effect is missing in the seismic RMSA, because the thunder activity does not affect the seismic track (Figure 4. 1 c, d).

The RMSA analysis allows to characterize a signal in terms of maximum amplitude, corresponding to the highest amplitude peak of the RMSA curve. If the RMSA analysis is equally applied to several events, the obtained RMSA curves and their peaks are comparable among the events.

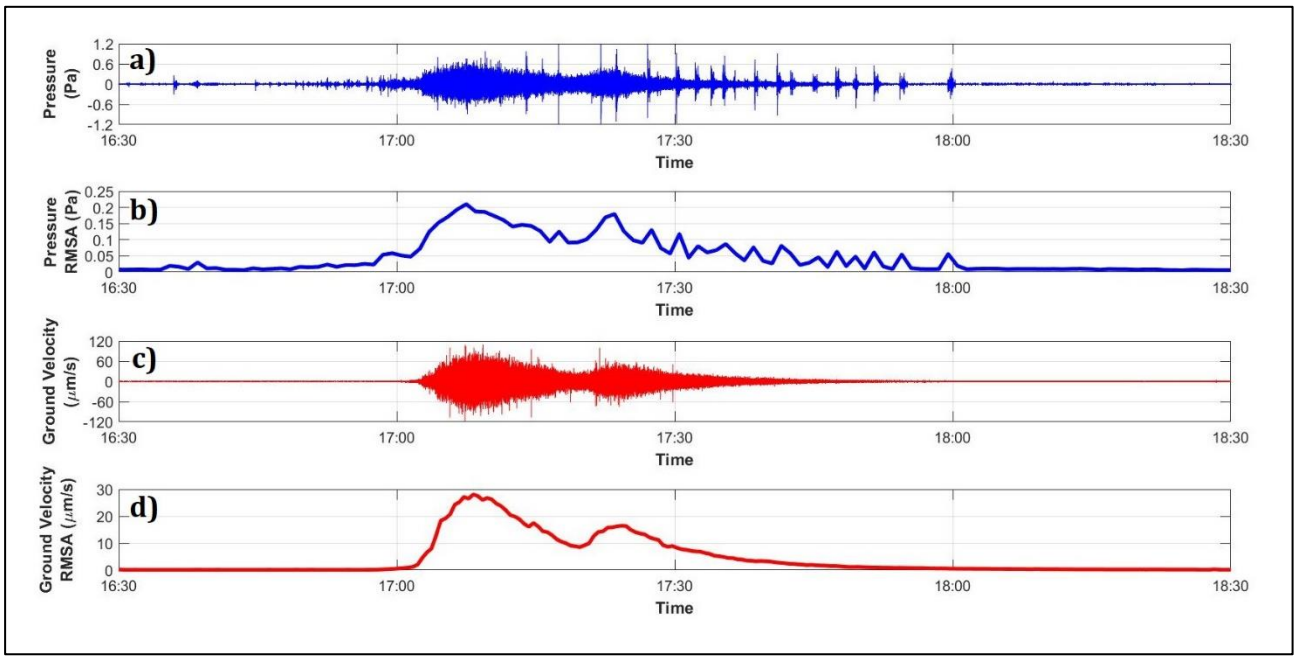

Figure 4. 1: exemple of RMSA analysis applied to infrasonic (blue) and seismic (red) signals generated by the Illgraben debris-flow event on 29/05/2017. Infrasonic (a) and seismic (c) 1-20 Hz band-pass filtered tracks. Infrasonic (b) and seismic (d) RMSA envelopes computed on 1-minute-long time windows.

4.2 Spectral analysis

Infrasonic and seismic signals generated by debris-flow activity were also analysed in the frequency domain. The spectral analysis of a signal operates on the basis of the Fourier transform and consists in reconstructing the frequency content of the signal. By means of the Fourier transform, a wave signal is decomposed into a series of sinusoids of variable amplitude and frequency, the sum of which represents the best possible approximation of the initial signal [Sneddon, 1995].

The result of the spectral analysis is the spectrum of the signal and is a representation of its frequency content averaged on the all signal (Figure 4. 2).

In several application, in particular when considering a signal that varies over time, rather than the spectrum, it might be useful to calculate a spectrogram, that is a spectral analysis performed over subsequent time windows of the signal and therefore shows how the spectral content of the signal changes over time (Figure 4. 3).

The frequency content of an infrasonic or seismic signal could be diagnostic in the investigation of the source. Indeed, the frequency of the signal, if not modified during the propagation by other secondary effect, directly represents the duration (period) of the source process [Matsuzawa et al., 2009] or the size of the source [Naugolnykh and Bedard, 2002]. In addition, while other original signal features, such as waveform, amplitude and duration, are seriously modified with the wave propagation, the frequency content is less affected, except for anelastic absorption [Shapiro and Kneib, 1993], that progressively attenuates the higher frequencies according to:

$$I(r) = I_0 e^{-Q_f r} \qquad \text{(Eq. 4. 4)},$$

where $I(r)$ is the intensity of the pressure wave at a given distance r and the and I_0 is intensity of the pressure wave at the source, and r is the source-to-receiver distance. The quality factor Q_f, being here expressed as dB/λ (where λ is the wavelength in meters), is frequency dependent.

Spectra of infrasonic and seismic debris-flow signals were computed in the form of Power Spectral Density (PSD) on 20 seconds long signal windows with 50% of overlap. The spectrum (PSD) computed for the Illgraben debris-flow event on 2017/05/29 is here presented as an example (Figure 4. 2). In both panels in Figure 4. 2, the vertical black line represents the Nyquist frequency, i.e. the limit frequency investigable for that specific signal [Robinson and Clark, 1991]. The Nyquist frequency coincides with half the sampling rate of the analysed data, so that, in our case, it is equal to 25 Hz for infrasound (sampled at 50 Hz) and 50 Hz for seismic data (sampled at 100 Hz).

The infrasound is always characterized by a red spectrum, i.e. a spectrum where the spectral amplitude of background noise increases as the frequency decreases due to the superposition of atmospheric sources [Bowman et al., 2005]. For this reason, when one aims to investigate the frequency content of an infrasound signal, only the concave portion of the PSD curve, in this example located above ~ 1 Hz (Figure 4. 2 a), must be considered, because only this portion is representative of the considered signal.

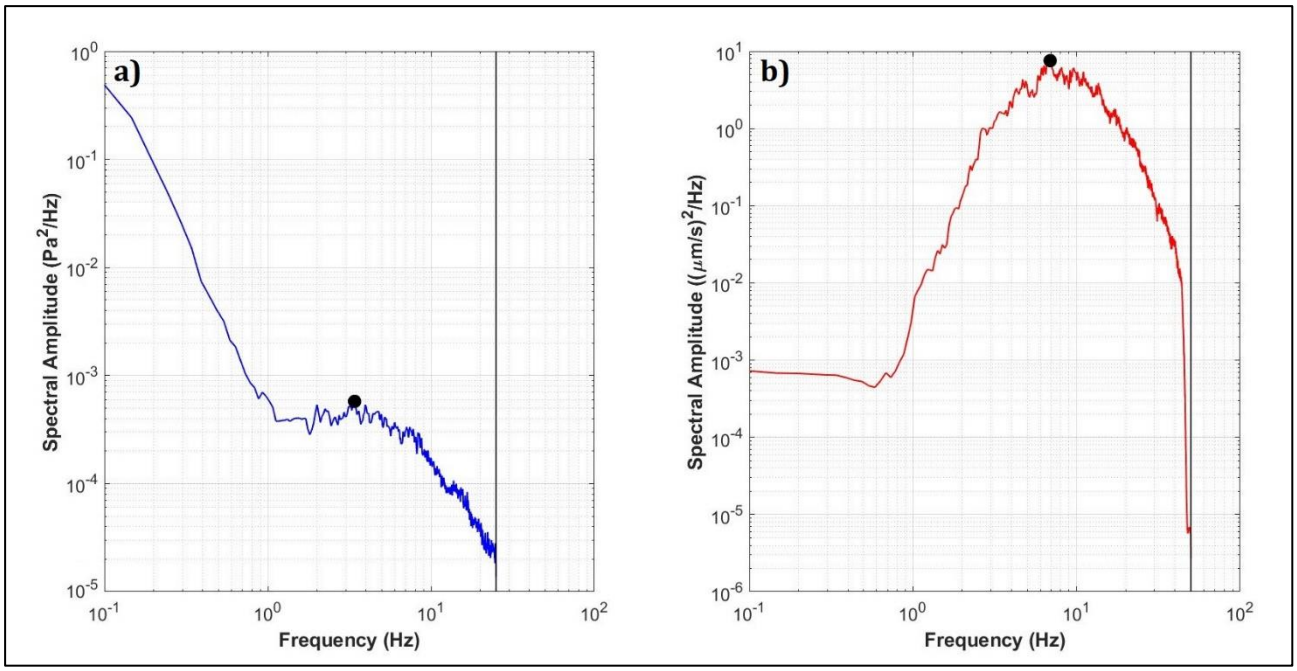

Figure 4. 2: infrasonic (a) and seismic (b) Power Spectral Density computed for the Illgraben debris flow on 2017/05/29. The black vertical lines, located at 25 Hz in a and at 50 Hz in b, represent the Nyquist frequency, i.e. the maximum analysable frequency, for data sampled at 50 Hz (infrasound) and 100 Hz (seismic) respectively. The sharp decrease observed in the seismic PSD in the proximity of the Nyquist frequency is due to the low pass analogue antialiasing filter of the digitizer of the seismometer. The black dot in each panel represents the peak frequency computed using Eq. 4. 5 and the maximum spectral amplitude relative of debris-flow signal.

From each spectrum we can extract the infrasonic and seismic peak frequencies, that correspond to the maximum spectral amplitude and represent the sinusoid that best approximates the time series of analysis. The peak frequency should be the most representative frequency for the source mechanism, or otherwise, should correspond to the most powerful active source process. Nevertheless, the identification of the actual peak frequency in the seismo-acoustic spectra, proved to be challenging. For all debris-flow events indeed, it is observed that both infrasonic and seismic signals are characterized by a wide spectrum, between ~1 and ~10 Hz and between ~1 and ~40 Hz respectively (see Chapter 5, Section 5.1.2). For the event of 2017/05/29, shown in Figure 4. 2, the infrasonic and seismic spectral peaks are located around 3-4 Hz and 7-8 Hz respectively. However, in each spectrum, the exact location of the peak frequency is not unambiguously determinable, due to the presence of several spectral peaks characterized by similar amplitude.

To avoid subjectivity in the identification of the peak frequency in the spectra, the peak frequency values (f_P) were computed from PSDs as the weighted average of the frequency (f) over the spectral

amplitude (Sa). For each event, the weighted average was calculated around the manually picked peak frequency value (f_{mp}), considering a frequency range of radius $df = 2$ Hz, as:

$$f_P = \frac{\sum_i Sa_i f_i}{\sum_i Sa_i} \qquad \forall\, f_i \in [f_{mp} - df, f_{mp} + df] \qquad \text{(Eq. 4. 5)},$$

where f_{mp} is appropriately picked as a frequency value roughly corresponding to the location of the peak of the signal spectrum; its role is to set the centre of the frequency interval over which the exact peak frequency (f_P) is computed with Eq. 4. 5. The large width of the considered frequency interval (4 Hz in our case) makes the initial choice of f_{mp} irrelevant at first approximation, allowing to obtain a peak frequency value that is objective, at least at first approximation.

The spectral analysis of the debris-flow events was performed also computing the spectrograms of the infrasonic and seismic signals. Infrasonic and seismic spectrograms were computed on raw data over 20 second time windows with 50% of overlap.

As an example, the spectrograms computed on infrasonic and seismic signals of the 03/06/2017 Illgraben debris-flow event are shown in Figure 4. 3. Here, the spectral amplitude is indicated by the colours, with red indicating the higher amplitudes, according to the colour bar (Figure 4. 3 b, d). The spectrogram shows the variation over time of the spectral content of a signal and therefore allows to highlight signal frequency changes during the event.

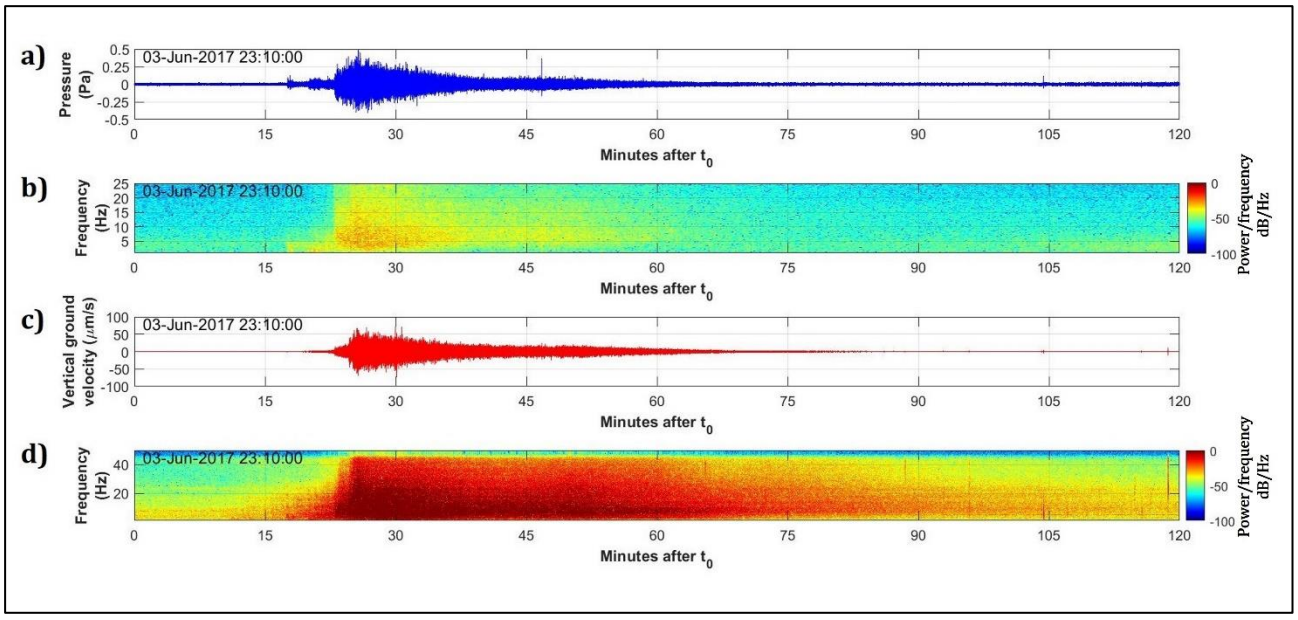

Figure 4. 3: spectrograms (b and d) computed on infrasonic (a) and seismic (c) signals for the 03/06/2017 Illgraben debris-flow event. The spectral amplitude, in dB/Hz, in b and d is given by colours, according to the colour bar.

4.4 Infrasonic array analysis

As explained in Section 2.2, the infrasound is a longitudinal pressure wave propagating in the atmosphere at the speed of sound. To record infrasound, you need a sensor able to detect the small pressure variations associated with the propagation of the infrasonic wave in the air, i.e. a pressure transducer.

The infrasonic wavefield is generally recorded using an array rather than a single sensor [Ulivieri et al., 2011]. An array is a network of at least three sensors deployed in space and arranged on a specific geometry, optimized for the specific problem to be addressed, and used as an antenna.
The use of an array rather than a single sensor offers numerous advantages, allowing a more accurate analysis of the data and providing important information otherwise not obtainable. One of the major problems of the infrasonic investigation is being able to discriminate the signal generated by a specific source from the noise, for which the wind is one of the most impactful sources [Bowman et al., 2005]. This discrimination is allowed by the array processing [Ulivieri et al., 2011]. This technique is based on the assumption that a signal is coherent at all the sensors of the array, i.e. it is recorded with similar waveforms at all the elements of the array and with time delays consistent with the array geometry and with the signal raypath.
The signal consistency across the array allows to discriminate it from the noise, which instead shows no correlation [Ulivieri et al., 2011; Marchetti et al., 2019].
Infrasound consistency across the array is evaluated using a multichannel correlation method based on the use of the cross-correlation analysis (see Section 4.3). The use of this function in the context of the infrasonic array processing allows to recognize the same signal in the records of the different sensors of the array.
However, the discrimination of signals from noise is not the only difficulty in the infrasonic investigation. The infrasound is generated by any process able to produce a pressure perturbation in the atmosphere, including natural and anthropic sources (see Section 2.2). This causes that several infrasonic sources are generally active simultaneously in the atmosphere, making it very difficult to discriminate and recognize the signal produced by the process of interest from the wavefields generated by the others, as the infrasonic track recorded at each sensor results from the superposition of the signals produced by the various sources. This difficulty can be strongly reduced thanks to the source characterization allowed by the array processing: the use of an array indeed allows to characterize a signal in terms of back-azimuth (B_{az}) and apparent velocity (c_a). The back-azimuth

(angular coordinate measured with respect to the North) represents the direction where the infrasonic wave comes from and is measured from the receiver to source (Figure 4. 4).

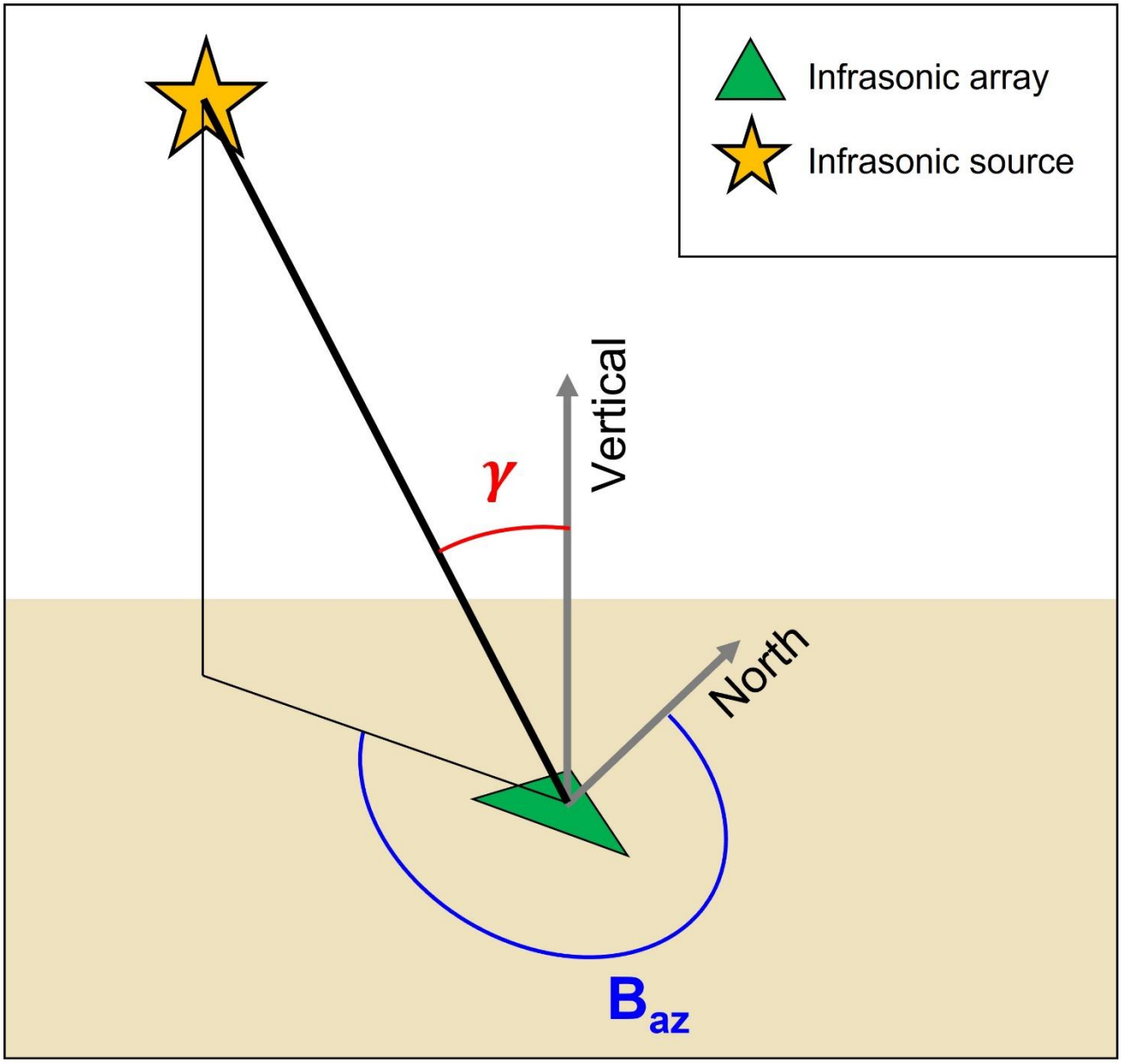

Figure 4. 4: graphical definition of the propagation back-azimuth (B_{az}) and of the take-off angle (γ), used in the computation of the apparent velocity (c_a). The back-azimuth is measured, on the plane of the array, form the receiver to the source as the angle formed between the source-to-receiver direction and the North.

The apparent velocity instead is the velocity the infrasonic ray would have if it was propagating on the plane of the array and is defined as:

$$c_a = \frac{c}{\sin\gamma} \qquad \text{(Eq. 4. 6)},$$

where c is the real sound propagation speed, which depends on several environmental parameters, including temperature, air humidity, direction and velocity of the wind and atmospheric pressure [Cramer, 1993]. γ is the take-off angle of the infrasonic ray, i.e. the angle formed by the direction of the signal propagation with the vertical to the ground, measured in degrees from the vertical to the ground (Figure 4. 4).

According to Eq. 4. 10, the apparent velocity is always higher than or equal to the real sound velocity ($c_a \geq c$) and equals it only when the recorded infrasonic ray propagates in the same plane as the array ($\gamma = 90°$). In case of a source located right above the array, the take-off angle would be null ($\gamma = 0$), so that the apparent velocity tends to infinite ($c_a \to \infty$), consistent with a signal being recorded simultaneously at all the elements of the array [Marchetti et al., 2015].

As defined, the apparent velocity allows to reconstruct the take-off angle of the infrasonic wave, which results from the altitude of the source and its distance from the array [Belli et al., 2021 (b)], so that the apparent velocity is indicative of the altitude of the source. For a given source-to-receiver distance, the larger the apparent velocity the higher the source altitude.

The computation of back-azimuth and apparent velocity is based on the assumption that the infrasonic wave propagates with a planar wavefront and with a constant velocity across the array (Figure 4. 5) [Ulivieri et al., 2011]. The planar wavefront assumption is all the better the larger the source-to-receiver distance, depending on the frequency content of the signal. For ILG array, characterized by an aperture of 160 m, and a signal frequency of 1 Hz, it is reasonable to assume the plane wavefront for sources located further than ~700 m from the array [Ulivieri et al., 2011]. If we consider a speed of sound (c) of 340 m/s, the distance of 700 m roughly corresponds to two wavelengths of the lowest frequency of interest for the debris flow analysis performed here (1 Hz). For shorter distances the infrasonic signal can still be detected, but the estimated value of back-azimuth and apparent velocity is less accurate.

Back-azimuth and apparent velocity are determined using recording time differences at all the possible triplets of sensors of the array. For a four-element array, there are four possible sensor triplets, while adding a fifth sensor increases the number of possible triplets to ten. Given the disposition and the geometrical orientation of the elements of the array, the differences in the arrival times of the infrasonic ray at the different sensors will vary depending on the direction of the incident wave. The angular variations resulting from the source direction determine variations of the different source-sensor distances and, for a planar wavefront, of the distance to travel from one sensor to the other within the array. This results in different arrival times at the sensors of the array and thus in different recording time differences between the sensors of each triplet.

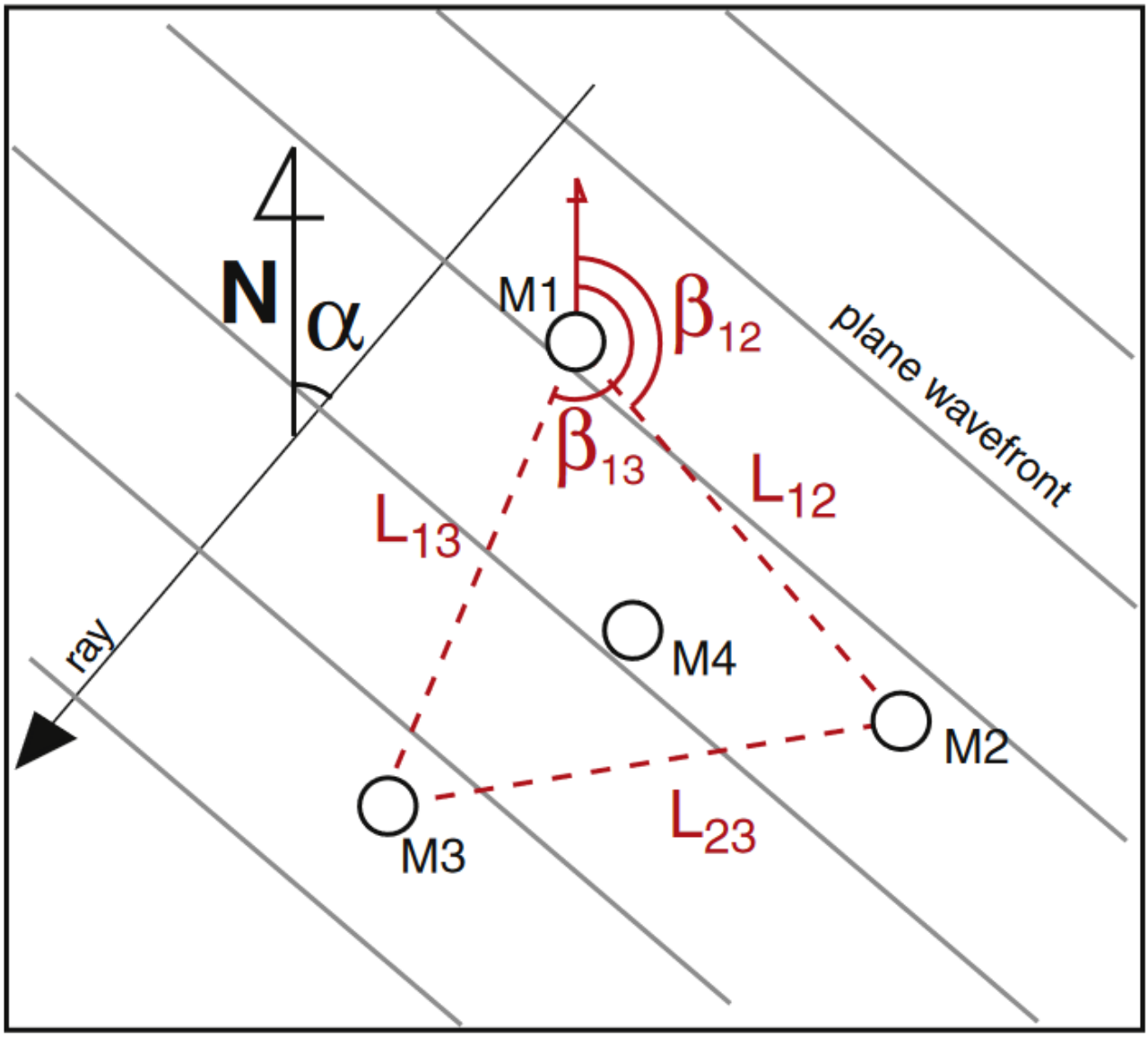

Figure 4. 5: a planar wavefront propagating with a back-azimuth $B_{az} = \alpha$ across an array made of 4 elements (M1, M2, M3, M4) (source: Ulivieri et al. [2011]). The red dashed lines mark one of the four possible sensor triplets used to determine the wave parameters (back-azimuth and apparent velocity). L_{ij} indicates the distance between the sensors i and j, while β_{ij} is the angle that the segment connecting the two sensors i and j forms with the North (with $i, j = 1, 2, 3$ in this case).

The processing is performed on successive signal windows, for all the possible sensor triplets of the array. Within each triplet, the cross-correlation analysis is carried out between the signal recorded at two different sensors i and j of the triplet and the arrival time difference (Δt_{ij}, time residual) is determined from the maximum value of the cross-correlation function [Marchetti et al., 2019].

The obtained time residuals (Δt_{ij}) are used to compute the back-azimuth (B_{az_n}) and the apparent velocity (c_{a_n}) for that specific triplet of sensors (indicated with the subscript n) solving the following system of two equations:

$$\frac{D_{ij}\cos(\beta_{ij}-B_{az_n})}{\Delta t_{ij}} = c_{a_{nij}} \qquad \text{(Eq. 4. 7)},$$

$$\frac{D_{ik}\cos(\beta_{ik}-B_{az_n})}{\Delta t_{ik}} = c_{a_{nik}} \qquad \text{(Eq. 4. 8)},$$

where the subscripts i, j and k indicate the sensors of the considered n^{th} triplet. D is the distance between the two sensors indicated by the subscripts, while β is the angle that the segment connecting the sensors indicated by the subscripts forms with the North (Figure 4. 5).
Given the assumption of a constant wave velocity across the array ($c_{a_{nij}} = c_{a_{nik}} = c_{a_n}$), the equation system (Eq. 4. 11 and Eq. 4. 12) can be solved to obtain the back-azimuth (B_{az_n}) and the apparent velocity (c_{a_n}) of the infrasonic ray across the n^{th} sensor triplet.
In addition, for each triplet, the total time residual (Δt_n) is computed as:

$$\Delta t_n = \left|\Delta t_{ij} + \Delta t_{jk} + \Delta t_{ki}\right| \qquad \text{(Eq. 4. 9)}.$$

The time residual Δt_n reflects the degree of correlation within the n^{th} triplet: for highly correlated signals the residual tends to zero ($\Delta t_n \to 0$), while it takes on a positive value for weakly correlated signals.
The back-azimuth (B_{az}), the apparent velocity (c_a) and the time residual (Δt) of the signal are then computed as the average of the value obtained considering all the possible N_t sensor triplets, as:

$$\mathrm{B_{az}} = \sum_{\mathrm{n=1}}^{\mathrm{N_t}} \frac{\mathrm{B_{az_n}}}{\mathrm{N_t}} \qquad \mathrm{n} = 1, \dots, \mathrm{N_t} \qquad \text{(Eq. 4. 10)},$$

$$\mathrm{c_a} = \sum_{\mathrm{n=1}}^{\mathrm{N_t}} \frac{\mathrm{c_{a_n}}}{\mathrm{N_t}} \qquad \mathrm{n} = 1, \dots, \mathrm{N_t} \qquad \text{(Eq. 4. 11)},$$

$$\Delta\mathrm{t} = \sum_{\mathrm{n=1}}^{\mathrm{N_t}} \frac{\Delta\mathrm{t_n}}{\mathrm{N_t}} \qquad \mathrm{n} = 1, \dots, \mathrm{N_t} \qquad \text{(Eq. 4. 12)}.$$

When the total time residual Δt is below a threshold value, an infrasonic detection is defined within the analyzed signal window. Each detection is characterized in terms of infrasonic amplitude (an average of the pressure recorded at the various sensors of the array), back-azimuth and apparent

velocity (Figure 4. 6) [Marchetti et al., 2019], the last two being indicative of the raypath and, to some extent, of the position of the source.

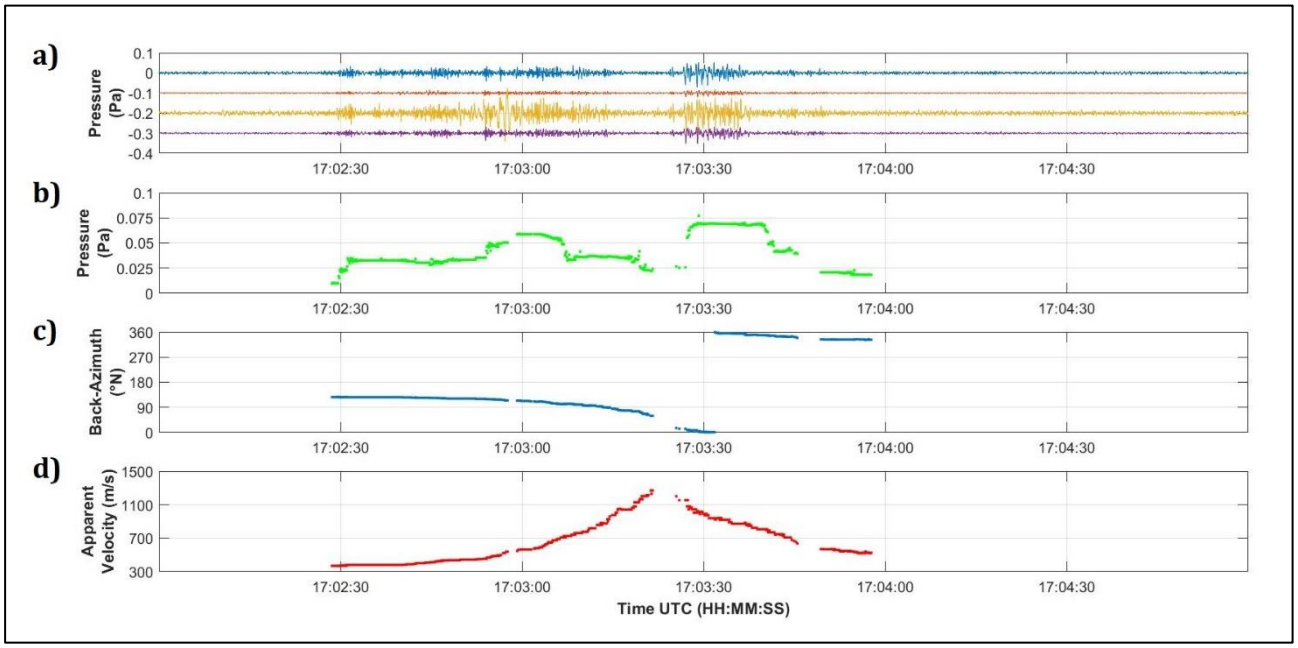

Figure 4. 6: example of the array processing of the infrasonic signal generated by an airplane and recorded by a 4-element array located in Valle d'Aosta (Italy). The signal recorded at the four sensors of the array (a). Infrasonic pressure (b), back-azimuth (c) and apparent velocity (d) of the infrasonic detection resulting from the array processing.

Figure 4. 6 shows as an example the results of the array processing applied to the infrasonic signal generated by a plane and recorded by a 4-element array located in Valle d'Aosta (Italy) and performed considering time windows of 5 seconds with 80% overlap and a threshold time residual $\Delta t = 0.01$ s. The array analysis of the signal recorded at the four sensors (Figure 4. 6 a) allowed to characterize the signal in terms of infrasonic amplitude (b), back-azimuth (c) and apparent velocity (d), for each time window. Each dot in Figure 4. 6 b, c, d represents an infrasonic detection defined with the array processing.

The back-azimuth trend, in particular, is indicative of a source moving from E-SE to N-NW with respect to the array (Figure 4. 6 c). The apparent velocity highlights a moving source too (Figure 4. 6 d). Its trend, initially ascending, reaching a maximum, and then descending, marks a signal characterized by a decreasing take-off angle at the beginning and then an ascending one, indicating a source that approaches the array, passes over it, and then moves away from it. Indeed, when a source is right above the array, the take-off angle is small and the apparent velocity settles on high values.

From the discussion presented here and the results in Figure 4. 6, the array analysis provides useful information on the ray parameters (back-azimuth and apparent velocity) of an infrasonic signal, which can be used to characterize the corresponding source and to discriminate it from the signals produced by the other sources.

Given the advantages offered by the array processing, this technique was applied to the infrasonic signals generated by the Illgraben debris flows, in order to investigate the infrasonic source mechanisms active within the flows.

Chapter 5

4.3 Cross-correlation analysis

A source acting at the ground-air interface, like volcanic eruptions, earthquakes, mass movements etc, is generally able to radiate both infrasound and seismic waves [McNutt et al., 2015; Marchetti et al., 2016; Belli et al., 2022]. Depending on the similarity of the infrasonic and seismic source mechanisms, the two wavefield can be closely related to each other, showing similar waveform and spectral features.

In addition to the primary signal component, directly radiated by the source, a supplemental component of the infrasonic signal is generated by the seismic waves, generated by the same source, that are locally transmitted to the air in the form of infrasound [Ichihara et al., 2012]. The same process occurs also for the seismic signal, for which a secondary component is produced by the local transmission to the ground of the infrasonic wave, generated by the same source, in the form of seismic waves [Ichihara et al., 2012]. These secondary components contribute to the signals that are recorded by the sensors.

The process through which the infrasonic and seismic waves are transmitted in the ground and in the air respectively, generating secondary seismic and infrasonic signal components, is known as seismo-acoustic coupling [De Angelis et al., 2012; Tauzin et al., 2013].

In case of seismo-acoustic coupling, the transmission of the infrasonic (or seismic) wave in the ground (air) determines a phase shift in the generated secondary seismic (infrasonic) wave, so that this

secondary component is delayed in time with respect to the incident primary infrasonic (seismic wave) of a quantity equal to [Ichihara et al., 2012]:

$t_s = \frac{1}{4f_0}$ (Eq. 4. 13),

where t_s (s) is the time delay determined by the phase shift associated with the seismo-acoustic coupling, while f_0 (Hz) is the characteristic frequency of the incident primary wave.

The interconnection between infrasonic and seismic waves can be evaluated using the cross-correlation analysis. Given two time series, x and y, made up of N terms,

$x = x_0, x_1, \dots x_{N-1}$,

$y = y_0, y_1, \dots y_{N-1}$,

the cross-correlation between them (R_{xy}) is a mathematical function defined as:

$R_{xy}(s) = \frac{1}{N-1}\sum_{j=0}^{N-i-1} x_j y_{s+j} \qquad \forall\, i \in [0, N-1]$ (Eq. 4. 14),

where x and y are interchangeable (i.e. first y translates with respect to x and then x translates with respect to y). s is the translation (shift) of one time series with respect to the other. For each value of s, one term of the cross-correlation function is defined. Since the two time series have N elements and since they are interchangeable in the order of translation, the cross-correlation between them R_{xy} is made of $2N-1$ terms.

For example, for $N = 4$, the two time series will be:

$x = x_0, x_1, x_2, x_3$,

$y = y_0, y_1, y_2, y_3$.

Therefore, given $s = 1$, the cross-correlation between them will be:

$R_{xy}(1) = \frac{1}{3}\sum_{j=0}^{2} x_j y_{1+j}$ (Eq. 4. 15),

and making the summation explicit:

$$R_{xy}(1) = \frac{1}{3}(x_0 y_1 + x_1 y_2 + x_2 y_3) \qquad \text{(Eq. 4. 16).}$$

As defined (Eq. 4. 7), the cross-correlation function represents the measure of the degree of similarity between the two time series as a function of the translation (s) of one series with respect to the other. Given two time series, which for a certain value of s are completely overlapping (i.e. they differ only in a translation along their elements), the cross-correlation between them will be maximum when s equals the value for which the series are completely overlapping, i.e. when the two series coincide at every element. The minimum cross-correlation value instead occurs for the value of s for which the overlap of the two time series take is the worst.
In general, when the two considered time series are not completely overlapping for any translation s, the cross-correlation function assumes its maximum value for the value of s for which the similitude of the two series is maximum.
For practical applications, the cross-correlation function is generally normalized to 1, where 1 represents the cross-correlation value obtained in case of a complete overlap of the two series.

As an example, Figure 4. 7 shows the autocorrelation (cross-correlation between a time series and itself, where x and y are identical) of a sinusoid. The resulting cross-correlation function spanning from negative to positive shift values: the positive values represent the situation in which y is translated with respect to x, vice versa the negative values indicate that x is translated with respect to y. Given that $x = y$, the resulting cross-correlation function is symmetrical with respect to the vertical axis passing from $s = 0$ s. It is evident that the overlapping of two perfectly identical functions is maximum when the displacement between them is null. For this reason, the maximum of the cross-correlation function is observed for a shift $s = 0$ s.

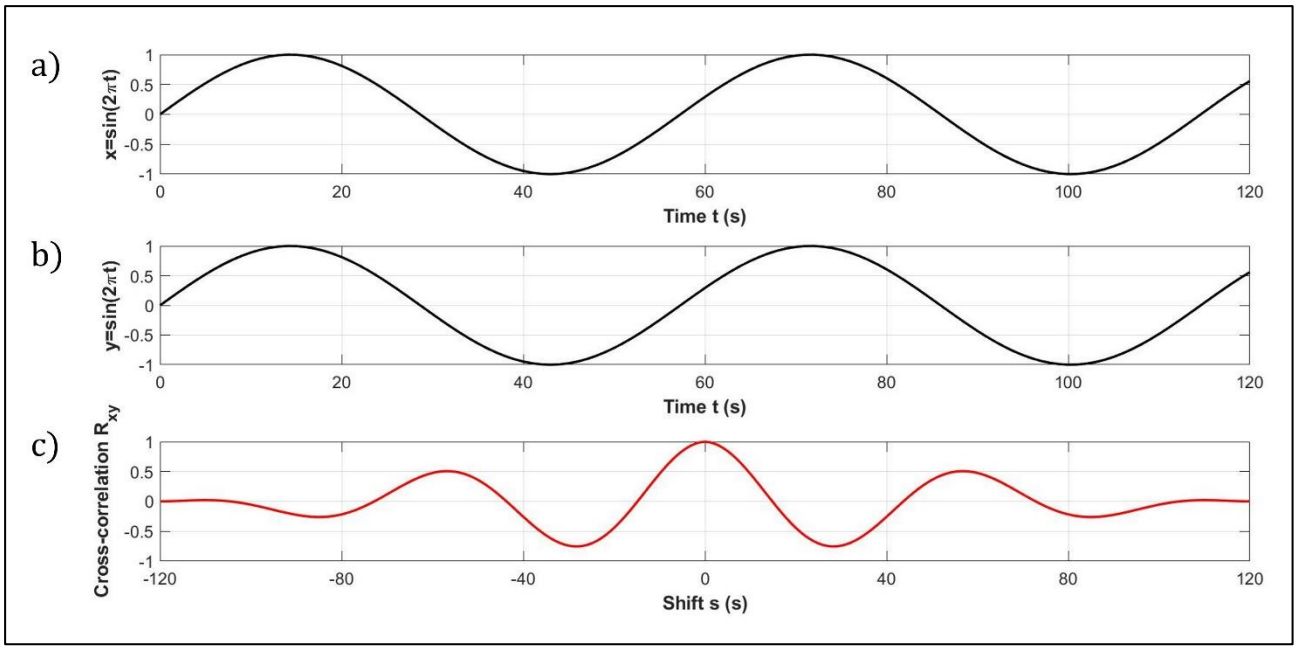

Figure 4. 7: autocorrelation (c) of a sinusoid (a, b). The maximum of the cross-correlation function (red curve in c) is observed for shift value $s = 0$ s. The cross-correlation function is normalized to 1.

The cross-correlation function shows also other local maximum points, of lower amplitude, that result from the periodicity of the sine function. The minor amplitudes of this secondary peaks, decreasing with increasing the shift, both in the positive and in the negative direction, are due to the fact that a translation of n elements of the second series leaves n elements of the first series without a corresponding elements, for the cross-correlation, in the second one.

The cross-correlation between a sine and cosine function, having the same argument, is shown instead in Figure 4. 8. In this case, the maximum of the resulting cross-correlation function is observed for a shift $s \approx 14.3$ s: this value corresponds to the time difference between the peaks of the sine function and the peak of the cosine function.

In addition, the maximum of the cross-correlation in Figure 4. 8 c is not equal to 1, because, as explained before, the shift $s \neq 0$ does not allow the complete overlapping of the two cross-correlated time series.

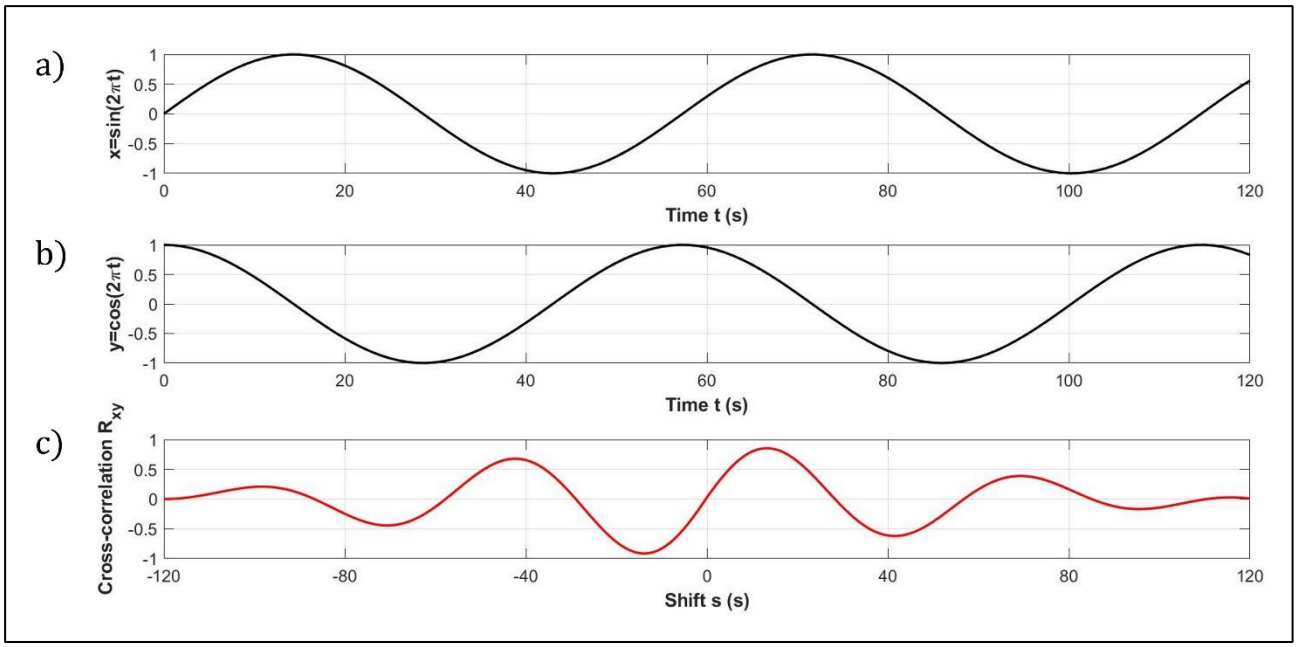

Figure 4. 8: cross-correlation (c) between a sine (a) and a cosine (b) function. The maximum of the cross-correlation function (red curve in c) is observed for shift value $s \approx 14.3$ *s, which is the time difference between the peak of the sine function and the peak of the cosine function. The cross-correlation function is normalized to 1.*

Chapter 5

Data analysis and results

5.1 Seismo-acoustic analysis of the Illgraben debris flows

In this thesis, the infrasonic and seismic signals generated by the 2017-2019 Illgraben debris-flow events have been analysed applying the techniques described in detail in Chapter 4. The obtained results are presented in the course of this Chapter.

In particular, the RMSA and the spectral analysis (see Chapter 4, Sections 4.1 and 4.2 respectively) were applied to seismo-acoustic signals to characterise them in terms of amplitude (Section 5.1.1) and frequency (Section 5.1.2) content. The obtained seismo-acoustic parameters have been then used as a basis for comparing debris-flow events to each other (Section 5.1.1) and then to the flow parameters derived from the measurements performed along the channel (see Section 5.2).

Section 5.1.3 is dedicated to the cross-correlation (see Chapter 4, Section 4.3) between the infrasonic and seismic signals generated by the Illgraben debris-flows, while Section 5.1.4 presents the results obtained from the application of the array processing (see Chapter 4, Section 4.4) to the infrasonic signals.

5.1.1 RMSA analysis of seismo-acoustic signals

The root mean square amplitude (RMSA) analysis, here applied to the debris-flow seismo-acoustic signals, was calculated along the entire duration of the events on 1-20 Hz band-pass filtered infrasound and seismic data, over 1-minute-long moving time windows. The resulting seismo-acoustic RMSA curves are shown in Figure 5. 1 b, below the debris-flow infrasonic and seismic waveforms, here shown again for a more convenient comparison with the RMSA curves in Figure 5. 1 a.

The obtained signal amplitude envelope shows a marked asymmetry, resulting from an amplitude rising time that is generally shorter than the amplitude fall-off tail. The observed asymmetry is a common feature with seismo-acoustic signals related to other mass movement processes [Allstadt et al., 2018], while it is not observed in the signals generated by earthquakes.

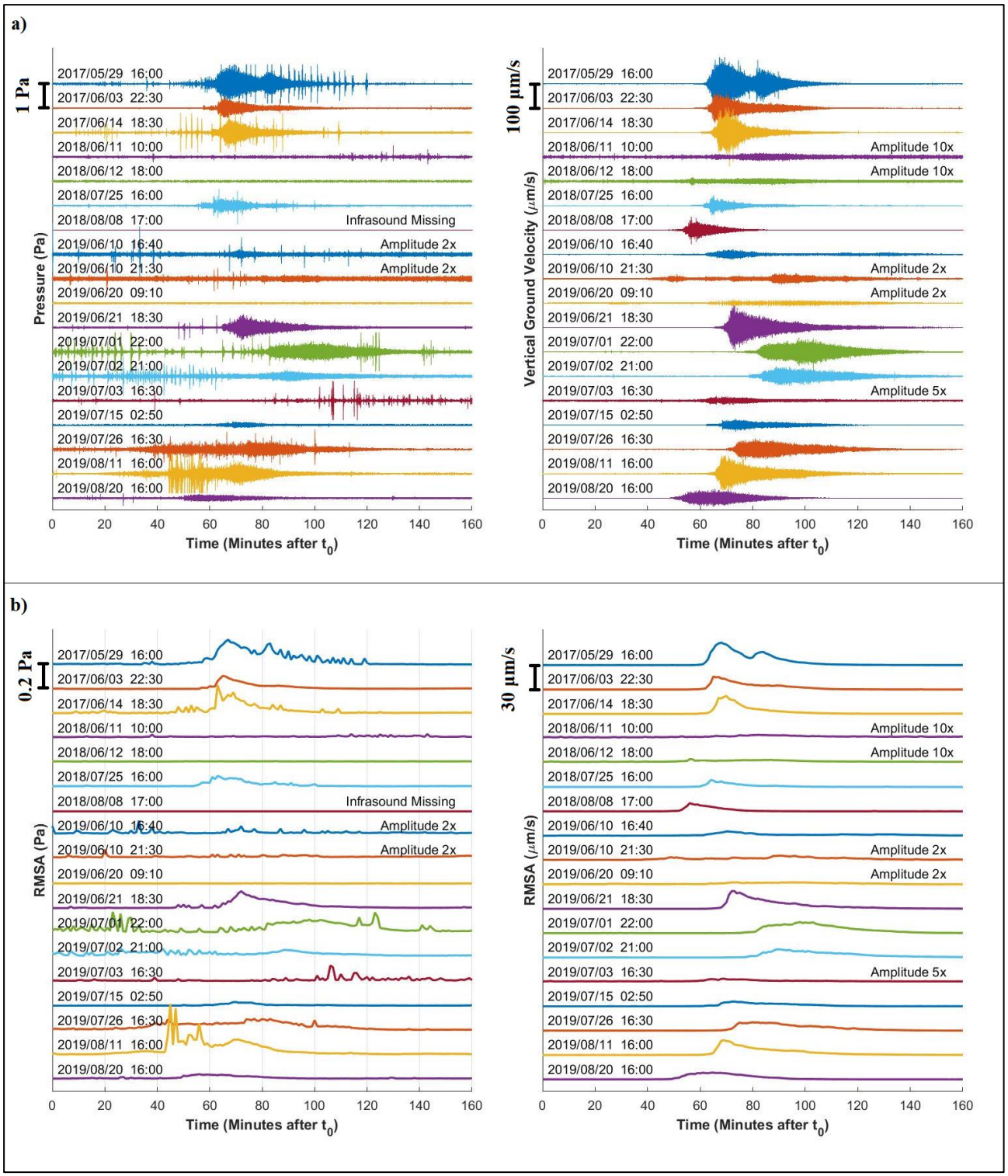

Figure 5. 1:1-20 Hz band-pass filtered infrasonic (left) and seismic (right) waveforms of the 18 debris flows at Illgraben between 2017 and 2019 (a). Infrasonic (left) and seismic (right) Root Mean Square Amplitude (RMSA) envelopes computed over 1-minute moving time windows on 1-20 Hz filtered data for all 18 events (b). For all signals, timing is expressed in minutes after the time reported on the left of each trace. For some events, the waveform and the RMSA envelope have been multiplied by an integer factor (2, 5 or 10) for visualization purposes.

Furthermore, as a result of their generally long duration, mass movements generate long duration signals (up to a few hours in case of debris flows) compared to the earthquake signals, for which the energy release associated with the brittle fracturing of rocks can be considered almost instantaneous. In addition, while earthquakes produce transient signal, in which the amplitude suddenly rises a reaches its maximum value in a few seconds, mass movements require some time after the initiation to release enough energy in the ground and in the air, so that a slowly rising amplitude is recorded.

For each RMSA envelope, the maximum value was determined. Some debris-flow events were accompanied by a simultaneous strong lightning activity (see Section 3.4.2, Figure 3. 17, Figure 5. 1 a), generating thunders associated with infrasonic transients characterized by an amplitude larger than the debris-flow signal. The computation of the maximum RMSA value for these events was performed excluding the thunders and limiting the search for the maximum only to the section of the infrasonic track corresponding to the debris-flow signal.
Obtained maximum RMSA varies between 0.035 and 0.208 Pa for infrasound and between 0.43 and 27.8 μm/s for seismic signals (Table 5. 1). The smaller variance of maximum infrasound RMSA, compared to the seismic RMSA, results from the infrasonic analysis having been performed only on the 11 events for which a clear infrasound signal was recorded, since the 6 smaller debris-flow events did not generate a distinguishable infrasound signal above the background noise level and had been therefore excluded from the infrasonic analysis (see Section 3.4.2). In contrast, in the case of seismic signals, the maximum RMSA was determined for all 18 events.

Table 5. 1: peak times and maximum RMSA of infrasound and seismic signals. "n.d." stands for "not detectable".

Debris-Flow Events	Infrasound RMSA Peak Time (UT)	Max Infrasound RMSA (Pa)	Seismic RMSA Peak Time (UT)	Max Seismic RMSA (μm/s)
2017/05/29	17:07	0.208	17:08	27.80
2017/06/03	23:35	0.113	23:35	16.12
2017/06/14	19:39	0.166	19:40	22.13
2018/06/11	n. d.	n. d.	11:22	0.46
2018/06/12	n. d.	n. d.	18:56	0.43
2018/07/25	17:03	0.090	17:04	8.52
2018/08/08	no infrasound	no infrasound	17:56	10.12
2019/06/10	n. d.	n. d.	17:50	5.38

2019/06/10	n. d.	n. d.	23:01	2.78
2019/06/20	n. d.	n. d.	09:37	0.50
2019/06/21	19:42	0.145	19:43	22.04
2019/07/01	23:38	0.112	23:38	13.78
2019/07/02	22:29	0.064	22:30	10.31
2019/07/03	n. d.	n. d.	17:39	0.81
2019/07/15	03:59	0.035	04:03	6.01
2019/07/26	17:47	0.098	17:50	10.39
2019/08/11	17:11	0.128	17:09	18.32
2019/08/20	16:56	0.044	17:05	8.45

Comparing infrasound and seismic maximum RMSA values in Table 5. 1, it is noticed that higher infrasonic maximum amplitudes tend to correspond to higher seismic maximum amplitudes. This positive relation becomes evident in Figure 5. 2, matching debris-flows infrasound and seismic maximum RMS amplitudes. Values are well arranged on a linear trend (black line in Figure 5. 2), characterized by a Pearson correlation factor $R = 0.96$. The fit appears significantly more accurate for higher seismo-acoustic amplitude events compared to lower amplitudes ones. This is to be expected considering that lower amplitude signals are characterized by a lower signal-to-noise ratio, generating a higher uncertainty.

Seismo-acoustic max RMSA data best-fit linear relation was computed (Figure 5. 2) and it resulted:

$$P_{max} = 0.0071 \frac{Pa}{\mu m/s} \cdot S_{max} + 0.0032\ Pa \qquad \text{(Eq. 5. 1)},$$

where P_{max} is infrasound maximum RMSA of a debris-flow event, expressed in Pa, and S_{max} is seismic maximum RMSA, in μm/s, of the same event. The Pearson correlation factor (R) was computed and it resulted $R = 0.96$.

Eq. 5. 1 and the excellent Pearson correlation factor indicate that, for Illgraben debris-flow events, infrasound and seismic maximum RMSA are always correlated and characterized by a ratio of ~ 0.007 Pa/(μm/s).

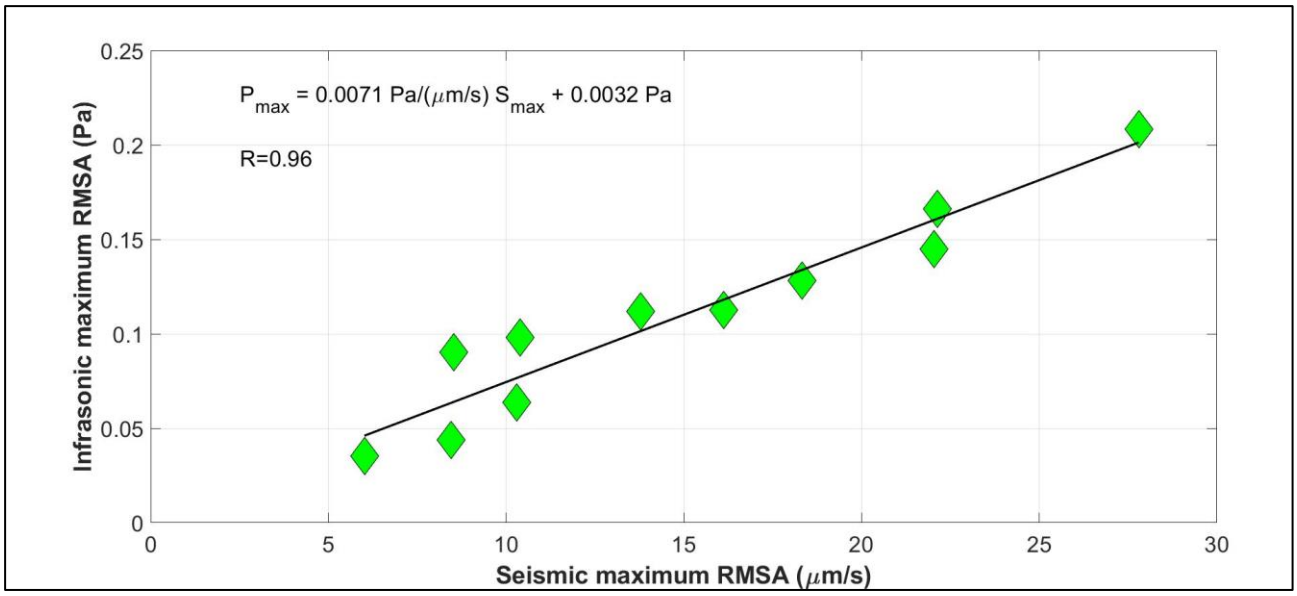

Figure 5. 2: relation between infrasound and seismic maximum RMSA. The black line represents the best fit regression line, whose equation is written within the panel, where also the Pearson correlation factor (R) is reported. P_{max} *and* S_{max} *are the infrasonic and seismic maximum RMSA, respectively.*

In Table 5. 1 it is also interesting to compare the times at which the infrasonic and seismic RMSA peaks are observed during the same event (Figure 5. 3). It is observed that the peak of infrasonic RMSA precedes the seismic one for almost all analysed events, with the only exception of the event of 2019/08/11, for which the seismic RMSA peak is observed 2 minutes before the infrasonic maximum.

However, the infrasonic and seismic RMSA are approximately simultaneous in time for most of the events, with the time difference between the peaks being ≤ 1 minute for 7 out of the 11 events recorded with detectable infrasonic and seismic signals (Figure 5. 3). The lag time between the RMSA peaks ranges between 2 and 4 minutes for 3 out of the 4 remaining events. Only the event of 2019/08/20 is characterized by a wider discrepancy in the peak times, with the infrasonic peak preceding the seismic maximum by 9 minutes.

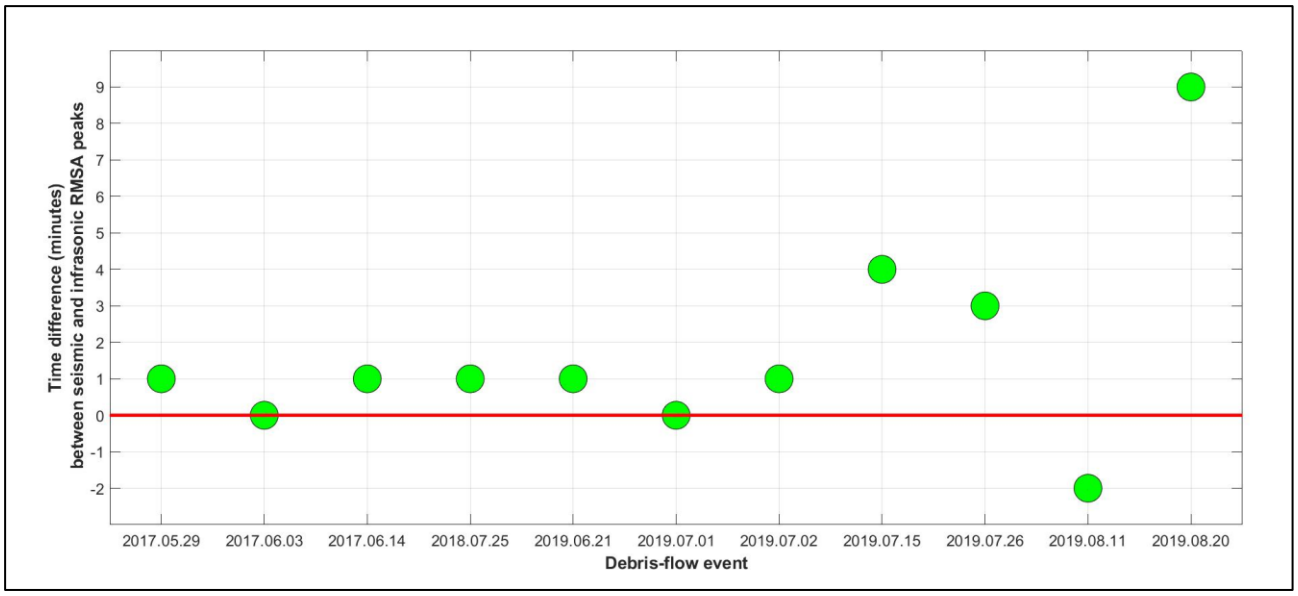

Figure 5. 3: comparison between infrasonic and seismic RMSA peak times. The red line marks a time difference between the infrasonic and seismic peaks equal to zero. Positive (negative) time difference values indicate that the infrasonic RMSA maximum is recorded before (after) the seismic one.

The overall small delay between the infrasonic and seismic RMSA peaks suggests that the maximum amplitudes of infrasonic and seismic signals are generated during the same phase of the debris-flow event, indicating that the peak phases of the radiation processes of the two wavefields coincide.

5.1.1.1 Seismo-acoustic RMSA ratio

To further investigate the relation between infrasonic and seismic signals, for each debris flow, the ratio between infrasonic and seismic RMSA curves was calculated over the entire duration of the event. Also for this analysis the infrasonic and seismic RMSA and their ratio were computed on 1-minute long moving time windows, along the entire event duration, for all the 11 debris-flow events recorded with both clear infrasonic and seismic signals.

Figure 5. 4 shows the results obtained for the 6 debris-flow events recorded with the greatest seismic-acoustic amplitude. It is observed that these events share a very similar RMSA time-trend for both infrasound and seismic signals. As a matter of fact, during the ~10 minutes long initial phase of each debris-flow event, i.e. before infrasonic and seismic RMSA curves reach their peak, the seismic RMSA always grows faster than the infrasonic one, despite, for each event, the infrasonic and seismic peaks are observed almost simultaneously (Figure 5. 3). Then, once the peak phase is reached, infrasonic and seismic RMSA curves equally decrease over time, gradually returning to the pre-event

levels. Analogous results are obtained also for the events recorded with lower seismo-acoustic amplitudes (see Section A2 of the Appendix).

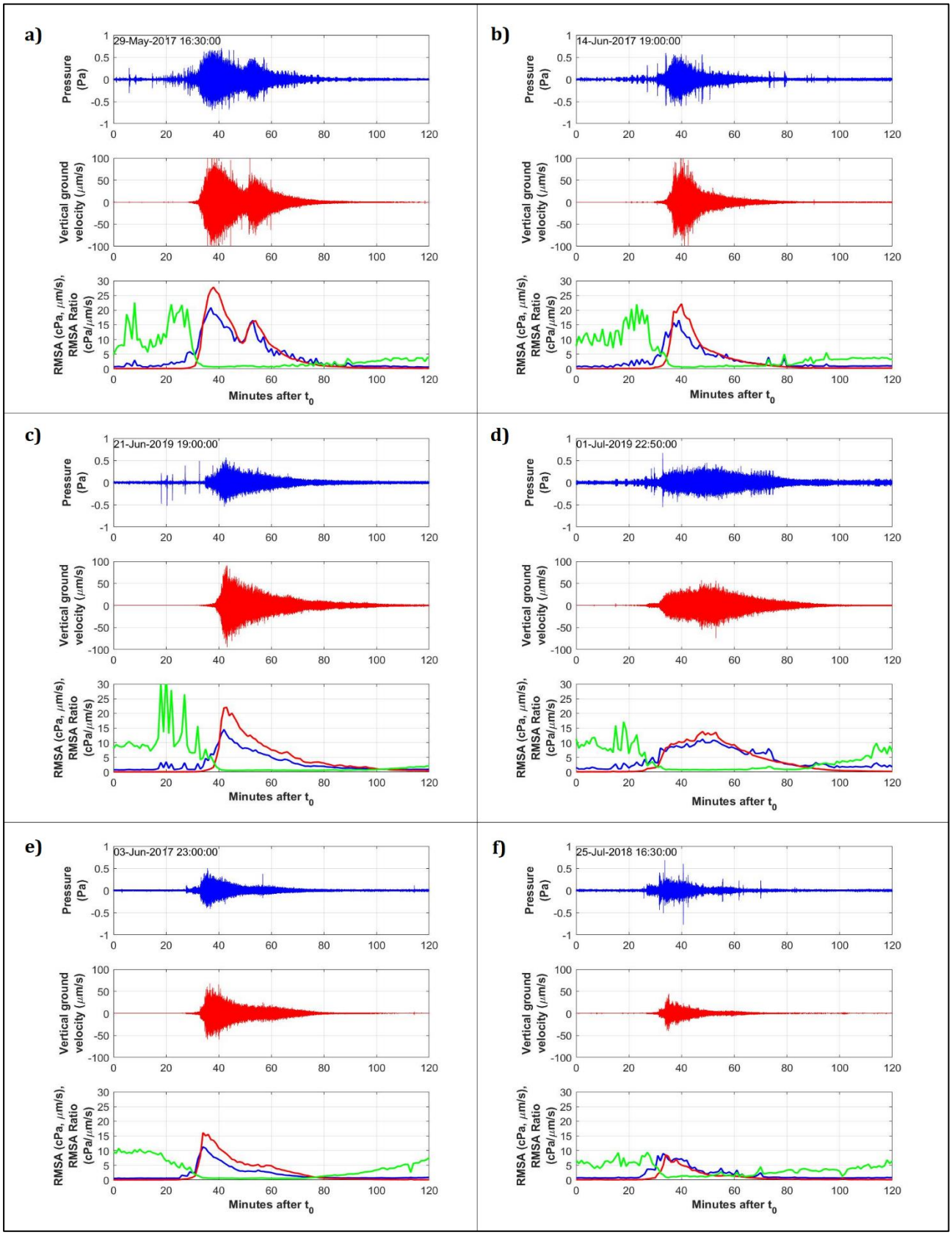

Figure 5. 4: infrasonic (blue) and seismic (red) RMSA analysis of the 6 major debris-flow events recorded at Illgraben between 2017 and 2019. The lower panel in each section shows both infrasonic (blue, cPa) and seismic (red, μm/s) RMSA, together with their ratio (green, cPa/(μm/s)).

This shared behaviour results into the characteristic infrasound-to-seismic RMSA ratio time-trend observed for all these 6 events (Figure 5. 4). As a matter of fact, for each event, the infrasound-to-seismic RMSA ratio rapidly decreases in the ~10 minutes long initial phase of the event, while, once the RMSA peaks have been reached, the RMSA ratio values remains constant in time, always ≈ 0.007 Pa/(μm/s) (0.7 cPa/(μm/s)), during almost all the remaining part of the event. This stable value, observed during the debris flow, is equal to the value of the RMSA ratio established at the seismo-acoustic amplitude peak phase of the event; indeed, this value is in agreement with the proportionality factor (0.71 cPa/(μm/s)) describing the linear relation resulted between infrasonic and seismic maximum RMSA in Figure 5. 2. Furthermore, it is observed that, during each event, the RMSA ratio during a debris-flow is always significantly lower (~ 0.0075 Pa/(μm/s)) than its pre-event and post-event values (~ 0.1 Pa/(μm/s)) (Figure 5. 4).

5.1.2 Spectral analysis of seismo-acoustic signals

Seismic and infrasonic signals generated by the Illgraben debris flows were also analysed in the frequency domain and spectra were computed in the form of Power Spectral Density (PSD) (Figure 5. 5).

The seismic signals of the events of 2018/06/11, 2018/06/12 and 2019/07/03 are characterized by a very low signal to noise ratio, therefore the PSD was not computed for these three events. Due to the recording sensor malfunction, for the event of 2018/07/25 the infrasonic PSD is not computable, so that the infrasound generated by this event was excluded from the frequency analysis below.

Computed PSD curves of seismic and infrasound signals are shown in Figure 5. 5. Results reveal that both infrasonic and seismic signals are characterized by broad spectra, spanning between ~1 and ~10 Hz and between ~1 and ~40 Hz respectively (Figure 5. 5 a, b).

However, the two wavefields are marked by significantly different frequency contents; the broad infrasound spectrum is centred around 4-6 Hz, with the peak frequency observed to vary from event to event (Figure 5. 5 a). In contrast, the seismic spectra are characterized by a stable broad peak

around 7 Hz for all events. The peak decreases rapidly below 2-3 Hz, well above the eigenfrequency of the Lennartz 3D seismometer, and above 20 Hz, well below the Nyquist frequency (50 Hz) of the A/D converter (Figure 5. 5 b).

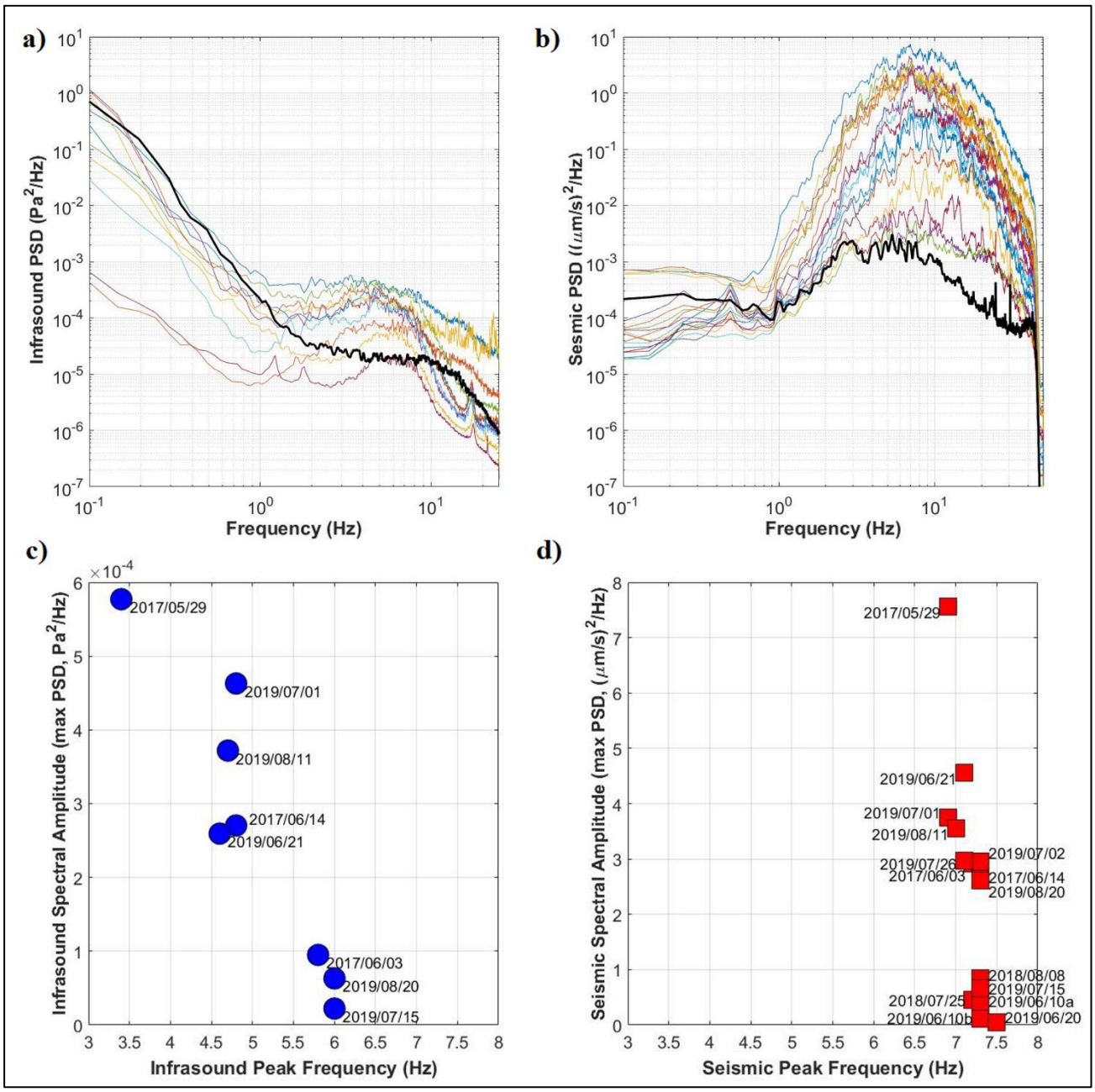

Figure 5. 5: power spectral density of infrasound (a) and seismic (b) records of the Illgraben debris-flow events. The black curves represent the spectrum of the infrasonic (a) and seismic (b) background noise: both the infrasonic and seismic noise spectra are calculated as the average of the spectra calculated over a 20-minute window of data recorded before each debris flow event here analysed. Spectral peak amplitudes of infrasonic (c) and seismic (d) signals as a function of peak frequencies (computed using Eq. 4. 5). In d, the two events on 2019/06/10 are marked in chronological order with the letters "a" and "b".

The frequency content of the infrasound generated by the events on 2019/07/02 and 2019/07/26 is strongly affected by the simultaneous thunderstorms (Figure 3. 17). Therefore, the infrasonic signals generated by these two events are excluded from Figure 5. 5 c and from the frequency analysis presented in the following Sections.

Each spectrum was then characterized in terms of maximum spectral amplitude and peak frequency (Table 5. 2). The peak frequency values were computed using Eq. 4. 5 (see Section 4.2, Chapter 4).

Table 5. 2: peak frequency (f_P, computed using Eq. 4.5) and maximum spectral amplitude of infrasonic and seismic signals. The symbol (*) marks the events for which infrasound peak frequency is strongly affected by rainstorms that occurred during the peak phase of the flow and produced infrasonic noise approximately of the same magnitude as the debris-flow signal. "n.d." ad "n.c." stand for "not detectable" and "not computable" respectively.

Debris-Flow Events	Infrasound Peak Frequency (Hz) (f_P)	Infrasound Maximum Spectral Amplitude (Pa^2/Hz)	Seismic Peak Frequency (Hz) (f_P)	Seismic Maximum Spectral Amplitude ($(\mu m/s)^2/Hz$)
2017/05/29	3.4	5.8×10^{-4}	6.9	7.6
2017/06/03	5.8	9.5×10^{-5}	7.2	2.9
2017/06/14	4.8	2.7×10^{-4}	7.3	2.8
2018/06/11	n. d.	n. d.	n. d.	n. d.
2018/06/12	n. d.	n. d.	n. d.	n. d.
2018/07/25	n. c.	n. c.	7.2	0.46
2018/08/08	no infrasound	no infrasound	7.3	0.85
2019/06/10	n. d.	n. d.	7.3	0.43
2019/06/10	n. d.	n. d.	7.3	0.11
2019/06/20	n. d.	n. d.	7.5	0.52
2019/06/21	4.6	2.6×10^{-4}	7.1	4.6
2019/07/01	4.8	4.6×10^{-4}	6.9	3.7
2019/07/02	not used (*)	not used (*)	7.3	3.0
2019/07/03	n. d.	n.d.	n. d.	n. d.
2019/07/15	6.0	2.2×10^{-5}	7.3	n. d.
2019/07/26	not used (*)	not used (*)	7.1	3.0
2019/08/11	4.7	3.8×10^{-4}	7.0	3.6

2019/08/20	6.0	6.3×10^{-5}	7.3	2.6

For each event, the infrasonic and seismic peak frequencies are different (Table 5. 2). Since the infrasonic peak frequency is systematically lower than the seismic one, this observed difference is not imputable to wave propagation, which in case of seismic waves induces a preferential depletion of the higher frequencies while it does not affect the infrasound frequency content over such short propagation distance (550-1300 m) [Lacanna et al., 2014]. Therefore, the difference observed in the infrasonic and seismic peak frequency suggests that the two wavefields are generated by two decoupled source mechanisms.

Furthermore, for each spectrum, the peak frequency was compared with the maximum spectral amplitude (Figure 5. 5 c, d). It is observed that the seismic peak frequency is almost constant for all events, regardless of the maximum spectral amplitude, varying between 6.9 and 7.5 Hz (Table 5. 2; Figure 5. 5). In contrast, among the infrasonic signals, the computed peak frequency significantly varies from a minimum of 3.4 Hz, observed for the 2017/05/29 event, up to 6 Hz, recorded for the events of 2019/07/15 and of 2019/08/20 (Table 5. 2). In addition, the peak frequency generally decrease as the maximum spectral amplitude increases (Figure 5. 5). This latter evidence likely suggests that the greater the infrasonic radiative power of the debris flows, the lower the generated infrasonic peak frequency. In contrast, this does not seem true in case of seismic signals.

To analyse in more detail the frequency content of the seismo-acoustic signals generated by the debris flows, spectrograms were computed on infrasonic and seismic data. As explained in Section 4.2 (Chapter 4), the spectrogram is a representation of the time evolution of the spectral content of a signal. Figure 5. 6 shows the seismo-acoustic spectrograms computed for the 2017/05/29 Illgraben debris-flow event, which was the largest debris flow observed at Illgraben in the period of analysis (see Table 3. 1, Section 3.4, Chapter 3) and was characterized by two successive debris-flow main surges.

The observed short duration events covering almost the entire investigated frequency window (0-25 Hz) in the infrasonic spectrogram (Figure 5. 6 b) are associated with thunders.

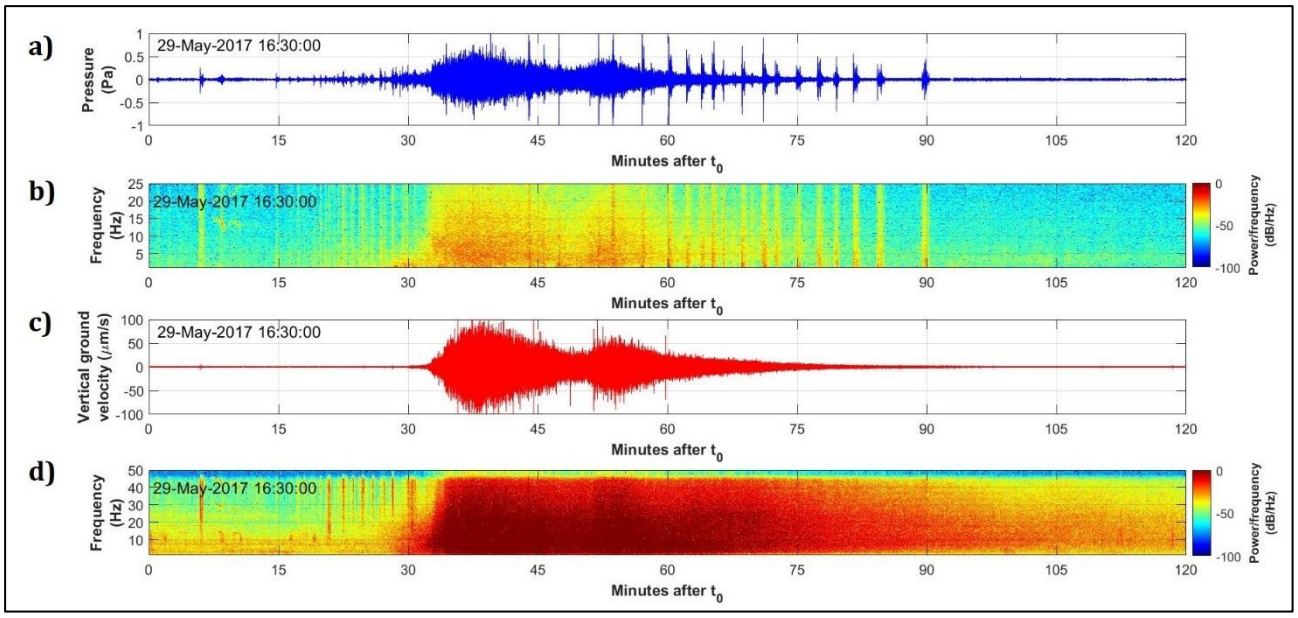

Figure 5. 6: seismo-acoustic spectrograms of the 2017/05/29 debris-flow event. Infrasonic signal (a) and its spectrogram (b). Seismic signal (c) and its spectrogram (d).

Results show that the seismic frequency content is distributed between 1 Hz and ~ 40 Hz during the entire duration of the event (Figure 5. 6 d). In contrast, the infrasonic signal spreads from 1 Hz up to ~ 20 Hz and its spectral content is not homogeneous during the event (Figure 5. 6 b); the covered spectral interval is observed indeed to vary during the debris-flow event. In particular, in the initial phase and during the two peak phases of the debris flow, corresponding to the two maxima of the signal amplitude, the infrasonic spectral content is more shifted towards the lower frequencies compared to the last phases of the event, characterized by a signal amplitude gradually decreasing, which are instead accompanied by a gradual migration of the spectral peak towards higher frequencies and by a progressive depletion of the lower frequencies (Figure 5. 6 b).

This trend in the infrasonic spectral content is particularly evident in Figure 5. 7, showing the spectrogram of the seismo-acoustic signals generated by the 2019/06/21 Illgraben debris-flow, which was one of the largest events observed in the period of analysis (see Table 3. 1, Section 3.4, Chapter 3). During the event, the infrasonic spectral broad peak, marked in Figure 5. 7 b by the darkest red-orange colours, gradually shifts from the lower frequencies, recorded in the initial and in the peak phases of the debris-flow event, towards the higher frequencies, observed in the final phases of the event, parallel to a gradual but still evident depletion of the lower infrasonic frequencies (Figure 5. 7 b). In contrast, a similar pattern is not found in the seismic spectrogram, where only a gradual decrease of the spectral amplitude, highlighted by the lightening gradual of the red colour, is observed, with the peak (darkest red) always stable around ~7 Hz (Figure 5. 7 d).

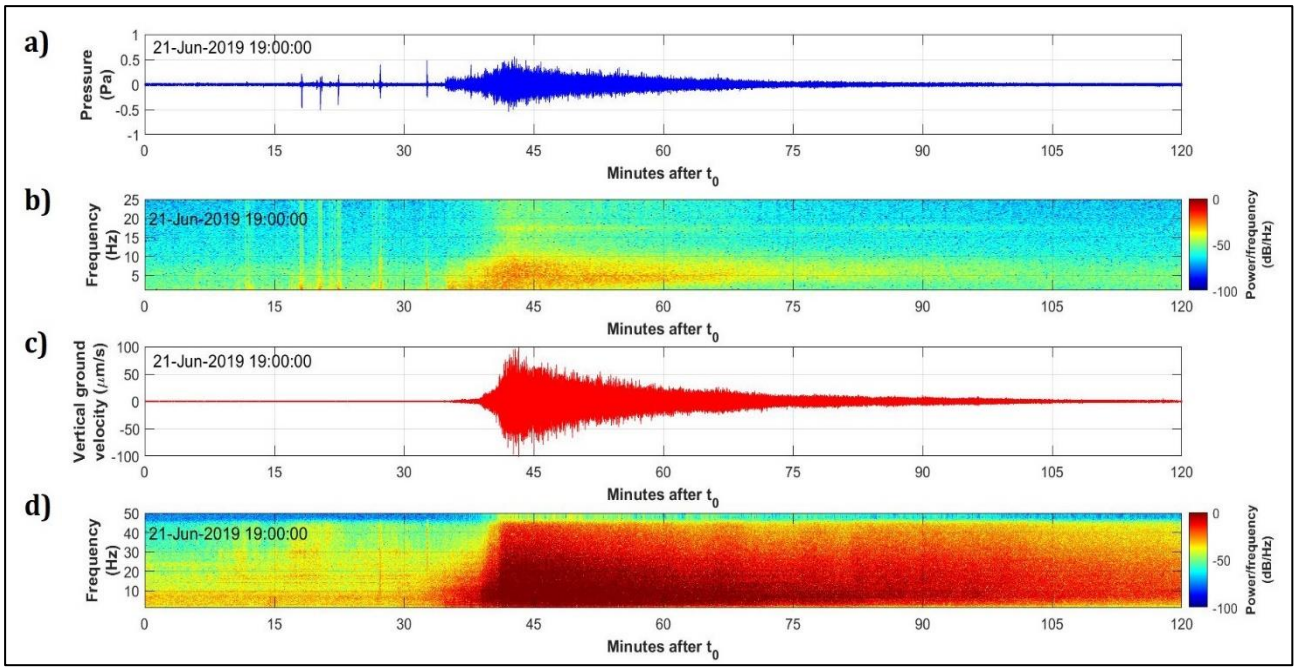

Figure 5. 7: seismo-acoustic spectrograms of the 2019/06/21 debris-flow event. Infrasonic signal (a) and its spectrogram (b). Seismic signal (c) and its spectrogram (d).

The evolution of the frequency content of the infrasonic signal generated by the 2019/06/21 debris flow is shown in more detail in Figure 5. 8, where the colour bar for the spectral amplitude values has been rescaled to empathize the infrasonic spectrogram pattern. The depletion in the lower frequencies is clearly observed during the event.

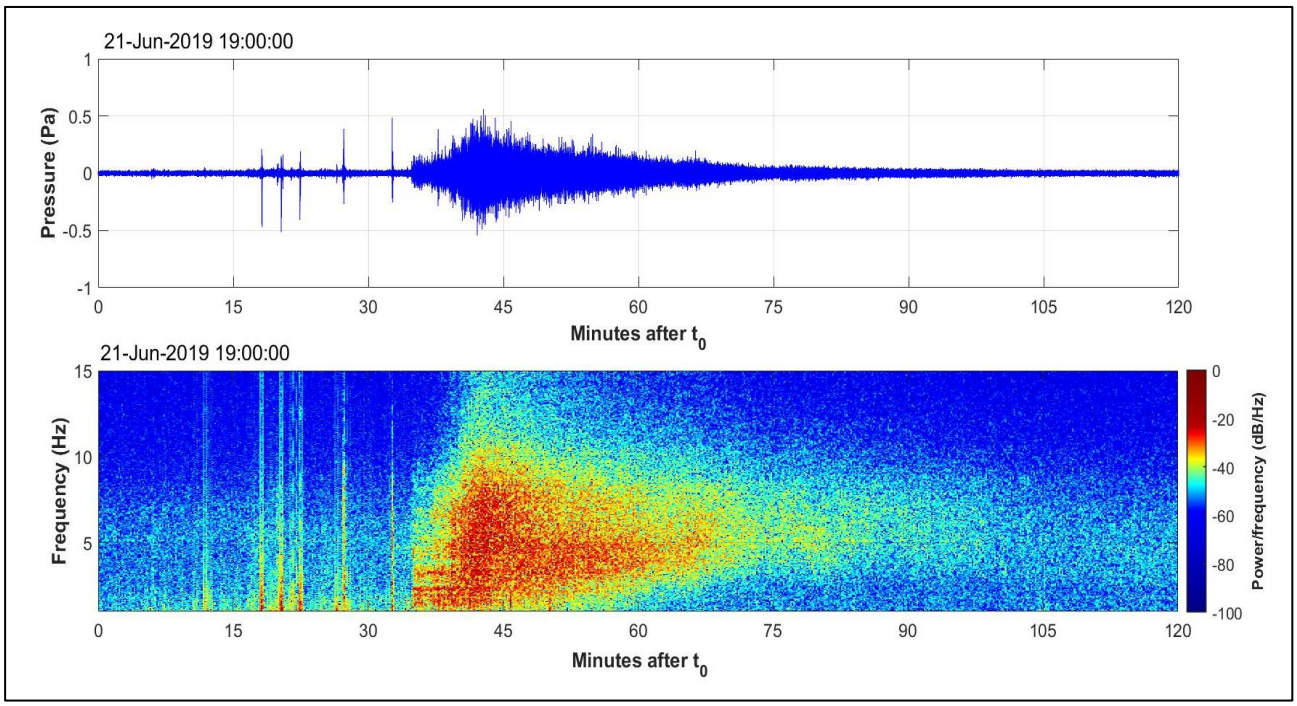

Figure 5. 8: detail of the spectrogram (bottom panel) of the infrasonic signal (top panel) generated by the 2019/06/21 Illgraben debris-flow event. The colour bar on the left of the bottom panel has been rescaled with respect to Figure 5. 7 to empathize the infrasonic spectrogram.

5.1.3 Seismo-acoustic cross-correlation analysis

To investigate whether and to what extent the infrasonic and seismic wavefields are related to each other, the cross-correlation analysis (see Section 4.3, Chapter 4) between infrasonic and seismic signals was performed.

The analysis was carried out correlating the infrasonic data recorded by the central element (m4) of the ILG array and the seismic data recorded by the ILL13 station of the seismic network. This choice was mated in order to compare the infrasonic and seismic signals recorded at the same location, since the central element of the ILG array and the ILL13 are separated by a distance $\leq$10 m (see Figure 3. 1, Section 3.1, Chapter 3).

The seismo-acoustic cross-correlation was computed over 1-minute moving signal windows on 1-20 Hz band-pass filtered data, along the entire duration of the debris-flow events.

The results obtained for the 2019/07/01 debris-flow event are presented in Figure 5. 9. The seismo-acoustic cross-correlation is shown in Figure 5. 9 c as a function of time (on the abscissas) and of the translation between infrasonic and seismic signals (*shift*, or lag, on the ordinate) (see Section 4.3, Chapter 4), and its values are indicated by colours, as reported in the colour bar on the side, with the maximum values indicated by red.

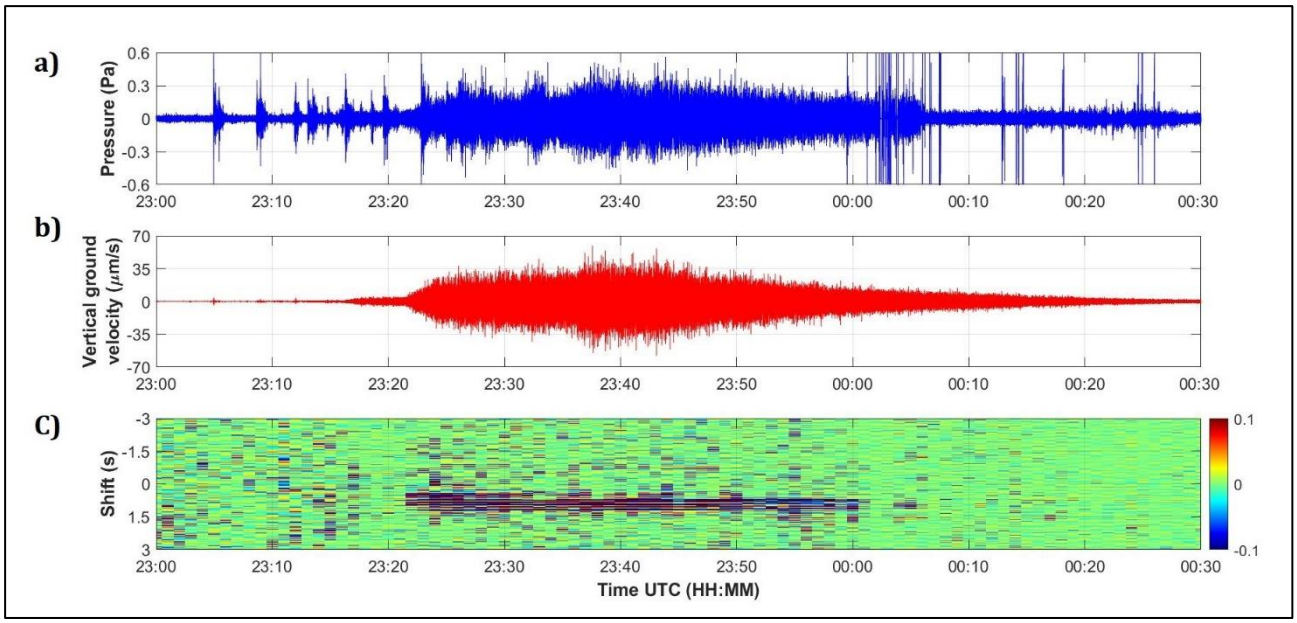

Figure 5. 9: cross-correlation (c) between infrasonic (a) and seismic (b) signals generated by the 2019/07/01 Illgraben debris-flow event. The values of the seismo-acoustic cross-correlation are indicated by the colour bar on the side (c).

The lag values on the ordinate axis can assume both positive and negative values: the positive ones indicate that the infrasonic track is shifted forward in time with respect to the seismic, while the negative ones indicate the opposite.

Results show that during the debris-flow event there is a strong seismo-acoustic cross-correlation, indicated by the red band observed along almost the entire duration of the event (Figure 5. 9 c). The cross-correlation is lost only in the very last phases of the debris flow, after 00:00 UTC, likely due to the spikes observed at that time in the infrasonic track, which are not related to the debris-flow event but probably result from the signal clipping due to some small malfunctions of the infrasonic sensor. In addition, the maximum of the cross-correlation function, corresponding to the centre of the red band in Figure 5. 9 c, is observed at shift values ~ 0.8 s. This value indicates that the maximum of the seismo-acoustic cross-correlation is observed when the seismic signal recorded at a specific time is compared with the infrasonic signal recorded 0.8 s later.

Furthermore, for the 2019/07/01 event, the shift value for which the seismo-acoustic cross-correlation is maximum is almost constant in time along the entire event.

A strong seismo-acoustic cross-correlation is also observed during the 2019/07/15 debris-flow (Figure 5. 10), which was one of the minor events recorded in the period of study with both detectable infrasonic and seismic signals (Table 5. 1).

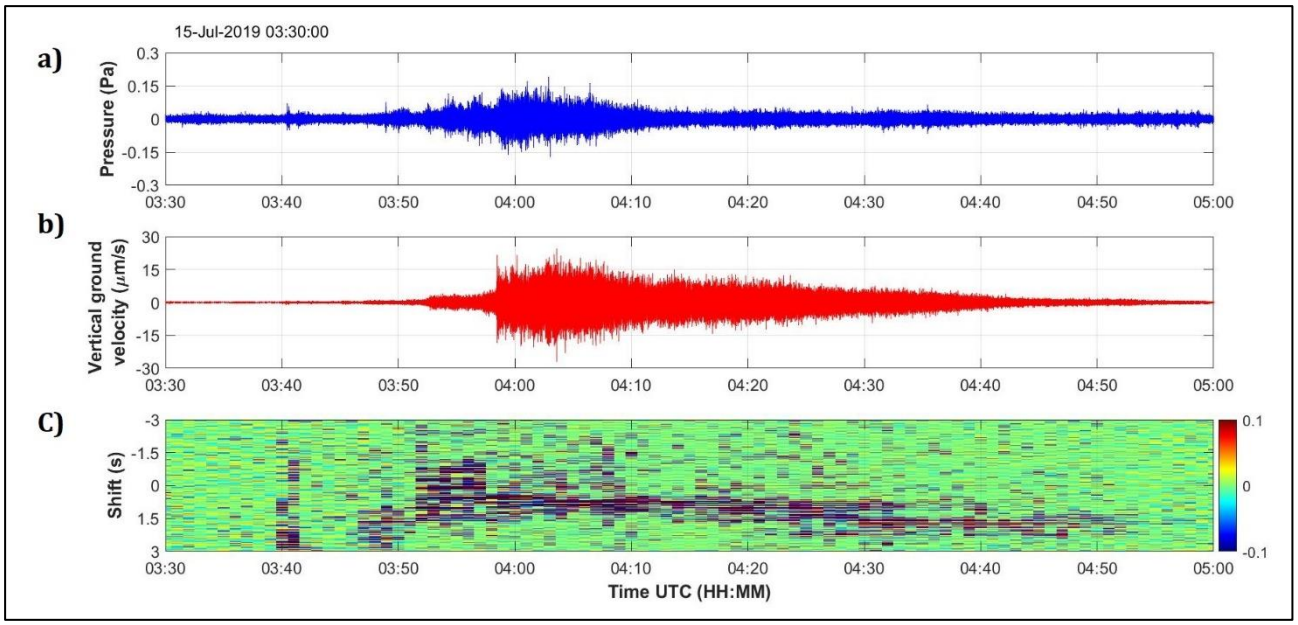

Figure 5. 10: cross-correlation (c) between infrasonic (a) and seismic (b) signals generated by the 2019/07/15 Illgraben debris-flow event. The values of the seismo-acoustic cross-correlation are indicated by the colour bar on the side (c).

Similar to what is observed for the 2019/07/01 debris-flow (Figure 5. 9), also the 2019/07/15 event shows a strong seismo-acoustic cross-correlation along the entire duration of the event (Figure 5. 10 c).

However, in this latter case, the evolution of the seismo-acoustic cross-correlation during the event is different compared to the previous one. Indeed, for the 2019/07/15 event, the location of the maximum of the cross-correlation function gradually migrates during the event (Figure 5. 10 c), passing from shift values ~1.5 s observed at the very beginning of the event (03:46-03:50 UTC), to the ~ 0.8 s, observed in the peak phase of the event (~ 04:00-04:20 UTC). Between 04:25 and 04:30, instead, two simultaneous cross-correlation peaks are observed, with the peak around ~1.3 s adding to the one around 0.8 s. Then the peak migrates to a shift of ~1.8 s, between 04:30 and 04:45, and finally to ~ 2.3 s, observed during the final stages of the event (after 04:45). These positive shift values indicate that, also for this event, the seismic signal precedes the cross-correlated infrasonic one.

The time interval between 03:51 and 03:58 (UTC) instead is characterized by a more complex trend of the seismo-acoustic cross-correlation, with several simultaneous red bands observed at different shift values, both positive and negative and approximately ranging between - 0.7 and + 1.5 s.

Comparable results are obtained also for the 2019/08/20 event, during which a strong seismo-acoustic cross-correlation is noticed too (Figure 5. 11).

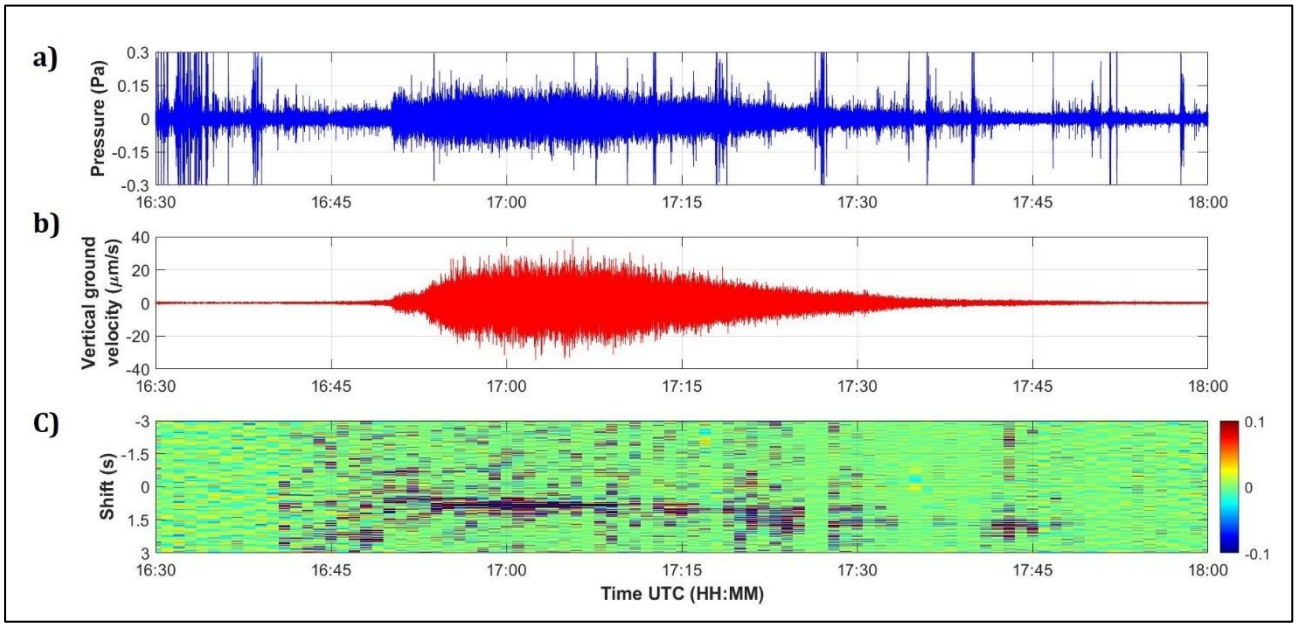

Figure 5. 11: cross-correlation (c) between infrasonic (a) and seismic (b) signals generated by the 2019/08/20 Illgraben debris-flow event. The values of the seismo-acoustic cross-correlation are indicated by the colour bar on the side (c).

Equally to what observed for the 2019/07/01 event, at the peak phase of the debris flow, the maximum of the cross-correlation function is observed for shift values equal to + 0.8 s. However, in the last ~30-minutes phase of the 2019/08/20 debris flow (after 17:15 UTC) the maximum of seismo-acoustic cross-correlation migrates to higher values, settling on shift values of ~1.1 s (17:15-17:20) and then of ~1.8 s at the end of the event (between 17:20 and 17:45, despite a gap is observed around 17:35 due to infrasound signals produced by lightning which overlap with the debris flow infrasound). Therefore, the seismo-acoustic cross-correlation of the 2019/08/20 debris flow shows a trend analogous, although less evident, to the one observed for the 2019/07/15 event. Also for this event, the observed positive shift values indicate that the seismic signal precedes the cross-correlated infrasonic one.

Similar results are obtained also for the other debris-flow events analysed in this thesis (see Section A3 of the Appendix).

The high cross-correlation observed between infrasonic and seismic signals during the Illgraben debris-flow events suggests that the two wavefields are to some extent related to each other and not completely independent.

5.1.4 Infrasonic array analysis

In order to further investigate the infrasonic source mechanisms within debris-flows, array processing was applied to infrasound data. The array analysis (see Section 4.4, Chapter 4) allows to characterize the signals in terms of wave parameters, including infrasonic pressure, back-azimuth and apparent velocity and thus allows to obtain crucial information on the location of the source as well as on the source mechanism.

The array processing was here performed on 1-20 Hz band-pass filtered infrasound data over 10 seconds long signal windows with 90% of overlap; a maximum of 1 detection per second is thus identifiable. A threshold time residual $\Delta t = 0.1$ s was considered. As the array processing is applied over a sliding window of data, a long-lasting infrasonic event results into a cluster of infrasonic detections.

The results obtained from the application of the array processing to the 2017/06/03 event are shown in Figure 5. 12. This event was one of the largest debris flows recorded in the period of analysis (recorded maximum flow depth = 1.9 m, see Table 3. 1, Section 3.1, Chapter 3).

The infrasonic signal generated by this debris-flow appears to be dominated by coherent clusters of infrasonic detections (each point in the Figure 5. 12 b, c, d is a single detection). Five distinct clear detection clusters are observed, while a sixth less evident one is visible at the end of the signal. Each cluster is characterized by constant back-azimuth values (Figure 5. 12 c), that however vary from cluster to cluster. In particular, the recorded back-azimuth values for the six detection clusters are the following: 190-182°N, 173°N, 156°N, 110°N, 90-80°N and ~35°N (Figure 5. 12 c).

On the other hand, the trend of the apparent velocity is more unclear: this is probably due to the small aperture of the ILG array, which prevents accurate estimates of the apparent velocity (Figure 5. 12 d).

The constant back-azimuth values characterizing the detection clusters indicate that each cluster is generated in a fixed position along the channel. In particular, the back-azimuth values of each

detection cluster point in the direction of some of the check dams located along the channel (Figure 5. 12 e).

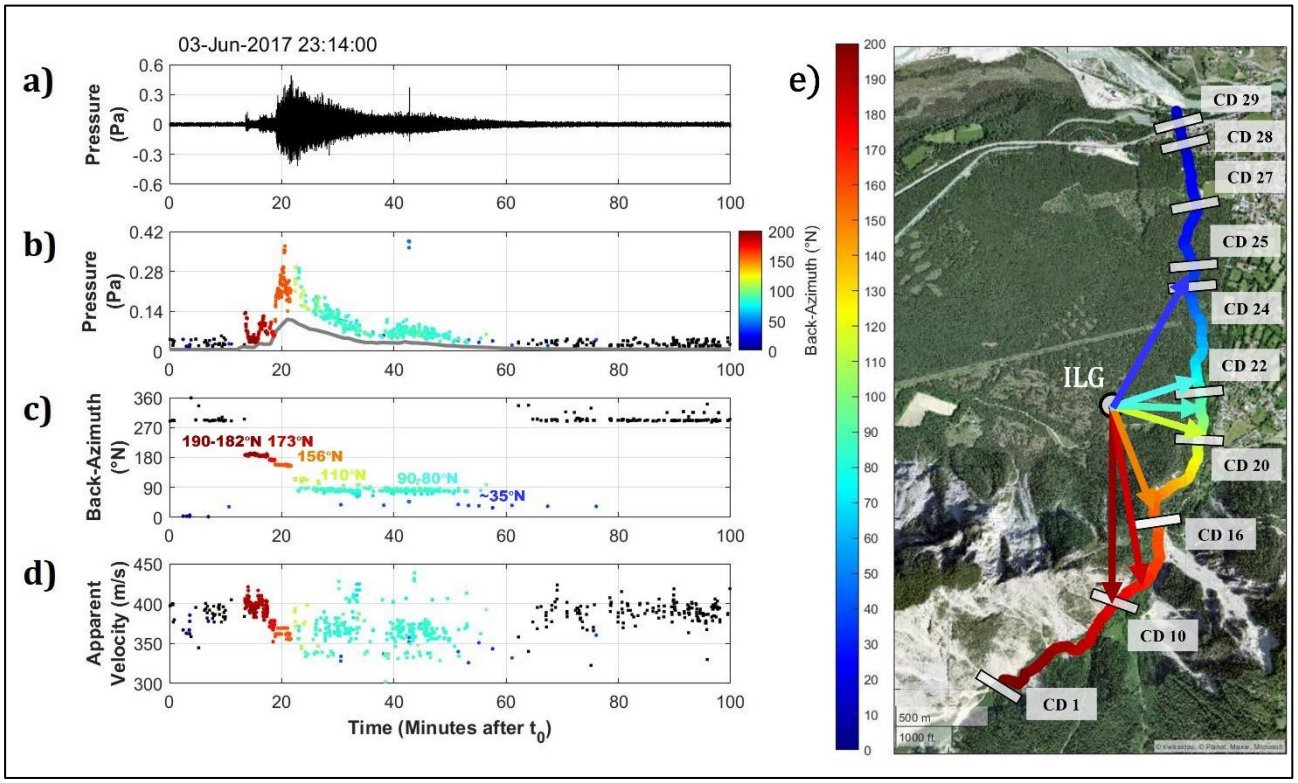

Figure 5. 12: array processing of the infrasonic signal generated by the 2017/06/03 Illgraben debris-flow event. 1-20 Hz band-pass filtered infrasonic track recorded at M1 (a); infrasonic pressure (b), back-azimuth (c) and apparent velocity (d) of the infrasonic detections identified with the array processing. The grey line in panel b represents the RMSA of the infrasonic signal computed over 1-minute windows. Back-azimuth values in panels b, c, d and e are indicated by colours according to the colour bar on the side of panel b. Map of the Illgraben channel showing for each point the back-azimuth measured with respect to the ILG array and coloured according to the colour bar alongside (e). In e, the location of some of the 30 check dams (CD) and of the ILG array (grey circle) are indicated. Arrows in e point in the directions indicated by the back-azimuth values highlighted in c and are coloured the same colour as the back-azimuth value they represent.

For example, the cluster characterized by a back-azimuth ~156°N (orange arrow in Figure 5. 12 e) exactly points at the CD 16, the cluster of 110°N individuates the CD 20, while the long duration cluster pointing at 90-80°N (cyan arrow) clearly indicates the direction of CD 21 and of CD 22 (Figure 5. 12 e). The 190-182°N and the cluster instead point at check dams located further upstream, in the upper catchment, while the weak cluster of ~35°N indicates the CD 24 (Figure 5. 12 e). The 173°N instead points at a highly irregular channel portion located right at the mouth of the Illgraben upper catchment, which also represents the first channel point from which the propagation of the infrasonic

ray to the array is approximately line-on-sight and does not require the infrasonic wave to overcome the northern ridge of the upper catchment: in this position therefore part of the infrasonic energy generated in the nearby upstream areas is more easily recorded at the array compared to the other more upstream portions of the basin.

The evidence that the computed back-azimuth values point in the direction of the check dams suggests that coherent components of the infrasonic signal are radiated in correspondence of check dams.

Furthermore, the back-azimuth variation observed during the event, showing a decrease over time from ~190 to ~80 °N, highlights a source approximately moving from south to east with respect to the array. This variation is perfectly consistent with the debris-flow movement within the catchment, given the channel geometry and the array location (Figure 5. 12 e). Moreover, the maximum infrasonic amplitudes are recorded for back-azimuth values ranging between 156 and 80°N (Figure 5. 12 b), so when the main body of the debris flow was located in the channel sector between CD 16 and CD 22.

A similar pattern is observed also for the 2019/06/21 debris-flow event (Figure 5. 13), which was one of the largest debris-flow at Illgraben in the period analysed in this thesis (second highest recorded maximum flow depth = 2.59 m, see Table 3. 1, Section 3.1, Chapter 3).

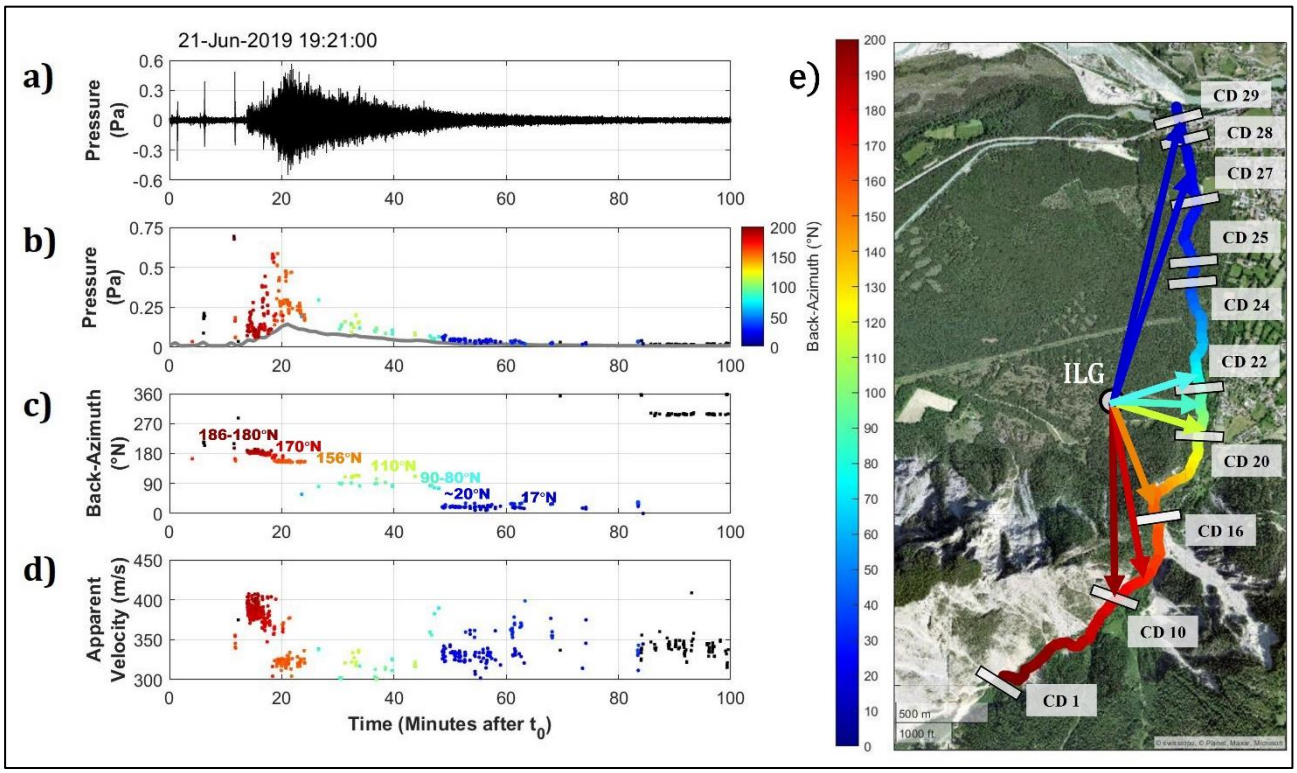

Figure 5. 13: array processing of the infrasonic signal generated by the 2019/06/21 Illgraben debris-flow event (same as Figure 5. 14).

Also for this event the array processing revealed that the recorded infrasonic signal appears to be dominated by clusters of coherent infrasonic detections, each characterized by constant back-azimuth values. Up to seven detection clusters are identified, with determined back-azimuth values of 186-180°N, ~170°N, 156°N, 110°N, 90-80°N, 20°N and 17°N (Figure 5. 13 c). Also for this event, the back-azimuth of each infrasonic detection cluster points at one of the check dams located along the Illgraben channel, with the new observed values of 20°N (blue arrow) and 17°N (darker blue arrow) indicating the sectors just downstream CD 27 and CD 28 respectively (Figure 5. 13 e). The only exception is represented by the ~170°N cluster, which identifies the highly irregular channel portion located right at the mouth of the upper catchment.

Similar to what has been observed for the 2017/06/03 event presented above, the back-azimuth variation from ~190 to ~20°N observed during the 2019/06/21 event, is perfectly consistent with a debris flow propagating along the Illgraben channel, almost until the Rhone river.

Moreover, it is interesting to note that the first identified detection clusters (186-180°N, ~170°N, 156°N, 110°N and 90-80°N; Figure 5. 13 a) are the same as the ones determined for the 2017/06/03 event (192-182°N, 173°N, 156°N, 110°N and 90-80°N; Figure 5. 12 a). This indicates that these two debris flows shared these directions for the radiation of coherent components of the generated infrasonic signal.

For the 2019/06/21 event, the maximum infrasonic amplitudes are recorded for back-azimuth of 156°N (Figure 5. 13 a), corresponding to the channel sector of CD 16.

Similar results are obtained also for the 2019/07/15 debris flow (Figure 5. 15), which was one of the smaller events recorded in the period of analysis with both detectable infrasonic and seismic signals (recorded maximum flow depth = 0.54 m, see Table 3. 1, Section 3.1, Chapter 3).

Indeed, also for this small size event, the recorded infrasonic signal is dominated by coherent clusters of infrasonic detections, each marked by constant back-azimuth values which however vary from cluster to cluster (Figure 5. 15 b, c, d).

In this case, five clusters are clearly identified during the event, characterized by the following back-azimuth values respectively: 156°N, 110°N, 90-80°N, ~35°N and 16°N (Figure 5. 15 c). These values point to the sectors corresponding to CD 16, CD 20, CD 21-22, CD 24 and C28 respectively (Figure 5. 15 e).

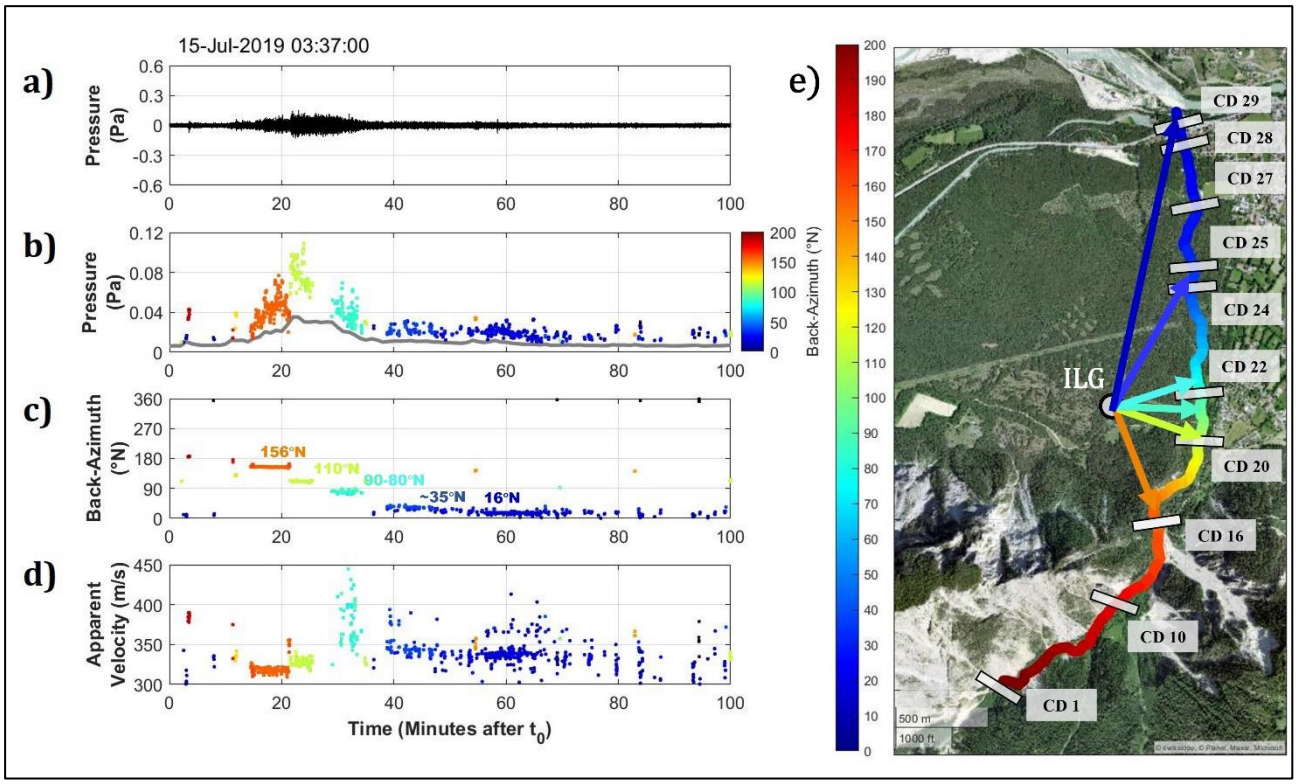

Figure 5. 15: array processing of the infrasonic signal generated by the 2019/07/15 Illgraben debris-flow event (same as Figure 5. 16).

Therefore, for this event, the array processing is able to follow the entire debris flow migration along the sector of the channel between CD 16 and CD 28, located near the coalescence of the Illgraben torrent with the Rhone River. Detection clusters pointing further upstream, observed for the two events presented above, are instead missing in this case: this likely indicates that the 2019/07/15 event developed, or at least started to efficiently radiate infrasound, in a section of the catchment located further downstream compared to previously presented larger events.

Once again, the check dams result as preferential locations for the generation of coherent components of the infrasonic signal.

Similar to the 2017/06/03 event, for the 2019/07/15 event the maximum infrasonic amplitudes are recorded for back-azimuth values ranging between 156 and 80°N (Figure 5. 15 b), corresponding to the channel sector between CD 16 and CD 22, and in particular for a back-azimuth of ~110°N (CD 20).

Finally, the results obtained for the 2019/08/20 debris-flow event are shown in Figure 5. 17. Also this event was one of the minor debris flows recorded with both clear infrasound and seismic signal in the investigated period (recorded maximum flow depth = 0.44 m, see Table 3. 1, Section 3.1, Chapter 3).

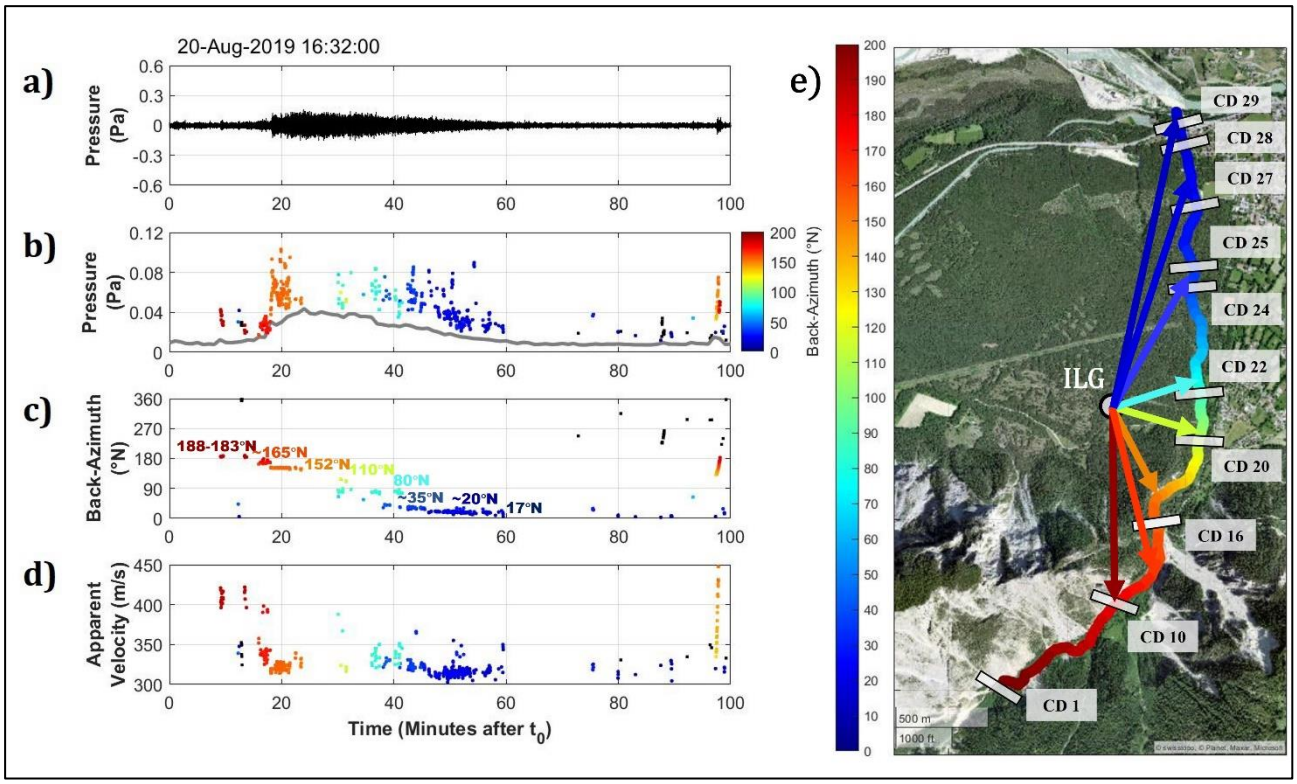

Figure 5. 17: array processing of the infrasonic signal generated by the 2019/08/20 Illgraben debris-flow event (same as Figure 5. 18).

Results showed that, similar to the events presented above, the infrasonic signal generated by this debris-flow appears to be dominated by clusters of infrasonic detections, each characterized by constant back-azimuth values, which vary from cluster to cluster (Figure 5. 17 c).

In particular, the array processing highlighted up to eight detection clusters, respectively identified by the following back-azimuth values: 188-183°N, 165°N, 152°N, 110°N, 80°N, ~35°N, ~20°N, 17°N. The cluster of 188-183°N, pointing at the dams located at the outlet of the upper catchment, was observed more clearly also for the 2017/06/03 and for the 2019/06/21 events. The 165°N and 152°N clusters instead point at very irregular channel sections, characterized by steep channel bends, located exactly at the outlet of the upper section of the Illgraben catchment and downstream CD 16 respectively.

For this event, similar to the previous events, the maximum infrasonic amplitudes are recorded for back-azimuth values ranging between 152 and 80°N (Figure 5. 17 b), corresponding to the channel sector between CD 16 and CD 22, and in particular for a back-azimuth ~152°N.

Array processing revealed that the infrasonic signal generated by Illgraben debris flows is dominated by coherent clusters of infrasonic detections that are generated in fixed position along the channel.

The evidence, observed also for the other debris-flow events analysed in this thesis (see Section A4 of the Appendix), of the infrasonic detection clusters pointing at some of the check dams located along the channel suggests that a preferential radiation of coherent infrasound by Illgraben debris-flows is triggered in correspondence of check dams.
In addition, it is observed that the maximum infrasonic amplitudes are recorded when the main body of the debris flow is located in the channel sector between C16 and C 22, which is the channel portion located at the minimum distance from the recording sensors. This agrees with what was already observed by Marchetti et al. [2019], who suggest that at Illgraben the maximum infrasonic amplitudes are recorded when the barycentre of the debris-flow is located at the minimum distance from the recording sensors.

5.2 Comparison between seismo-acoustic signals and flow parameters

In order to investigate how flow parameters and fluid dynamic processes influence the seismo-acoustic energy radiation by debris flows, the seismo-acoustic signal features were compared with available hydraulic data. The comparison has been limited to the debris-flow events for which both seismo-acoustic and hydraulic data are available.
First the flow parameters were compared with seismo-acoustic RMSA (Section 5.2.1), then to seismo-acoustic peak frequencies (Section 5.2.2).
In particular, for the comparison between the infrasound records and the hydraulic data we focused on the infrasonic data recorded at the m1 sensor of the ILG array, with the exception of the event on 07/25/2018, for which data recorded at the m5 sensor were used, as the m1 sensor was not functioning at the time of the event.

5.2.1 Comparison between seismo-acoustic RMSA and flow parameters

First, the seismic and infrasonic maximum RMSA were compared with debris-flow front velocity (Figure 5. 19). Due to the availability of the compared data, the comparison was possible for 11 events, in case of infrasound, and for 13 events, in case of seismic signals.

Results reveal that seismo-acoustic maximum RMSA shows a general positive relation with the debris flow front velocity at intermediate velocity values (i.e. between 3 and 8 m/s). The slowest (~1 m/s) and fastest (~9 m/s) events depart from this trend and thus prevent defining a clear correlation function.

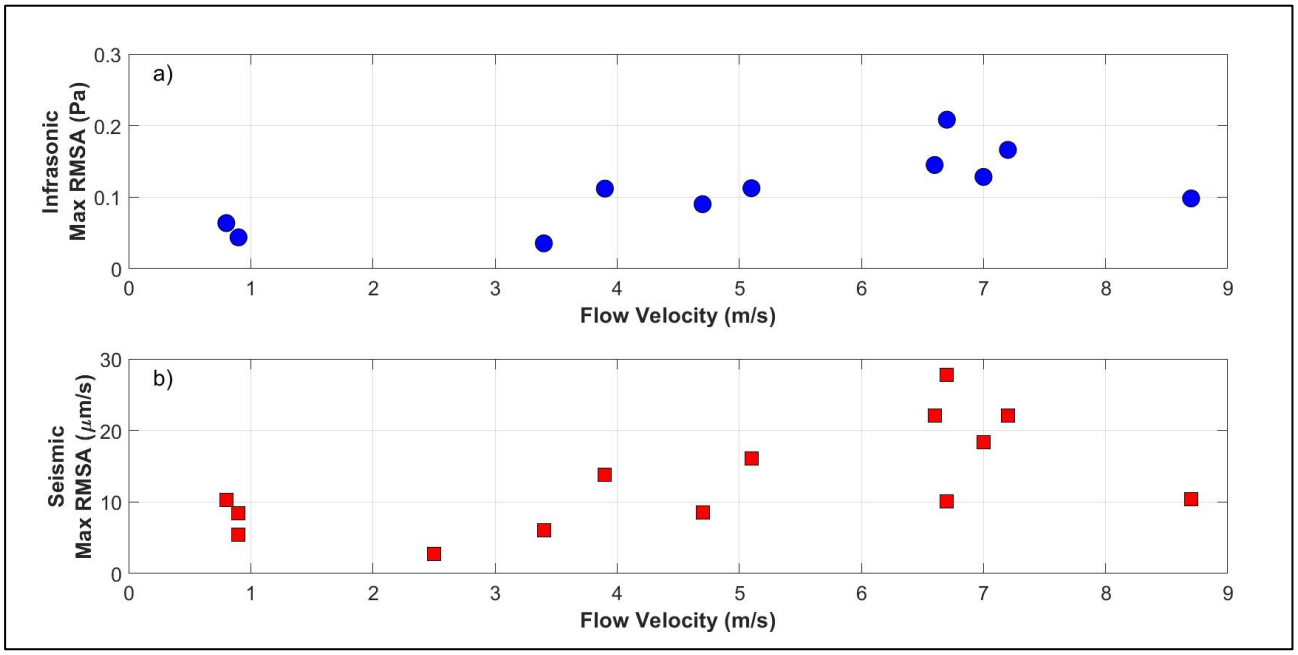

Figure 5. 19: comparison between debris-flow front velocity and both infrasonic (a) and seismic (b) maximum RMSA. A general positive relation is observed in both panels, with the exception of the fastest (~9 m/s) and the slowest (~1 m/s) debris flows.

The comparison between seismo-acoustic peak RMSA and maximum flow depth is shown in Figure 5. 20. Differently from the front velocity, results show an excellent linear relation for both infrasonic (Figure 5. 20 a) and seismic (Figure 5. 20 b) signals, with the seismo-acoustic maximum RMSA linearly increasing with increasing the maximum flow depth. The computed Pearson correlation coefficients are equal to 0.94 and 0.95 for infrasound and seismic signal respectively.

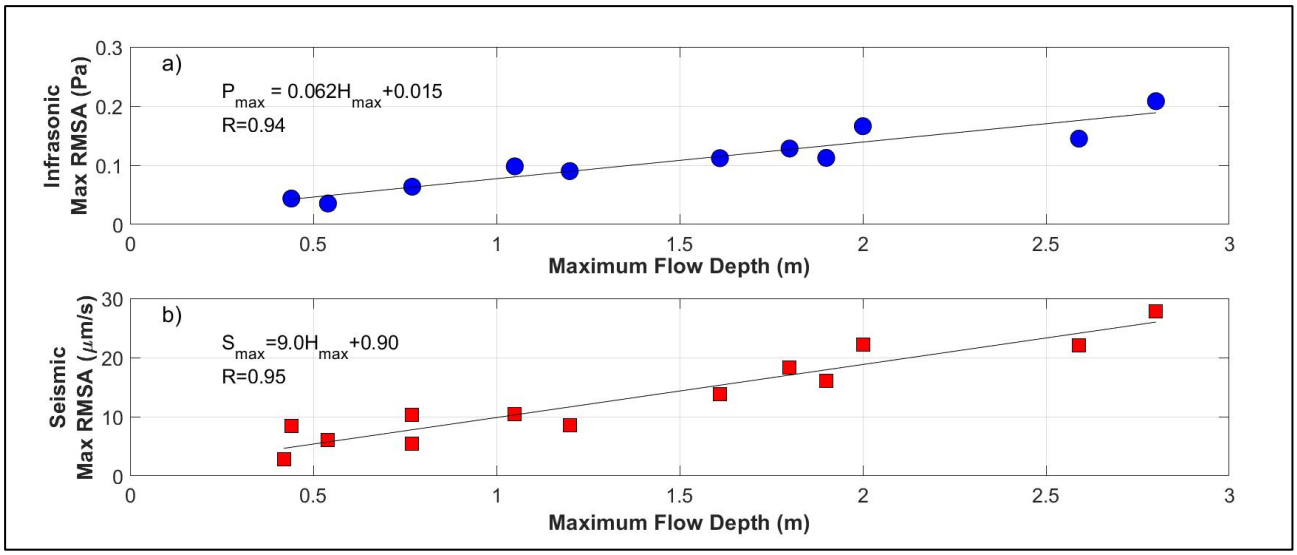

Figure 5. 20: comparison between debris-flow maximum flow depth and infrasonic (a) and seismic (b) maximum RMSA. A positive linear relation is observed in both panels. The black lines in both panels represent the best linear fit, whose equations are written within the panels, where also the Pearson correlation factor (R) is reported.

For infrasound and seismic signals, the best fit regression lines were computed (black line in Figure 5. 20) and their equations were determined as:

$$P_{max} = 0.062\ \frac{Pa}{m} \cdot\ H_{max} - 0.015\ Pa \qquad \text{(Eq. 5. 2)},$$

$$S_{max} = 9.0\ \frac{\mu m/s}{m} \cdot\ H_{max} - 0.90\ \mu m/s \qquad \text{(Eq. 5. 3)},$$

where P_{max} is expressed in Pa, S_{max} in μm/s and H_{max} in m.

To further investigate the linear relation between the seismo-acoustic maximum RMSA and the maximum flow depth, the infrasonic and seismic RMSA curves computed for the 2019/06/21 and for the 2019/07/01 debris flows were compared also with the hydrograms recorded for these two events at CD 29 (Figure 5. 21). To reduce the effect of water splashes and to compare the hydrograms to the seismo-acoustic RMSA curves (computed on 1-minute windows, see Section 5.1.1), the hydrograms were resampled to one depth value per minute and a smoothing function was applied.

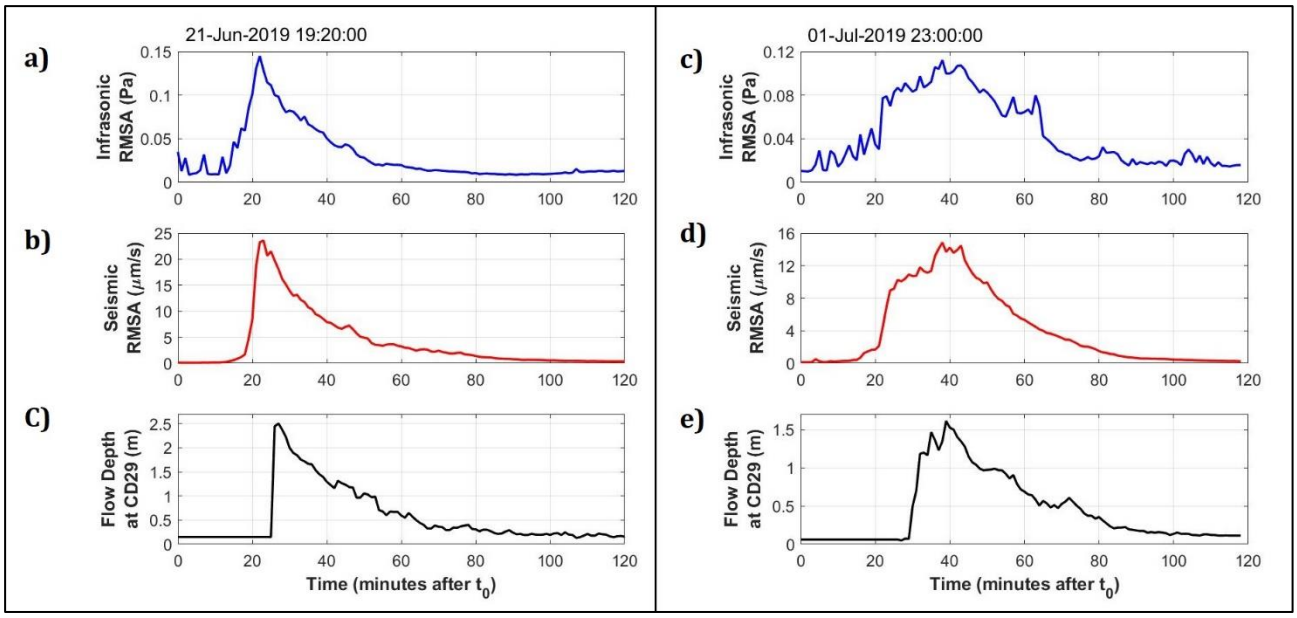

Figure 5. 21: infrasonic (a, d) and seismic (b, e) RMSA curves and the hydrograms (c, f) recorded at CD 29 during the 2019/06/21 (left) and the 2019/07/01 (right) debris-flow events.

Since the hydrograms are acquired at CD 29, near the end of the Illgraben channel, the infrasonic and seismic signals begin to be recorded before the flow depth at CD 29 exceeds the pre-event levels (Figure 5. 21). Indeed, it has been observed that the Illgraben debris flow radiate infrasonic and seismic signals already when they are still within the upper catchment or at least near its mouth [Marchetti et al., 2019], as also indicated by the infrasonic array processing results shown in Section 5.1.4. Therefore, the RMSA curves are systematically anticipated with respect to the hydrograms. In addition, the seismo-acoustic peak amplitudes are recorded when the barycentre of the debris flow is in the sector of the channel located at the minimum distance from the recording sensors [Marchetti et al., 2019], which for the Illgraben roughly corresponds to the sector between CD 16 and CD 22. This is in agreement with the infrasonic array processing results presented above (Section 5.1.4). Therefore, the seismo-acoustic RMSA peaks are supposed to be observed systematically before the peak of the hydrogram, acquired at CD 29.

Despite this systematic delay, for both the events, a strong resemblance in shape appears at a first glance between the seismo-acoustic RMSA and the hydrogram (Figure 5. 21).

The comparison between both infrasonic and seismic RMSA and the recorded flow depth, for both the events, is shown in Figure 5. 22.

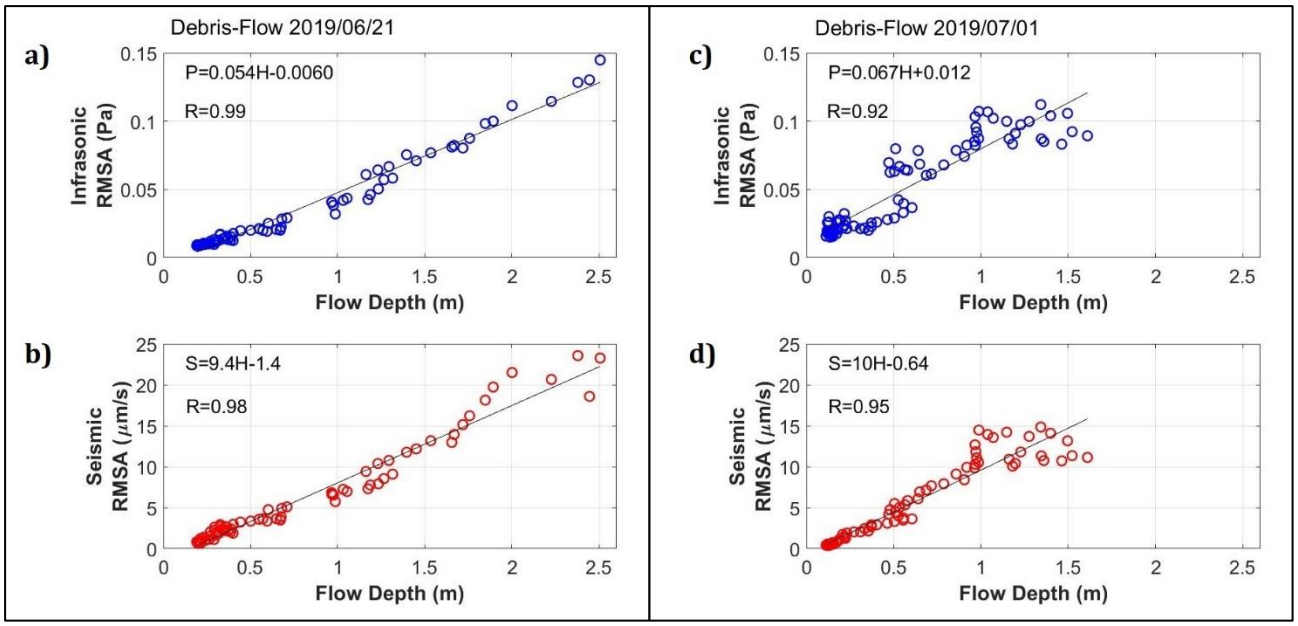

Figure 5. 22: comparison between infrasonic (a, c) and seismic (b, d) RMSA values with recorded flow depth, for the debris flow of 2019/06/21 (left side) and for the debris flow of 2019/07/01 (right side). The black lines in the panels represent the best fit regression lines, whose equations are written within the panels, where also the Pearson correlation factor (R) is reported. P and S are the infrasonic and seismic RMSA, respectively, and H is the flow depth.

To correct for the systematic delay of the hydrogram with respect to the seismo-acoustic signals of the same event, for each RMSA curve, only the values recorded after the peak were considered. The infrasonic and seismic amplitudes recorded before the RMSA peak are indeed not comparable to any recorded flow depth value, as they represent signals generated before the flow reached the channel sector characterized by the minimum source-to-receiver distance.

A positive linear relation resulted between seismo-acoustic RMSA and the recorded flow depth, for both events (Figure 5. 22), despite the relation is a bit perturbated for the 2019/07/01 event, especially in case of infrasound (Figure 5. 22 c). In particular, the linear relations are almost perfect for the 2019/06/21, both for infrasound and for seismic waves, as evidenced by the excellent Pearson correlation factors ($R = 0.99$ and $R = 0.98$ respectively).

The best fit regression lines were computed and their equations were determined. For the 2019/06/21 we get:

$$P(t) = 0.054 \frac{Pa}{m} \cdot H(t) - 0.0060\ Pa \qquad \text{(Eq. 5. 4)},$$

$$S(t) = 9.4 \frac{\frac{\mu m}{s}}{m} \cdot H(t) - 1.4\ \mu m/s \qquad \text{(Eq. 5. 5)},$$

where P and S are the infrasonic and seismic RMSA recorded over time (t), expressed in Pa and μm/s, respectively, and H is the flow depth recorded in time and expressed in m.
For the 2019/07/01 instead we get:

$$P(t) = 0.067\frac{Pa}{m} \cdot H(t) + 0.012\ Pa \qquad \text{(Eq. 5. 6)},$$

$$S(t) = 10\frac{\frac{\mu m}{s}}{m} \cdot H(t) - 0.64\ \mu m/s \qquad \text{(Eq. 5. 7)}.$$

The slope coefficients obtained in Eq. 5. 4-5. 7 (0.054 and 0.067 Pa/m for infrasound, 9.4 and 10 (μm/s)/m for seismic signals) are in agreement with the slope coefficients in Eq. 5.2 and Eq. 5. 3 (0.062 Pa/m and 9.0 (μm/s)/m) obtained for the relation between the seismo-acoustic maximum RMSA and the maximum flow depth, shown in Figure 5. 20. This suggests that the linear relationship observed between the maximum seismic-acoustic RMSA and the maximum depth values of the flow (Figure 5. 20) holds monotonically also for the non-peak values.
This outlies how the seismo-acoustic RMSA could be used to estimate in real time the flow depth of an occurring debris flow at Illgraben.

Seismo-acoustic maximum RMSA values were also compared with flow bulk density (Figure 5. 23), estimated from the weight measurements provided by the force plate deployed at CD 29 (see Section 3.4, Chapter 3). As the force plate measurements are available only since 2019, this comparison was possible only for 7 events and for 9 events, in case of infrasound and seismic signals, respectively.
Different from debris-flow front velocity and flow depth, in this case, no clear relations are observed between debris-flows density and both infrasonic and seismic maximum RMSA (Figure 5. 23).

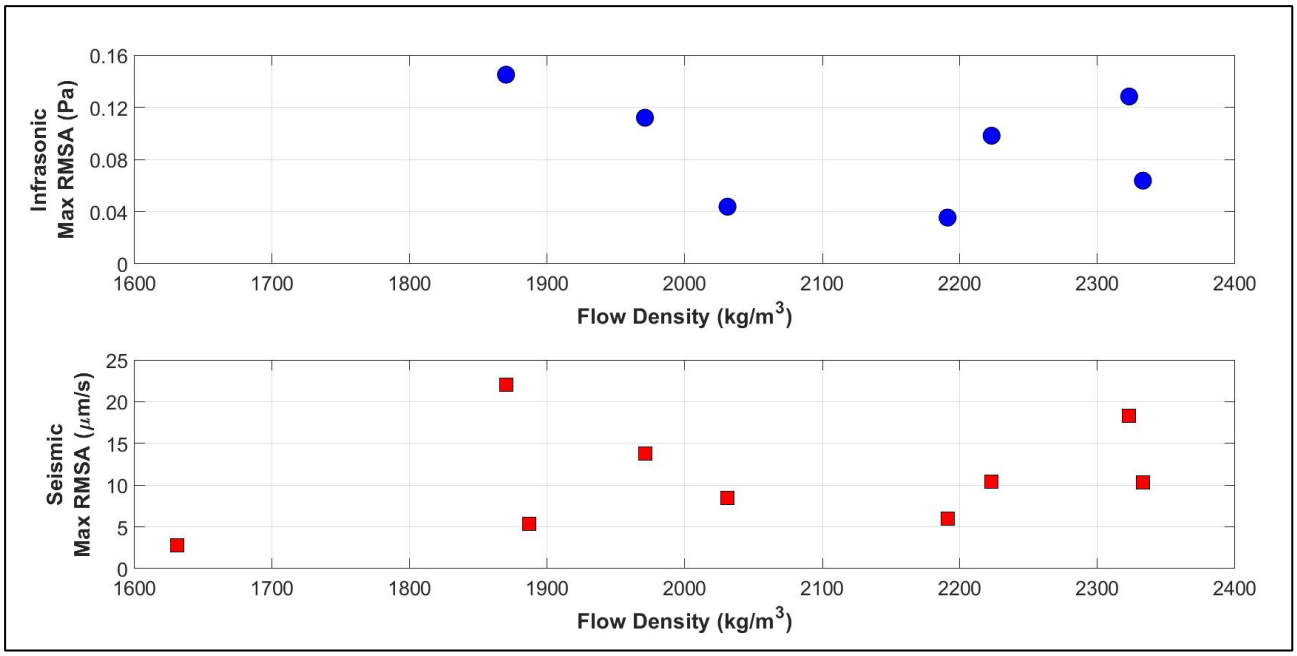

Figure 5. 23: comparison between debris-flow bulk density and infrasonic (a) and seismic (b) maximum RMSA. In both panels, no clear relations are observed.

This suggests that flow density does not significantly affect the amplitude of the infrasonic and seismic signals generated by debris flows. However, the limited number of density measurements available for this comparison prevents ruling out a primary influence of this parameter on the seismo-acoustic energy radiation by debris flows.

In light of the positive relations between seismo-acoustic amplitudes and both debris-flow front velocity (Figure 5. 19) and flow depth (Figure 5. 20, Figure 5. 22), the infrasonic and seismic maximum RMSA values were compared also with the flow peak discharge per unit channel width (Q_u, m^2/s). As described in Section 3.4 (Chapter 3), this parameter was computed by multiplying the velocity and the maximum depth values ($Q_u = v \cdot H_{max}$), and assuming a rectangular channel section, which is a good assumption for the Illgraben. With the assumption of a rectangular channel, the flow peak discharge per unit channel width is proportional to the peak discharge (m^3/s).
Results show that, as observed in the comparison with the maximum flow depth (Figure 5. 20), the maximum RMSA scales linearly with flow unit discharge, for both infrasonic and seismic signals (Figure 5. 24), with seismo-acoustic amplitudes increasing with increasing flow unit discharge.

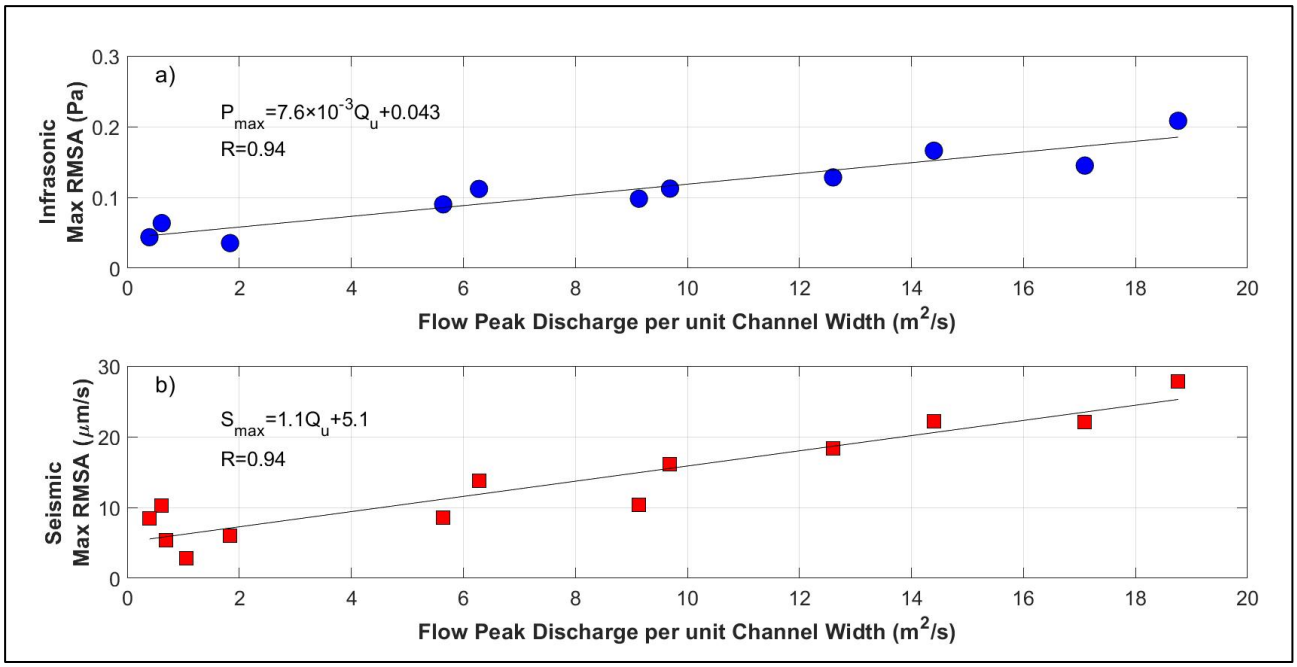

Figure 5. 24: comparison between debris-flow peak discharge per unit channel width (Q_u) and infrasonic (a) and seismic (b) maximum RMSA. A positive linear relation is observed in both panels. The black lines in both panels represent the best fit regression lines, whose equations are written within the panels, where also the Pearson correlation factor (R) is reported. P_{max} and S_{max} are the infrasonic and seismic maximum RMSA, respectively.

The linear trends are reflected in the high Pearson correlation factors ($R = 0.94$ for both the wavefields).

The best fit regression equations were determined as:

$$P_{max} = 0.0076\ \frac{Pa}{m^2/s} \cdot\ Q_u + 0.043\ Pa \qquad \text{(Eq. 5. 8)},$$

$$S_{max} = 1.1\ \frac{\mu m/s}{m^2/s} \cdot\ Q_u + 5.1\ \mu m/s \qquad \text{(Eq. 5. 9)}.$$

The seismo-acoustic maximum RMSA values were also compared with the debris-flow peak mass flux per unit channel width (MF_u) (Figure 5. 25), which was computed by multiplying the flow discharge per unit channel width and the flow density, as $MF_u = Q_u \cdot \rho$ (see Section 3.4, Chapter 3). In this case the comparison is possible only for 7 events for infrasound and for 9 events for seismic signals.

Similar to unit flow discharge (Figure 5. 24), the unit peak mass flux shows a linear relation ($R = 0.92$ for infrasound, $R = 0.89$ for seismic signals) when compared with seismo-acoustic maximum RMSA (Figure 5. 25).

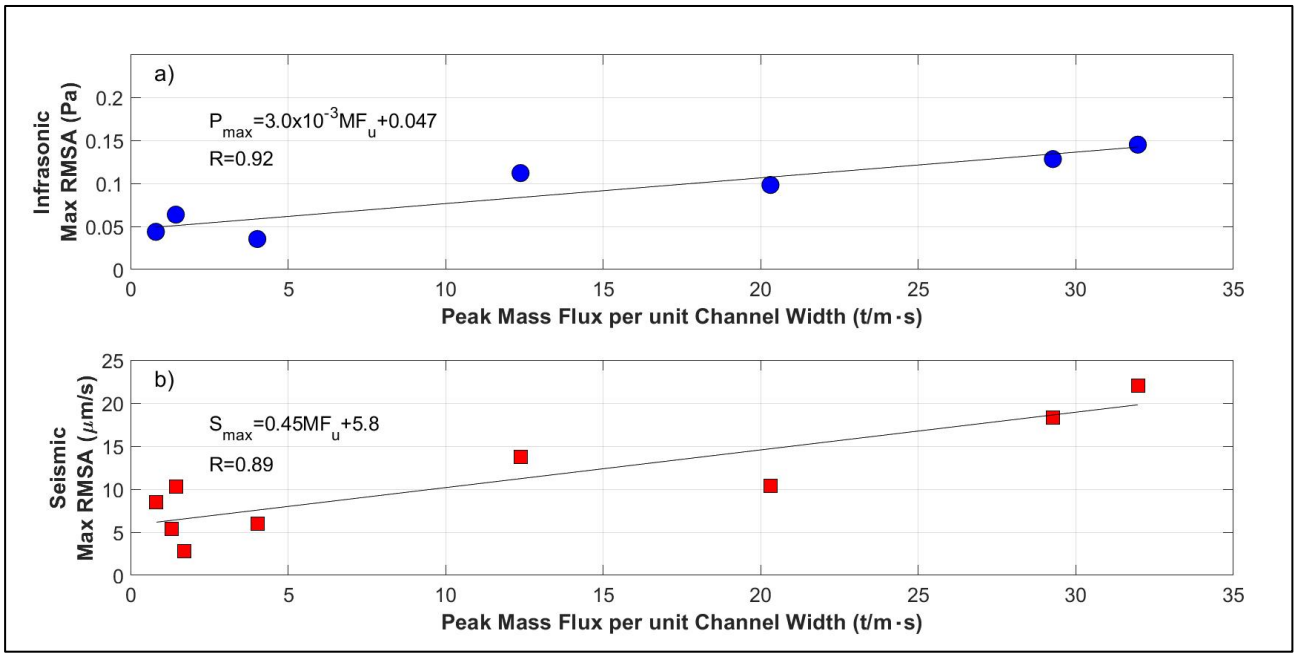

Figure 5. 25: comparison between debris-flow peak mass flux per unit channel width (MF_u) and infrasonic (a) and seismic (b) maximum RMSA. A positive linear relation is observed in both panels. The black lines in both panels represent the best fit regression lines, whose equations are written within the panels, where also the Pearson correlation factor (R) is reported. P_{max} and S_{max} are the infrasonic and seismic maximum RMSA respectively.

Also for these relations, the best fit regression equations were determined as:

$$P_{max} = 0.0030 \ \frac{Pa}{t/m{\cdot}s} \cdot \ MF_u + 0.047 \ Pa \qquad \text{(Eq. 5. 10)},$$

$$S_{max} = 0.45 \ \frac{\mu m/s}{t/m{\cdot}s} \cdot \ MF_u + 5.8 \ \mu m/s \qquad \text{(Eq. 5. 11)}.$$

The lower Pearson correlation factors derive from the combination of uncertainties linked to discharge and density estimations for selected events. Moreover, the lower number of available observations must be considered when evaluating the quality of the obtained relations, since they may not be so accurate.

In conclusion, the observed linear relations suggest that, for Illgraben debris flows, higher flow velocity, depth and discharge generate higher amplitude infrasonic and seismic signals. Furthermore, the experimental data were used to derive empirical relationships which can be useful for estimating the flow parameters only from seismic and infrasonic recordings of the events.

5.2.2 Comparison between seismo-acoustic peak frequency and flow parameters

To further investigate how flow parameters influence the radiation of seismo-acoustic signals by debris flows, the measured hydraulic and physical data were also compared with the frequency content of the infrasonic and seismic signals, in particular with the peak frequencies determined from computed PSD curves (see Section 4.2, Chapter 4 and Section 5.1.2, Chapter 5). This comparison was performed for all the debris-flow events for which the measured flow parameters (see Table 3. 1, Section 3.4, Chapter 3) and the computed seismo-acoustic peak frequency values (see Table 5. 2, Section 5.1.2) are available.

Figure 5. 26 shows the comparison between the seismo-acoustic peak frequencies and the debris-flow front velocity. The systematic difference between infrasonic and seismic peak frequencies, already highlighted in Section 5.1.2, is evident, with seismic peak frequency stable around 7.1 Hz (7.1 ± 0.2 Hz) for all the events regardless the front velocity, while the infrasonic one varies between 3.4 and 6 Hz, showing a general decrease with increasing front velocity.

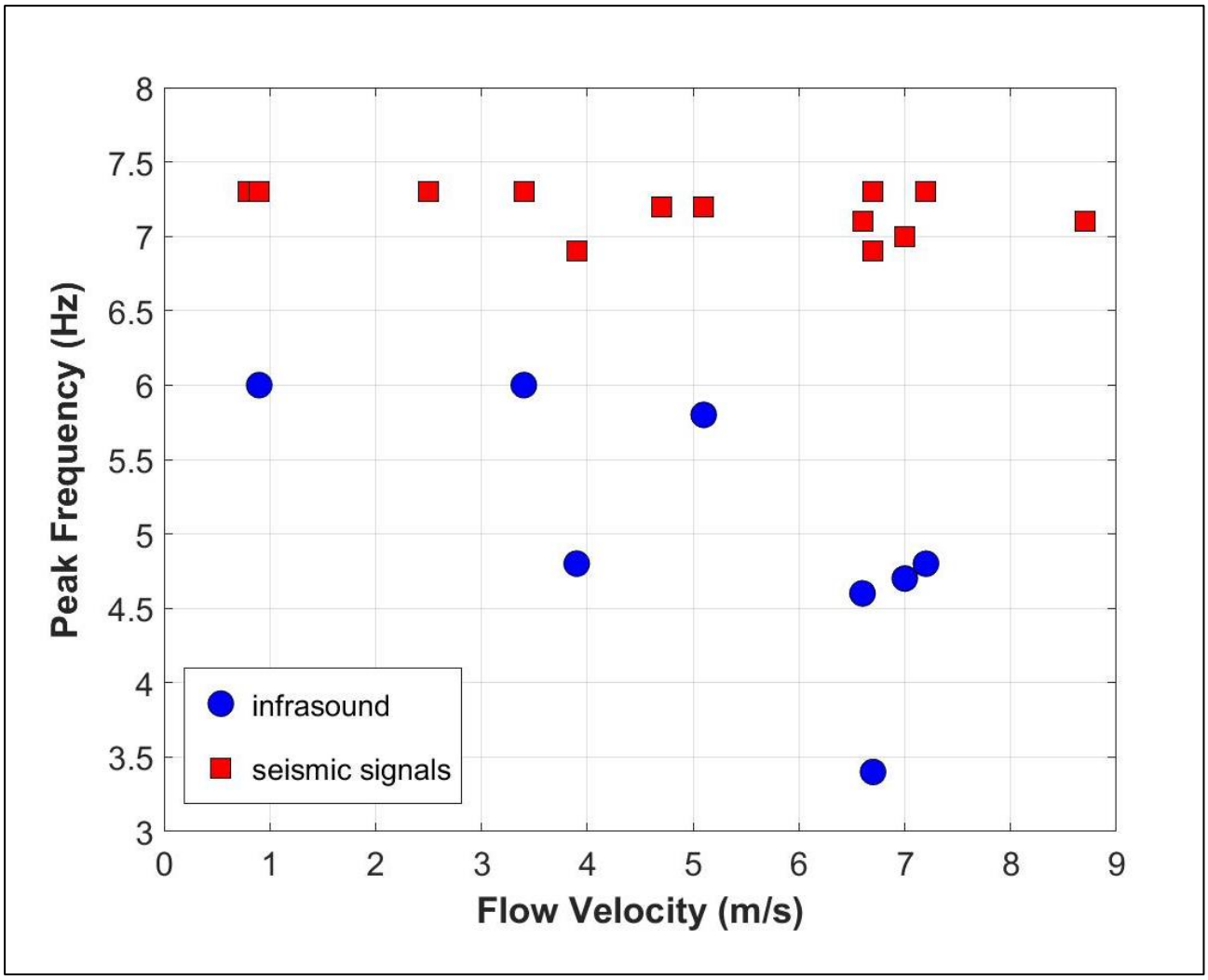

Figure 5. 26: comparison of infrasonic (blue circle) and seismic (red squares) peak frequencies with debris-flow front velocity.

A similar trend is also found when the seismo-acoustic peak frequencies are compared to the maximum flow depth of the debris-flow events (Figure 5. 27), with the seismic peak frequency appearing independent of the recorded maximum flow depth, while the infrasonic peak frequency scales inversely with the maximum flow depth (Figure 5. 27).

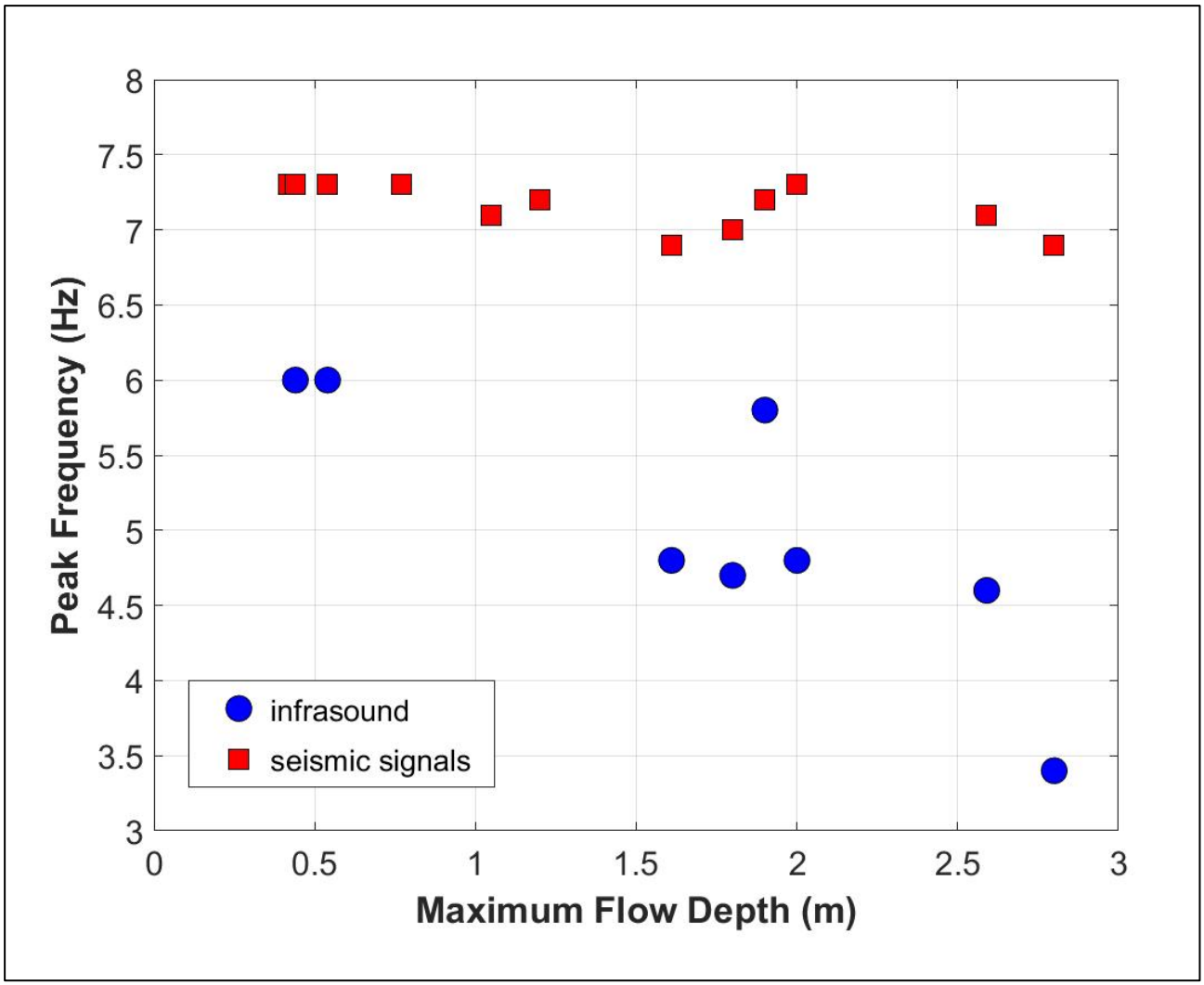

Figure 5. 27: comparison of infrasonic (blue circles) and seismic (red squares) peak frequencies with debris-flow maximum depth.

In contrast, no trend is observed when the seismo-acoustic peak frequencies are compared with flow bulk density (Figure 5. 28).

However, as already discussed for Figure 5. 23 (see Section 5.2.1), the limited number of observations greatly affects this comparison, preventing a thorough investigation.

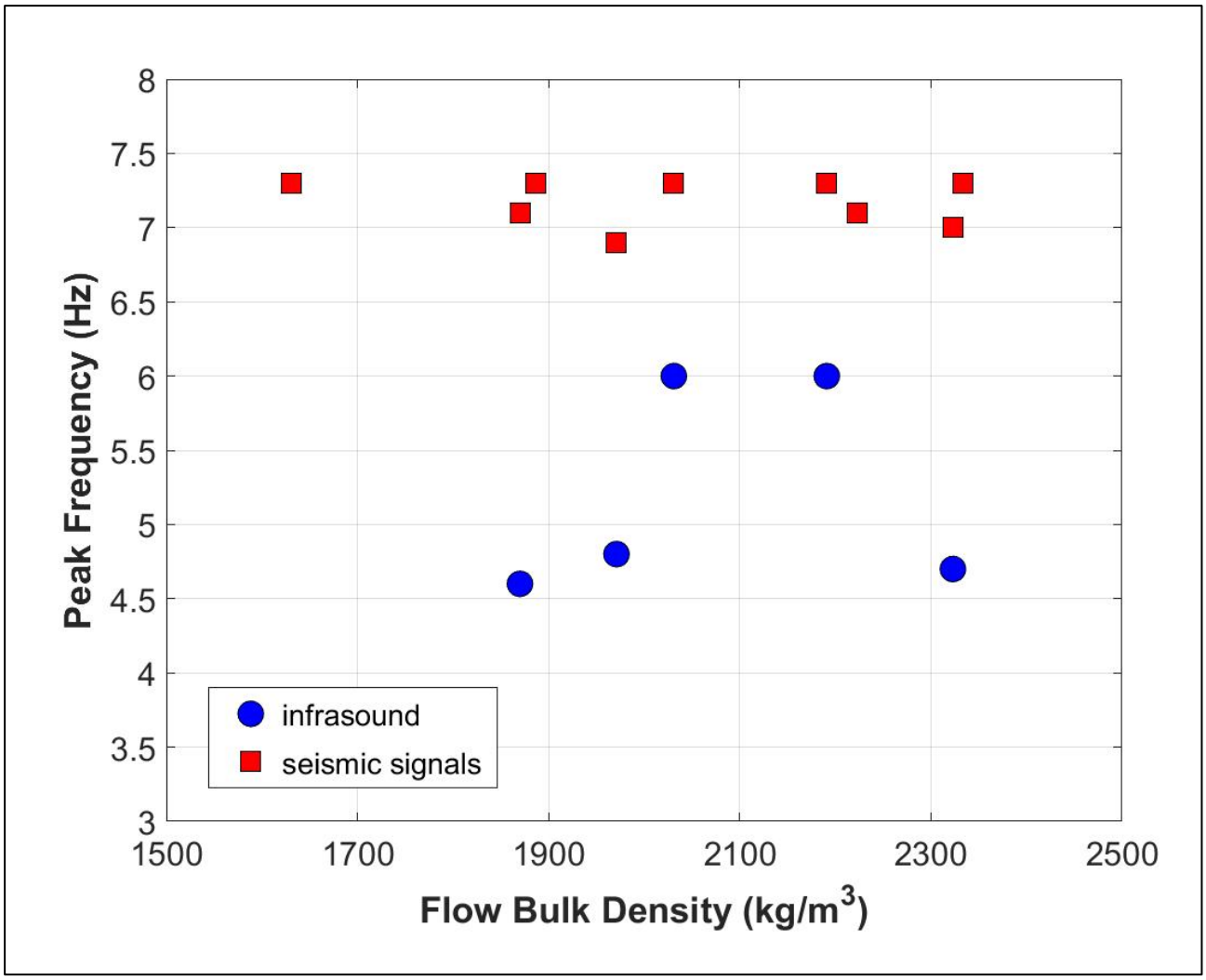

Figure 5. 28: comparison of infrasonic (blue circles) and seismic (red squares) peak frequencies with debris-flow bulk density.

The seismo-acoustic peak frequency values were also compared with the debris-flow peak discharge per unit channel width (Figure 5. 29).

The separation between infrasonic and seismic peak frequencies is evident also in this case. As expected in accordance with Figure 5. 26 and Figure 5. 27, the peak frequency of infrasonic signals scales inversely with flow unit discharge (Figure 5. 29).

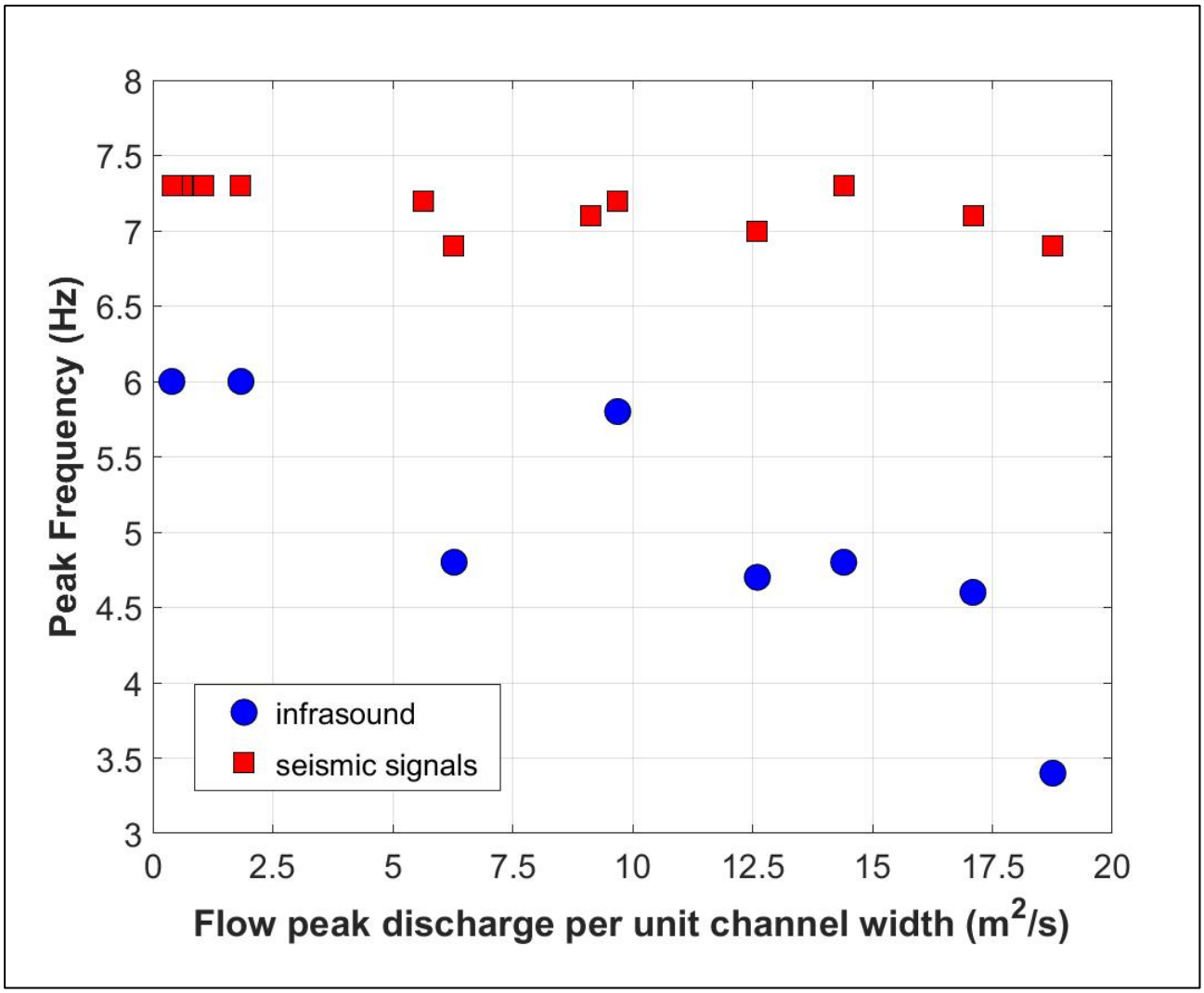

Figure 5. 29: comparison of infrasonic (blue circles) and seismic (red squares) peak frequencies with debris-flow peak discharge per unit channel width.

Chapter 6

Discussion

In this chapter we discuss the results presented in Chapter 5, highlighting what each experimental evidence reveals about the seismo-acoustic energy radiation by debris (Section 6.1 and Section 6.2), and present a source model for acoustic energy radiation both in the ground (seismic waves) and in the atmosphere (infrasound) (Section 6.3). In particular, the proposed source mechanism of the infrasonic waves in debris flows, which likely represent the most important new contribution of this thesis to the debris-flow research, is described in detail in Section 6.3.1. Finally, we discuss the implications for the debris-flow monitoring and warning (Section 6.4).

6.1 What does the seismo-acoustic analysis of the Illgraben debris flows reveal?

6.1.1 RMSA analysis of seismo-acoustic signals

The simple visual analysis of the infrasonic and seismic waveforms of the 18 debris-flow events, observed at the Illgraben in the period 2017-2019, shown above in Figure 3. 17 (Section 3.4, Chapter 3) and here shown again for convenience (Figure 6. 1), revealed a wide variability in the amplitudes and in the duration of the recorded seismo-acoustic signals, which probably reflects the large variability observed in the hydraulic/physical features of the Illgraben debris-flows.

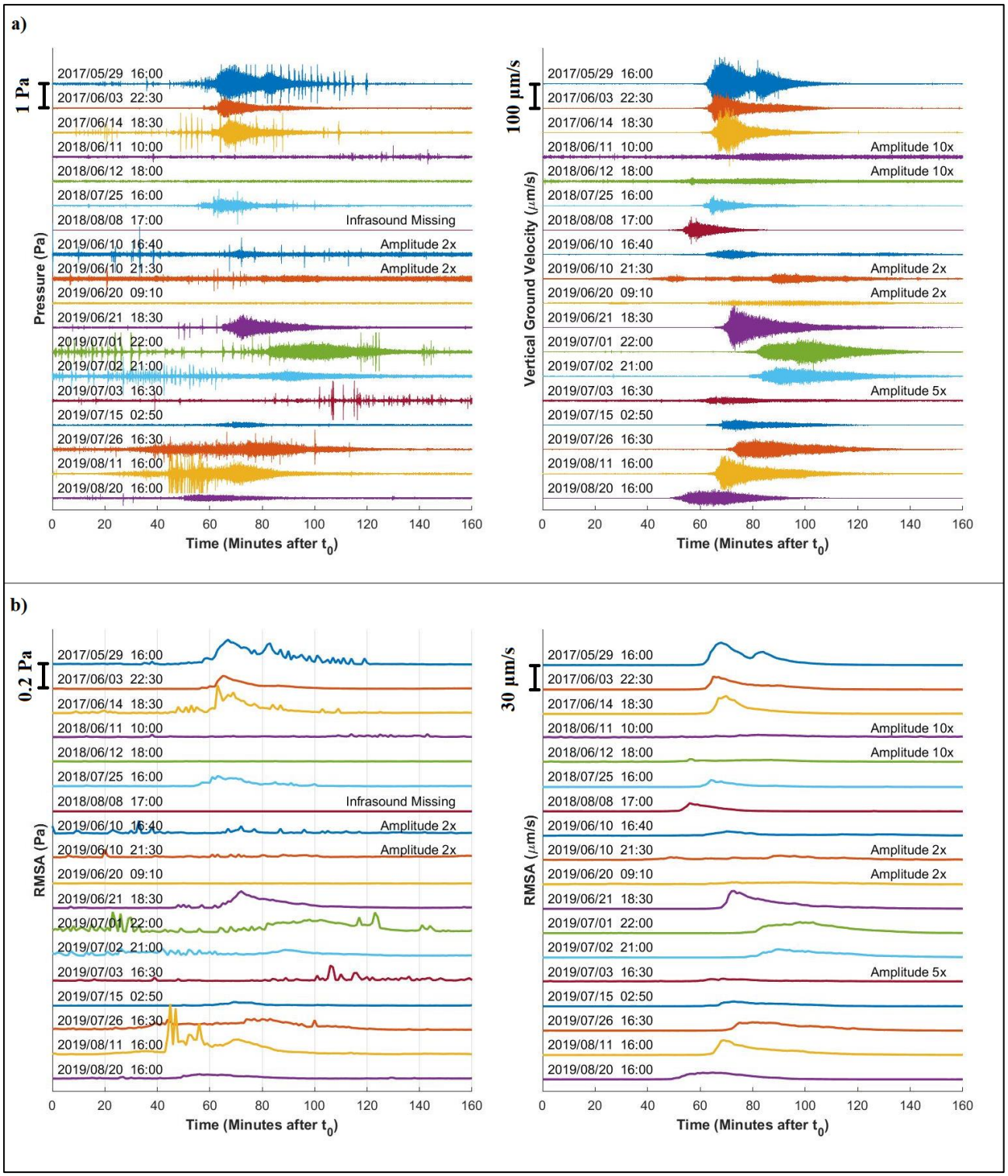

Figure 6. 1: infrasound (left) and seismic (right) waveforms of the 18 debris flow at Illgraben between 2017 and 2019 (a). Infrasound (left) and seismic (right) Root Mean Square Amplitude (RMSA) envelopes computed over 1-minute-long moving time windows for all 18 events (b). For all signals, timing is expressed in minutes after the time reported on the left of each trace. For some events, the waveform and the RMSA envelope have been multiplied by an integer factor (2, 5 or 10) for visualization purposes.

In addition, seismic signals, being distinguishable above background noise levels for all the 18 analysed events (Figure 6. 1 b), appear significantly clearer compared to infrasonic signals, not discernible for the 6 smallest events (Figure 6. 1 a). It seems thus that, also considering the local background seismic and acoustic noise levels, debris flows tend to generate higher signal-to-noise ratios for seismic signal than for infrasound. This appears true especially for the smaller debris-flow events, for which the generated infrasound is not able to overcome the background noise levels; compared to corresponding seismic signals, infrasound signals require larger debris-flow events to be able to overcome background noise levels and to be thus clearly recorded.

Seismo-acoustic signals were then analysed computing the root mean square amplitude during the entire duration of the events, as described in Section 4.1 (Chapter 4) and in Section 5.1 (Chapter 5). The computed RMSA curves, shown again in Figure 6. 1, are characterized by a marked asymmetry, with the rising ramp significantly shorter and steeper than the descending one. This likely results from the hydrodynamic features presented in Figure 3. 16, characterized by a sudden initiation, with the flow depth rising almost instantaneously from zero up to the 2-3 meters of the boulder-rich front, while gradually diminishing in the final phases of the event, gently returning to the background levels. This trend is recognised also in the infrasonic and seismic signals, within which the initial sharp increase is observed, despite being a bit dampened for site and propagation effects.

The comparison of maximum RMSA values shows a good match between infrasonic and seismic signals. In particular, in Figure 6. 2 a, matching debris-flows infrasonic and seismic maximum RMS amplitudes, it is observed that the recorded infrasonic and seismic maximum RMSA values of the various events follow a linear relationship, with higher (lower) infrasonic amplitudes corresponding to higher (lower) seismic amplitudes.

This linear interpolation is highlighted by the high Pearson correlation factor of 0.96, and indicates that for Illgraben debris flows, a stable ratio of ~0.0075 Pa/(μm/s) is observed between generated infrasound and seismic maximum RMSA, according to:

$$P_{max} = 0.0071 \frac{Pa}{\mu m/s} \cdot S_{max} + 0.0032\ Pa \qquad \text{(Eq. 6. 1).}$$

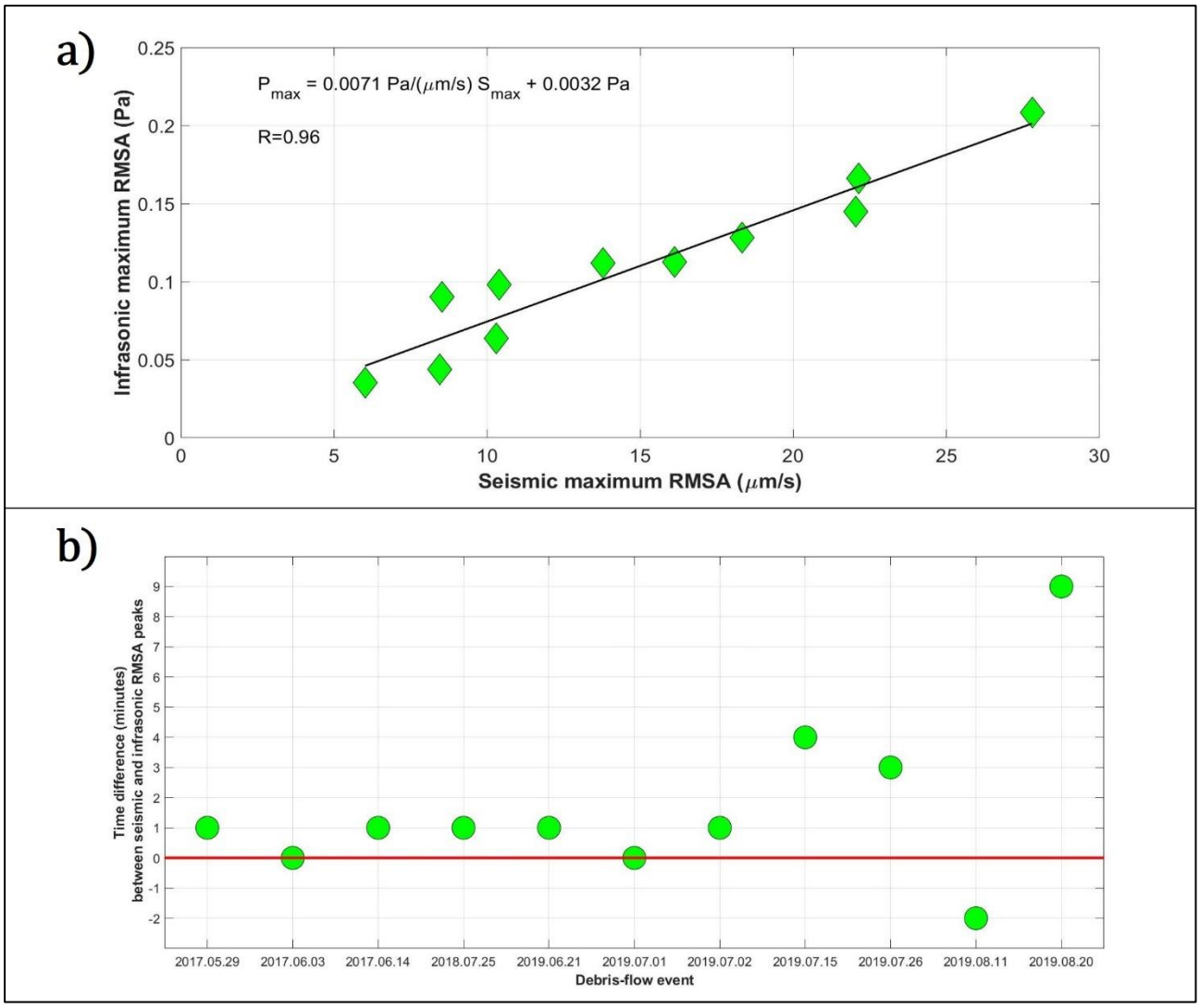

Figure 6. 2: a): relationship between infrasound and seismic maximum RMSA. The black line represents the best fit regression line, whose equation is written within the panel, where also the Pearson correlation factor (R) is reported. P_{max} and S_{max} are the infrasonic and seismic maximum RMSA, respectively. b): comparison between infrasonic and seismic RMSA peak times. The red line marks simultaneity of the seismo-acoustic peaks. Positive (negative) time differences indicate that the infrasonic RMSA maximum is recorded before (after) the seismic one.

Furthermore, the derived best fit relation (Eq. 6. 1) appears to be more accurate for higher seismo-acoustic amplitudes debris-flow events compared to lower amplitudes ones. This is to be expected considering that larger events likely generate stronger infrasound and seismic signals above background levels, resulting in a clearer seismo-acoustic amplitude relation.

In addition to this correspondence between the maximum amplitude values, a good matching is observed also in the timing of the infrasonic and seismic RMSA peaks (Figure 6. 2 b), with the time difference between peak values $\leq$ 1 minute for 8 out of the 11 analysed events. Considering the fact

that the seismo-acoustic RMSA curves are computed over 1-minute signal windows, so one value per minute is calculated, for these eight events the infrasonic and seismic RMSA can be considered as synchronous. Only for the 2019/08/20 debris-flow event this difference exceeds 5 minutes, with the peak of the infrasonic signal recorded at ILG array well in advance compared to the peak of the seismic signal at ILL13 seismometer (Figure 6. 2 b; positive (negative) time difference values indicate that the infrasonic RMSA maximum is recorded before (after) the seismic one).
The observed linear relation between infrasound and seismic maximum RMS amplitudes (Figure 6. 2 a), combined with the good correlation between their timing (Figure 6. 2 b), suggests that the radiation of infrasonic and seismic waves by debris-flows are related to each other and indicates that the two wavefield are likely generated by processes triggered, sustained and/or controlled by the same debris-flows dynamic processes and/or hydraulic parameter variations.

The emerged correlation between infrasonic and seismic energy radiation processes by debris-flows seems further confirmed by the results obtained from the analysis of the evolution over time of the ratio between infrasonic and seismic RMSA during the six larger debris-flow events at Illgraben in the period of analysis (see Section 5.1.1, Chapter 5).
In particular, results revealed that Illgraben debris-flow events share a similar trend of the infrasound-to-seismic RMSA ratio, as presented again in Figure 6. 3. For each event it is observed that the ratio always decreases in the ~10 minutes long initial phase of the debris flow. After the peak phase of the event is reached, the ratio remains constant and stable over time, always ~0.006-0.01 Pa/(μm/s) (or 0.6-1 cPa/(μm/s)) for all the events, until the end of the debris flow.

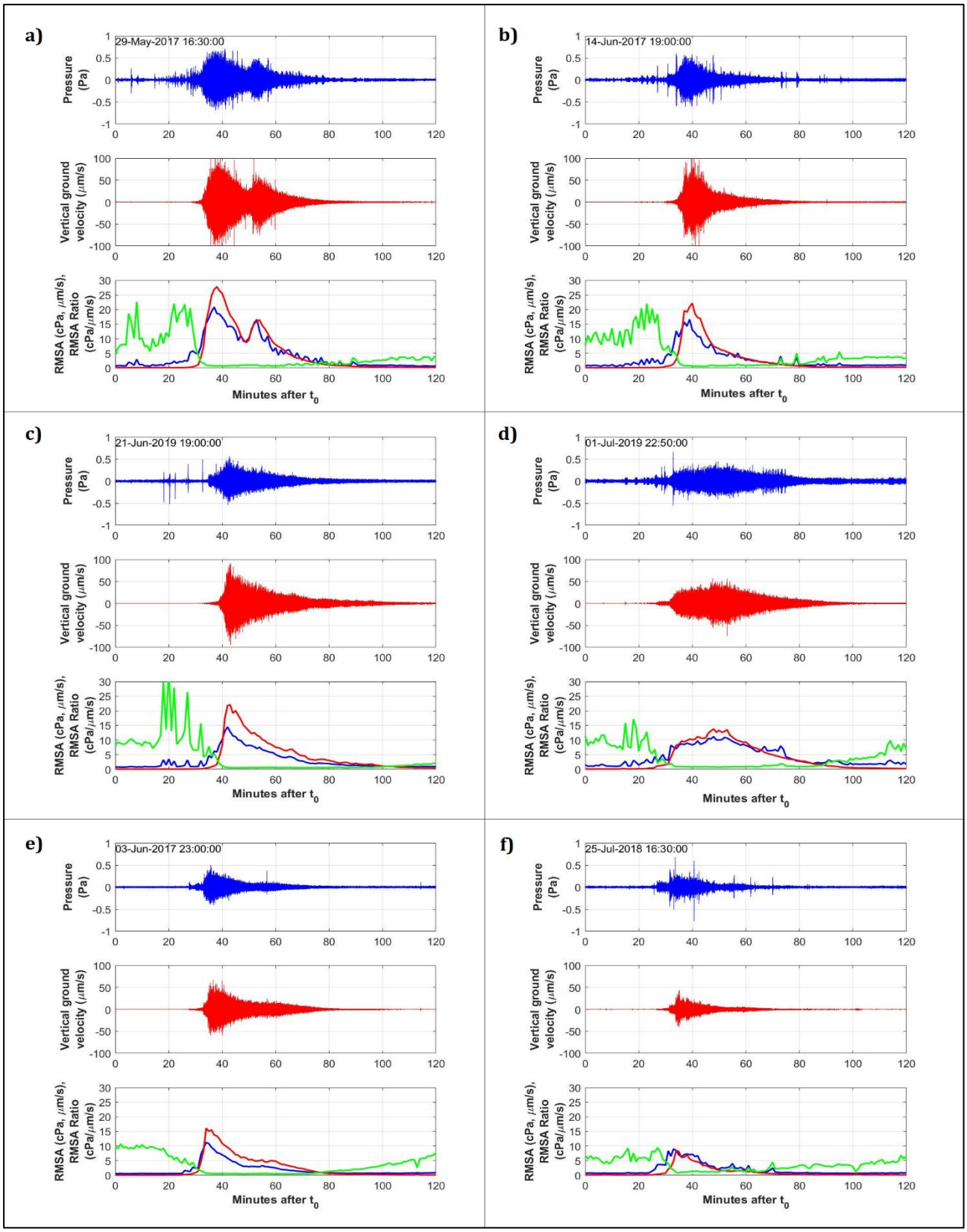

Figure 6. 3: infrasonic (blue) and seismic (red) RMSA analysis of the 6 major debris-flow events recorded at Illgraben between 2017 and 2019. The lower panel in each section shows both infrasonic (blue, cPa) and seismic (red, μm/s) RMSA, together with their ratio (green, cPa/(μm/s)).

Figure 6. 4 shows the infrasonic-to-seismic RMSA ratio time evolution computed for the 6 major debris flows at Illgraben in the investigated period.

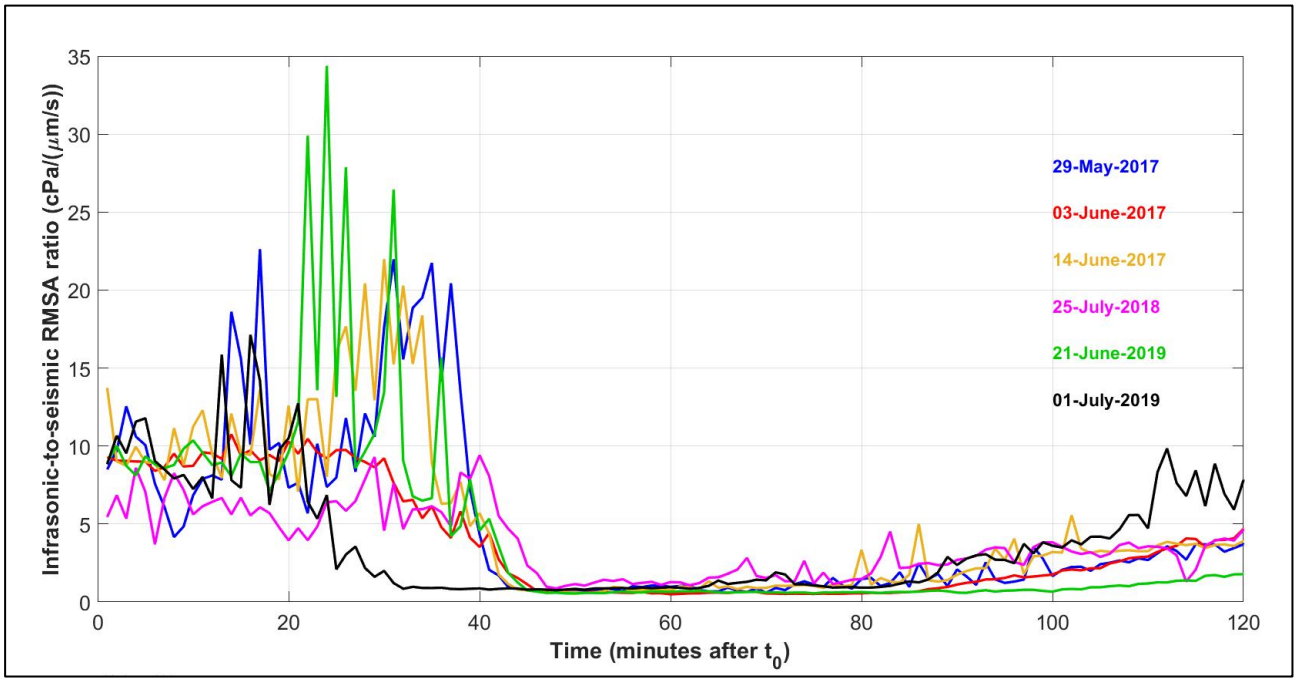

Figure 6. 4: evolution over time of the infrasound-to-seismic RMSA ratio computed for 6 higher seismo-acoustic amplitude Illgraben debris-flow events. The ratio remains constant in time (~0.75 cPa/(μm/s)) after the amplitude peak phase of each event. The dates of the events are reported in the figure in the same colour as the corresponding debris-flow RMSA ratio curve.

This constant infrasound-to-seismic amplitude ratio suggests that Illgraben debris-flow events are characterized by a characteristic succession of the seismo-acoustic energy generating processes, which tend to occur in the same order during each Illgraben debris-flow event. In particular, the decrease of the infrasound-to-seismic RMSA ratio observed in the initial phase of each debris-flow event (Figure 6. 4), indicates that, during this ~10 minutes long stage, seismic energy radiation into the ground grows faster and more effectively compared to infrasonic energy radiation in the atmosphere. This indicates that in the early stage of a debris-flow, once the infrasonic and seismic signals increase more rapidly, the seismic radiation processes are more energetic compared to the infrasonic ones. This is consistent with the hydraulic feature of a debris flow, in whose first stages the boulder-rich front, being associated to a more frictional flow mode and to more frequent and stronger impacts between transported solid particles and the riverbed, compared to other flow portions, represents the dominant source of the generated seismic signal and probably produce the higher energy seismic waves. A preferential energy radiation by the flow front, instead, is not

expected for the debris-flow infrasound, which, being radiated at the flow free surface, is believed to be independent of the processes acting at the flow-ground interface.

The stability of the infrasound-to-seismic RMSA ratio (~0.0075 Pa/(μm/s)), established for all events once the peak phase of each debris-flow event has been reached (Figure 6. 4), indicates that, during the debris-flow waning phase, the energy partition between the atmosphere and the ground is constant in time and equal to the one observed during the peak phase of the event.

The observed stable ratio value is also in agreement with the previously presented linear relationship between infrasonic and seismic maximum RMSA (Figure 6. 2 a), expressed by Eq. 6. 1 and characterized by an slope coefficient of 0.0071 Pa/(μm/s). This evidence suggests that the linear relation observed between the infrasonic and seismic amplitude at the debris flow peak phase, holds monotonously even during the non-peak phases.

Furthermore, in Figure 6. 4 it is observed that, in each debris-flow event, the RMSA ratio during the debris-flow is always significantly lower than its pre and post event values (~0.1 Pa/(μm/s)). Such evidence suggests that Illgraben debris-flows generate higher signal-to-noise ratios for seismic signals than for infrasonic signals.

Finally, the differences observed in Figure 6. 4 between the initial growing phase of the debris-flow event, marked by a decreasing infrasonic-to-seismic RMSA ratio and therefore suggesting a prevalence of the seismic source processes in this phase, and the waning phase of the event, when the stable ratio is observed, indicating a constant energy partition between the infrasonic and seismic sources, recalls the hysteresis pattern observed in river seismicity (see Figure 2. 2, Section 2.1, Chapter 2). Indeed, when compared to the flow depth or discharge recorded during a rainfall season or major storms, the seismic noise by rivers reveals a strong hysteresis, in which, for the same water level, the generated seismic amplitude is systematically higher at the beginning of the flood/rainfall season with respect to its end [Burtin et al., 2008; Hsu et al., 2011; Tsai et al., 2012]. This pattern has been explained considering the solid bedload transported by rivers, which depends not only on the water level/discharge but also by the sediment availability in the catchment. At the beginning of the flood/rainfall season, there is a higher availability of solid particles which, at the end of the event/season, have been instead partially removed by the river transport. As the solid particle collisions with the riverbed are considered one of the main source processes for the seismic noise by rivers, these differences in the sediment availability explain the observed hysteresis [Burtin et al., 2008; Hsu et al., 2011; Tsai et al., 2011].

The same reasoning can be extended to debris flows (Figure 6. 4). Here, most of the available sediments are taken up by the debris flow in its initial stages, also creating the boulder-rich snout, therefore leading to an enhancement of the seismic source process, mostly based on solid particle

collisions [Kean et al., 2015; Lai et al., 2018; Farin et al., 2019; Zhang et al., 2021]. In the final stages, instead, the flow transports fewer solid particles, thus weakening its seismic radiation.

6.1.2 Spectral analysis of seismo-acoustic signals

The spectral analysis of the generated infrasonic and seismic signals, described in Section 5.1.2 (Chapter 5), revealed that the two wavefields are characterized by different frequency contents as well as different peak frequency values. Indeed, while the seismic energy is distributed from ~1 Hz up to ~40 Hz (Figure 6. 5 b, d) and peaks around a stable value of 7.2 Hz, the generated infrasonic signals are limited to the ~1-10 Hz spectral window (Figure 6. 5 a, c), with peak values ranging between 3.4 and 6 Hz.

Furthermore, it is observed that while the recorded seismic peak frequency is almost constant and equal to 7.2 ± 0.3 Hz for all the events, the infrasonic peak frequency varies from event to event, between 3.4 and 6 Hz, and inversely scales with the recorded spectral amplitude, decreasing as the infrasonic spectral amplitude increases. This trend is evident also in Figure 6. 6, comparing the maximum RMSA and the peak frequency for both infrasonic and seismic signals.

A slightly inverse trend is perhaps observed also in case of seismic signals; however, the variation among the recorded peak frequency values is too small (≤ 0.6 Hz) to be considered significant (Figure 6. 6).

The constant recorded seismic peak frequency (6.9–7.3 Hz), regardless of the maximum amplitude (or spectral amplitude) of the recorded signal (Figure 6. 5 d, Figure 6. 6), is in accordance with the model proposed by Tsai et al. [2012] for seismic noise produced by bed load transport in rivers, that explains the recorded frequency content in terms of propagation effects of surface waves and that was observed to be valid also for debris flows [Lai et al., 2018] and also specifically for the Illgraben site [Wenner et al., 2019]. The models by Tsai et al. [2012] and Lai et al. [2018] predict that the peak frequency of the recorded seismic signals only depends on the minimum distance between the channel and the recording sensor, with seismic peak frequencies observed to systematically decrease with increasing distance from the source, due to higher seismic wave attenuation at higher frequencies.

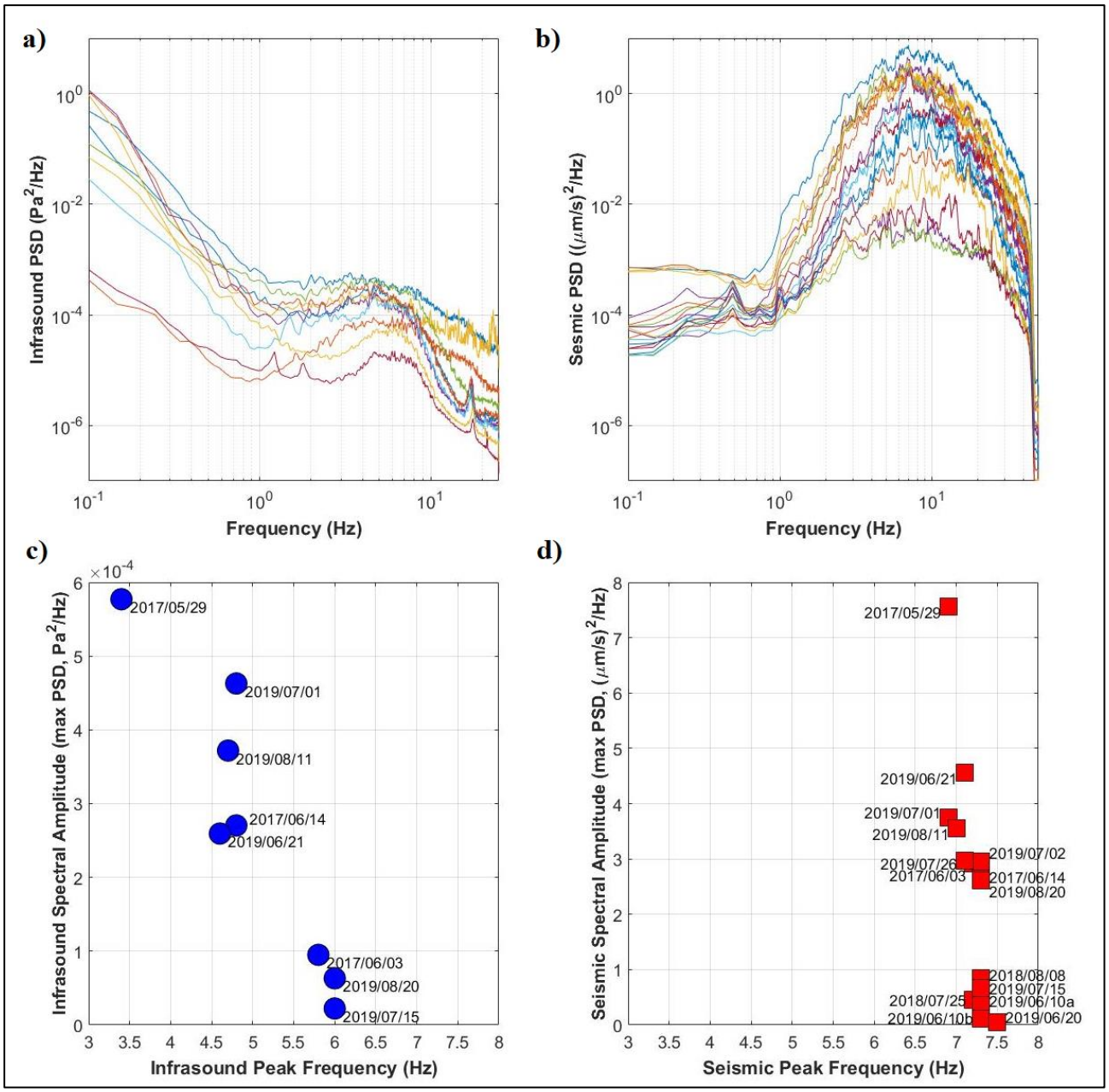

Figure 6. 5: power spectral density of infrasound (a) and seismic (b) records of the Illgraben debris-flow events. Spectral peak amplitudes of infrasonic (c) and seismic (d) signals as a function of peak frequencies. In (d) the two events on 2019/06/10 are marked in chronological order with the letters "a" and "b".

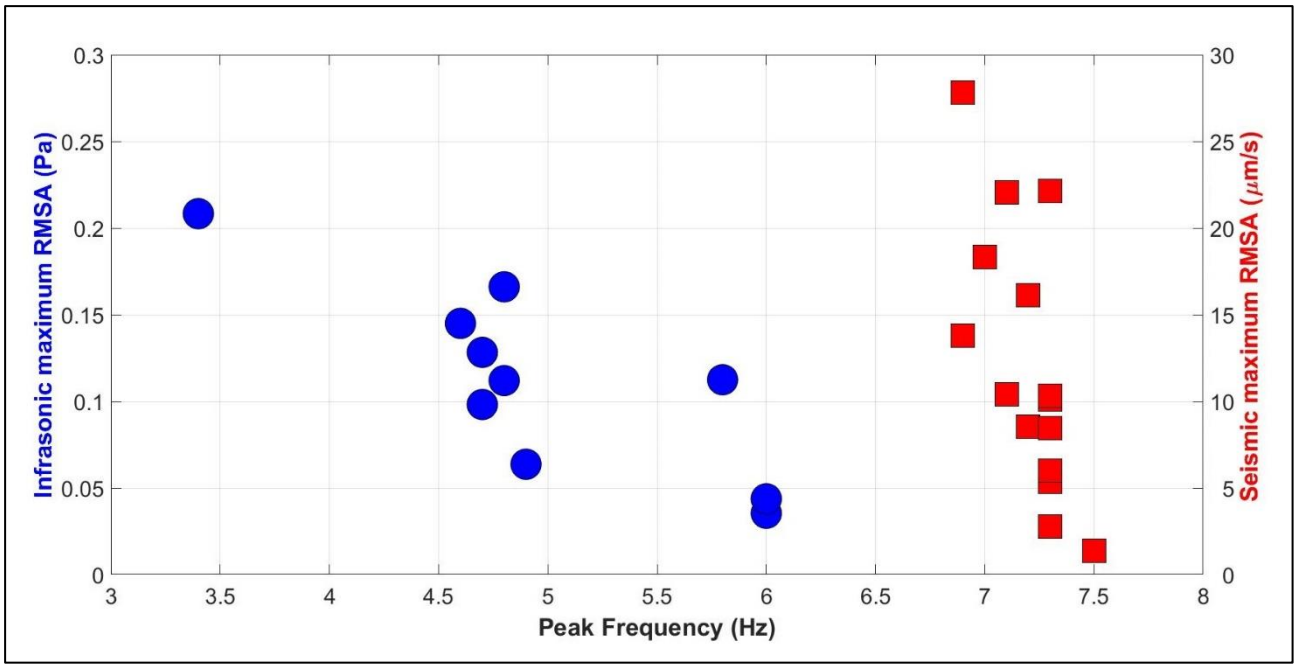

Figure 6. 6: comparison between signal peak frequency and maximum RMSA for both infrasonic (blue) and seismic (red) signals.

The measured value of ~7 Hz is in good agreement with the minimum distance of ≈550 m between the ILL13 seismometer and the Illgraben channel [Tsai et al., 2012; Belli et al., 2022].

In contrast, infrasonic peak frequency varies from event to event and appears to systematically decrease with increasing infrasonic maximum amplitude (RMSA or spectral amplitude). This inverse relation suggests that the higher the infrasonic amplitude radiated by the debris flow the lower the produced infrasonic frequency.

This hypothesis is confirmed also in the spectrogram of the infrasonic signals generated by Illgraben debris flows (see Section 5.1.2, Chapter 5), where a progressive depletion in the lower frequencies is observed during the post-peak, decreasing phase of the event (Figure 6. 7). As the magnitude (flow depth and/or discharge) of the event and the amplitude of the generated infrasound decreases, the recorded infrasonic peak frequency progressively increases.

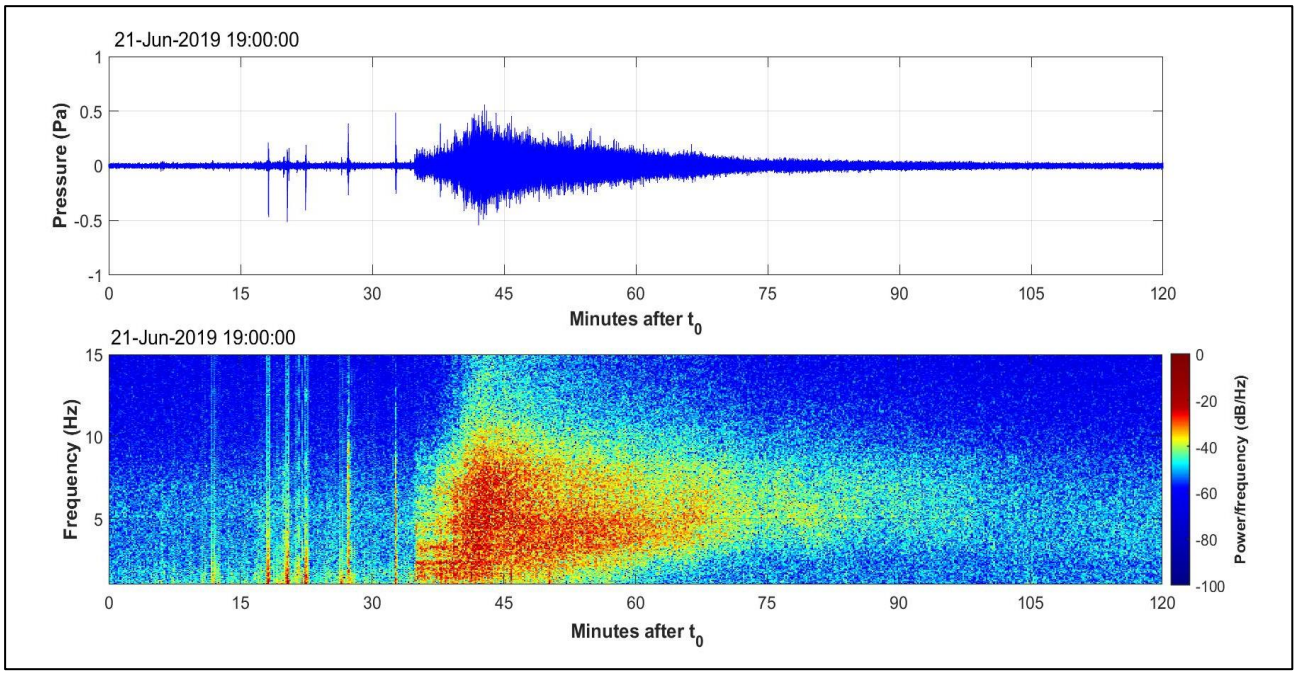

Figure 6. 7: detail of the spectrogram (bottom panel) of the infrasonic signal (top panel) generated by the 2019/06/21 Illgraben debris-flow event. In the spectrogram (bottom panel), the spectral amplitude is indicated by the colour bar on the right.

The spectral differences that resulted between the infrasonic and seismic signals (Figure 6. 5 and Figure 6. 6) are not imputable to propagation effects. Indeed, the infrasonic frequency content is expected to be preserved almost unchanged in the wave propagation over the distance of 550-1300 m separating the Illgraben channel from the recording sensors. For seismic waves, instead, a preferential depletion of the higher frequencies, due to anelastic dumping, is predicted during the wave propagation in the ground, which is a more inhomogeneous medium compared to the air.

In addition, the constant recorded seismic peak frequency is not imputable to sites effects, such as seismic amplification phenomena. To confirm that, the horizontal to vertical spectral ratio (HVSR) [Martorana et al., 2018] was computed on 3 hours of seismic background noise recorded by the ILL13 seismic station on 10/05/2021 (Figure 6. 8), where no significant seismic activity was recorded at this station. The HVSR curve (Figure 6. 8 b) was computed as the ratio between the sum of the spectra of the two horizontal seismic components (black and grey in Figure 6. 8 a) and the spectrum of the vertical one (red in Figure 6. 8 a). Results highlight peaks at ~1.7 Hz and ~3.6 Hz, with secondary peaks around 2 Hz and 4.3 Hz.

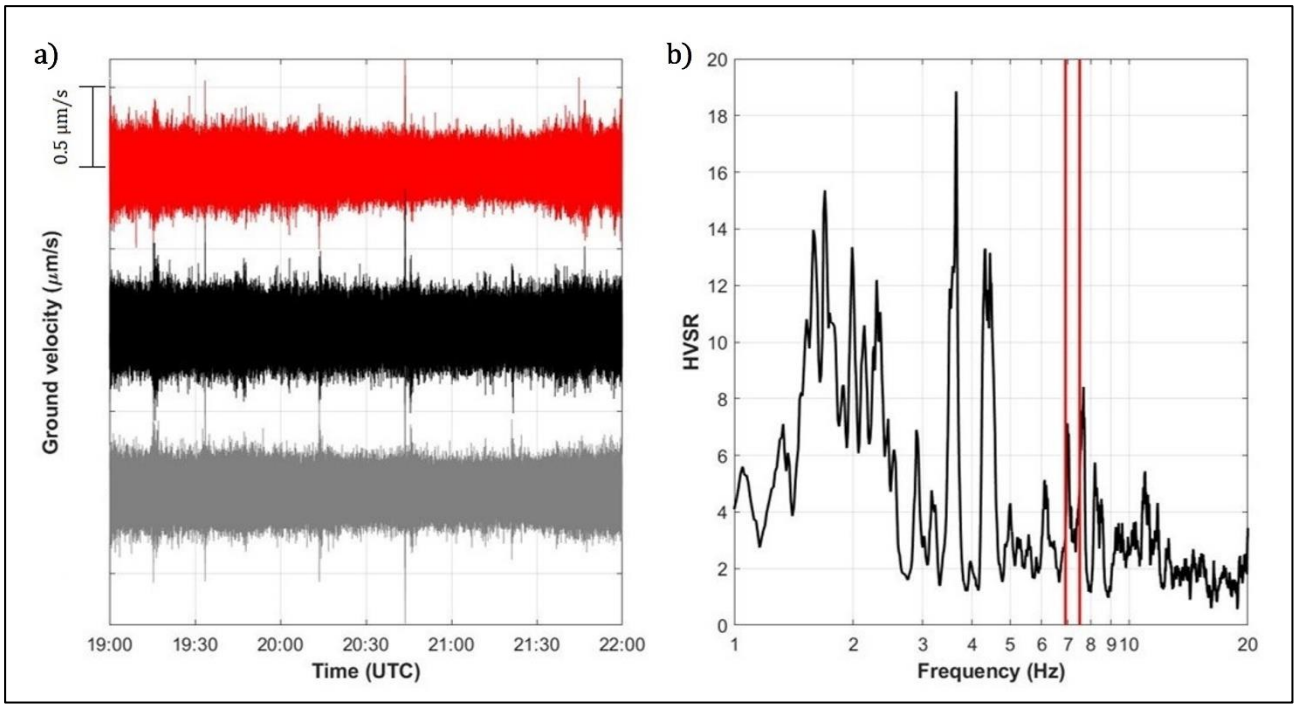

Figure 6. 8: HVSR (b) computed on 3 hours of background noise (a) recorded at ILL13 seismic station on 10/05/2021. Vertical (red), North-South (black) and East-West (grey) seismic components (a). The vertical red lines in b mark the range of the recorded debris-flow seismic peak frequencies (6.9-7.5 Hz), which is well far from the HVSR peaks observed at ~1.7 Hz and ~3.6 Hz.

The peak of the HVSR (f_{HVSR}) can be used to estimate the depth of bedrock, i.e. the thickness of the resonant sediment layer (T_s) [Martorana et al., 2018], according to:

$$T_s = \frac{c_s}{4 f_{HVSR}} \qquad \text{(Eq. 6. 2)},$$

where c_s is the velocity of seismic shear waves.

Assuming $c_s \approx 800$ m/s, which is a reasonable value for a rather compact rocky conoid like the Illgraben debris fan [Wills et al., 2000], the observed peaks at 1.7 Hz and 3.6 Hz give a thickness of the sediment layer of ~120 m and ~60 m, respectively. These values are in good agreement with the morphology of the Illgraben debris fan, given the altitude difference of~130 m between the ILL13 seismometer and the Rhone riverbed, and thus testify for the accuracy of the presented HVSR analysis.

The range of the recorded seismic peak frequency (6.9-7.5 Hz, between the red lines in Figure 6. 8 b) is well apart from the main HSRV peak. This allows to exclude the seismic amplification from the causes of the observed constant peak frequency of the Illgraben debris-flow seismic signals, which

thus likely only results from its dependence on the minimum source-to-receiver distance [Tsai et al., 2012; Wenner et al., 2019].

Therefore, in conclusion, despite the evident correspondence observed between the amplitude of the recorded infrasonic and seismic signals (Section 6.1.1), their different spectral contents and different peak frequencies reveal that the two wavefield are generated by different, decoupled source processes simultaneously acting within the debris flows.

6.1.3 Seismo-acoustic cross-correlation analysis

To further investigate the relation between infrasonic and seismic debris flow signals, the cross-correlation analysis was performed between recorded infrasonic and seismic signals (see Section 5.1.3, Chapter 5). The analysis revealed that a high seismo-acoustic cross-correlation is observed during the debris-flow events (Figure 6. 9).

Despite the spectral analysis highlighted that the infrasonic and seismic signal radiated by the flow are decoupled, the evident seismo-acoustic cross-correlation observed during the debris flow suggests that the two wavefields are to some extent correlated with each other. In particular, the infrasonic and seismic signals generated by Illgraben debris flows are equally modulated in amplitude during the event (i.e. the seismo-acoustic amplitudes vary in the same way during the event). This is in agreement with the positive correspondence between the recorded infrasonic and seismic amplitudes, highlighted by the linear relation between the maximum infrasonic and seismic RMSA shown above in Figure 6. 2 (Section 6.1.1).

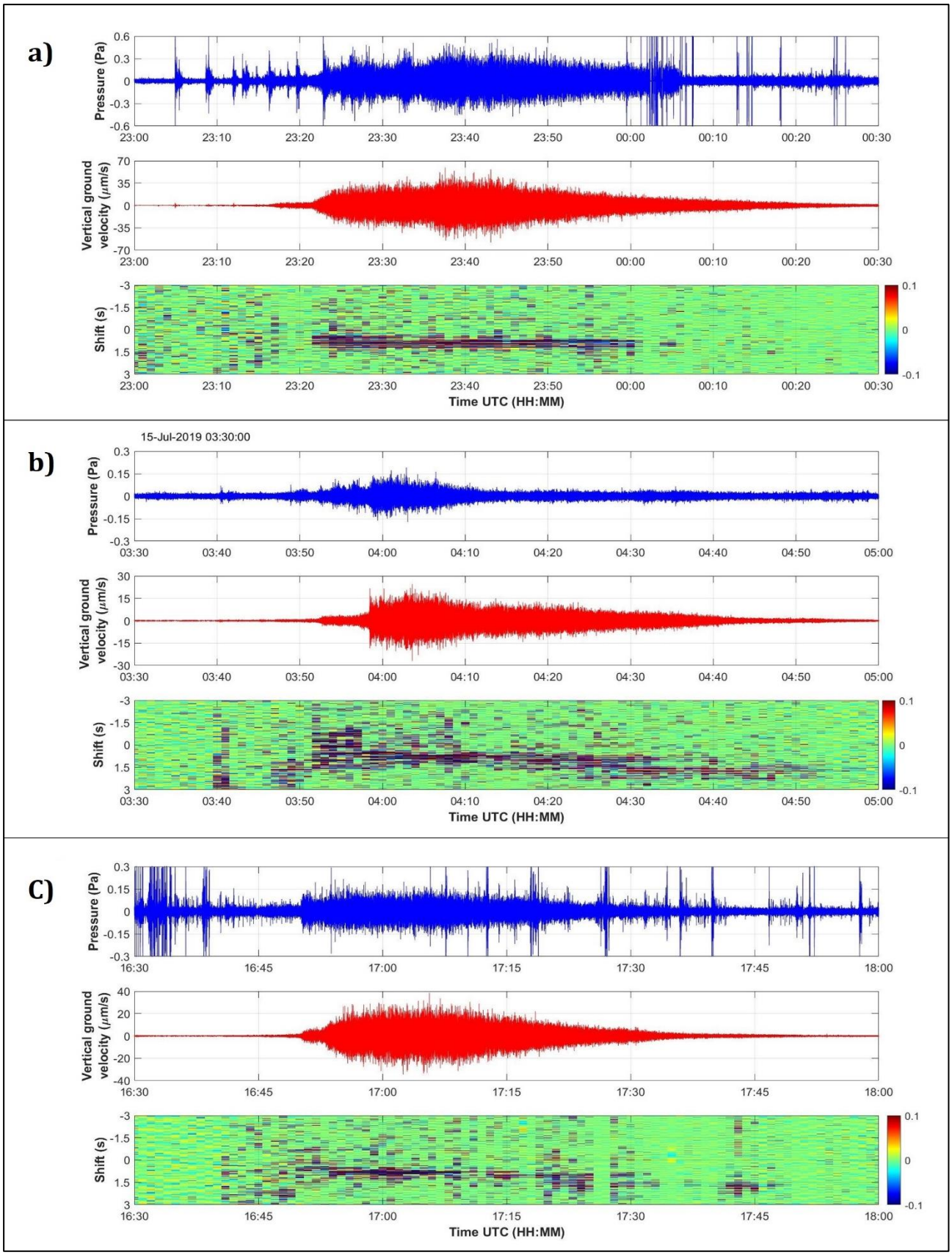

Figure 6. 9: cross-correlation (bottom) between infrasonic (top) and seismic (middle) signals during the 2019/07/01 (a), 2019/07/15 (b) and 2019/08/20 (c) Illgraben debris-flow events. The values of the cross-correlation function are indicated by colours, as shown in the colour bars.

Further details emerge from the location of the maximum of the cross-correlation function, which during the main part of the event is always observed at shift values around + 0.8 s. The positive sign of the shift values indicates that the seismic signal precedes in time by 0.8 s the cross-correlated infrasound component. This value is almost constant during the entire event for the 2019/07/01 debris flow (Figure 6. 9 a), while it significantly varies during the 2019/07/15 event (Figure 6. 9 b) and, to a lesser extent, during the 2019/08/20 event (Figure 6. 9 c).
The variable shift allows to exclude that the observed intense seismo-acoustic cross-correlation is produced by the coupling between the seismic and infrasonic signals at the recording station. Indeed, according to Eq. 4. 6 (see Section 4.3, Chapter 4), in case of an effective seismo-acoustic coupling, given the characteristic frequency of the incident seismic wave of 6.9-7.5 Hz, the maximum of the cross-correlation function would have been stable at shift values around 0.035 s. This value is one order of magnitude lower (more than 20 times lower) than the recorded shift, indicating that the seismo-acoustic coupling does not appreciably affect the recorded seismic and infrasonic signals.

The observed delay between the seismic signal and the cross-correlated infrasound instead results solely from the different propagation velocities of the two wavefields. Indeed, the seismic signal generated by solid particle transport in rivers and debris flow is dominated by surface seismic waves [Tsai et al., 2012; Kean et al., 2018], which, in a rather compact rocky conoid like the Illgraben debris fan, are expected to travel at a velocity (c_{ss}) of ~700 m/s [Wills et al., 2000]. The infrasound instead propagates in the air at the speed of sound (c), which, at sea level, is ~340 m/s [Kirtskhalia, 2012]. The seismo-acoustic cross-correlation analysis here discussed compares, in every moment, the infrasonic and seismic signal components recorded with the higher amplitude. The debris flow is an extended source, radiating infrasonic and seismic waves along its entire length [Marchetti et al., 2019]. The recorded seismo-acoustic amplitudes depend both on the magnitude (depth and/or discharge) of the flow and on its distance from the recording sensors [Belli et al., 2022]. In agreement with Marchetti et al. [2019], who observed that the barycentre of the debris flow dominates the amplitude of the generated seismo-acoustic signals, we can assume that, in every moment, the recorded main components of the infrasonic and seismic waves are radiated approximately from the same section of the debris flow, roughly corresponding to its barycentre. Given the different propagation velocities, the infrasonic and seismic waves generated by the same portion of the debris flow are recorded, at the central element of the ILG array and at the collocated ILL13 seismometer, respectively, with slightly different times. In particular, the delay time (Δt_{s-i}) between the seismic signal and the infrasound depends on the source-to-receiver distance as:

$$\Delta t_{s-i} = r\left(\frac{1}{c} - \frac{1}{c_{ss}}\right) = r\left(\frac{1}{340\ m/s} - \frac{1}{700\ m/s}\right) \qquad \text{(Eq. 6. 3)}.$$

The time delays (shift values) measured in the seismo-acoustic cross-correlation can thus be used to estimate the source-to-receiver distance, which in our case is assumed equal to the distance between the recording sensors and the portion of the channel where, in that specific moment, the debris flow is radiating the main component of the recorded infrasonic and seismic signals. Since the flow moves downhill, r is not fixed but varies during the event.

Figure 6. 10 shows how the source-to-receiver distance varies along the Illgraben channel between CD 1 and CD 30: r varies between a minimum of ~550 m (darkest blue), observed in the channel sector approximately around CD 22, to a maximum of ~ 1700 m (darkest red), where the Illgraben stream flows into the Rhone River (Figure 6. 10). In addition, the source-receiver distance is always ≤600 m over the entire ~1-kilometre-long channel sector between the point A in Figure 6. 10, located ~150 m downstream CD 16, and the point B, located ~200 m downstream CD 22.

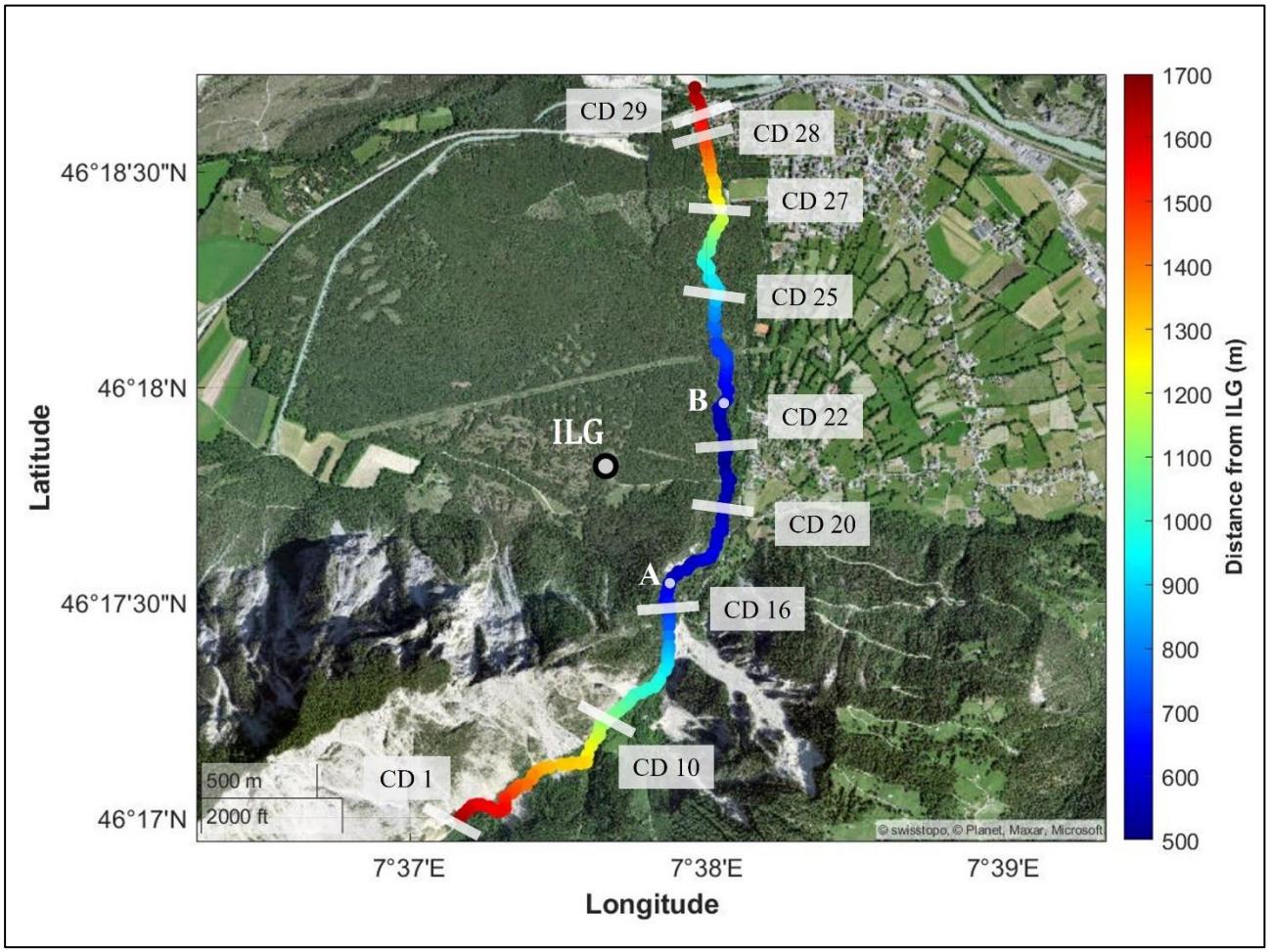

Figure 6. 10: map of the Illgraben channel between CD 1 and CD 30 showing the distance between the channel and the central element (m4) of the ILG array (grey circle), where also the ILL13 seismometer is located. The

distance is indicated by colours, as shown in the colour bar alongside. The light grey bars indicate the locations of some of the main check dams. Points A and B delimit, respectively upstream and downstream, the channel sector characterized by a distance from the sensor m4 ≤ 600 m.

According to Marchetti et al. [2019], the maximum seismo-acoustic amplitudes are generated when the barycentre of the debris flow is at the minimum distance from the recording sensors, which in our case is ~550 m. Putting this value into Eq. 6. 3, we get a predicted recording time difference between the seismic signal and the infrasound equal to 0.83 s. This value is in agreement with the shift value observed in the cross-correlation analysis during the debris-flow phase corresponding to the maximum recorded seismo-acoustic amplitudes (0.8 s; Figure 6. 9), although the uncertainty associated with the estimation of the velocity of the surface seismic waves is to be considered. Therefore, the shift values resulting from the cross-correlation analysis suggest that the high seismo-acoustic cross-correlation, recorded during the debris flow, is supported by the correlation between the primary seismic and infrasonic signals produced roughly in the same portion of the channel.

In the light of this evidence, we will now discuss the variation of the shift value corresponding to the maximum of the seismo-acoustic cross-correlation observed during the debris flows of 2019/07/15 (Figure 6. 11) and, to a lesser extent, of 2019/08/20.

During the 2019/07/15 event, the maximum of the cross-correlation function gradually migrates over time, passing from the shift values ~1.5 s observed at the very beginning of the event (03:46-03:50 UTC), to the ~ 0.8 s observed in the peak phase of the event (~ 04:00-04:10 UTC), to ~1.3 s around 04:25, to ~1.8 s between 04:30 and 04:45, and finally to ~ 2.3 s, observed during the final stages of the event (after 04:45) (Figure 6. 9 b, Figure 6. 11 c). This indicates a variation in the delay between the recording time of the seismic signal and the cross-correlated infrasound, consisting of a decrease in the time delay in the first phases of the event, until the peak phase of the event is reached, followed by a gradual increase after the peak phase.

This trend is to be expected considering the motion of the debris flow along the Illgraben channel. Indeed, in the first phases of the event, the debris flow, coming from the upper catchment, approaches the recording site, so that the source-to-receiver distance progressively decreases (Figure 6. 10, Figure 6. 11 e). In this phase, the cross-correlation maximum is observed at shift values around 1.5 s: using Eq. 6. 3, this shift gives a source-to-receiver distance of ~ 1000 m, which corresponds to the channel sector located right at the end of the upper catchment (Figure 6. 11 e). The gradual decrease of the propagation distance of the seismo-acoustic signals determines the migration of the maximum of the cross-correlation function towards lower shift values observed in the initial phase of the event. This persists until the debris flow enters the channel sector characterized by the minimum source-to-

receiver distance of 550-600 m (between points A and B in Figure 6. 11). In this phase, corresponding to the phase of maximum seismo-acoustic amplitudes, the delay time obtained from the seismo-acoustic cross-correlation is ~0.8 s and agrees with the 550-600 m distance from the seismo-acoustic sensors.

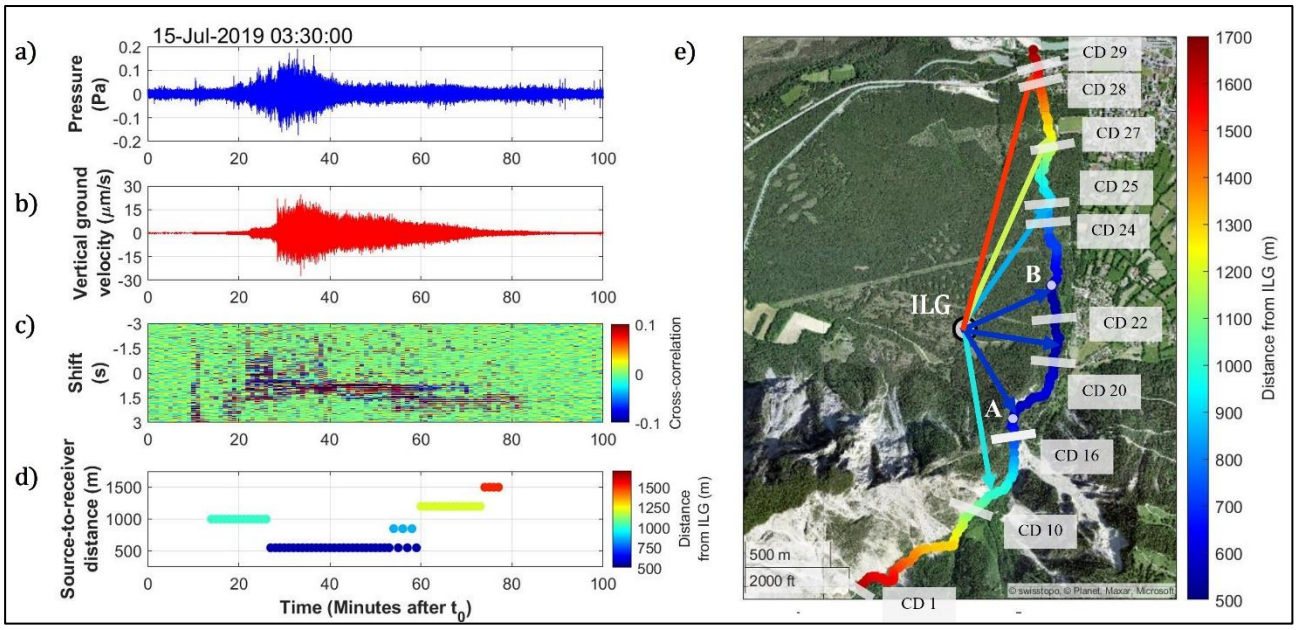

Figure 6. 11: cross-correlation (c) between infrasonic (a) and seismic (b) signals generated by the 2019/07/15 Illgraben debris-flow event. The cross-correlation values are indicated by colours according to the colour bar on the side of panel c. Evolution over time of the source-to-receiver distance estimated from the shift values of the maximum of the seismo-acoustic cross-correlation and using Eq. 6. 3 (d): the distances are indicated by colours according to the colour bar alongside. Map of the Illgraben channel between CD 1 and 30 with the location of some of the 30 check dams (CD) (e): the channel is coloured based on its distance from the seismo-acoustic sensors (grey circle) as indicated by the colour bar alongside. Arrows in e point in the direction corresponding to the source-to-receiver distances shown in d and are coloured the same colour as the distance value they represent. In the map, three different dark blue arrows are shown to indicate that the 550 m distance could correspond to each point inside the entire channel sector between points A and B.

Once the barycentre of the debris flow exits from the channel sector characterized by the minimum source-to-receiver distance, it progressively increases over time its distance from the seismo-acoustic recording site (Figure 6. 10, Figure 6. 11 e). This gradual increase in the propagation distance causes that the recording time delay, between the seismic signal and the infrasound simultaneously radiated in the same channel sector, gradually increases in time during the debris flow event, in agreement with the trend of the seismo-acoustic cross-correlation. In these phases, the observed shift migrates from 0.8 s, to ~1.3 s, to 1.8 s and finally to 2.3 (Figure 6. 11 c).

Using Eq. 6. 3, the shift values of 1.3 s and 1.8 s give a source-to-receiver distance of ~850 m and ~1200 m, respectively (Figure 6. 11 d). These values correspond to the channel sectors immediately downstream of CD 24 and CD 27 respectively (Figure 6. 11 e).

Finally, the shift of 2.3 s, recorded in the last phases of the 2019/07/15 event, gives a source to receiver distance of ~ 1500 m (Figure 6. 11 d). This distance corresponds to the channel sector immediately downstream CD 28 (Figure 6. 11 e), located within the last 250 m of the Illgraben stream, and thus is in agreement with having recorded the corresponding shift value close to the end of the recorded seismo-acoustic signals (Figure 6. 11 c).

Therefore, the variation over time of the time delay between the recorded seismic and infrasonic signals, highlighted by the seismo-acoustic cross-correlation, allows to follow the movement of the debris flow along the Illgraben channel. This highlights how the seismo-acoustic cross-correlation could be used to approximately locate, at different times, the source of the main components of the recorded seismo-acoustic signals within the debris flow (Figure 6. 11).

A similar trend, although less clear, is observed also for the 2019/08/20 event (Figure 6. 9 c), which was a small debris flow too (see Table 3. 1, Section 3.4, Chapter 3).

The migration of the seismo-acoustic cross-correlation peak, instead, is not visible during the 2019/07/01 event, for which the cross-correlation peak is observed to be stable at a shift of ~ 0.8 s (Figure 6. 9 a). This is probably due to the thunderstorm and to the spikes recorded in the infrasonic data at the beginning and at the end of the debris-flow signal, preventing the initial and the waning phase to be properly detected.

6.1.4 Infrasonic array analysis

To investigate the infrasonic source mechanism within Illgraben debris flows, the array processing was applied to infrasound data. As described in Section 5.1.4 (Chapter 5), the infrasonic signals generated by the debris flows resulted to be dominated by coherent clusters of infrasonic detections, each characterized by constant back-azimuth values, which however varies from cluster to cluster. This is observed for both large (Figure 6. 12) and small (Figure 6. 13) Illgraben debris-flow events.

In addition, the back azimuth values of the different detection clusters indicate the direction of some of the check dams located along the Illgraben channel (B_{az} = ~185, 156, 110, 90, 80, 35, 20 and 17°N) or the direction of some very irregular channel sectors (B_{az} =~170, 165 and 152 °N) (Figure 6. 12 and Figure 6. 13, f panels).

These results suggest that the infrasound by Illgraben debris-flow, despite being likely produced in every point along the flow [Marchetti et al., 2019], is dominated by the coherent infrasound components generated in fixed positions along the channel, wherever channel irregularities, such as topographic steps and steep channel bends, are present. In particular, in the Illgraben channel, the check dams act as dominant sources of infrasound.

As described in Section 2.2 (Chapter 2), infrasound is likely generated by flow waves that develop at the free surface of the flow [Marchetti et al., 2019]. At Illgraben, the formation of these flow surface waves is probably enhanced just downstream of each check dam, which is a significant channel irregularity. The free overfall at drops, indeed, generates strong circulation and heavy turbulence at the base of the fall, so that massive oscillations and heavy water splashes are induced at the flow surface [Tokyay and Yildiz, 2007]. Such surface oscillations hit the air and result as the primary source of infrasound within the debris flow [Feng et al., 2014; Belli et al., 2022]. This mechanism is probably active in correspondence of every channel irregularity, causing the flow to radiate infrasound along its entire length, but it is all the more accentuated the more significant the irregularity is (e.g. for higher check dam) [Tokyay and Yildiz, 2007], so that infrasound is dominated by signal produced by the debris flow when it passes over larger irregularities (check dams and accentuated channel bends).

For all the presented events, the array processing revealed that the maximum infrasonic amplitudes are recorded for back-azimuth values ranging between 156 and 80°N (Figure 6. 12, Figure 6. 13). These values correspond to the channel sector characterized by the lower distance from the ILG infrasonic array. This confirms the predictions of Marchetti et al. [2019], who state that the higher infrasonic amplitudes are generated when the barycentre of the debris flow is located at the minimum distance from the recording sensor.

Furthermore, it is interesting to note that the infrasonic array processing permits locating the infrasonic source along the entire event, thus allowing to track the motion of the debris flow along the entire Illgraben channel (Figure 6. 12, Figure 6. 13). Indeed, each back-azimuth value determined with the array processing identifies a specific position of the channel.

For each event, the determined back-azimuth values initially point at the upstream check dams and then, as the debris flow continues its descent towards to Rhone River, progressively indicate the further downstream ones. For example, for the 2019/07/15 event, the array processing allows to follow the motion of the debris flow between CD 16 and CD 29, highlighting its passage at CD 20, 21, 22 and 24 too.

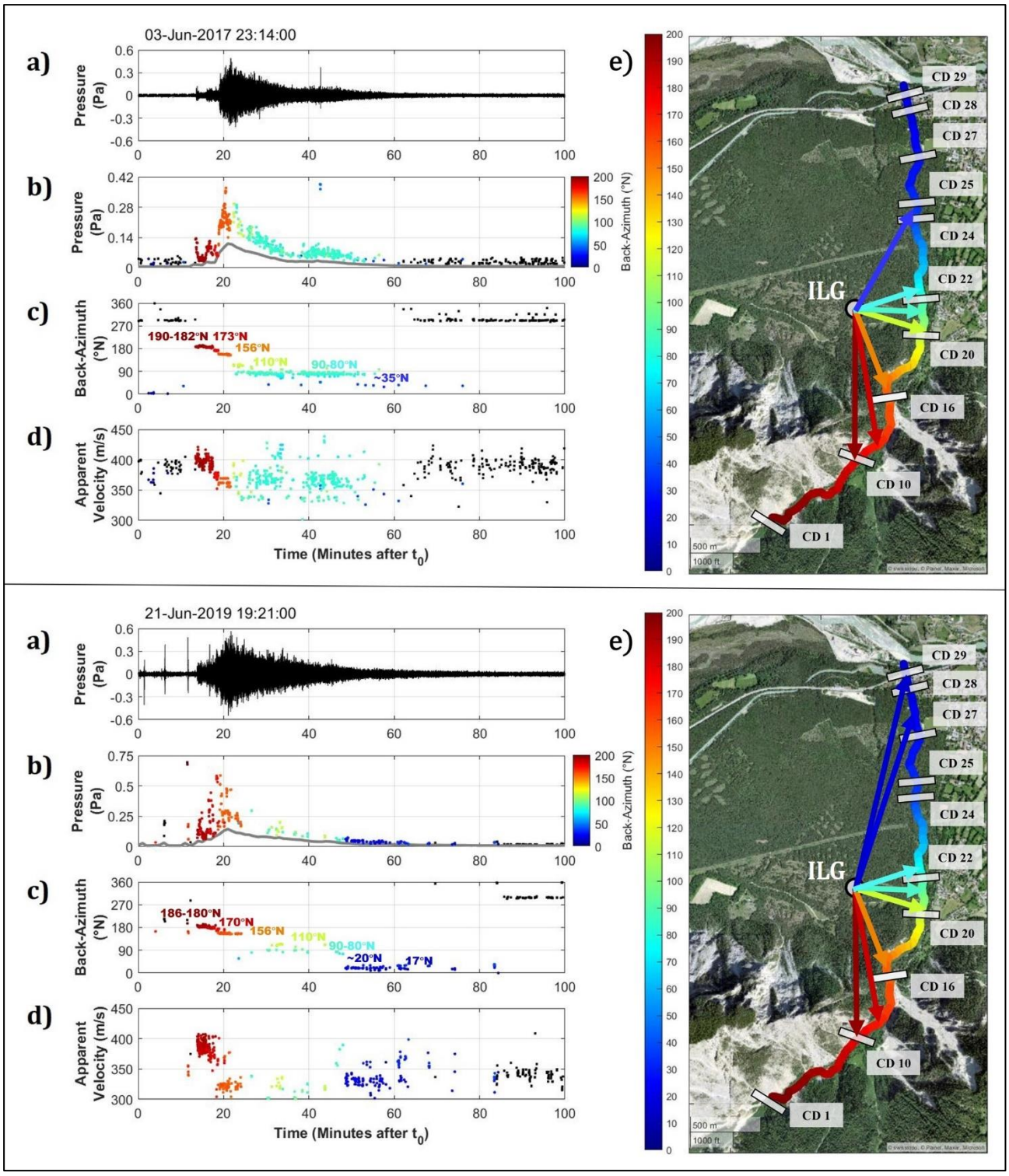

Figure 6. 12: array processing of the infrasonic signals (a) generated by the Illgraben debris-flow events of 2017/06/03 (top panel) and 2019/06/21 (bottom panel). Infrasonic pressure (b), back-azimuth (c) and apparent velocity (d) of the infrasonic detections identified with the array processing. The grey line in panel b represents the RMSA of the infrasonic signal computed over 1-minute windows. Back-azimuth values in panels b, c, d and e are indicated by colours according to the colour bar on the side of panel b. Map of the Illgraben channel showing for each point the back-azimuth measured with respect to the ILG array and coloured according to the colour bar alongside (e). In e, the location of some of the 30 check dams (CD) and of the ILG array (grey

circle) are indicated (e). Arrows in e point in the directions indicated by the back-azimuth values highlighted in c and are coloured the same colour as the back-azimuth value they represent.

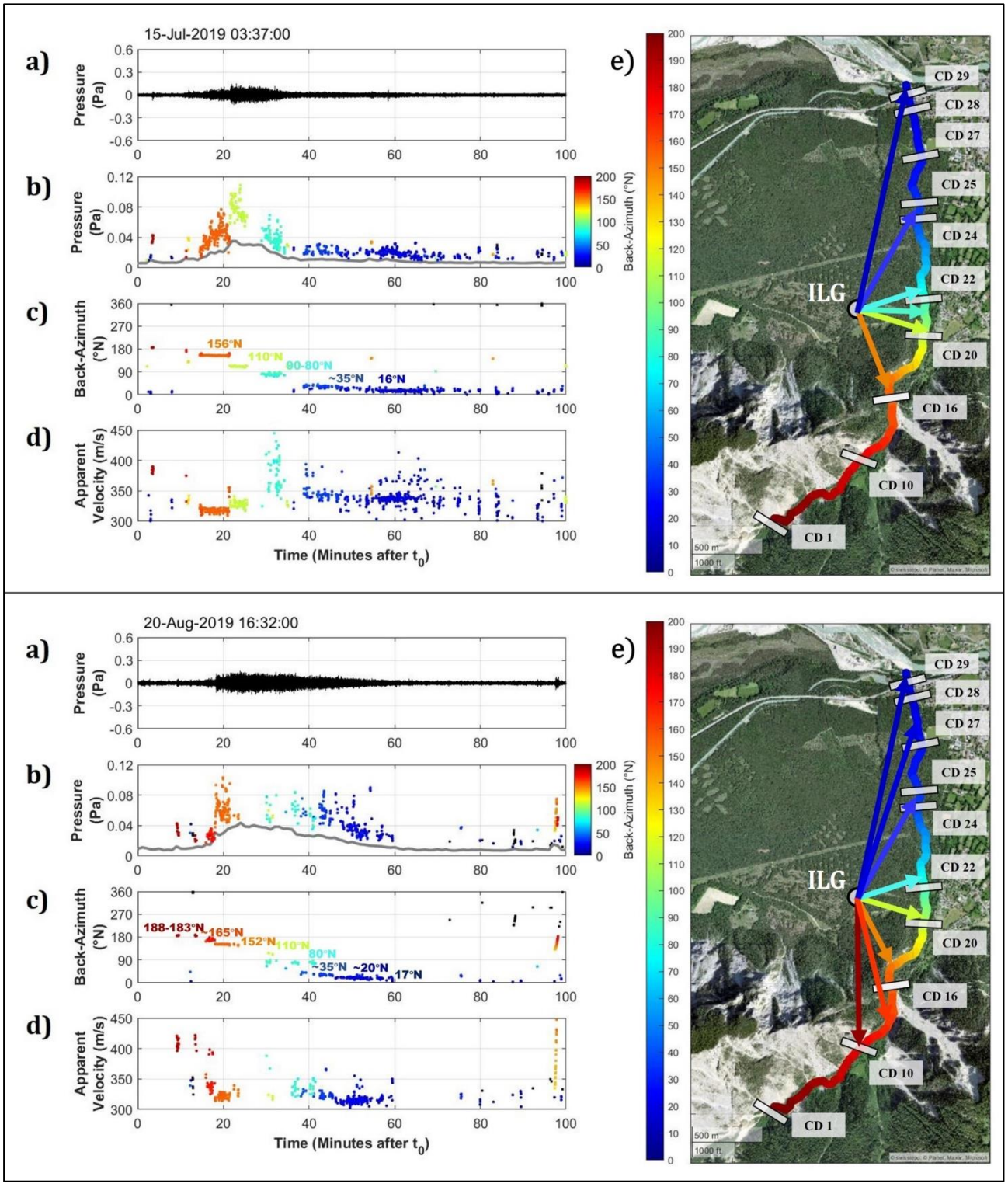

Figure 6. 13: array processing of the infrasonic signals (a) generated by the Illgraben debris-flow events of 2019/07/15 (top panel) and 2019/08/20 (bottom panel) (same as Figure 6. 14).

In addition, as shown in Figure 6. 15, each channel point is characterized by a specific couple of values of back-azimuth and distance from the recording seismo-acoustic sensors. The variation of these two parameters along the channel is not uniform, due to the irregular planar geometry of the Illgraben stream path with respect to the recording seismo-acoustic sensors. For example, the channel sector between CD 16 and CD 22, marked by an almost constant sensor-to-source distance, is characterized by a wide variation of the sensor-to-source back-azimuth (~75°, Figure 6. 15). In contrast, in the channel sectors between CD 1 and CD 16 and between CD 24 and CD 30 a large variation is observed for the sensor-to-source distance (~700 m), while the back-azimuth varies to much lesser extent (~20°, Figure 6. 15).

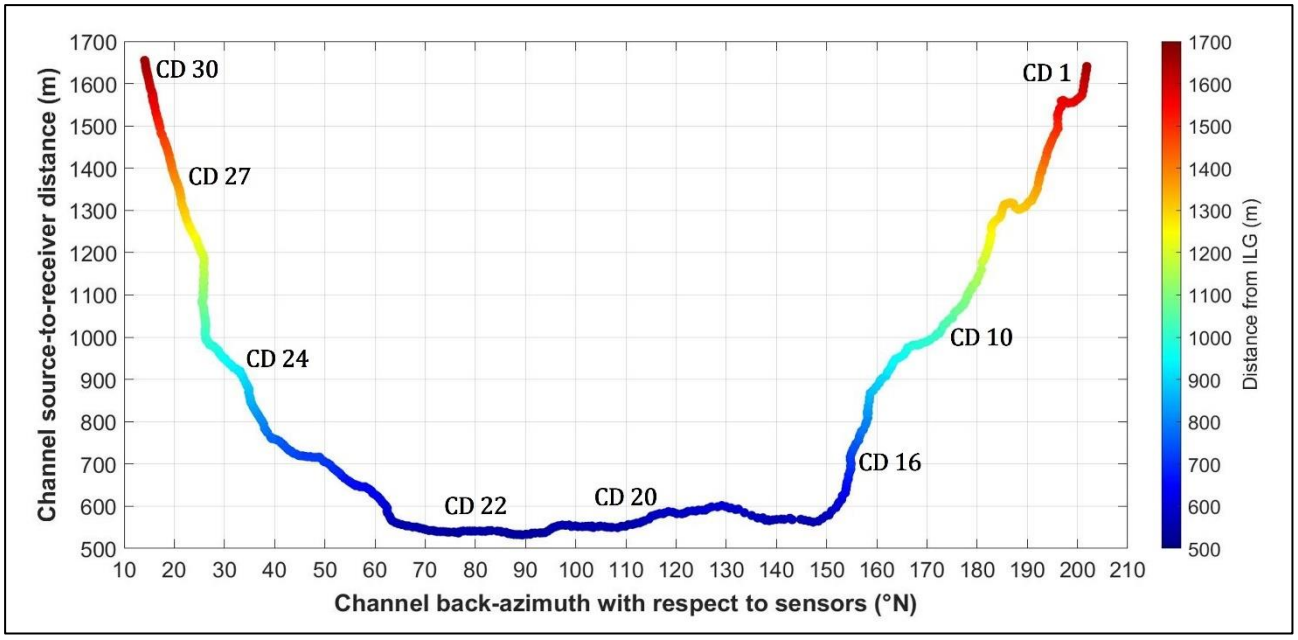

Figure 6. 15: sensor-to-source distance and back-azimuth of 575 points distributed along the channel between CD 1 and CD 30. Both the parameters are calculated with respect to the location of the central element (m4) of the ILG array. Check-dam labels are indicated in the panel too.

Based on the relation shown in Figure 6. 15, the back-azimuth trend obtained with the array processing can be inverted to derive the evolution over time of the distance between the source of the infrasonic signal and the recording array. Figure 6. 16 shows the evolution over time of the sensor-to-source distance determined from the back-azimuth values obtained with the infrasonic array analysis of the 2019/07/15 Illgraben debris flow.

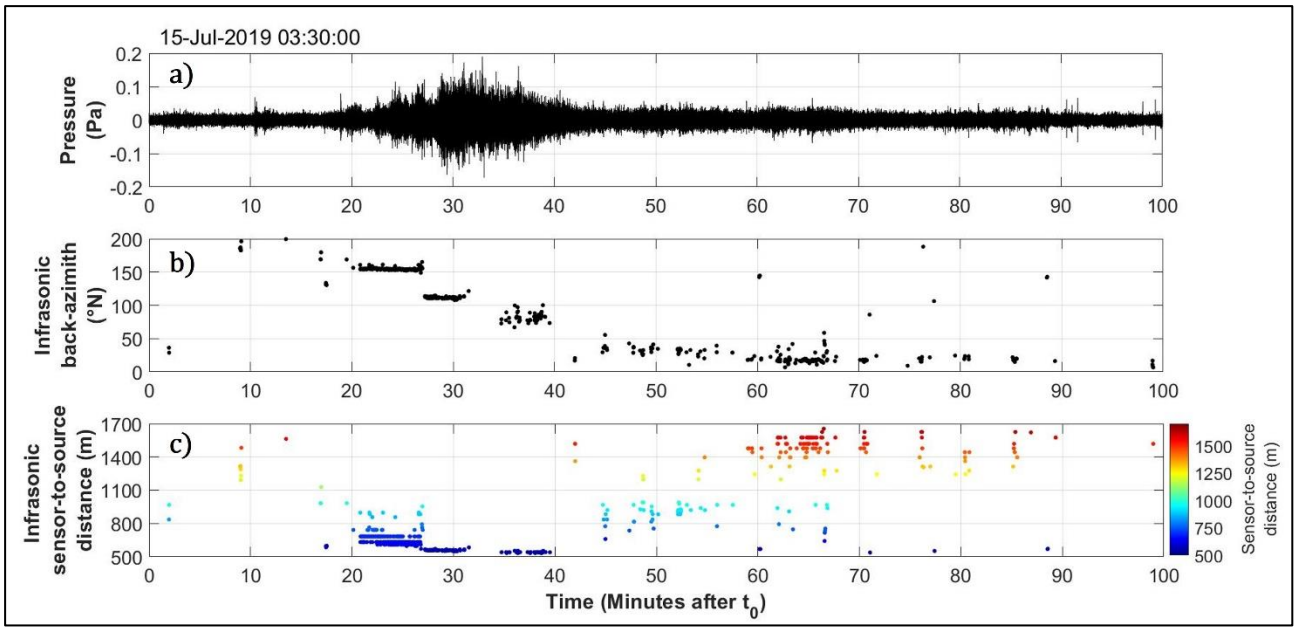

Figure 6. 16: sensor-to-source distance (c) determined using the back-azimuth values (b) obtained from the array processing of the infrasonic signal (a) generated by the 2019/07/15 Illgraben debris flow. The distance values in c are coloured according to the colour bar alongside.

The inversion of the back-azimuth values obtained from the array processing in the corresponding sensor-to-source distance (Figure 6. 16) allows to compare the localisation of the infrasonic source obtained with the array processing (Figure 6. 13) with the one obtained with the seismo-acoustic cross-correlation (Figure 6. 11).

The comparison for the 2019/07/15 event, shown in Figure 6. 17, reveals that the two localisations are in good agreement. Indeed, a good correspondence between the two distance-reconstruction methods is observed during the event (Figure 6. 17 c, d).

Figure 6. 17 also shows that both the seismo-acoustic cross-correlation and the array processing locate the source of the maximum amplitude of the recorded debris-flow infrasonic and seismic signals within the channel sector located at the minimum distance from the recording seismo-acoustic sensors. Once again this agrees with Marchetti et al. [2019], who predict that the maximum seismo-acoustic amplitudes are generated when the barycentre of the debris flow is at the minimum distance from the recording sensors.

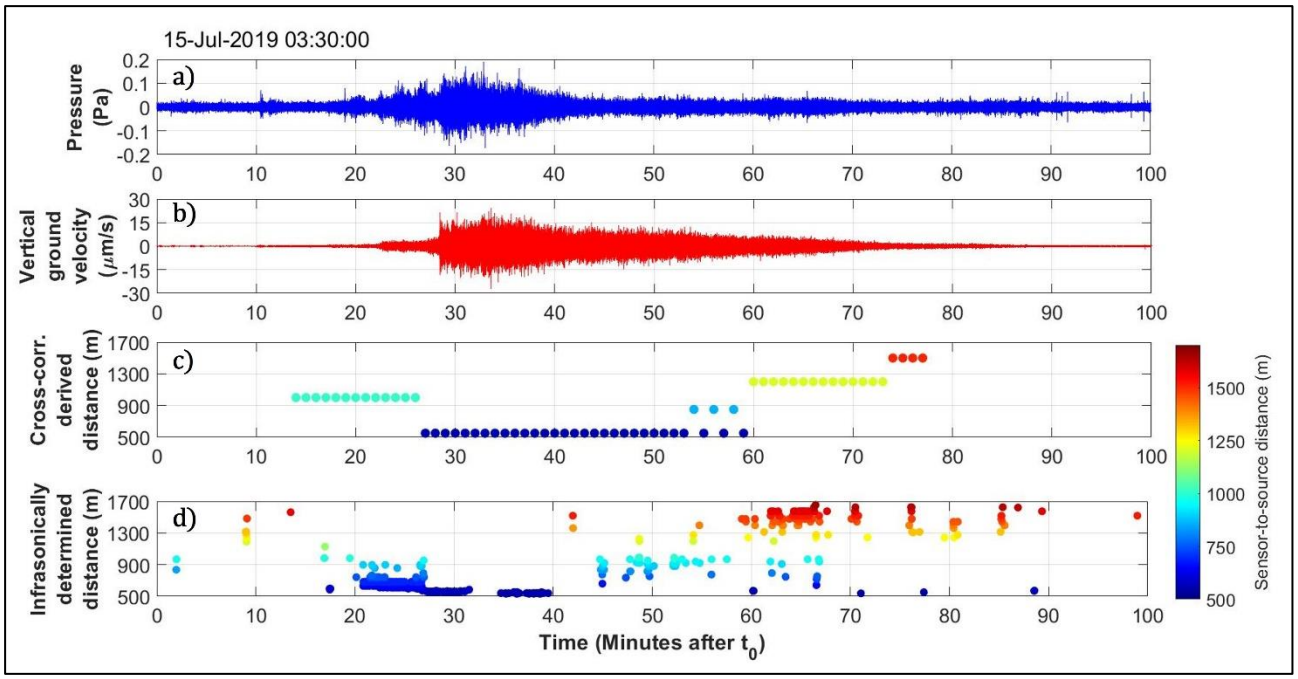

Figure 6. 17: comparison between the reconstructions of the sensor-to-source distance performed with the seismo-acoustic cross-correlation (c) and with the infrasonic array processing (d) for the 2019/07/15 debris-flow event. 1-20 Hz band-pass filtered infrasonic (a) and seismic (b) signals. The distance values in c and d are coloured according to the alongside colour bar. A good correspondence is observed between the two reconstructions in c and d.

6.2 What does the comparison between seismo-acoustic signals and flow parameters reveal?

In order to investigate the debris-flow seismo-acoustic energy source processes and mechanisms and how the flow parameters influence the seismo-acoustic radiation, the features of the infrasound and seismic signals were compared with available hydraulic and physical data (see Section 5.2, Chapter 5). The obtained results, largely already the subject of a publication by Belli et al. [2022], are discussed in the following sections.

6.2.1 Comparison between seismo-acoustic RMSA and flow parameters

The comparison between the hydraulic data and the maximum infrasonic and seismic RMSA showed general positive trends between the debris-flow parameters and the generated maximum seismo-acoustic amplitudes (Figure 6. 18) [Belli et al., 2022].

In agreement with Marchetti et al. [2019] and with the outcomes discussed in Section 6.1.3 and 6.1.4, the maximum seismo-acoustic amplitudes are generated when the barycentre of the flow is located at the minimum distance from the recording seismo-acoustic sensors. Flow velocity and flow depth are measured ~1,500 m further downstream (CD 27-29) from the position of minimum distance between the channel and the recording seismo-acoustic sensors. This introduces some uncertainties when comparing seismo-acoustic signals with flow parameters, since the measured values could differ from the actual value the flow had in the sector closest to the recording sensors. However, a relative comparison is still permissible [Belli et al., 2022] as the maximum amplitude of the recorded seismo-acoustic signals is generated always in the same channel sector.

Results revealed a general positive relation between the seismo-acoustic maximum RMSA and the front velocity (Figure 6. 18 a, b). Much better results, with excellent linear relations, as testified by the computed Pearson correlation factors ($R = 0.94$-0.95), are instead obtained when the maximum RMSA is compared with the maximum flow depth (Figure 6. 18 c, d) and with the flow peak discharge per unit channel width (Figure 6. 18 e, f).

The positive relations between maximum RSMA and flow properties suggest that the maximum amplitude of both seismic and infrasound energy radiation by debris flows is strongly influenced by the flow characteristics; higher flow velocities and/or larger flow depths generally correspond to higher amplitude infrasonic and seismic debris-flow signals [Belli et al., 2022]. Moreover, despite some uncertainty for single data points, the measured high values of the Pearson correlation factor ($R = 0.94$-0.95) shown in Figure 6. 18 c and d and in Figure 6. 18 e and f, suggest that flow depth and peak discharge per unit channel width linearly control the maximum amplitude of recorded seismo-acoustic signals [Belli et al., 2022].

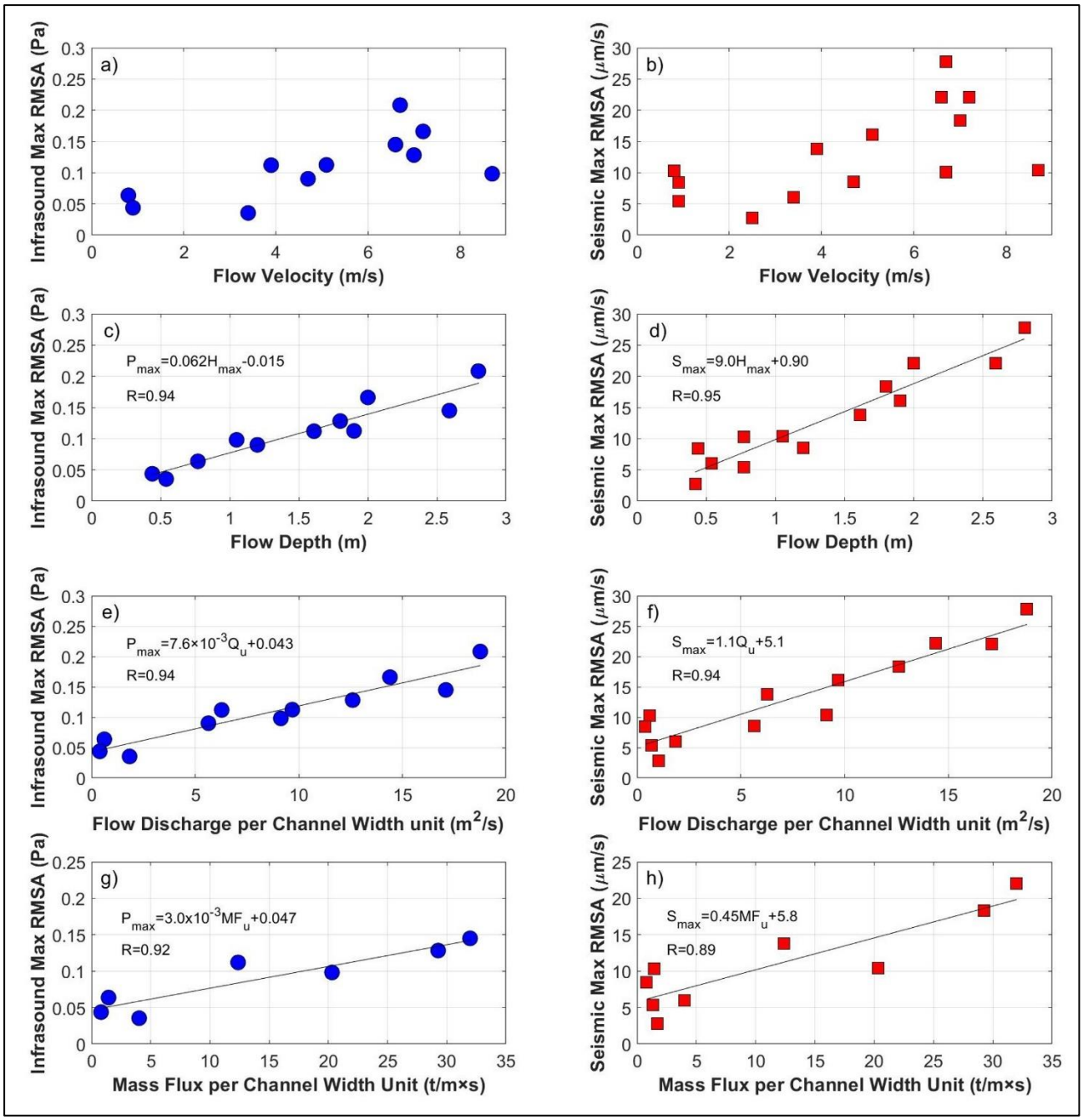

Figure 6. 18: comparisons between infrasonic (blue circles, left side) and seismic (red squares, right side) maximum RMSA and debris-flow front velocity (a, b), maximum flow depth (c, d), flow discharge per unit channel width (e, f) and mass flux per unit channel width (g, h).

The observed linear relationship between seismic amplitude and unit flow discharge is in agreement with Andrade et al. [2022], who also found a linear relation between flow discharge and seismic peak amplitude radiated by lahars observed at Tungurahua and Cotopaxi volcanoes. Results shown in Figure 6. 18 are also consistent with findings by Coviello et al. [2019] who analysed debris-flow

events in Gadria catchment (Italy, see Figure 1. 11, Section 1.3, Chapter 1) and found that the generated seismic amplitudes correlate positively with the kinetic energy of the flow.
For both infrasonic and seismic maximum RMSA, the best fit regression lines with both maximum flow depth and flow unit discharge were computed:

$$P_{max} = 0.062\ \frac{Pa}{m} \cdot\ H_{max} - 0.015\ Pa \qquad \text{(Eq. 6. 4)},$$

$$S_{max} = 9.0\ \frac{\mu m/s}{m} \cdot\ H_{max} - 0.90\ \mu m/s \qquad \text{(Eq. 6. 5)},$$

$$P_{max} = 0.0076\ \frac{Pa}{m^2/s} \cdot\ Q_u + 0.043\ Pa \qquad \text{(Eq. 6. 6)},$$

$$S_{max} = 1.1\ \frac{\mu m/s}{m^2/s} \cdot\ Q_u + 5.1\ \mu m/s \qquad \text{(Eq. 6. 7)}.$$

Since the maximum of the seismo-acoustic radiation is generated before the debris flow reaches the CD 29, where the flow depth is measured, the empirical relations Eq. 6. 4-7 could be used at Illgraben to roughly estimate the expected maximum flow depth of debris flow some minutes before the it reaches the main road and the inhabited area.

The linear influence of the flow depth on the generated seismo-acoustic amplitudes seems further confirmed by the comparison between the infrasonic and seismic RMSA curves and the hydrograms recorded during the Illgraben debris-flow events of 2019/06/21 and 2019/07/01 (Figure 6. 19).
Results showed excellent linear relations between the seismo-acoustic RMSA and the recorded flow depth, for both events, in particular for the 2019/06/21 event (Figure 6. 19 a, b), as evidenced by the Pearson correlation factors ($R = 0.99$ and $R = 0.98$ for infrasonic and seismic signals respectively). The linear relation, although still good ($R = 0.92$), is instead a bit disturbed for the 2019/07/01 event, especially in case of infrasound (Figure 6. 19 c).

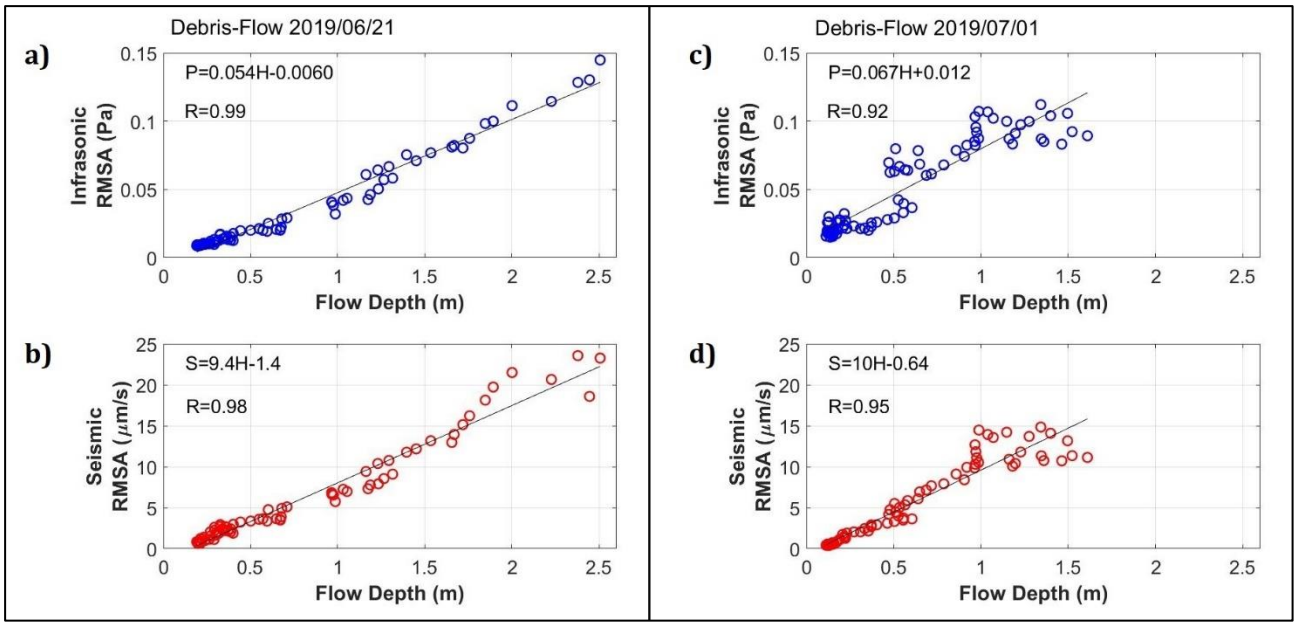

Figure 6. 19: comparison between infrasonic (blue, a, c) and seismic (red, b, d) RMSA values with recorded flow depth, for the debris flow of 2019/06/21 (left side) and for the debris flow of 2019/07/01 (right side). The black lines in the panels represent the best fit regression lines, whose equations are written within the panels, where also the Pearson correlation factor (R) is reported. P and S are the infrasonic and seismic RMSA respectively and H is the flow depth.

The best fit regression lines were calculated for both infrasonic and seismic signals, and for the 2019/06/21 event we got:

$$P(t) = 0.054\,\frac{Pa}{m} \cdot H(t) - 0.0060\,Pa \qquad \text{(Eq. 6. 8)}$$

$$S(t) = 9.4\,\frac{\frac{\mu m}{s}}{m} \cdot H(t) - 1.4\,\mu m/s \qquad \text{(Eq. 6. 9)},$$

while for the 2019/07/01 event we got:

$$P(t) = 0.067\,\frac{Pa}{m} \cdot H(t) + 0.012\,Pa \qquad \text{(Eq. 6. 10)}$$

$$S(t) = 10\,\frac{\frac{\mu m}{s}}{m} \cdot H(t) - 0.64\,\mu m/s \qquad \text{(Eq. 6. 11)}.$$

A good agreement is observed when these relations (Eq. 6. 8-11) are compared to the relations obtained between the maximum seismo-acoustic RMSA and the maximum flow depth values recorded for all the Illgraben events (Eq. 6. 4 and Eq. 6. 5) (Figure 6. 20).

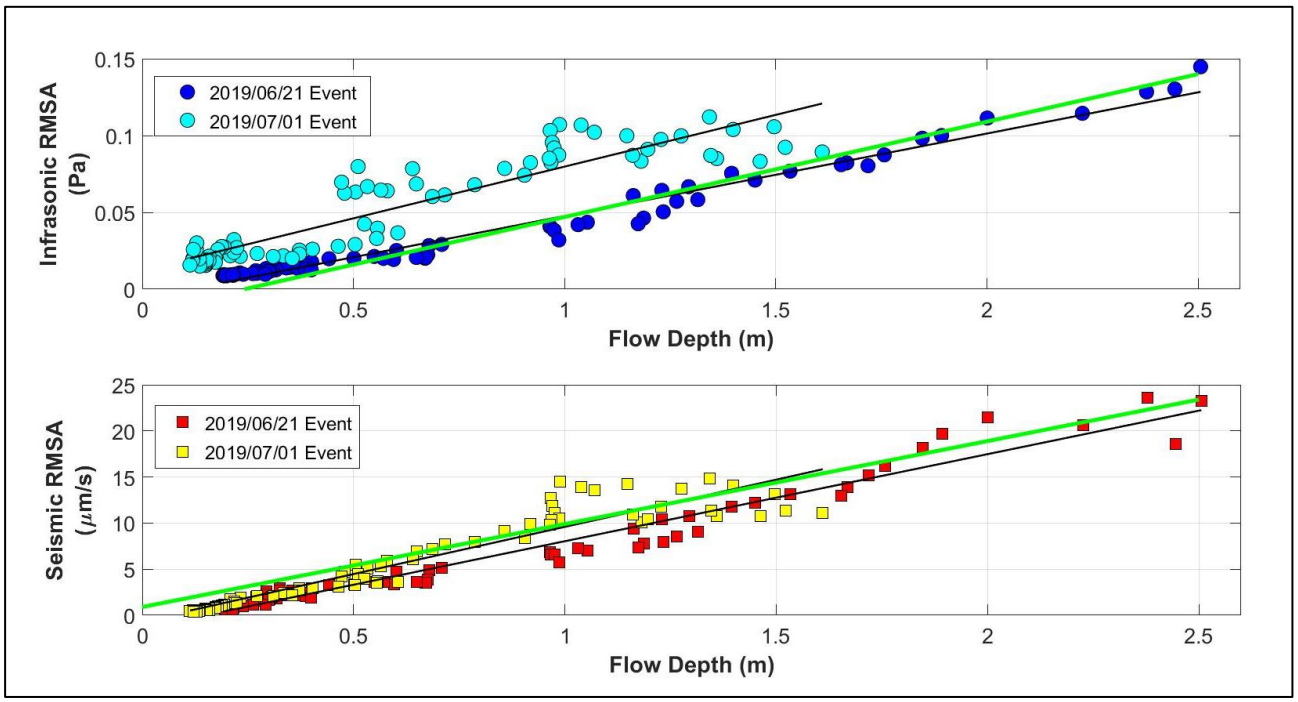

Figure 6. 20: comparison between infrasonic (top) and seismic (bottom) RMSA values with recorded flow depth, for the debris flow of 2019/06/21 and for the debris flow of 2019/07/01. The black lines in the panels represent the best fit regression lines. Colours indicates the debris flow event as reported in the panels. In each panel, the green line represents the best fit regression line computed for the relations between the maximum RMSA and maximum flow depth in Figure 6. 18 c and d (Eq. 6. 4 and Eq. 6. 5).

In particular, Figure 6. 20 shows that, in case of infrasound (Figure 6. 20, top panel), the relation based on peak values of multiple events (Eq. 6. 4, green line) almost overlaps the relation obtained between the infrasonic RMSA and the flow depth values (Eq. 6. 8) for the 2019/06/21 event (darker blue points). In constrast, the green line deviates more from the best fit regression line (Eq. 6. 10) obtained for the event 01/07/2019 (cyan points), for which the relationship between the infrasonic RMSA and the measured flow depth is more irregular. For seismic signals instead (Figure 6. 20, bottom panel), a strong agreement is observed between the relation based on peak values of multiple events (Eq. 6. 5, green line) and the best fit relations calculated between recorded seismic RMSA and measured flow depth for both events (Eq. 6. 9 and Eq. 6. 11).

The agreement (Figure 6. 20) between the empirical relations expressed by Eq. 6. 8-11, obtained between the seismo-acoustic RMSA curves and the hydrograms for the two presented events, and Eq.

6. 4 and Eq. 6. 5, based on RMSA and flow depth peak values of multiple events, suggests that the linear relation observed between the maximum seismo-acoustic RMSA and maximum flow depth value holds monotonously even for the non-peak values, suggesting that the flow depth linearly controls the amplitude of the seismo-acoustic radiation by debris flows, both for multiple events as well as during the evolution of a single event.
This highlights how, once empirical relations like Eq. 6. 4-11 have been defined, the real-time seismo-acoustic RMSA, and not just its maximum value, could be used to estimate in real time the flow depth (and/or the discharge rate) of a debris flow occurring at Illgraben, even if no in-channel measurement, e.g. of the flow velocity and flow depth, is available, with strong implication for monitoring purposes.

When compared to seismo-acoustic maximum RMSA, the peak mass flux per unit channel width also produced a rather good linear trend ($R = 0.92$ and $R = 0.89$ for infrasound and seismic signals respectively) (Figure 6. 18 g, h); however, the limited number of data available for this comparison prevents us from evaluating the actual accuracy of the derived relations. In addition, carefully comparing Figure 6. 18 e and f with Figure 6. 18 g and h, results suggest that the flow discharge likely controls Illgraben debris-flow seismo-acoustic energy radiation and partition more than the mass flux does, with the density acting, in Figure 6. 18 g and h, only as an approximately constant coefficient multiplying the unit flow discharge values plotted in Figure 6. 18 e and f.

In contrast to the positive relations shown in Figure 6. 18, no clear relations are observed when the seismo-acoustic maximum amplitudes are compared to the flow density (Figure 6. 21).
This may appear rather counterintuitive when the seismic signal is considered, as a larger density should likely reflect a higher amount of transported solid particles, whose impacts with the riverbed are believed to be the main seismic source process within debris flows [Burtin et al., 2009; Kean et al., 2015; Lai et al., 2018; Zhang et al., 2021(a)]. However, the measured density represents the debris flow as a whole; an increased flow density leads to a larger buoyancy of the transported solid particles, which determines a partial reduction of the particle impact force with the ground [Piantini et al., 2023]. Therefore, the role of an increased density on the seismic amplitude is not univocal, so that the presented results (Figure 6. 21) are less surprising.
However, the flow density database is probably too limited (only 7-9 events) to derive any significative conclusion and certainly more data are required.
In addition, the complete characterization of the debris-flow seismicity would require a compared analysis with the boulder size, as grain size has been shown to be the dominant controlling factor in

impact generated seismic waves [Tsai et al., 2012]. Nevertheless, this will involve further data analysis of videos of the flow to determine the boulder size that could be addressed in future studies.

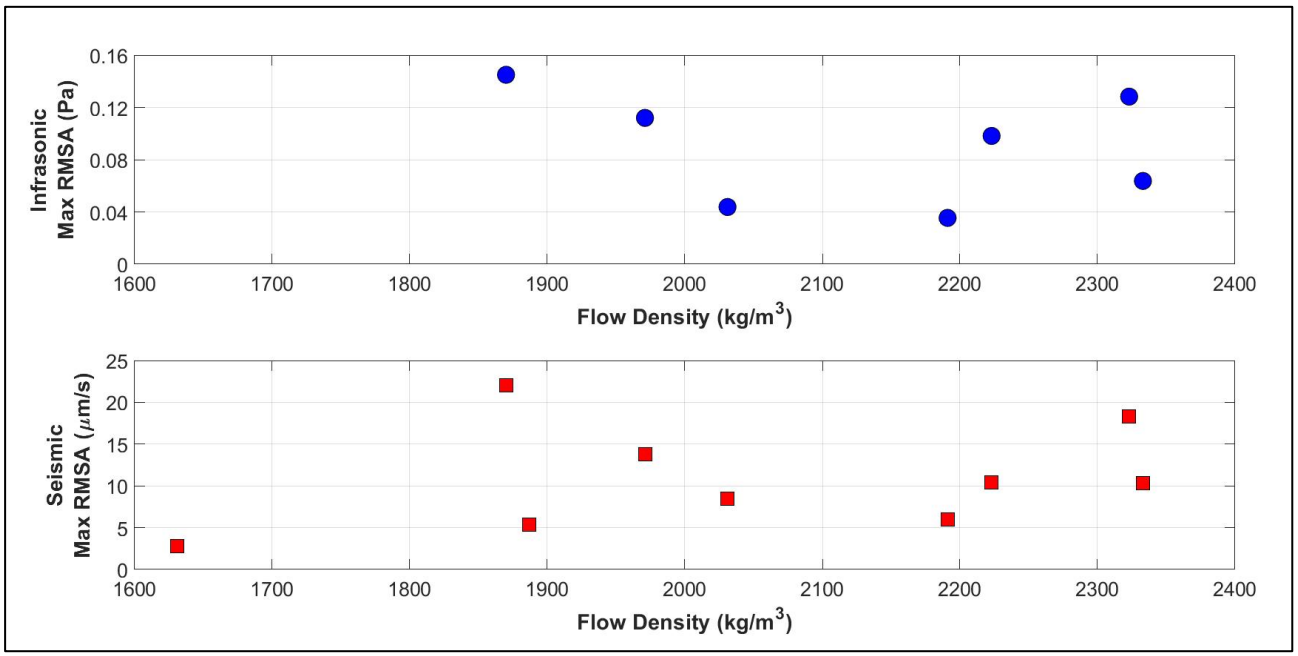

Figure 6. 21: comparison between debris-flow bulk density and both infrasonic (a) and seismic (b) maximum RMSA. In both panels, no clear relations are observed.

The observed relation between flow parameters and seismo-acoustic observations agrees with the source process accepted for the infrasonic and seismic radiation by debris flows. As described in Section 2.1 (Chapter 2), existing models attribute the generation of the seismic waves by debris-flows to solid particle collisions with the riverbed [Kean et al., 2015; Lai et al., 2018; Farin et al., 2019; Zhang et al., 2021]. The growth of the flow depth (or discharge) leads to a larger transport capability of the debris flow, increasing the amount and the size of the solid particles potentially carried by the flow. This determined the increase of the rate and the energy of the particle-riverbed impacts, thus enhancing the seismic source processes.

The infrasonic waves are instead thought to be generated by waves and oscillations that develop at the air-water interface [Marchetti et al., 2019; Belli et al., 2022] (see Section 2.2, Chapter 2). According to fluid dynamic models and flume experiments on water flows, these waves are induced at the flow surface by turbulence structures generated as the flow interacts with channel irregularities, for example for water falling at free overfalls at check-dams [Coco et al., 2021; Feng et al., 2014; Tokyay and Yildiz, 2007], or with the riverbed roughness Horoshenkov et al., 2013] (see Section 1.2.2, Chapter 1).

An increased flow depth (or discharge) involves a growth of the energy of the flow [Henderson, 1996; Chaudhry, 2008] and leads to the development of larger amplitude waves at the surface of the flow [Tokyay and Yildiz, 2007]. Indeed, Tokyay and Yildiz [2007], performing flume experiments on water flows over a topographic step, found that, downstream a supercritical ($Fr > 1$) free waterfall, the amplitude of the generated water splash increases with increasing the Froude number (which depends on the flow velocity), the flow depth and the height of the fall, according to Eq. 1. 10, here shown again:

$$A_{sp} = 0.4532\, Fr\sqrt{z\, H_b} \qquad \text{(Eq. 6. 12).}$$

Such a flow behaviour is to be expected also in case of the Illgraben debris flows that undergo free overfall at the check-dams, since computation of the Froude number performed in this thesis and presented in Section 3.4.1 (Chapter 3) revealed that almost all larger ($H > 1$ m) Illgraben debris flows fall into the supercritical conditions domain (see Figure 3. 15 and Table 3. 1, Section 3.4.1, Chapter 3). As the flow depth increases, larger amplitude waves and oscillations are generated at the base of free overfalls. These larger waves collide with a larger energy with the air and thus radiate higher amplitude infrasound.

6.2.2 Comparison between seismo-acoustic peak frequency and flow parameters

The comparison with flow parameters was also extended to the peak frequency of the infrasonic and seismic debris-flow signals (see Section 5.2.2, Chapter 5).

Despite the similarities emerged in the analysis of the amplitude of seismo-acoustic signals and in its comparison with hydraulic data, discussed in Section 6.1.1 and 6.1.3 and in Section 6.2.1 respectively, the spectral analysis discussed in Section 6.1.2 highlighted significant differences between infrasonic and seismic debris-flow signals. As a matter of fact, the two wavefields are characterized by different frequency content and different peak frequencies (see Section 5.1.2, Chapter 5). This has been interpreted as the evidence of the fact that the two wavefield are likely generated by different source processes, which, while acting simultaneously and propagating downstream as the flow evolves, are decoupled (Section 6.1.2) [Belli et al., 2022].

These outcomes seem further confirmed by the comparison between the seismo-acoustic peak frequencies and the flow parameters, here proposed again in Figure 6. 22.

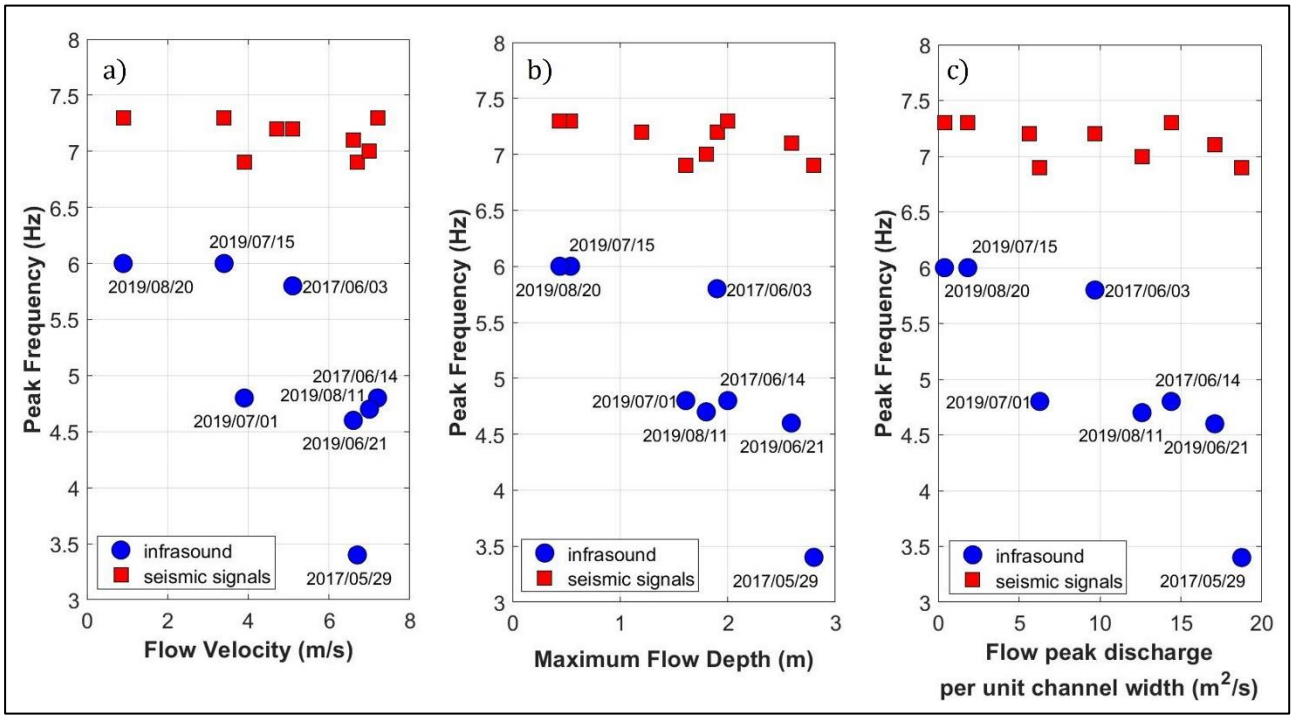

Figure 6. 22: comparison between infrasonic (blue circles) and seismic (red squares) peak frequencies with debris-flow front velocity (a), flow maximum depth (b) and flow discharge per unit channel width (c). The infrasonic peak frequency scales inversely with flow parameters. The seismic peak frequency instead is almost constant for all events, regardless of the flow parameters.

While the peak frequency of seismic signals is almost constant for all events (6.9-7.5 Hz) regardless of the flow parameters (Figure 6. 22, red squares) [Belli et al., 2022], in agreement with models on seismic radiation by particle-riverbed collisions in rivers [Tsai et al., 2012] and debris flows [Lai et al., 2018], the infrasonic peak frequency scales inversely with the flow parameters, decreasing as the front velocity, the flow maximum depth or the unit peak discharge increase (Figure 6. 22, blue circles). This suggests that larger flows (events with larger discharge and/or flow depth) radiate lower frequency infrasound [Belli et al., 2022].

This result is consistent with the findings by Marchetti et al. [2019], who analysed only 3 debris-flow events that occurred in 2017 at the Illgraben (also included in this work), and preliminarily observed a decrease of the recorded infrasonic peak frequency with increasing magnitude of the events. The observed inverse trend between infrasound peak frequency and flow magnitude is also in agreement with the numerical modelling by Coco et al. [2021] and with the flume experiments by Tokyay and Yildiz [2007].

Indeed, Coco et al. [2021], modelling the infrasonic pressure field produced by a water flow downstream a topographic step (dam), predicts a decrease in peak frequency of the generated infrasonic waves as the flow depth or the height of the step increases (see Section 2.2, Chapter 2). Tokyay and Yildiz [2007], performing flume experiments on water flows, found that the wavelengths of the water waves and splashes generated at the base of a supercritical ($Fr > 1$) waterfall increase with increasing the flow depth. As discussed above (Section 6.2.1), this scenario is to be expected also in case of the debris flows that undergo free overfall at the check-dams at Illgraben, since almost all larger ($H > 1$ m) debris flows analysed in this thesis turned out to be supercritical (see Figure 3. 15 and Table 3. 1, Section 3.4.1, Chapter 3). Since the waves and oscillation at the flow surface are believed to be the source of the infrasound radiation by debris flows [Marchetti et al., 2019], the increase of their wavelength (and therefore of their period) with increasing the flow depth [Tokyay and Yildiz, 2007] likely leads to the generation of lower frequency infrasound, as a result of the longer duration of the source process [Ostrovsky and Bedard, 2002]. This agrees with the experimental evidence presented in Figure 6. 22.

The inverse relation in Figure 6. 22 holds for all considered hydraulic parameters (v, H and Qu), but the best fit is obtained when the maximum flow depth and with the flow peak discharge per unit channel width are considered (Figure 6. 22 b, c). Whereas the number of observations is still limited, this inverse relation between peak infrasound frequency and flow parameters seems however to be limited to larger events ($v > 4$ m/s, $H > 1.5$ m, $Q_u > 10$ m^2/s), while for smaller events, infrasound peak frequency seems to be almost independent of flow magnitude. This could be at least partly explained by the signal-to-noise ratio, which affects determination of the peak frequency of smaller events, which implies a source of smaller amplitude (and higher frequency), of the same order as the ambient noise [Belli et al., 2022].

6.3 The physical interpretation

Based on the outcomes inferred from all the presented experimental evidence (see Chapter 5 and Section 6.1 and 6.2, Chapter 6), previous theoretical [Farin et al., 2019; Gimbert et al., 2014; Tsai et

al., 2012] and numerical models [Coco et al., 2021], as well as field observations of infrasound and seismic signals radiated by debris flows [Belli et al., 2021(a); Belli et al., 2022; Kean et al., 2015; Lai et al., 2018; Marchetti et al., 2019], a simplified conceptual source mechanism is proposed for the seismo-acoustic energy radiation by debris flows, where the infrasonic and seismic waves are radiated by different decoupled processes simultaneously acting at the ground and at the flow surface and migrating downstream during the event (Figure 6. 23).

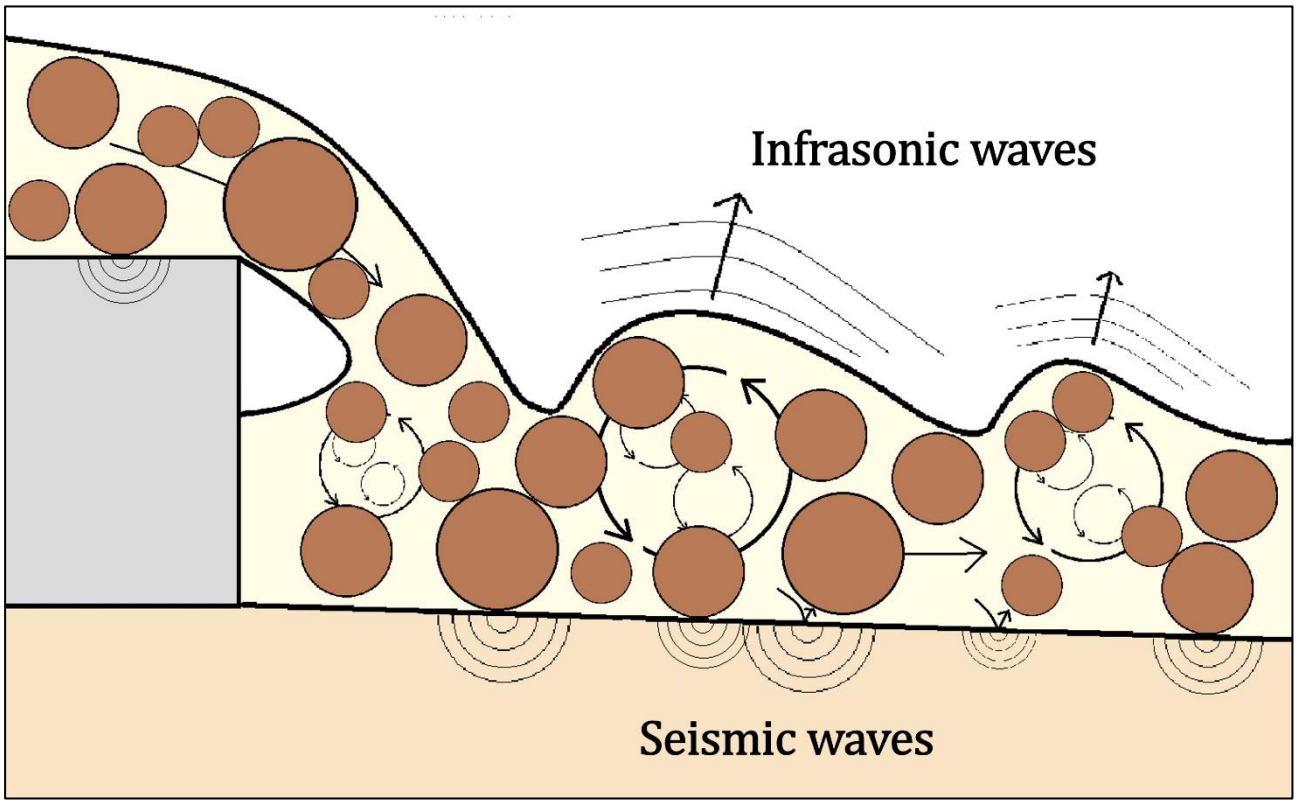

Figure 6. 23: sketch of the proposed conceptual model for the radiation of infrasonic and seismic waves by debris flows. The infrasound is radiated by waves that develop at the flow free surface, while the seismic waves are mostly generated by solid particle impacts with the riverbed.

The findings presented in this thesis and discussed in Section 6.1.1 showed that the radiation processes of infrasound and seismic waves by debris flows are closely related to each other, showing a clear amplitude correspondence during the event and similar relations with flow parameters.
In addition, results indicate a constant partition of the elastic energy radiation by the debris flows between the ground, in the form of seismic waves, and the air, in the form of infrasound, revealing that, for all events, the infrasonic and seismic source processes act with a constant energy ratio between each other.

Despite all these similarities, the observed different frequency content clearly demonstrates that the infrasonic and seismic waves by debris flows are generated by different decoupled source processes, separately acting at the flow interface with the ground and with the air respectively.
In addition, the lack of a detectable infrasonic signal observed for smaller events indicates that the infrasonic source mechanism develops effectively only above a certain discharge rate (or flow depth), different from the seismic signals, whose radiation has been recorded for all investigated debris flows, regardless of the flow size. This evidence also suggests that debris flows generate seismic signals with a higher signal-to-noise ratio compared to the generated infrasound. This is true especially for smaller events, as the infrasound requires a higher flow depth/discharge to overcome the background noise levels, which, in case of infrasound, may be larger compared to the generally quieter seismic wavefield [Bowman et al., 2005; Brune and Oliver, 1959].

The distinct proposed infrasonic and seismic source processes are discussed in detail in the following Section 6.3.1 and 6.3.2 respectively.

6.3.1: The infrasound source mechanism within debris flows

According to previous experimental studies and numerical modelling on water flows [Schmandt et al., 2013] and debris flows [Marchetti et al., 2019; Coco et al., 2021], the infrasound by debris flow is thought to be radiated by flow waves and oscillations that develop at the free surface of the flow and collide with the atmosphere generating small pressure perturbances in the air.
The results presented in this thesis suggest additional constraints on the source mechanism of infrasound by debris flows. In particular, we propose that, within debris flows, the infrasound is radiated by turbulence induced non-stationary free surface waves and oscillations (Figure 6. 23), generated as the flow interacts with channel irregularities [Belli et al., 2021(a); Belli et al., 2022; Coco et al., 2021] or with the riverbed roughness [Horoshenkov et al., 2013].
Although these infrasonic sources are likely active along the entire length of the flow [Marchetti et al., 2019], the infrasonic array processing performed in this thesis, and discussed in Section 6.1.4, clearly revealed that the infrasonic signals by Illgraben debris flows are dominated by the coherent signal components generated at fixed positions along the channel.

In agreement with the infrasonic array processing results, we propose that, at Illgraben, the infrasound radiation by debris flows is enhanced downstream of check dams and steep bends, and therefore we suggest that the infrasound by debris flows, despite being likely generated along the entire flow, is preferentially radiated in fixed locations corresponding to significant channel irregularities.

This interpretation agrees with fluid dynamic theory [Henderson, 1996; Chaudhry, 2008] and with previous experimental studies [Feng et al., 2014; Tokyay and Yildiz, 2007] and numerical models [Coco et al., 2021], predicting that the water surface displacements (waves and oscillations) are mostly generated where the turbulence is stronger and, therefore, wherever the flow encounters significant channel irregularities [Belli et al., 2022]. In particular, Feng et al. [2014] observed an intense infrasound radiation at the base of a dam and, based on the model by Ostrovsky and Bedard [2002] on infrasound produced by the fall of large objects into water, proposed that, there, infrasonic waves are preferentially radiated by a dipole-type source generated by water falling into the absorption pool.

Therefore, the channel irregularities, such as topographic steps (check dams) and accentuated channel bends, represent the main sources of the flow surface oscillations and thus act as locations for a preferential infrasound radiation (Figure 6. 24).

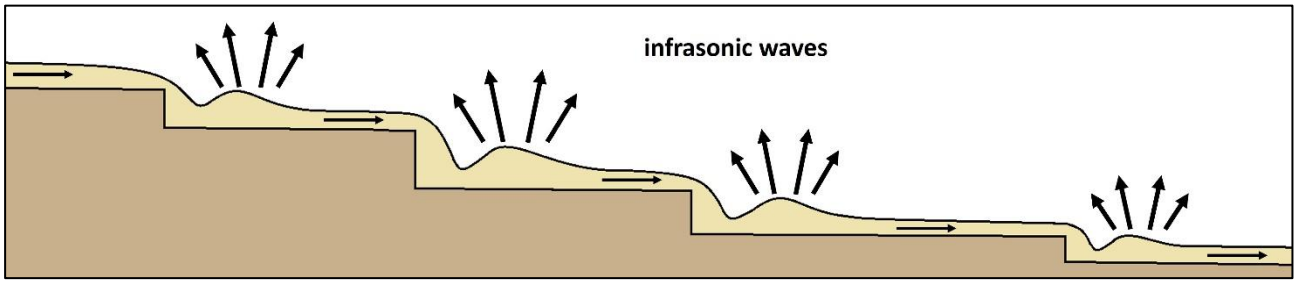

Figure 6. 24: sketch of a debris flow flowing along a channel sector with four check dams. The development of the flow surface waves and water splash downstream the free overfall at check dams causes these structures to act as locations of a preferential infrasound radiation by the debris flow.

This interpretation, suggested by the results of the array processing applied to the debris-flow infrasonic signals (Section 6.1.3), is also consistent with the experimental relations observed between the debris-flow parameters and the recorded infrasonic maximum RMSA (Figure 6. 18, Section 6.2.1) [Belli et al., 2022], showing an increase of the generated infrasonic amplitude as flow velocity, maximum depth or unit discharge increase. According to fluid dynamics [Henderson, 1996; Chaudhry, 2008], an increase in these flow parameters indeed enhances the development of a higher and more intense turbulence in the flow, thus inducing larger waves and water splashes at the free

surface of the flow. This scenario is in agreement with Tokyay and Yildiz [2007], who predict an increase in the amplitude and length of the waves induced at the base of a supercritical waterfall as the flow depth increases (see Eq. 1. 10, Section 1.2.2, Chapter 1).

These increased amplitude surface waves collide with a higher energy with the atmosphere, causing stronger pressure perturbations in air and hence radiating higher-amplitude infrasound waves [Ostrovsky and Bedard, 2002].

The proposed infrasound source mechanism based on turbulence induced surface oscillations, developing mostly at topography changes (e.g., free overfall at drop/dams) or other channel irregularities (e.g., bends), is also in agreement with the inverse relation observed between the infrasonic peak frequency and the flow parameters [Belli et al., 2022], showing a decrease of the peak frequency with increasing the flow velocity, depth or discharge (Figure 6. 22, Section 6.2.2).

Larger flows generate surface oscillations with longer wavelengths [Tokyay and Yildiz, 2007] (see Section 1.2.2, Chapter 1), which, for the same flow speed, lead to longer periods of the infrasonic sources and therefore radiate lower frequency infrasound [Belli et al., 2022].

This agrees with the numerical modelling by Coco et al. [2021] of the infrasonic pressure field generated by a water flow downstream a dam for different flow depths and dam heights. They predict a decrease of the radiated infrasound frequency when the flow depth (or discharge) increases for a fixed dam height. Instead, they predict the absence of significant infrasound radiation, regardless of the flow discharge, when the flow occurs within flat channels lacking any irregularities (bed roughness topographic steps, bends), consistent with the infrasonic source mechanism based on the waves and water splashes induced at the channel irregularities, presented in this section.

Furthermore, the infrasound source mechanism based on turbulence-induced surface oscillations discussed here also qualitatively explains the observed wide infrasound spectrum: turbulence structures, like eddies, cover a wide range of dimensions over which they also generate non-stationary flow surface displacements [Belli et al., 2022]. This produces a wide frequency spectrum of pressure variation in the atmosphere [Feng et al., 2014].

6.3.1.1 The physical model: the wave-piston analogy

The waves and water splashes induced by the turbulence downstream the channel irregularities in supercritical flows, such as almost all Illgraben debris flows (see Figure 3. 15, Section 3.4.1, Chapter 3), do not remain in fixed position along the channel but migrate along it with a velocity which is the

vectorial sum of the velocity of the flow and of the velocity of the waves with respect to the flow (see Eq. 1. 7-9, Section 1.2.2, Chapter 1).

The development and motion of the waves causes, at each point, the surface of the flow to move continuously up and down, pushing the atmosphere and thus radiating infrasound. We propose that the motion of the flow surface can be modelled as a series of vertically oscillating pistons ("wave-piston analogy") (Figure 6. 25), perturbating the atmosphere and thus generating pressure disturbance in the air propagating as infrasound. The generated pressure field can be defined starting from the wave equation of the acoustic pressure, describing the properties of a sound field in space and time and how those properties evolve, defined as [Carley, 2001]:

$$\frac{\partial^2 p}{\partial t^2} = c^2 \nabla^2 p \qquad \text{(Eq. 6. 13)}$$

where p is the acoustic pressure field.

A piston oscillating periodically along the z axis at frequency ω and with maximum velocity amplitude u_{max} will be moving vertically with a velocity (u) equal to:

$$u(t,z) = u_{max} e^{i(\omega t - kz)} \qquad \text{(Eq. 6. 14)},$$

where k is the wavenumber and i is the imaginary unit.

The piston hits the air and induces the acoustic pressure field given by [Carley, 2001]:

$$p(t,z) = c\rho u_{max} e^{i(\omega t - kz)} = p_{max} e^{i(\omega t - kz)} \qquad \text{(Eq. 6. 15)},$$

where p_{max} is the maximum pressure amplitude.

Therefore, the pressure field generated by the piston oscillates with a frequency (ω) equal to the oscillation frequency of the piston itself.

Based on our wave-piston analogy (Figure 6. 25), the expression defined for the acoustic pressure field generated by a moving piston (Eq. 6. 15) is assumed to be valid also for the infrasonic field generated by the oscillating surface of a debris flow. Therefore, the oscillation frequency ω depends on the length (L_{sp}) of the waves and water splashes generated at the flow surface and on the velocity (v_{wc}) at which these surface structures migrate along the channel and, as:

$$\omega = \frac{v_{wc}}{L_{sp}} \qquad \text{(Eq. 6. 16)}.$$

The size of the surface waves, as well as their velocity (see Eq. 1. 7, Section 1.2.2, Chapter 1), in turn is controlled by flow velocity and depth (or discharge rate) and channel geometry, as previous theoretical, numerical and experimental studies on water flows predict [Henderson, 1996; Chaudhry, 2008; Tokyay and Yildiz, 2007; Coco et al., 2021].

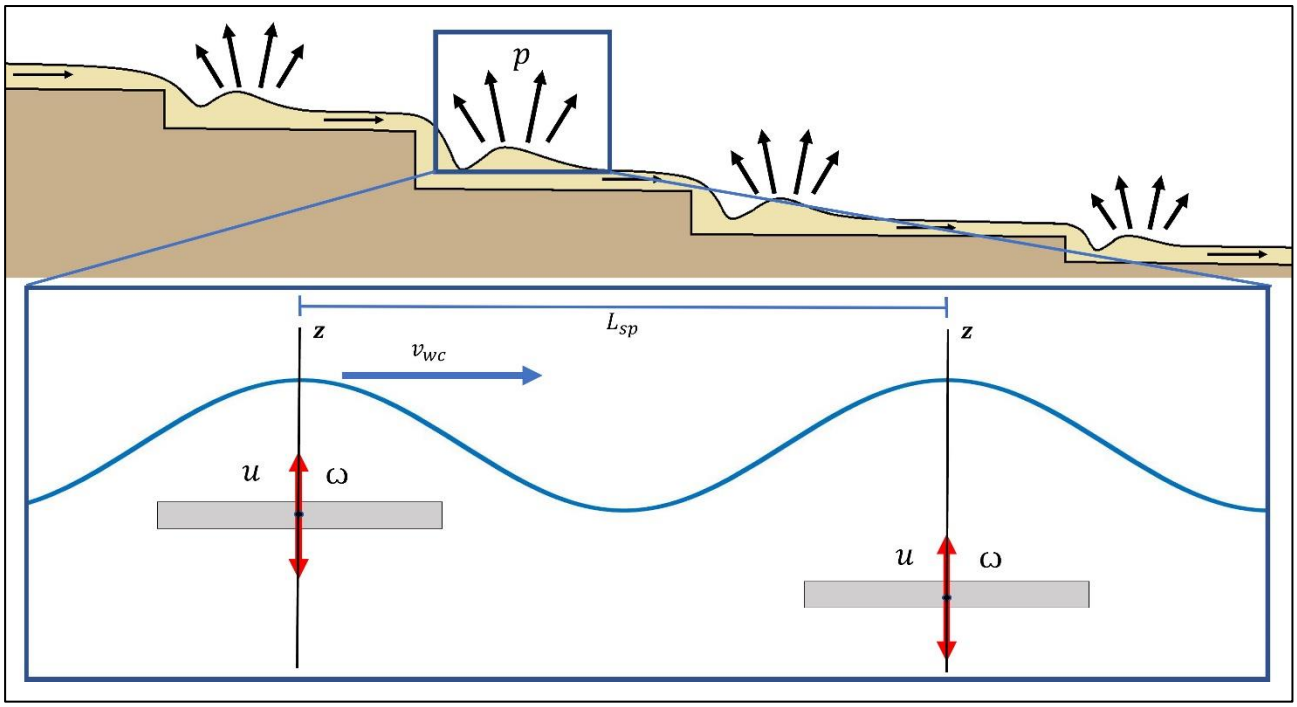

Figure 6. 25: the "wave-piston analogy". The motion of the debris-flow surface waves can be modelled as a series of pistons moving up and down and oscillating at a given frequency ω. The motion of the flow surface radiates an acoustic pressure field which oscillates at the same frequency as the pistons (as defined by Eq. 6. 15).

The physical model for the infrasonic radiation by debris flows described in this Section (Figure 6. 25) is consistent with the decrease observed in the recorded infrasonic peak frequency with increasing debris-flow depth and discharge (see Figure 6. 22, Section 6.2.2). Indeed, as their flow depth increases, the debris-flows are predicted to generate larger turbulence-induced waves at the flow free surface [Belli et al., 2022]. According to Eq. 6. 16, the development of these longer waves causes, for the same flow velocity, the flow surface to oscillate at a lower frequency and therefore radiates lower frequency infrasound (Eq. 6. 15), in agreement with the numerical modelling by Coco et al. [2021] (see Section 2.2, Chapter 2).

6.3.1: The seismic source mechanism within debris flows

Concerning the seismic wavefield, the results presented in this thesis do not allow to add significant constraints to the seismic source mechanism by debris flows. Therefore, we rely on the existing models for seismic energy radiation by rivers [Burtin et al., 2008; Schmandt et al., 2013; Tsai et al., 2012] and debris flows [Burtin et al., 2009; Kean et al., 2015; Lai et al., 2018; Farin et al., 2019; Zhang et al., 2021a] (see Section 2.1, Chapter 2), which attribute the generation of seismic waves to solid particle collisions and friction at the channel bed and banks and to fluid dynamic structures. These processes all induce fluctuations of the force exerted at the base of the debris flow, which in turn trigger the radiation of the seismic waves.

However, the analyses carried out in this thesis revealed that, within debris flows, the seismic source processes act independently of the infrasound source mechanism (see Section 5.1, Chapter 5, and Section 6.1, Chapter 6).

In addition, this thesis highlighted a strong influence of the debris flow parameters on its seismic radiation [Belli et al., 2022]. In particular, it is observed that the generated seismic amplitude linearly scales with the flow depth and discharge (see Section 5.2.1, Chapter 5, and Section 6.2.1, Chapter 6). These findings are in excellent accordance with the accepted source mechanism for debris-flow seismicity. An increased flow depth or discharge increases transport capability of the solid particles, with debris flows that have proved capable of transporting boulders with a diameter as large as the flow depth [Badoux et al., 2009]. In addition, the increased water level leads to a larger development of fluid dynamic structures [Tokyay and Yildiz, 2007] and a larger wetted perimeter.

The evaluation of the different contribution of these processes to the recorded seismic signals is impossible with our seismic data only and further dedicated field analysis and study would be required for this purpose. In addition, experimental confirmations would involve the comparison with boulder size data from video analysis, that needs to be addressed in future studies.

However, it is reasonable to expect that the greater transport capability, the increased development of fluid dynamics structures and the enlarged wetted perimeter, all result in stronger and more frequent solid particle impacts and in an increased friction with channel bed and banks. This scenario of more energetic and frequent particle collisions and of increased friction leads to the generation of larger stress fluctuations at the base of the flow, so that higher amplitude seismic waves are expected to be radiated by a debris flow as a result of the increased water level [Belli et al., 2022].

In contrast the comparison performed in this thesis between the seismic frequency content generated by the debris flows and the flow parameters (see Section 5.2.2, Chapter 5, and Section 6.2.2, Chapter 6) revealed that the increase of the debris flow depth or discharge does not affect the peak frequency of the recorded seismic signals. This agrees with the physical models for the seismic waves radiated by solid particle collisions in rivers [Tsai et al., 2012] and debris flows [Kean et al., 2015; Lai et al., 2018; Farin et al., 2019; Zhang et al., 2021a], predicting that the recorded seismic peak frequency only depends on the minimum distance between the channel and the recording sensor, consistently with what has been already observed for Illgraben debris flows [Wenner et al., 2019; Marchetti et al., 2019].

6.4 Implications for debris-flow monitoring

The results obtained in this thesis also highlight the potential of using the seismo-acoustic signals for the debris-flow monitoring, specifically for the Illgraben catchment.

Among them, in particular, the array processing revealed that the infrasonic signals are dominated by clusters of coherent detections generated in fixed positions along the channel, in particular in correspondence with significant channel irregularities, such as the check dams and some steep bends of the channel. In addition, the analysis showed that many detection clusters highlighted by the array processing applied to the four presented debris-flow events (see Section 5.1.4, Chapter 5, and Section 6.1.4, Chapter 6) are observed for multiple events (Table 6. 1). These shared detection clusters point at some channel positions that act as locations for preferential infrasonic radiation for most Illgraben debris flows.

Table 6. 1: list of the infrasonic detection clusters identified for the four presented Illgraben debris-flow events. For each cluster both the back-azimuth values and the corresponding channel position are reported.

Infrasonic detection cluster		Debris-flow event			
B_{az} (°N)	Identified channel position	2017/06/03	2019/06/21	2019/07/15	2019/08/20
190-180	More upstream dams (CD 10)	✓	✓		✓
170-173	Upper catchment mouth	✓	✓		

165	Irregular channel section				✓
156	CD 16	✓	✓	✓	
152	Steep channel bend				✓
110	CD 20	✓	✓	✓	✓
90	CD 21	✓	✓	✓	
80	CD 22	✓	✓	✓	✓
35	CD 24	✓		✓	✓
20	CD 27		✓		✓
17-16	CD 28		✓	✓	✓

The fact that recurrent infrasonic detection clusters are observed for multiple events reveals that the Illgraben debris flows share a common infrasonic signature, which can be used to automatically identify a debris flow in progress [Marchetti et al., 2019]. An ongoing event can therefore be detected in real time through the identification of the sequence of some of the detection clusters expected at Illgraben, which instead is not predicted for other sources.

For early warning purposes, the cluster pointing at the most upstream channel locations are of course the most significant, because these allow to identify the debris flow when it is still in the most upstream channel sectors, thus guaranteeing an earlier detection of the event. In particular, among these, the clusters of 190-180°N (~CD 10), 156°N (CD 16), 110°N (CD 20), 90°N (CD 21) and 80°N (CD 22) are observed for at least three of the four presented events (Table 6. 1). Therefore, for example an early warning system at the Illgraben can be designed to issue an alert once two (or more) of these detection clusters are sequentially identified within a reasonable amount of time.

Since the infrasonic radiation by debris flows proved to depend on the channel geometry and irregularities, the use of the infrasonic array processing for the event detection in other debris flow basins requires a prior analysis aimed to identify the recurrent features of the recorded infrasonic signals, which can then be used as attributes of the events occurring in that specific site. In agreement with our findings, the potential and timing of an infrasound based early warning system for a given debris-flow catchment can be evaluated theoretically a priori, with an analysis of the channel morphology aimed to identify the channel irregularities virtually able to radiate coherent infrasonic signal components.

In addition to automatic event detection via the real-time infrasonic array analysis, other elements useful for the debris flow monitoring are suggested by the comparison between the seismo-acoustic signals and the debris flow hydraulic and physical features shown in this thesis (see Section 5.2,

Chapter 5, and Section 6.2, Chapter 6). In particular, results showed that the amplitudes of the recorded infrasonic and seismic signals linearly scale with the flow depth and with the discharge per unit channel width, while an inverse relation is observed between the infrasonic peak frequency and the flow velocity, depth and unit discharge.

These relations indicate how the infrasonic and seismic amplitudes and, at least for major events, also the infrasonic peak frequency could be used for monitoring purposes at the Illgraben. More specifically, the computed best fit empirical equations (Eq. 6. 4-11), once correctly derived and tested, are potentially able to provide in real-time an indirect estimate of the flow depth and/or discharge of an ongoing debris flow based only on the seismo-acoustic observations, even if no in-torrent measurement, e.g. flow velocity and flow depth, is available [Belli et al., 2022].

The installation of a seismo-acoustic station in the upstream portion of a debris-flow catchment can thus provide crucial information on the size of a debris flow before it reaches the most sensible areas of the catchment.

The same goal could also be achieved with the deployment of altimeters in the upstream sectors of the channel. However, despite being able to provide more reliable depth measurements, these sensors involve installation and maintenance difficulties, since they require to be hung over the channel and are therefore prone to be destruction by the debris flows; in addition, the upstream sections of a debris-flow catchment are usually hardly accessible sites where sensor deployment and maintenance and real time data streaming is usually complex. On the contrary, being installable some hundreds of meters from the channel, the seismo-acoustic sensors can be deployed in more accessible sites and therefore they do not risk damage from the debris flows and commonly require less deployment and maintenance efforts. This further highlights the potential to use seismo-acoustic signals for debris-flow monitoring and risk management, not only for event detection [Chmiel et al., 2021; Kogelnig et al., 2014; Marchetti et al., 2019; Walter et al., 2017], but also for real-time estimates of debris-flow depth and/or discharge [Belli et al., 2022]. For example, Schimmel et al. [2022] recently showed that for small sensor-to-channel distances (a few meters), a first order estimation of the debris-flow volume can be obtained based on the recorded seismic signal.

Again, since the characteristics of the generated seismic-acoustic signals have proved to be strongly dependent on the characteristics of the debris flow basin and the events that occur there, before the recorded seismic-acoustic signals can be used to estimate the depth and or the discharge of the debris flows occurring at other sites, detailed analyses are needed to derive empirical relationships as accurate as possible for the debris flow basin under consideration.

In conclusion, obtained results show how the debris-flow activity at Illgraben, and maybe at other sites, could be effectively monitored with the use of a seismo-acoustic station, consisting of an infrasonic array and a seismometer collocated with the central element of the array. The infrasonic array processing has been shown indeed to detect in real time an occurring debris flow at Illgraben, by highlighting the coherent signal components generated at some of the check dams displaced along the channel. Once the debris flow has been detected, the array processing and, although more roughly, the seismo-acoustic cross-correlation allow to approximately locate the debris flow through time, following its motion downstream the channel. Furthermore, based on predetermined and tested empirical relations (like Eq. 6. 4-11), the recorded seismic and infrasonic amplitudes could be used to estimate in real time the flow depth and/or discharge and the corresponding expected peak values of an ongoing debris flow some minutes before it reaches the most sensible locations, allowing to implement risk reduction interventions (e.g. the evacuation of dangerous areas).

Conclusions

This doctoral thesis was focused on the analysis of the infrasonic and seismic energy radiation by debris flows. Occurring as sudden fast floods capable of carrying meter sized boulders within steep catchments [Coussot and Meunier, 1996], debris flows represent a major hazard in worldwide mountain environments [Dowling and Santi, 2014] (see Section 1.1-3, Chapter 1).
Although the debris-flow alert systems have been traditionally based on rainfall and in-channel flow measurements [Arattano and Marchi, 2008; Hürlimann et al., 2019] (see Section 1.4, Chapter 1), in the last decades the use of seismo-acoustic signals for studying and monitoring debris flows emerged as a new promising technique [Arattano, 1999; Burtin et al., 2009; Burtin et al., 2014; Walter et al., 2017; Lai et al., 2018; Marchetti et al., 2019] (see Chapter 2).
A debris flow is indeed an energetic source of both seismic and infrasonic waves. However, the source mechanisms of both infrasonic and seismic waves and their connection to debris-flow dynamics are not yet fully understood and an accurate infrasound radiation model is still missing.

Given this framework, in this thesis the infrasonic and seismic signals generated by debris flows that occurred at the Illgraben during the three debris flow seasons 2017-2019 were analysed, during which 18 events were observed (see Chapter 3).
Thanks to the measurement system displaced along the Illgraben channel, these events were characterized in terms of physical and hydraulic parameters, such as total volume, front velocity, maximum depth and flow bulk density (see Section 3.4, Chapter 3).
More specifically, we analysed the data recorded by a seismo-acoustic station, consisting of an infrasonic array and a collocated seismometer, located on the debris fan in front of the catchment at a minimum distance of ~550 m from the channel (see Section 3.3, Chapter 3). By analysing the recorded signals, it is observed that the seismic signals are systematically characterized by a higher signal-to-noise ratio compared to the corresponding infrasonic ones.

The recorded infrasonic and seismic debris-flow signals were analysed in the time domain by applying the RMSA analysis (see Section 4.1, Chapter 4). The RMSA analysis allowed to characterize the seismo-acoustic signals in terms of amplitude envelopes, maximum RMSA values and amplitude peak times. The comparison between infrasonic and seismic signals (see Section 5.1, Chapter 5) revealed that, for Illgraben debris flows, higher infrasonic amplitude generally corresponds to higher seismic amplitudes and that the radiation peaks of the two wavefields are almost simultaneous during each event (see Section 6.1, Chapter 6).
In addition, the ratio between the infrasonic and seismic RMSA envelope curves was computed for the entire duration of the debris-flow events. The results obtained for the six larger analysed events

showed that the Illgraben debris flows are characterized by a shared trend of the infrasonic-to-seismic RMSA ratio, indicating that Illgraben debris-flow events are characterized by a peculiar succession of the seismo-acoustic energy generating processes, which tend to be repeated during each event (see Section 6.1, Chapter 6). In particular, the constant infrasound-to-seismic RMSA ratio, established for all events once the peak phase has been reached, indicates that, during the debris-flow degrowth phase, the energy partition between the atmosphere and the ground is almost perfectly constant in time and equal to the one observed at the event seismo-acoustic peak phase.

The recorded seismo-acoustic signals were also analysed in the frequency domain (see Section 4.2, Chapter 4) and, for each event, the spectra and the spectrograms of both infrasonic and seismic signals were computed. The spectral analysis revealed that the two wavefields are characterized by different frequency contents, with the seismic energy widely distributed from ~1 Hz up to ~40 Hz and the infrasonic one limited just to the ~1-10 Hz spectral window (see Section 5.1, Chapter 5). In addition, the seismo-acoustic signals are characterized by different peak frequencies, ranging between 3.4 and 6 Hz for infrasound and stable at 7.2 ± 0.3 Hz for seismic signals. Furthermore, while the recorded seismic peak frequency is almost constant for all the events, the infrasonic peak frequency varies from event to event and inversely scales with the recorded signal amplitude.
The different frequency content of the recorded infrasonic and seismic signals, being demonstrated to be not imputable to propagation and site effects, clearly indicates that the two wavefields are generated by different decoupled processes simultaneously acting at the flow surface and at the riverbed respectively (see Section 6.1, Chapter 6). In addition, the constant seismic peak frequency is in perfect accordance with the models by Tsai et al. [2012] and Lai et al. [2018] for the seismicity of rivers and debris flows, which predict that the peak frequency of the recorded seismic signals only depends on the minimum distance between the channel and the recording sensor.

To explore the interconnection between the infrasonic and seismic wavefields generated by debris flows, the seismo-acoustic cross-correlation analysis (see Section 4.3, Chapter 4) was applied to the recorded signals. The analysis revealed that the Illgraben debris flows are characterized by a strong seismo-acoustic cross-correlation, observed along almost the entire duration of the events (see Section 5.1, Chapter 5).
Therefore, despite the spectral analysis highlighted that the infrasonic and seismic signals radiated by the flow are decoupled, the high seismo-acoustic cross-correlation suggests that the two wavefields are to some extent correlated with each other and are equally modulated in amplitude during the event

(see Section 6.1, Chapter 6). This evidence is in perfect agreement with the positive correspondence emerged between the recorded infrasonic and seismic amplitudes.
Furthermore, the maximum of the cross-correlation function is observed for a time delay of the infrasound with respect to the cross-correlated seismic signal (shift) ranging between a minimum of ~0.8 s and a maximum of ~2.3 s (see Section 5.1, Chapter 5). These values allow to exclude a local seismic-to-infrasonic energy transmission, that would produce a high cross-correlation but with a stable shift value dependent solely on signal characteristic frequency, and are instead consistent with the correlation between the infrasonic and seismic primary signals produced at the source. Given the different propagation velocity of the two wavefields and assuming that the two wavefields are radiated approximately at the same location, the varying time delay observed in the seismo-acoustic cross-correlation indeed results from the signal propagation distance. Therefore, the time delay can be used to reconstruct the source-to-receiver distance and thus to locate in the channel the main source of the recorded seismo-acoustic signals through time (see Section 6.1, Chapter 6). The localization of the source performed for the 2019/07/15 event is perfectly consistent with the migration of the debris flow along the Illgraben channel (see Section 6.1, Chapter 6). This highlights how the seismo-acoustic cross-correlation could be used to approximately locate ongoing debris flows at Illgraben.

To deeply investigate the infrasound source mechanism within debris flows we applied the array processing (see Section 4.4, Chapter 4) to infrasound data. Results show that the generated infrasound is dominated by coherent signal components, each characterized by constant back-azimuth and thus produced in fixed position along the torrent channel (see Section 5.1, Chapter 5). In particular, the computed back-azimuth values point at some of the check dams displaced along the stream or at other channel sectors characterized by significant irregularities, such as steep bends and/or topographic steps. This evidence suggests that, despite the infrasound is likely produced along the entire length of the debris flow, the significant channel irregularities act as location of preferential infrasonic radiation (see Section 6.1, Chapter 6). In particular, for the Illgraben, the check dams result as the dominant sources of infrasound. The observed predominance of the significant channel irregularities on the infrasound radiation by debris flows is in agreement with fluid dynamics predictions [Henderson, 1996; Chaudhry, 2008] and with previous numerical models [Coco et al., 2021] and experimental observations [Feng et al., 2014; Tokyay and Yildiz, 2007] (see Section 6.1, Chapter 6).
Furthermore, the infrasonic array processing permits to identify the position of the infrasonic source along the entire event, thus allowing to track the motion of the debris flow along the entire Illgraben channel. The obtained localization is perfectly consistent with the rough one based on the seismo-acoustic cross-correlation (see Section 6.1, Chapter 6). In addition, for all events, the array processing

showed that the maximum infrasonic amplitudes are generated when the main body of the debris flow is within the channel sector characterized by the minimum distance from the recording site, in agreement with predictions by Marchetti et al. [2019].

In order to explore how the generated seismo-acoustic signals relate to the debris flow dynamics and to its hydraulic specifics, the features of the infrasound and seismic signals were compared with measured flow parameters, i.e. flow velocity, flow depth and flow density (see Section 5.2, Chapter 5).

Results show that infrasonic and seismic maximum RMSA positively correlate with front velocity and scale linearly with maximum depth and flow peak discharge per unit channel width, computed as the product of front velocity and maximum depth, while no clear relation is instead observed with flow density. The observed positive linear relationship between seismic amplitude and flow depth or discharge is in excellent agreement with Andrade et al. [2022] and Coviello et al. [2019], who, analysing lahars and debris flows respectively, also observed positive relation between seismic amplitudes and flow discharge or kinetic energy of the flow.

These results suggest that the seismo-acoustic energy radiation by debris flows is strongly influenced by the flow features, with higher flow velocities and/or larger flow depths observed to generally produce higher infrasonic and seismic amplitudes, and that it is likely linearly controlled by the debris flow depth and/or discharge (see Section 6.2, Chapter 6). The linear influence of the flow depth on the generated seismo-acoustic amplitudes appears furtherly confirmed by the comparison between the infrasonic and seismic RMSA curves and the hydrograms recorded during the Illgraben debris-flow events of 2019/06/21 and 2019/07/01, showing an excellent linear correspondence between the seismo-acoustic RMSA and the recorded flow depth.

The comparison between the seismo-acoustic frequency content and flow features instead revealed that, differently from seismic signals, characterized by an almost constant peak frequency regardless of the hydraulic data, the infrasonic peak frequency inversely scales with flow parameters, decreasing as the front velocity, the flow maximum depth or the unit peak discharge increases (see Section 5.2, Chapter 5). This evidence is in perfect agreement with previous experimental observations on debris flows by Marchetti et al. [2019] and with the numerical modelling by Coco et al. [2021], this latter modelling the infrasonic pressure field produced by a water flow downstream a topographic step (dam) and predicting a decrease in peak frequency of the generated infrasonic waves as the flow depth or the height of the step increases.

The observed inverse trend between infrasound peak frequency and flow parameters suggests that larger flows (events with larger discharge and/or flow depth) radiate lower frequency infrasound [Belli et al., 2022]. According to fluid dynamics and experimental observation [Tokyay and Yildiz, 2007], an increased flow depth/discharge produces larger and longer waves at the flow surface. Since the waves and oscillation at the flow surface are believed to be the source of the infrasound radiation by debris flows [Marchetti et al., 2019], the increase of their wavelength (and therefore of their period) leads to the generation of lower frequency infrasound, as a result of the longer duration of the source process [Ostrovsky and Bedard, 2002], explaining the experimental evidences presented in this thesis. A similar trend is not expected for seismic signals, whose peak frequency only depends on the minimum distance between the channel and the seismometer [Tsai et al., 2012; Lai et al., 2018].

Based on presented results and taking into account previous models and experiments, a simplified conceptual source mechanism is proposed for the seismo-acoustic energy radiation by debris flows, according to which the infrasonic and seismic waves by debris flows are generated by different source processes acting simultaneously at the ground and at the surface of flow respectively, which, despite being intimately related to each other (i.e. controlled by the same flow parameters) and equally modulated in amplitude, are clearly decoupled (see Section 6.3, Chapter 6).

For seismic signals, presented results agree with previous models and observation of seismic energy radiation by rivers [Burtin et al., 2008; Schmandt et al., 2013; Tsai et al., 2012] and debris flows [Burtin et al., 2009; Kean et al., 2015; Lai et al., 2018; Farin et al., 2019; Zhang et al., 2021a], indicating that seismic waves are generated by solid particle collisions and friction with the riverbed and banks and by fluid dynamic structures. In addition, the comparison with hydraulic data presented in this thesis highlighted a strong influence of the debris flow parameters on its seismic radiation [Belli et al., 2022]. This agrees with accepted source models: an increased flow depth/discharge leads to a larger transport capability by the debris flow, to a larger wetted perimeter and to a larger development of the fluid dynamic structures, all resulting in stronger and more frequent solid particle impacts and in an increased friction with channel bed and banks, thus radiating higher amplitude seismic [Belli et al., 2022] (see Section 6.3, Chapter 6).

For the infrasound we propose a source mechanism in which infrasonic waves are generated by non-stationary turbulence-induced waves and oscillations that develop at the free surface of the flow [Feng et al., 2014; Marchetti et al., 2019; Ostrovsky and Bedard, 2002]. Despite being likely produced along the entire debris flow length, according to fluid dynamics and to the presented array processing

results, the formation of such surface waves is enhanced wherever the flow encounters channel irregularities, such as significative topographic steps, like check dams, and steep bends [Belli et al., 2022; Coco et al., 2021; Tokyay and Yildiz, 2007; Feng et al., 2014], which act as locations of preferential infrasound radiation. The development and the motion of these flow surface waves at the base of free overfall at check dams causes that, in every point, the flow surface continuously moves up and down, radiating infrasound [Ostrovsky and Bedard, 2002]. We therefore propose that this motion of the flow surface can be modelled as a series of pistons vertically moving and generating infrasound with a frequency that is equal to the oscillation frequency of the pistons themselves (see Section 6.3, Chapter 6). This oscillation frequency coincides with the rate of motion of the flow surface, which depends on flow velocity and on the size of the generated waves, that in turn is controlled by flow discharge rate and channel geometry, as previous numerical and experimental studies predict [Tokyay and Yildiz, 2007].

This model based on non-stationary turbulence induced flow surface oscillations is in also agreement with the relationships resulted between the infrasonic features and flow parameters. An increase in the flow depth/discharge enhances the development of larger turbulent flow structures [Henderson, 1996; Chaudhry, 2008], that in turn generate larger waves and turbulence-induced water splashes at the flow free surface [Tokyay and Yildiz, 2007], thus radiating higher-amplitude and lower frequency infrasound [Coco et al., 2021; Marchetti et al., 2019; Ostrovsky and Bedard, 2002] as a result of an increased flow depth/discharge (see Section 6.3, Chapter 6).

The validation of the proposed seismo-acoustic source mechanism would require additional numerical modelling aimed to reproduce the radiation processes and/or experimental tests that could be addressed in future studies.

Eventually, presented results highlights the potential of using the seismo-acoustic signals for debris flow monitoring and early warning. First, the infrasonic array processing has proven to be able to identify the debris flow passage at the main check dams located along the Illgraben channel, so that it can be used to detect in real time an ongoing debris flow in its initial phases. Moreover, the obtained empirical relations linking the seismo-acoustic signal features to the flow parameters suggests how infrasound and seismic signals could be used for the near real-time estimation of the size of an ongoing debris flow, at locations where seismo-acoustic recordings of past events are available, also when direct flow measurements are prevented, furtherly highlighting their potential for debris-flow monitoring and risk management.

Acknowledgements

I am grateful to reviewers Prof. Fabian Walter and the late lamented Dr. Velio Coviello for their valuable comments and suggestions that helped improve my thesis.
My thoughts go in particular to Velio Coviello, who tragically passed away a few days after having revised this thesis. Velio was a wonderful person and I'm sure he will leave a beautiful memory and a great void in anyone who knew him.

I also thank Doc. Brian McArdell for sharing the measured flow parameters of the analysed Illgraben debris flows.

Furthermore, I am very grateful to Prof. Emanuele Marchetti for supervising all my thesis work and my PhD. I also thank my colleague and friend Duccio Gheri, for the genuine cooperation we had during our PhD years.

Finally, a special thanks to Ilaria, who has always supported me and helped me through all the difficult moments.

Appendix

A1. Equation variables (in order of appearance)

Table A. 1: list of variables that appear in the equations presented in the thesis. For each variable, the used symbol and the unit of measurement are reported.

Symbol	Variable	Unit of measurement
τ	Shear stress	Pa
η	Rigidity coefficient	Pa·s
ε	Shear rate	1/s
τ_b	Yield stress	Pa
h_{cB}	Bingham fluid critical depth	m
ρ_f	Fluid density	Kg/m^3
E_s	Energy slope	-
v_w	Velocity of flow surface perturbations and waves (with respect to the flow)	m/s
Fr	Froude number	-
H	Flow depth	m
g	Acceleration of gravity	m/s^2
v_c	Flow critical velocity	m/s
E	Flow specific energy	m
v	Flow velocity	m/s
$\frac{v^2}{g}$	Velocity head	m
v_{wc}	Velocity of flow surface perturbations and waves (with respect to the channel banks)	m/s
A_{sp}	Height of water splash	m
z	Height of the fall	m
H_b	Flow depth over the brink of a dam	m

L_{sp}	Length of the water splash	m
Re	Reynolds number	-
L_f	Characteristic dimension of the flow	m
μ	Dynamic viscosity	Pa·s
B	Bingham number	-
μ_b	Dynamic viscosity Bingham material	Pa·s
$P_v(f, D)$	PSD of ground velocity	$(m/s)^2/Hz$
f	Frequency	Hz
D	Grain size	m
n_p	Number of particles	-
m_p	Mass of the particle	kg
ρ_s	Solid phase density	Kg/m^3
w_i	Particle impact velocity	m/s
t_i	Time interval between impacts	s
c_c	Rayleigh waves phase velocity	m/s
c_u	Rayleigh waves group velocity	m/s
$\chi(\beta)$	Dimensionless Seismic parameter	-
r_0	Source-to-receiver minimum distance	m
$P_v^T(f)$	Total PSD of ground velocity	$(m/s)^2/Hz$
L_s	Length of the debris-flow front (snout)	m
W_f	Flow width	m
D_{94}	Grain size 94^{th} percentile	m
ξ	Seismic ground parameter	- -
f_P	Peak frequency	Hz
Q_f	Quality factor	or dB/m
H_{max}	Maximum flow depth	m
ρ	Flow bulk density	Kg/m^3
Q_u	Peak flow discharge per unit channel width	m^2/s
MF_u	Peak mass flux discharge per unit channel width	Kg/m·s
n_w	Number of signal time windows	-
d_s	Signal duration	s

d_w	Window duration	s
ns_w	Number of samples in a signal time window	-
smp	Sampling rate	Hz
A	Signal amplitude	Pa or μm/s
$RMSA_i$	RMSA value corresponding to i-th signal window	Pa or μm/s
$I(r)$	Wave intensity at the distance r from the source	J/s·m^2
I_0	Wave intensity at the source	J/s·m^2
r	Source-to-receiver distance	m
λ	Wavelength	m
f_P	Peak frequency	Hz
Sa	Spectral amplitude	(Pa)^2/Hz or (μm/s)^2/Hz
f_{mp}	Manually picked frequency	Hz
df	Frequency interval	Hz
t_s	Time shift of the seismo-acoustic coupling	s
f_0	Characteristic frequency of the incident wave	Hz
x, y	Numerical series	-
N	Length of the numerical series	-
R_{xy}	Cross-correlation between x and y	-
s	Translation in the cross-correlation	-
B_{az}	Back-azimuth	°N
c	Speed of sound	m/s
c_a	Apparent velocity	m/s
L	Distance between two sensors of the array	m
β	Angle between the segment connecting two sensors of the array and the North	°
Δt	Time residual	s
N_t	Total number of sensor triplets	-
P_{max}	Infrasonic maximum RMSA	Pa
S_{max}	Seismic maximum RMSA	μm/s
R	Pearson correlation factor	-
P	Infrasonic RMSA	Pa
S	Seismic RMSA	μm/s

t	Time	s
T_s	Thickness of the resonant sediment layer	m
c_s	Propagation velocity of seismic shear waves	m/s
f_{HVSR}	Peak frequency of the HVSR curve	Hz
Δt_{s-i}	Recording time difference between seismic and infrasonic signals	s
c_{ss}	Propagation velocity of seismic surface waves	m/s
p	Acoustic pressure field	Pa
u	Piston velocity	m/s
u_{max}	Maximum piston velocity amplitude	m/s
ω	Oscillation frequency of the piston	rad/s or Hz
k	Wavenumber of the piston oscillation	1/m
p_{max}	Maximum pressure amplitude	Pa

A2. Seismo-acoustic RMSA ratio

In this section we show the evolution over time of infrasonic-to-seismic RMSA ratio array processing computed for the debris-flow events for which these results have not been presented earlier in the thesis (Figure A. 3).

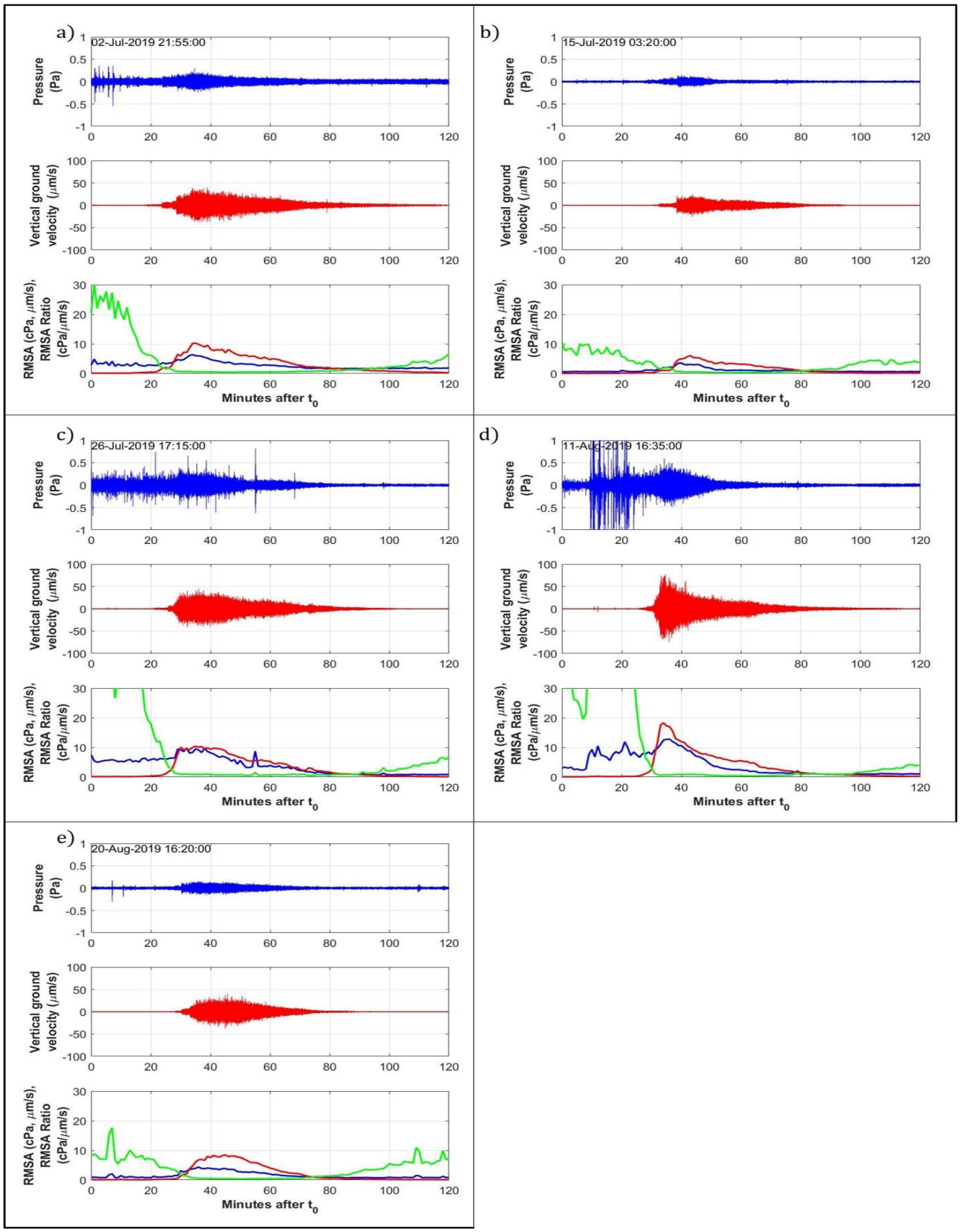

Figure A. 1: infrasonic (blue) and seismic (red) RMSA analysis of the 6 debris-flow events recorded at Illgraben on 2019/07/02 (a), 2019/07/15 (b), 2019/07/26 (c), 2019/08/11 (d) and 2019/08/20 €. The lower panel in each section shows both infrasonic (blue, cPa) and seismic (red, μm/s) RMSA, together with their ratio (green, cPa/(μm/s)).

A3. Seismo-acoustic cross-correlation

In this section we show the seismo-acoustic cross-correlation computed for the Illgraben debris-flow event on 2019/07/02 (Figure A. 2). For all the other events for which the seismic-acoustic cross-correlation was not shown in the thesis, the infrasonic track recorded at M4 sensor of the ILG array presented an anomalous high-frequency component or spikes due to signal clipping, which prevented the cross-correlation analysis with the seismic data recorded at the co-located ILL13 seismometer.

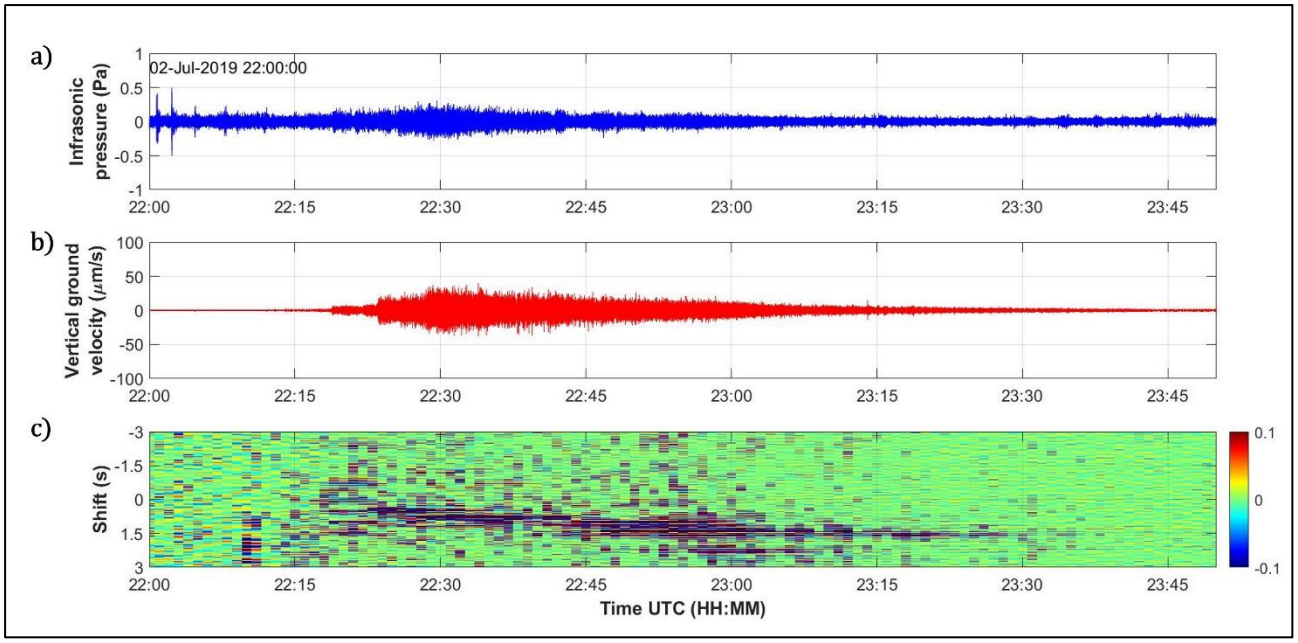

Figure A. 2: cross-correlation (c) between infrasonic (a) and seismic (b) signals generated by the 2019/07/02 Illgraben debris-flow event. The values of the seismo-acoustic cross-correlation are indicated by the colour bar on the side (c).

A4. Infrasonic array processing

In this section we show the infrasonic array processing results obtained for the debris-flow events for which these results have not been presented earlier in the thesis (Figure A. 3). For the 2018/07/25 event, here not shown, the array processing was not appliable cause only 2 sensors of the ILG array were working during the event. During the 2019/07/26 and 2019/08/11 events, the low signal-to-noise ratio, due to the intense thunder activity at the time of the events, prevented the computation of detailed infrasonic detections of the debris flows.

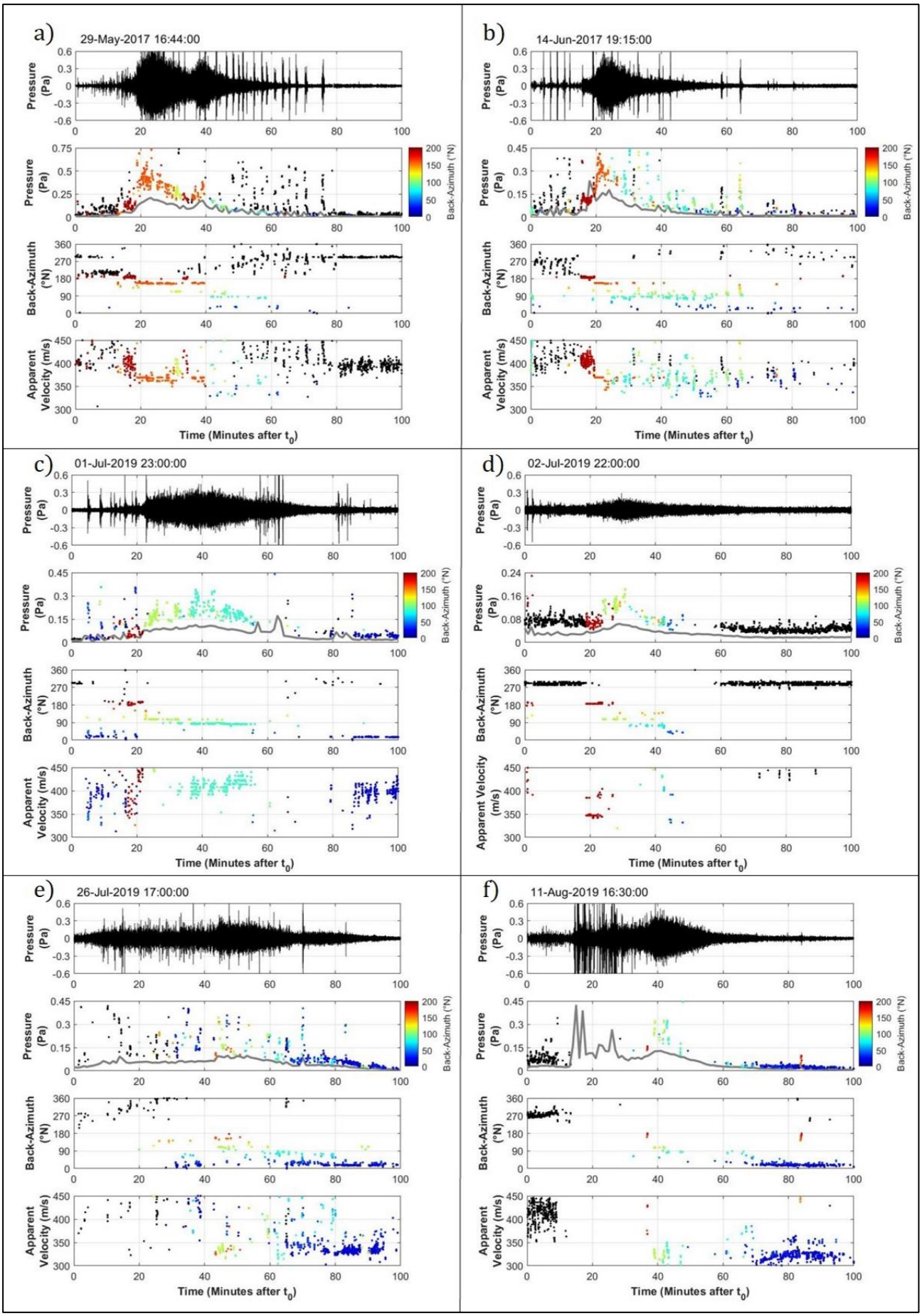
a)
29-May-2017 16:44:00
b)
14-Jun-2017 19:15:00
c)
01-Jul-2019 23:00:00
d)
02-Jul-2019 22:00:00
e)
26-Jul-2019 17:00:00
f)
11-Aug-2019 16:30:00
Pressure (Pa)
Back-Azimuth (°N)
Apparent Velocity (m/s)
Time (Minutes after t0)

Figure A. 3: infrasonic array processing results obtained for the Illgraben debris flows on 2017/05/29 (a), 2017/06/14 (b), 2019/07/01 (c), 2019/07/02 (d), 2019/07/26 (e) and 2019/08/11 (f). For each event we show: the 1-20 Hz band-pass filtered infrasonic track recorded at M and the infrasonic pressure, back-azimuth and apparent velocity of the infrasonic detections identified with the array processing. The grey line represents the RMSA of the infrasonic signal computed over 1-minute windows. Back-azimuth values in panels b, c, d and e are indicated by colours according to the colour bar.

References

Addison, K. (1987). Debris flow during intense rainfall in Snowdonia, North Wales: a preliminary survey. *Earth Surface Processes and Landforms*, *12*(5), 561-566.

Aki, K., & Richards, P. G. (2002). *Quantitative seismology*.

Allstadt, K. E., Farin, M., Lockhart, A. B., McBride, S. K., Kean, J. W., Iverson, R. M., ... & George, D. (2019). *Overcoming barriers to progress in seismic monitoring and characterization of debris flows and lahars* (Doctoral dissertation, Colourado School of Mines. Arthur Lakes Library).

Allstadt, K. E., Matoza, R. S., Lockhart, A. B., Moran, S. C., Caplan-Auerbach, J., Haney, M. M., ... & Malone, S. D. (2018). Seismic and acoustic signatures of surficial mass movements at volcanoes. *Journal of Volcanology and Geothermal Research*, *364*, 76-106.

Andrade, S. D., Almeida, S., Saltos, E., Pacheco, D., Hernandez, S., & Acero, W. (2022). A simple and general methodology to calibrate seismic instruments for debris flow quantification: application to Cotopaxi and Tungurahua volcanoes (Ecuador). *Landslides*, *19*(3), 747-759.

Angeli, M. G., Pasuto, A., & Silvano, S. (2000). A critical review of landslide monitoring experiences. *Engineering Geology*, *55*(3), 133-147.

Arattano, M. (1999). On the use of seismic detectors as monitoring and warning systems for debris flows. *Natural Hazards*, *20*(2-3), 197-213.

Arattano, M., & Marchi, L. (2008). Systems and sensors for debris-flow monitoring and warning. *Sensors*, *8*(4), 2436-2452.

Aulitzky, H. (1989). The debris flows of Austria. *Bulletin of the International Association of Engineering Geology-Bulletin de l'Association Internationale de Géologie de l'Ingénieur*, *40*(1), 5-13.

Badoux, A., Graf, C., Rhyner, J., Kuntner, R., & McArdell, B. W. (2009). A debris-flow alarm system for the Alpine Illgraben catchment: design and performance. *Natural hazards*, *49*(3), 517-539.

Bagnold, R. A. (1954). Experiments on a gravity-free dispersion of large solid spheres in a Newtonian fluid under shear. *Proceedings of the Royal Society of London. Series A. Mathematical and Physical Sciences*, *225*(1160), 49-63.

Bedard, A. J. (2021). Waterfall low-frequency vibrations and infrasound: implications for avian migration and hazard detection. *Journal of Comparative Physiology A*, *207*(6), 685-700.

Bedard, A., & Georges, T. (2000). Atmospheric infrasound. *Acoustics Australia*, *28*(2), 47-52.

Belli, G., Marchetti, E., Walter, F., McArdell, B., Chmiel, M., and Wenner, M.: Investigating infrasound sources within Illgraben debris-flows, EGU General Assembly 2021, online, 19–30 Apr 2021, EGU21-1226, https://doi.org/10.5194/egusphere-egu21-1226, 2021 (a).

Belli, G., Pace, E., & Marchetti, E. (2021) (b). Detection and source parametrization of small-energy fireball events in Western Alps with ground-based infrasonic arrays. *Geophysical Journal International*, *225*(3), 1518-1529.

Belli, G., Walter, F., McArdell, B., Gheri, D., & Marchetti, E. (2022). Infrasonic and Seismic Analysis of Debris-Flow Events at Illgraben (Switzerland): Relating Signal Features to Flow Parameters and to the Seismo-Acoustic Source Mechanism. *Journal of Geophysical Research: Earth Surface*, *127*(6), e2021JF006576.

Bennett, G. L., Molnar, P., McArdell, B. W., & Burlando, P. (2014). A probabilistic sediment cascade model of sediment transfer in the Illgraben. *Water Resources Research*, *50*(2), 1225-1244.

Bennett, G. L., Molnar, P., McArdell, B. W., Schlunegger, F., & Burlando, P. (2013). Patterns and controls of sediment production, transfer and yield in the Illgraben. Geomorphology, 188, 68-82.

Berger, C., McArdell, B. W., & Schlunegger, F. (2011). Direct measurement of channel erosion by debris flows, Illgraben, Switzerland. *Journal of Geophysical Research: Earth Surface*, *116*(F1).

Bessason, B., Eiríksson, G., Thórarinsson, Ó., Thórarinsson, A., & Einarsson, S. (2007). Automatic detection of avalanches and debris flows by seismic methods. *Journal of Glaciology*, *53*(182), 461-472.

Bingham, E. C., & Green, H. (1919). Paint, a plastic material and not a viscous liquid; the measurement of its mobility and yield value. In *Proc. Am. Soc. Test. Mater* (Vol. 19, pp. 640-664).

Bossan, E., 1992. Analysis of Debris Flow Initiation in French Alps. Cemagref, Intern. Rep. (in French).

Bowman, J. R., Baker, G. E., & Bahavar, M. (2005). Ambient infrasound noise. *Geophysical research letters*, *32*(9).

Brune, J. N., & Oliver, J. (1959). The seismic noise of the earth's surface. *Bulletin of the Seismological Society of America*, *49*(4), 349-353.

Burtin, A., Bollinger, L., Cattin, R., Vergne, J., & Nábělek, J. L. (2009). Spatiotemporal sequence of Himalayan debris flow from analysis of high-frequency seismic noise. *Journal of Geophysical Research: Earth Surface, 114*(F4).

Burtin, A., Bollinger, L., Vergne, J., Cattin, R., & Nábělek, J. L. (2008). Spectral analysis of seismic noise induced by rivers: A new tool to monitor spatiotemporal changes in stream hydrodynamics. *Journal of Geophysical Research: Solid Earth, 113*(B5).

Burtin, A., Hovius, N., McArdell, B. W., Turowski, J. M., & Vergne, J. (2014). Seismic constraints on dynamic links between geomorphic processes and routing of sediment in a steep mountain catchment. *Earth Surface Dynamics, 2*(1), 21.

Cannon, S. H., Gartner, J. E., Parrett, C., & Parise, M. (2003). Wildfire-related debris-flow generation through episodic progressive sediment-bulking processes, western USA. *Debris-Flow Hazards Mitigation: Mechanics, Prediction, and Assessment. Millpress, Rotterdam*, 71-82.

Chan, R. K. S., & Pun, W. K. (2004). Landslip warning system in Hong Kong. *Geotechnical News*, *22*(4), 33-35.

Chanson, H. (2000). Boundary shear stress measurements in undular flows: Application to standing wave bed forms. *Water Resources Research*, *36*(10), 3063-3076.

Chaudhry, M. H. (2008). Open-channel flow (Vol. 523). New York: Springer.

Chen, C. L. (1988). Generalized viscoplastic modeling of debris flow. *Journal of hydraulic engineering, 114*(3), 237-258.

Chmiel, M., Walter, F., Wenner, M., Zhang, Z., McArdell, B. W., & Hibert, C. (2021). Machine Learning improves debris flow warning. *Geophysical Research Letters, 48*(3), e2020GL090874.

Christie, D. R., & Campus, P. (2010). The IMS infrasound network: Design and establishment of infrasound stations. In *Infrasound monitoring for atmospheric studies* (pp. 29-75). Springer, Dordrecht.

Coco, M., Marchetti, E., & Morandi, O. (2021). Numerical Modeling of Infrasound Energy Radiation by Debris Flow Events. *Pure and Applied Geophysics*, 1-13.

Comiti, F., & Lenzi, M. A. (2006). Dimensions of standing waves at steps in mountain rivers. *Water resources research*, *42*(3).

Comiti, F., Marchi, L., Macconi, P., Arattano, M., Bertoldi, G., Borga, M., ... & Theule, J. (2014). A new monitoring station for debris flows in the European Alps: first observations in the Gadria basin. *Natural hazards*, *73*(3), 1175-1198.

Costa, J. E., & Williams, G. P. (1984). Debris-flow dynamics: US Geological Survey Open File Report 84-606, 1 VHS videotape.

Coussot, P., & Meunier, M. (1995). Experimental Study of Debris Flows. *Journal of Hydraulic Engineering*, *121*(5), 438-440.

Coussot, P., & Meunier, M. (1996). Recognition, classification and mechanical description of debris flows. *Earth-Science Reviews*, *40*(3-4), 209-227.

Coussot, P., & Piau, J. M. (1994). On the behaviour of fine mud suspensions. *Rheologica acta*, *33*(3), 175-184.

Coussot, P., & Piau, J. M. (1994). Rheology of very concentrated suspensions of force-free particles. *Les Cahiers de Rhéologie*, *13*, 266-277.

Coviello, V., Arattano, M., Comiti, F., Macconi, P., & Marchi, L. (2019). Seismic characterization of debris flows: insights into energy radiation and implications for warning. *Journal of Geophysical Research: Earth Surface*, *124*(6), 1440-1463.

Cramer, O. (1993). The variation of the specific heat ratio and the speed of sound in air with temperature, pressure, humidity, and CO2 concentration. *The Journal of the Acoustical Society of America*, *93*(5), 2510-2516.

Cui, P., Zeng, C., & Lei, Y. (2015). Experimental analysis on the impact force of viscous debris flow. *Earth Surface Processes and Landforms*, *40*(12), 1644-1655.

D'agostino, V., & Marchi, L. (2001). Debris flow magnitude in the Eastern Italian Alps: data collection and analysis. *Physics and Chemistry of the Earth, Part C: Solar, Terrestrial & Planetary Science*, *26*(9), 657-663.

Damm, B., & Felderer, A. (2013). Impact of atmospheric warming on permafrost degradation and debris flow initiation: A case study from the eastern European Alps. *E&G Quaternary Science Journal*, *62*(2), 136-149.

Davies, T. R. H. (1986). Large debris flows: a macro-viscous phenomenon. *Acta Mechanica*, *63*(1-4), 161-178.

De Angelis, S., Fee, D., Haney, M., & Schneider, D. (2012). Detecting hidden volcanic explosions from Mt. Cleveland Volcano, Alaska with infrasound and ground-coupled airwaves. *Geophysical Research Letters*, *39*(21).

De Carlo, M., Ardhuin, F., & Le Pichon, A. (2020). Atmospheric infrasound generation by ocean waves in finite depth: unified theory and application to radiation patterns. *Geophysical Journal International*, *221*(1), 569-585.

de Groot-Hedlin, C. D., & Hedlin, M. A. (2014). Infrasound detection of the Chelyabinsk meteor at the USArray. *Earth and Planetary Science Letters*, *402*, 337-345.

Delle Donne, D., Ripepe, M., De Angelis, S., Cole, P. D., Lacanna, G., Poggi, P., & Stewart, R. (2014). Thermal, acoustic and seismic signals from pyroclastic density currents and Vulcanian explosions at Soufrière Hills Volcano, Montserrat. *Geological Society, London, Memoirs*, *39*(1), 169-178.

Dowling, C. A., & Santi, P. M. (2014). Debris flows and their toll on human life: a global analysis of debris-flow fatalities from 1950 to 2011. *Natural hazards*, *71*(1), 203-227.

Drob, D. P., Picone, J. M., & Garcés, M. (2003). Global morphology of infrasound propagation. *Journal of Geophysical Research: Atmospheres*, *108*(D21).

Eckerstorfer, M., Bühler, Y., Frauenfelder, R., & Malnes, E. (2016). Remote sensing of snow avalanches: Recent advances, potential, and limitations. *Cold Regions Science and Technology*, *121*, 126-140.

Enos, P. (1977). Flow regimes in debris flow. *Sedimentology*, *24*(1), 133-142.

Estep, J., & Dufek, J. (2012). Substrate effects from force chain dynamics in dense granular flows. *Journal of Geophysical Research: Earth Surface*, *117*(F1).

Farin, M., Tsai, V. C., Lamb, M. P., & Allstadt, K. E. (2019). A physical model of the high-frequency seismic signal generated by debris flows. *Earth Surface Processes and Landforms*, *44*(13), 2529-2543.

Feng, H. N., Yang, Y. C., Chunchuzov, I. P., & Teng, P. X. (2014). Study on Infrasound From a Water Dam. *Acta Acustica united with Acustica*, *100*(2), 226-234.

Ferrick, M. G. (1985). Analysis of river wave types. *Water Resources Research*, *21*(2), 209-220.

Firth, B.A. and Hunter, R.J., 1976. Flow properties of coagulated suspensions. *J. Colloid Interface Sci.*, *57*: 248-275.

Frank, F., McArdell, B. W., Huggel, C., & Vieli, A. (2015). The importance of entrainment and bulking on debris flow runout modeling: examples from the Swiss Alps. *Natural Hazards and Earth System Sciences*, *15*(11), 2569-2583.

Friedman, G. M., Sanders, J. E., & Kopaska-Merkel, D. C. (1992). Principles of sedimentary deposits: stratigraphy and sedimentology. Macmillan College.

García-Martínez, R., & López, J. L. (2005). Debris flows of December 1999 in Venezuela. In *Debris-flow hazards and related phenomena* (pp. 519-538). Springer, Berlin, Heidelberg.

Giannecchini, R., Galanti, Y., Avanzi, G. D. A., & Barsanti, M. (2016). Probabilistic rainfall thresholds for triggering debris flows in a human-modified landscape. *Geomorphology*, *257*, 94-107.

Gimbert, F., Tsai, V. C., & Lamb, M. P. (2014). A physical model for seismic noise generation by turbulent flow in rivers. *Journal of Geophysical Research: Earth Surface*, *119*(10), 2209-2238.

Glassey, T. (2013). Hydrology and check dam analysis in the debris flow context of Illgraben torrent, VS. *Collection des articles des travaux de diplôme Collection of papers of the diploma theses*.

Gregoretti, C., & Dalla Fontana, G. (2008). The triggering of debris flow due to channel-bed failure in some alpine headwater basins of the Dolomites: Analyses of critical runoff. Hydrological Processes: *An International Journal*, *22*(13), 2248-2263.

Haeberli, W., Guodong, C., Gorbunov, A. P., & Harris, S. A. (1993). Mountain permafrost and climatic change. *Permafrost and Periglacial Processes*, *4*(2), 165-174.

He, S., Liu, W., & Li, X. (2016). Prediction of impact force of debris flows based on distribution and size of particles. *Environmental Earth Sciences*, *75*, 1-8.

Hedstrm, B. O. (1952). Flow of plastic materials in pipes. *Industrial & Engineering Chemistry*, 44(3), 651-656.

Henderson, F. M. (1996). Open channel flow.

Horoshenkov, K. V., Nichols, A., Tait, S. J., & Maximov, G. A. (2013). The pattern of surface waves in a shallow free surface flow. *Journal of Geophysical Research: Earth Surface*, *118*(3), 1864-1876.

Hsu, L., Finnegan, N. J., & Brodsky, E. E. (2011). A seismic signature of river bedload transport during storm events. *Geophysical Research Letters*, *38*(13).

Hu, K., Wei, F., & Li, Y. (2011). Real-time measurement and preliminary analysis of debris-flow impact force at Jiangjia Ravine, China. *Earth Surface Processes and Landforms*, *36*(9), 1268-1278.

Hübl, J., Suda, J., Proske, D., Kaitna, R., & Scheidl, C. (2009, September). Debris flow impact estimation. In *Proceedings of the 11th international symposium on water management and hydraulic engineering, Ohrid, Macedonia* (Vol. 1, pp. 1-5).

Hübl, J., Zhang, S. C., & Kogelnig, A. (2008, June). Infrasound measurements of debris flow. In *WIT Transactions on Engineering Sciences, Second International Conference on Monitoring, Simulation, Prevention and Remediation of Dense and Debris Flows II* (Vol. 60, pp. 3-12).

Hürlimann, M., Coviello, V., Bel, C., Guo, X., Berti, M., Graf, C., ... & Yin, H. Y. (2019). Debris-flow monitoring and warning: Review and examples. *Earth-science reviews*, *199*, 102981.

Hürlimann, M., Rickenmann, D., & Graf, C. (2003). Field and monitoring data of debris-flow events in the Swiss Alps. *Canadian geotechnical journal*, *40*(1), 161-175.

Ichihara, M., Takeo, M., Yokoo, A., Oikawa, J., & Ohminato, T. (2012). Monitoring volcanic activity using correlation patterns between infrasound and ground motion. *Geophysical Research Letters*, *39*(4).

Inouye, D. W. (2020). Effects of climate change on alpine plants and their pollinators. *Annals of the New York Academy of Sciences*, *1469*(1), 26-37.

Iverson, R. M. (1997, August). Hydraulic modeling of unsteady debris-flow surges with solid-fluid interactions. In Proceedings, First International Conference on Debris-Flow Hazards Mitigation: Mechanics, Prediction, and Assessment: Hydraulics Division, American Society of Civil Engineers (pp. 550-560).

Iverson, R. M., & Vallance, J. W. (2001). New views of granular mass flows. *Geology*, *29*(2), 115-118.

Iverson, R. M., Reid, M. E., & LaHusen, R. G. (1997). Debris-flow mobilization from landslides. *Annual Review of Earth and Planetary Sciences*, *25*(1), 85-138.

Jakob, M., Holm, K., Lange, O., & Schwab, J. W. (2006). Hydrometeorological thresholds for landslide initiation and forest operation shutdowns on the north coast of British Columbia. *Landslides*, *3*(3), 228-238.

Johnson, A. M. (1970). Physical processes in geology: A method for interpretation of natural phenomena; intrusions in igneous rocks, fractures, and folds, flow of debris and ice. Freeman, Cooper.

Johnson, A. M., & Rodine, J. R. (1984). Debris flow (Chapter 8). Slope Instability, eds. D. Brunsden & DB Prior.

Johnson, J. B., & Palma, J. L. (2015). Lahar infrasound associated with Volcán Villarrica's 3 March 2015 eruption. *Geophysical Research Letters*, *42*(15), 6324-6331.

Johnson, J. B., & Ripepe, M. (2011). Volcano infrasound: A review. *Journal of Volcanology and Geothermal Research*, *206*(3-4), 61-69.

Johnson, K. L., & Johnson, K. L. (1987). *Contact mechanics*. Cambridge university press.

Kataoka, K. S., Matsumoto, T., Saito, T., Kawashima, K., Nagahashi, Y., Iyobe, T., ... & Suzuki, K. (2018). Lahar characteristics as a function of triggering mechanism at a seasonally snow-clad

volcano: contrasting lahars following the 2014 phreatic eruption of Ontake Volcano, Japan. *Earth, Planets and Space*, *70*(1), 1-28.

Kean, J. W., Coe, J. A., Coviello, V., Smith, J. B., McCoy, S. W., & Arattano, M. (2015). Estimating rates of debris flow entrainment from ground vibrations. *Geophysical Research Letters*, *42*(15), 6365-6372.

Kean, J. W., McCoy, S. W., Tucker, G. E., Staley, D. M., & Coe, J. A. (2013). Runoff-generated debris flows: Observations and modeling of surge initiation, magnitude, and frequency. *Journal of Geophysical Research: Earth Surface*, *118*(4), 2190-2207.

Keefer DK, Wilson RC, Mark RK, Brabb EE, Brown WM, Ellen SD, Harp EL, Wieczorek GF, Alger CS,Zatkin RS (1987) Real-time landslide warning during heavy rainfall. *Science* 238:921–925. doi:10.1126/science.238.4829.921.

Kirtskhalia, V. G. (2012). Speed of sound in atmosphere of the Earth. *Open Journal of Acoustics*, *2*(2), 80-85.

Kogelnig, A., Hübl, J., Suriñach, E., Vilajosana, I., & McArdell, B. W. (2014). Infrasound produced by debris flow: propagation and frequency content evolution. *Natural hazards*, *70*(3), 1713-1733.

Kogelnig, A., Suriñach, E., Vilajosana, I., Hübl, J., Sovilla, B., Hiller, M., & Dufour, F. (2011). On the complementariness of infrasound and seismic sensors for monitoring snow avalanches. *Natural Hazards and Earth System Sciences*, *11*(8), 2355-2370.

Kudo, N. (1993). Control of infrasonic noise from a waterfall. *Journal of Low Frequency Noise, Vibration and Active Control*, *12*(4), 149-155.

Lacanna, G., Ichihara, M., Iwakuni, M., Takeo, M., Iguchi, M., & Ripepe, M. (2014). Influence of atmospheric structure and topography on infrasonic wave propagation. *Journal of Geophysical Research: Solid Earth*, *119*(4), 2988-3005.

Lai, V. H., Tsai, V. C., Lamb, M. P., Ulizio, T. P., & Beer, A. R. (2018). The seismic signature of debris flows: Flow mechanics and early warning at Montecito, California. *Geophysical Research Letters*, *45*(11), 5528-5535.

Lamb, M. P., Dietrich, W. E., & Sklar, L. S. (2008). A model for fluvial bedrock incision by impacting suspended and bed load sediment. *Journal of Geophysical Research: Earth Surface*, *113*(F3).

Lavigne, F., Thouret, J. C., Voight, B., Young, K., LaHusen, R., Marso, J., ... & Dejean, M. (2000). Instrumental lahar monitoring at Merapi Volcano, Central Java, Indonesia. *Journal of volcanology and geothermal research*, *100*(1-4), 457-478.

Le Pichon, A., Ceranna, L., Pilger, C., Mialle, P., Brown, D., Herry, P., & Brachet, N. (2013). The 2013 Russian fireball largest ever detected by CTBTO infrasound sensors. *Geophysical Research Letters*, *40*(14), 3732-3737.

Liszka, L. (2004). On the possible infrasound generation by sprites. *Journal of low frequency noise, vibration and active control*, *23*(2), 85-93.

Liszka, L., & Waldemark, K. (1995). High resolution observations of infrasound generated by the supersonic flights of Concorde. *Journal of Low Frequency Noise, Vibration and Active Control*, *14*(4), 181-192.

Liu, D. L., Leng, X. P., Wei, F. Q., Zhang, S. J., & Hong, Y. (2015). Monitoring and recognition of debris flow infrasonic signals. *Journal of Mountain Science*, *12*(4), 797-815.

Liu, D., Leng, X., Wei, F., Zhang, S., & Hong, Y. (2018). Visualized localization and tracking of debris flow movement based on infrasound monitoring. *Landslides*, *15*(5), 879-893.

Lliboutry, L. (1977). Glaciological problems set by the control of dangerous lakes in Cordillera Blanca, Peru. II. Movement of a covered glacier embedded within a rock glacier. *Journal of Glaciology*, *18*(79), 255-274.

Lopez, J. L., Perez, D., & Garcia, R. (2003, September). Hydrologic and geomorphologic evaluation of the 1999 debris-flow event in Venezuela. In *3rd international conference on debris flow hazard mitigation: mechanics, prediction, and assessment. Davos, Switzerland* (pp. 13-15).

Luzi, G., Pieraccini, M., Mecatti, D., Noferini, L., Guidi, G., Moia, F., & Atzeni, C. (2004). Ground-based radar interferometry for landslides monitoring: atmospheric and instrumental decorrelation sources on experimental data. *IEEE transactions on geoscience and remote sensing*, *42*(11), 2454-2466.

Major, J. J., Iverson, R. M., McTigue, D. F., Macias, S., & Fiedorowicz, B. K. (1997). Geotechnical properties of debris-flow sediments and slurries. In *Proceedings of the 1997 1st International*

Conference on Debris-Flow Hazards Mitigation: Mechanics, Prediction, and Assessment (pp. 249-259).

Marchetti, E., Lacanna, G., Le Pichon, A., Piccinini, D., & Ripepe, M. (2016). Evidence of large infrasonic radiation induced by earthquake interaction with alluvial sediments. *Seismological Research Letters*, *87*(3), 678-684.

Marchetti, E., Ripepe, M., Ulivieri, G., & Kogelnig, A. (2015). Infrasound array criteria for automatic detection and front velocity estimation of snow avalanches: towards a real-time early-warning system. *Natural Hazards and Earth System Sciences*, *15*(11), 2545-2555.

Marchetti, E., Ripepe, M., Ulivieri, G., Caffo, S., & Privitera, E. (2009). Infrasonic evidences for branched conduit dynamics at Mt. Etna volcano, Italy. *Geophysical research letters*, *36*(19).

Marchetti, E., van Herwijnen, A., Christen, M., Silengo, M. C., & Barfucci, G. (2020). Seismo-acoustic energy partitioning of a powder snow avalanche. *Earth Surface Dynamics*, *8*(2), 399-411.

Marchetti, E., Walter, F., Barfucci, G., Genco, R., Wenner, M., Ripepe, M., ... & Price, C. (2019). Infrasound array analysis of debris flow activity and implication for early warning. *Journal of Geophysical Research: Earth Surface*, *124*(2), 567-587.

Marchi, L., Arattano, M., & Deganutti, A. M. (2002). Ten years of debris-flow monitoring in the Moscardo Torrent (Italian Alps). *Geomorphology*, *46*(1-2), 1-17.

Marcial, S. E. R. G. I. O., Melosantos, A. A., Hadley, K. C., LaHusen, R. G., & Marso, J. N. (1996). Instrumental lahar monitoring at Mount Pinatubo. *Fire and mud: eruptions and lahars of Mount Pinatubo, Philippines, edited by: Newhall, CG and Punongbayan, RS, Washington Press, Seattle*, 1015-1022.

Martorana, R., Capizzi, P., D'Alessandro, A., Luzio, D., Di Stefano, P., Renda, P., & Zarcone, G. (2018). Contribution of HVSR measures for seismic microzonation studies. *Annals of Geophysics*.

Matsuzawa, T., Obara, K., & Maeda, T. (2009). Source duration of deep very low frequency earthquakes in western Shikoku, Japan. *Journal of Geophysical Research: Solid Earth*, *114*(B11).

McArdell, B. W., & Badoux, A. (2007, April). Influence of rainfall on the initiation of debris flows at the Illgraben catchment, canton of Valais, Switzerland. In *Geophysical Research Abstracts* (Vol. 9, p. 08804).

McArdell, B. W., & Sartori, M. (2021). The illgraben torrent system. *Landscapes and landforms of Switzerland*, 367-378.

McArdell, B. W., Bartelt, P., & Kowalski, J. (2007). Field observations of basal forces and fluid pore pressure in a debris flow. *Geophysical research letters*, *34*(7).

McNutt, S. R., Thompson, G., Johnson, J., De Angelis, S., & Fee, D. (2015). Seismic and infrasonic monitoring. In *The encyclopedia of volcanoes* (pp. 1071-1099). Academic Press.

M'Ewen, M. B., & Pratt, M. I. (1957). The gelation of montmorillonite. Part 1. The formation of a structural framework in sols of Wyoming bentonite. *Transactions of the Faraday Society*, *53*, 535-547.

Meyrat, G., McArdell, B., Ivanova, K., Müller, C., & Bartelt, P. (2021). A dilatant, two-layer debris flow model validated by flow density measurements at the Swiss illgraben test site. *Landslides*, 1-12.

Mikoš, M., & Majes, B. (2010). *Mitigation of large landslides and debris flows in Slovenia, Europe* (pp. 105-131). Nova Science Publishers.

Mutschlecner, J. P., & Whitaker, R. W. (2005). Infrasound from earthquakes. *Journal of Geophysical Research: Atmospheres*, *110*(D1).

Naugolnykh, K., & Bedard, A. (2002, June). A model of the avalanche infrasonic radiation. In *IEEE International Geoscience and Remote Sensing Symposium* (Vol. 2, pp. 871-872). IEEE.

Ng, C. W., Liu, H., Choi, C. E., Kwan, J. S., & Pun, W. K. (2021). Impact dynamics of boulder-enriched debris flow on a rigid barrier. *Journal of Geotechnical and Geoenvironmental Engineering*, *147*(3), 04021004.

Nikolopoulos, E. I., Borga, M., Creutin, J. D., & Marra, F. (2015). Estimation of debris flow triggering rainfall: Influence of rain gauge density and interpolation methods. *Geomorphology*, *243*, 40-50.

Okuda, S., Okunishi, K., Yokoyama, K., & Nakano, M. (1980). Observations on the motion of a debris flow and its geomorphological effects. *Zeitschrift für Geomorphologie. Supplementband Stuttgart*, (35), 142-163.

Ostrovsky, L. A. & Bedard, A. J. (2002, June). On generation of infrasound by large objects falling into water. In *IEEE International Geoscience and Remote Sensing Symposium* (Vol. 2, pp. 873-875). IEEE.

Pérez, F. L. (2001). Matrix granulometry of catastrophic debris flows (December 1999) in central coastal Venezuela. *Catena*, *45*(3), 163-183.

Phillips, C. J., & Davies, T. R. (1991). Determining rheological parameters of debris flow material. *Geomorphology*, *4*(2), 101-110.

Piantini, M., Gimbert, F., Korkolis, E., Rousseau, R., Bellot, H., & Recking, A. (2023). Solid concentration as a main proxy for basal force fluctuations generated by highly concentrated sediment flows. *Geophysical Research Letters*, *50*(1), e2022GL100345.

Pierson, T. C. (1980). Erosion and deposition by debris flows at Mt Thomas, north Canterbury, New Zealand. *Earth Surface Processes*, *5*(3), 227-247.

Pierson, T. C. (1985). Effects of slurry composition on debris flow dynamics, Rudd Canyon, Utah. Delineation of Landslide, Flash Flood, and Debris-Flow Hazard in Utah, Logan, Utah Water Research Laboratory, Utah State University, General series UWRL/G.

Pierson, T. C. (1986). Flow behaviour of channelized debris flows Mount St. Helens Washington. *Hillslope processes*, 269-296.

Pierson, T. C. (1995). Flow characteristics of large eruption-triggered debris flows at snow-clad volcanoes: constraints for debris-flow models. *Journal of volcanology and geothermal research*, *66*(1-4), 283-294.

Pierson, T. C., Costa, J. E., & Vancouver, W. (1987). A rheologic classification of subaerial sediment-water flows. Debris flows/avalanches: process, recognition, and mitigation. *Reviews in Engineering Geology*, *7*, 1-12.

Plafker, G., Ericksen, G. E., & Fernandez Concha, J. (1971). Geological aspects of the May 31, 1970, Peru earthquake. *Bulletin of the Seismological Society of America*, *61*(3), 543-578.

Ponziani, M., Pogliotti, P., Stevenin, H., & Ratto, S. M. (2020). Debris-flow Indicator for an early warning system in the Aosta valley region. *Natural Hazards*, *104*(2), 1819-1839.

Ravanel, L., Magnin, F., & Deline, P. (2017). Impacts of the 2003 and 2015 summer heatwaves on permafrost-affected rock-walls in the Mont Blanc massif. *Science of the Total Environment, 609*, 132-143.

Reid, M. E., LaHusen, R. G., & Iverson, R. M. (1997). Debris-flow initiation experiments using diverse hydrologic triggers. *Debris-Flow Hazards Mitigation: Mechanics, Prediction and Assessment*, 1-11.

Rickenmann, D. (1999). Empirical relationships for debris flows. *Natural hazards*, *19*(1), 47-77.

Rickenmann, D., Hürlimann, M., Graf, C., Näf, D., & Weber, D. (2001). Murgang-beobachtungsstationen in der Schweiz. *Wasser Energie Luft, 93*(1/2), 1-8.

Ripepe, M., De Angelis, S., Lacanna, G., Poggi, P., Williams, C., Marchetti, E., ... & Ulivieri, G. (2009). Tracking pyroclastic flows at Soufrière Hills volcano. *Eos, Transactions American Geophysical Union, 90*(27), 229-230.

Robinson, E., & Clark, D. (1991). Sampling and the Nyquist frequency. *The Leading Edge*, *10*(3), 51-53.

Sattler, K., Keiler, M., Zischg, A., & Schrott, L. (2011). On the connection between debris flow activity and permafrost degradation: a case study from the Schnalstal, South Tyrolean Alps, Italy. *Permafrost and Periglacial Processes*, *22*(3), 254-265.

Schimmel, A., & Hübl, J. (2015). Approach for an early warning system for debris flow based on acoustic signals. In *Engineering Geology for Society and Territory-Volume 3* (pp. 55-58). Springer, Cham.

Schimmel, A., & Hübl, J. (2016). Automatic detection of debris flows and debris floods based on a combination of infrasound and seismic signals. *Landslides*, *13*, 1181-1196.

Schimmel, A., Coviello, V., & Comiti, F. (2022). Debris flow velocity and volume estimations based on seismic data. *Natural Hazards and Earth System Sciences*, *22*(6), 1955-1968.

Schlunegger, F., Badoux, A., McArdell, B. W., Gwerder, C., Schnydrig, D., Rieke-Zapp, D., & Molnar, P. (2009). Limits of sediment transfer in an alpine debris-flow catchment, Illgraben, Switzerland. *Quaternary Science Reviews*, *28*(11-12), 1097-1105.

Schmandt, B., Aster, R. C., Scherler, D., Tsai, V. C., & Karlstrom, K. (2013). Multiple fluvial processes detected by riverside seismic and infrasound monitoring of a controlled flood in the Grand Canyon. *Geophysical Research Letters, 40*(18), 4858-4863.

Schmid, F., Fraefel, M., & Hegg, C. (2004). Unwetterschäden in der Schweiz 1972–2002: Verteilung, Ursachen, Entwicklung. *Wasser energ. luft*, *96*(1), 2.

Schonfeld, B. (1996). Roll waves in granular flows and debris flows.

Sepúlveda, S. A., Rebolledo, S., & Vargas, G. (2006). Recent catastrophic debris flows in Chile: Geological hazard, climatic relationships and human response. *Quaternary International*, *158*(1), 83-95.

Shapiro, S. A., & Kneib, G. (1993). Seismic attenuation by scattering: theory and numerical results. *Geophysical Journal International*, *114*(2), 373-391.

Sharp, R. P., & Nobles, L. H. (1953). Mudflow of 1941 at Wrightwood, southern California. *Geological Society of America Bulletin, 64*(5), 547-560.

Sheko. A.I.. 1988. Mudflows. In: Landslides and Mudflows (vol. 1). Ch. 3. UNESCO-UNEP, Moscow, USSR, pp. 54-74.

SHIEH, C. L., Chen, Y. S., Tsai, Y. J., & Wu, J. H. (2009). Variability in rainfall threshold for debris flow after the Chi-Chi earthquake in central Taiwan, China. *International Journal of Sediment Research*, *24*(2), 177-188.

Silbert, L. E., Ertaş, D., Grest, G. S., Halsey, T. C., Levine, D., & Plimpton, S. J. (2001). Granular flow down an inclined plane: Bagnold scaling and rheology. *Physical Review E, 64*(5), 051302.

Singh, R., Shekhar, M., Pandey, V. K., Kumar, R., & Sharma, R. K. (2018). Causes and geomorphological effects of large debris flows in the lower valley areas of the Meru and Gangotri glaciers, Bhagirathi basin, Garhwal Himalaya (India). *Remote Sensing Letters, 9*(8), 809-818.

Smart, G., & Jäggi, M. (1983). Sediment transport on steep slopes. Mitteilung. 64. *Versuchsanstalt fu r Wasserbau, Hydrologie und Glaziologie*.

Sneddon, I. N. (1995). *Fourier transforms*. Courier Corporation.

Solonenko, V.P., 1963. Mudflow activity in the pleistoseist region of catastrophic earthquakes. Bull. Moscow Sot. *Nature Workers Geol., 2*: 1333 140.

Stoffel, M., Mendlik, T., Schneuwly-Bollschweiler, M., & Gobiet, A. (2014). Possible impacts of climate change on debris-flow activity in the Swiss Alps. *Climatic Change*, *122*(1), 141-155.

Takahashi, T. (1981). Debris flow. *Annual review of fluid mechanics*, *13*(1), 57-77.

Tauzin, B., Debayle, E., Quantin, C., & Coltice, N. (2013). Seismoacoustic coupling induced by the breakup of the 15 February 2013 Chelyabinsk meteor. *Geophysical Research Letters*, *40*(14), 3522-3526.

Tecca, P. R., Galgaro, A., Genevois, R., & Deganutti, A. M. (2003). Development of a remotely controlled debris flow monitoring system in the Dolomites (Acquabona, Italy). *Hydrological processes*, *17*(9), 1771-1784.

Tokyay, N. D., & Yildiz, D. (2007). Characteristics of free overfall for supercritical flows. *Canadian Journal of Civil Engineering*, *34*(2), 162-169.

Tokyay, N. D., & Yildiz, D. (2007). Characteristics of free overfall for supercritical flows. *Canadian Journal of Civil Engineering*, *34*(2), 162-169.

Tsai, V. C., Minchew, B., Lamb, M. P., & Ampuero, J. P. (2012). A physical model for seismic noise generation from sediment transport in rivers. *Geophysical Research Letters*, *39*(2).

Ulivieri, G., Marchetti, E., Ripepe, M., Chiambretti, I., De Rosa, G., & Segor, V. (2011). Monitoring snow avalanches in Northwestern Italian Alps using an infrasound array. *Cold Regions Science and Technology*, *69*(2-3), 177-183.

Underwood, S. J., Schultz, M. D., Berti, M., Gregoretti, C., Simoni, A., Mote, T. L., & Saylor, A. M. (2016). Atmospheric circulation patterns, cloud-to-ground lightning, and locally intense convective rainfall associated with debris flow initiation in the Dolomite Alps of northeastern Italy. *Natural Hazards and Earth System Sciences*, *16*(2), 509-528.

Vázquez, R., Suriñach, E., Capra, L., Arámbula-Mendoza, R., & Reyes-Dávila, G. (2016). Seismic characterisation of lahars at Volcán de Colima, Mexico. *Bulletin of Volcanology*, *78*(2), 1-14.

Vergoz, J., Hupe, P., Listowski, C., Le Pichon, A., Garcés, M. A., Marchetti, E., ... & Mialle, P. (2022). IMS observations of infrasound and acoustic-gravity waves produced by the January 2022 volcanic eruption of Hunga, Tonga: A global analysis. *Earth and Planetary Science Letters*, *591*, 117639.

Vilajosana, I., Surinach, E., Abellán, A., Khazaradze, G., Garcia, D., & Llosa, J. (2008). Rockfall induced seismic signals: case study in Montserrat, Catalonia. *Nat. Hazards Earth Syst. Sci*, *8*(4), 805-812.

Voight, B. (1990). The 1985 Nevado del Ruiz volcano catastrophe: anatomy and retrospection. *Journal of volcanology and geothermal research*, *42*(1-2), 151-188.

Walsh, B., Jolly, A. D., & Procter, J. N. (2016). Seismic analysis of the 13 October 2012 Te Maari, New Zealand, lake breakout lahar: Insights into flow dynamics and the implications on mass flow monitoring. *Journal of Volcanology and Geothermal Research*, *324*, 144-155.

Walter, F., Burtin, A., McArdell, B. W., Hovius, N., Weder, B., & Turowski, J. M. (2017). Testing seismic amplitude source location for fast debris-flow detection at Illgraben, Switzerland. *Natural Hazards and Earth System Sciences*, *17*(6), 939-955.

Walter, F., Chmiel, M., & Hovius, N. (2022). Debris flows at Illgraben, Switzerland–From seismic wiggles to machine learning. *Geomechanics and Tunnelling*, *15*(5), 671-675.

Wang, B., Li, Y., Liu, D., & Liu, J. (2018). Debris flow density determined by grain composition. *Landslides*, *15*(6), 1205-1213.

Wenner, M., Walter, F., McArdell, B., & Farinotti, D. (2019). Deciphering debris-flow seismograms at Illgraben, Switzerland. In *Association of Environmental and Engineering Geologists; special publication 28*. Colourado School of Mines. Arthur Lakes Library.

Whipple, K. X., & Dunne, T. (1992). The influence of debris-flow rheology on fan morphology, Owens Valley, California. *Geological Society of America Bulletin*, *104*(7), 887-900.

Wieczorek, G. F. (2001). Debris-flow and flooding hazards caused by the December 1999 storm in coastal Venezuela. *US Geological Survey Open File Report*, *1*, 40.

Wills, C. J., Petersen, M., Bryant, W. A., Reichle, M., Saucedo, G. J., Tan, S., ... & Treiman, J. (2000). A site-conditions map for California based on geology and shear-wave velocity. Bulletin of the Seismological Society of America, 90(6B), S187-S208.

Yamasato, H. (1997). Quantitative analysis of pyroclastic flows using infrasonic and seismic data at Unzen volcano, Japan. *Journal of Physics of the Earth, 45*(6), 397-416.

Zhang, Z., Walter, F., McArdell, B. W., de Haas, T., Wenner, M., Chmiel, M., & He, S. (2021) (b). Analyzing bulk flow characteristics of debris flows using their high frequency seismic signature. *Journal of Geophysical Research: Solid Earth*, e2021JB022755.

Zhang, Z., Walter, F., McArdell, B. W., Wenner, M., Chmiel, M., de Haas, T., & He, S. (2021) (a). Insights from the particle impact model into the high frequency seismic signature of debris flows. *Geophysical Research Letters*, e2020GL088994.

Zimmermann, M. (2004). Managing debris flow risks. *Mountain Research and Development*, *24*(1), 19-23.